Electrochemical Society

GET YOUR FREE COPY OF THIS INFORMATIVE, ILLUSTRATED BROCHURE

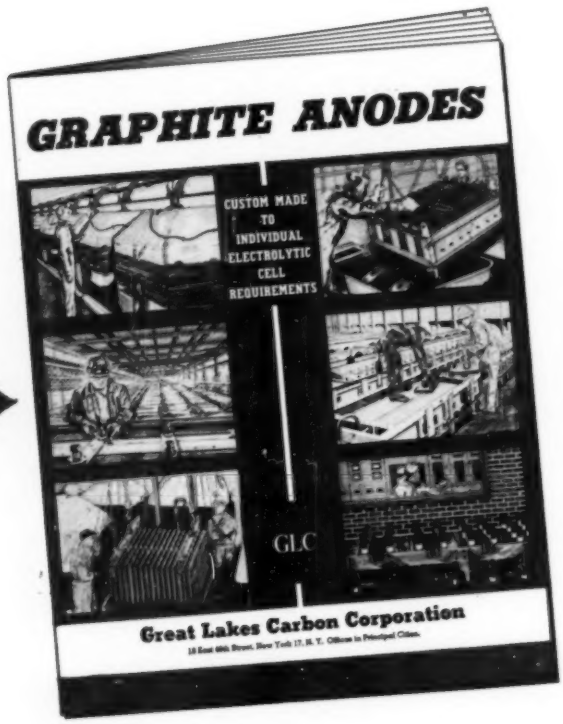

Everyone connected with electrolytic cell operations should have a copy of our new brochure GRAPHITE ANODES. It contains a wealth of useful information.

Here you will find tables of standard sizes and grades of square and rectangular anodes for diaphragm and mercury cells...reasons why anodes custom made to individual cell requirements are more economical and efficient...a brief review of our special anode production and machining facilities...and an explanation of our technical exchange program which has helped our customers lower cell operating costs.

Write us for a copy of GRAPHITE ANODES— it is yours for the asking.

PRODUCTS ELECTRODE GLC DIVISION YOU CAN TRUST ®

GREAT LAKES CARBON CORPORATION

18 EAST 48TH STREET, NEW YORK 17, N. Y.

EDITORIAL STAFF

C. L. Faust, Chairman, Publication Committee
Cecil V. King, Editor
Norman Hackerman, Technical Editor
Ruth G. Sterns, Managing Editor
U. B. Thomas, News Editor
H. W. Salzberg, Book Review Editor
Natalie Michalski, Assistant Editor

DIVISIONAL EDITORS

W. C. Vosburgh, Battery
Milton Stern, Corrosion
R. T. Foley, Corrosion
Louis J. Frisco, Electric Insulation
Seymour Senderoff, Electrodeposition
H. C. Froelich, Electronics
Ephraim Banks, Electronics
Ernest Paskell, Electronics—Semiconductors
D. R. Frankl, Electronics—Semiconductors
Sherlock Swann, Jr., Electro-Organic
Stanley Wawzonek, Electro-Organic
John M. Blocher, Jr., Electrothermics and Metallurgy
J. H. Westbrook, Electrothermics and Metallurgy
N. J. Johnson, Industrial Electrolytic
C. W. Tobias, Theoretical Electrochemistry
A. J. deBethune, Theoretical Electrochemistry
R. M. Hurd, Theoretical Electrochemistry

ADVERTISING OFFICE

ECS

1860 Broadway, New York 23, N. Y.

ECS OFFICERS

Henry B. Linford, President
Columbia University, New York, N. Y.

F. L. LaQue, Vice-President
International Nickel Co., Inc.,
New York, N. Y.

W. J. Hamer, Vice-President
National Bureau of Standards,
Washington, D. C.

Lyle I. Gilbertson, Vice-President
Air Reduction Co., Murray Hill, N. J.

Ernest G. Enck, Treasurer
Felicity Farm,
Gwynedd Valley, Pa.

Ivor E. Campbell, Secretary
National Steel Corp., Weirton, W. Va.

Robert K. Shannon, Executive Secretary
National Headquarters, The ECS,
1860 Broadway, New York 23, N. Y.

Manuscripts submitted to the Journal should be sent, in triplicate, to the Editorial Office at 1860 Broadway, New York 23, N. Y. They should conform to the revised Instructions to Authors, last published on pp. 145C-146C of the July 1961 issue. Manuscripts so submitted become the property of The Electrochemical Society and may not be published elsewhere, in whole or in part, unless permission is requested of and granted by the Editor.

The Electrochemical Society does not maintain a supply of reprints of papers appearing in its Journal. A photoprint copy of any particular paper, however, may be obtained by corresponding direct with the Engineering Societies Library, 29 W. 39 St., New York 18, N. Y.

Inquiries re positive microfilm copies of volumes should be addressed to University Microfilms, Inc., 313 N. First St., Ann Arbor, Mich.

Walter J. Johnson, Inc., 111 Fifth Ave., New York 3, N. Y., have reprint rights to out-of-print volumes of the Journal, and also have available for sale back volumes and single issues, with the exception of the current calendar year. Anyone interested in securing back copies should correspond direct with them.

Journal of the Electrochemical Society

OCTOBER 1961 **VOL. 108 • NO. 10**

CONTENTS

Editorial

Page Charge for Publication? 224C

Technical Papers

Gravity Field Effects on Zinc Anode Discharge in Alkaline Media. *M. Eisenberg, H. F. Bauman, and D. M. Brettner* 909

A Model for Electrochemical Reaction Kinetics of Solid-State Phase Transformations in Reversible Electrodes. *G. T. Croft and D. Tuomi* 915

Investigation of the Electrochemical Characteristics of Organic Compounds, VIII. Hydrazine and Hydroxylamine Compounds. *R. Glicksman* 922

Cathodic Behavior of Iron Single Crystals and the Oxides Fe_3O_4, Gamma-Fe_2O_3, and Alpha-Fe_2O_3. *C. D. Stockbridge, P. B. Sewell, and M. Cohen* 928

An Electrometric and Electron Diffraction Study of Air-Formed Oxide Films on Iron. *P. B. Sewell, C. D. Stockbridge, and M. Cohen* 933

The Formation of Porous Oxides on Metals, II. Tungsten and the Paralinear Rate Law. *W. B. Jepson and D. W. Aylmore* 942

Effect of Reynolds Number on Corrosion of Copper by Sulfuric Acid. *I. Cornet, E. A. Barrington, and G. U. Behrsing* 947

The Role of a Displacement Reaction in the Kinetics of Oxidation of Alloys. *R. L. Levin and J. B. Wagner, Jr.* 954

Composition and Thickness Effects on Magnetic Properties of Electrodeposited Nickel-Iron Thin Films. *I. W. Wolf* 959

Electrodeposition of Molten Metals and Alloys from Glycerine Solutions. *G. L. Schnable* 964

The Shape of Melt-Crystal Interfaces During Float Zoning of Silicon. *J. H. Braun and R. A. Pellin* 969

Characteristics of the {111} Surfaces of the III-V Intermetallic Compounds, III. The Effects of Surface Active Agents on InSb and the Identification of Antimony Edge Dislocations. *M. C. Lavine, H. C. Gatos, and M. C. Finn* 974

Polarography and Voltammetry in Dimethylsulfoxide. *I. M. Kolthoff and T. B. Reddy* 980

The Application of an X-Y Pulsed Measuring System to Polarization Studies, I. The Hydrogen Reaction on Platinum. *C. H. Presbrey, Jr., and S. Schuldiner* 985

Technical Notes

Effects of Saccharin on the Structural and Magnetic Properties of Iron-Nickel Films. *R. S. Smith, L. E. Godycki, and J. C. Lloyd* 996

Some New Measurements of Infrared Luminescence in Tunnel Diodes. *J. I. Pankove.* 998

Cell Conductivity Measuring Circuit. *F. E. Dickey* 1000

Technical Review

Report of the Chlor-Alkali Committee of the Industrial Electrolytic Division for the Year 1960. *J. E. Currey and C. A. Hampel* 1001

Feature Section

Professor Colin Garfield Fink. *H. B. Linford and H. K. Fink* 229C

Current Affairs 232C-238C

Published monthly by The Electrochemical Society, Inc., from Manchester, N. H., **Executive Offices, Editorial Office** and **Circulation Dept.,** and **Advertising Office** at 1860 Broadway, New York 23, N. Y., combining the JOURNAL and TRANSACTIONS OF THE ELECTROCHEMICAL SOCIETY. Statements and opinions given in articles and papers in the JOURNAL OF THE ELECTROCHEMICAL SOCIETY are those of the contributors, and The Electrochemical Society assumes no responsibility for them. Subscription to members as part of membership service; subscription to nonmembers $24.00. Single copies $1.70 to members, $2.25 to nonmembers.

Copyright 1961 by The Electrochemical Society, Inc.

Entered as second-class matter at the Post Office at Manchester, N. H., under the act of August 24, 1912.

Editorial

Page Charge for Publication?

SIXTEEN months ago our Society had a balanced budget, but an uncomfortably small reserve fund which was in danger of decreasing rather than increasing. The committees involved, and the Board of Directors, considered the desirability of imposing a page charge for the publication of technical articles in the JOURNAL, which had been facing rising costs for several years. The decision was, instead, to raise membership dues and subscription rates, and to intensify the drive for new Active, Sustaining, and Patron members. We believe this decision was a sound one, in view of the increased offering of the JOURNAL and of the obvious interest of many nonmembers in the Meeting programs and in the JOURNAL.

The American Institute of Physics many years ago instituted a page charge for its numerous publications, and several other Societies have done the same. The American Chemical Society has considered a page charge; ACS is faced, for example, with a larger and larger journal and a falling number of subscribers. The cost problems, and the pros and cons of the page charge, have been discussed by R. H. Belknap, ACS Director of Planning for Fundamental Journals, in the July 17 and 24 issues of *Chemical and Engineering News*.

The most widely used argument to justify a page charge is that publication cost is a part of the cost of research, and a small part at that; a research is not complete until its results have been made available to the public. While this argument has validity, the real reason for the page charge is, of course, to raise money in a way which causes the minimum of "squawking." If subscription rates go up, the customers can complain very effectively by resigning, and there is a point of diminishing return. On the other hand, the page charge is requested but not made mandatory; authors are never expected to pay personally, their sponsors do not have to pay if they feel it a hardship or even if they object. The return is 75-95%, with companies and government agencies accepting the charge as a matter of course.

A principal objection to the page charge is that authors might expect anything they send in to be published without regard to length or quality. Fortunately, this has not been a serious problem for two reasons: the charge is always well below the actual cost of publication; and, especially, because the integrity of editorial and review staffs simply does not permit it.

The cost of printing and mailing our JOURNAL is, at present, about $40.00 per page, including the pages used for advertising, which, of course, more than pay for themselves. Other costs, including postage (a not inconsiderable item since every manuscript is mailed several times), salaried staff, and office space, are difficult to estimate; probably come to about $15.00 per page. Societies which make a charge would perhaps ask $35.00 per page; this would apply to the technical articles, about 75% of our JOURNAL. Reprints (a limited number) would be supplied without further cost.

This is a problem which is engaging the attention of most societies these days.

—CVK

WHAT ARE YOU DOING TO STOP CELL ROOM FLOOR DETERIORATION?

You Could Save Thousands Of Dollars By Resurfacing Floors Now With—

EPOLOID

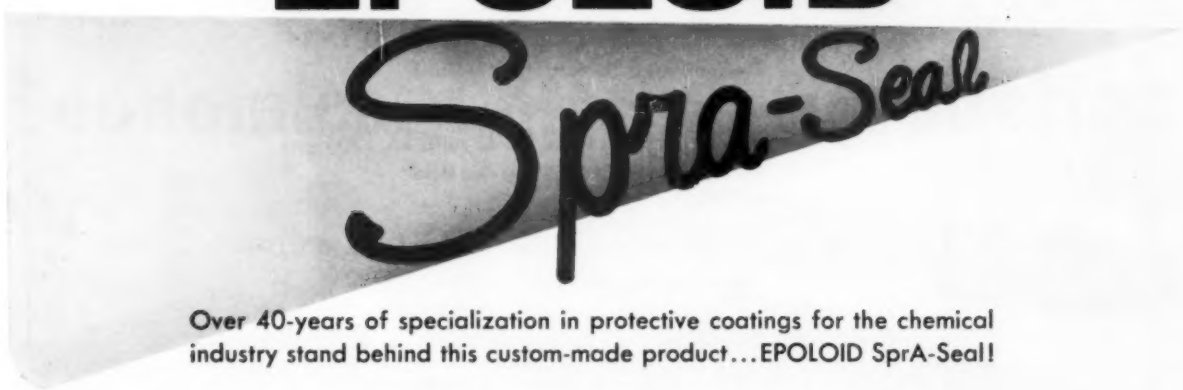

Over 40-years of specialization in protective coatings for the chemical industry stand behind this custom-made product...EPOLOID SprA-Seal!

For Full Information, Mail The Attached Coupon To:

ROWE PRODUCTS INC.

College Ave. and Hyde Park Blvd.
Niagara Falls, New York
Phone: Butler 5-9348

RE: EPOLOID SPRA-SEAL

NAME

TITLE

COMPANY

ADDRESS

FUTURE MEETINGS OF
The Electrochemical Society

Detroit, Mich., October 1, 2, 3, 4, and 5, 1961
Headquarters at the Statler Hilton Hotel
Sessions will be scheduled on
Batteries, Corrosion (including a Symposium on Surface Structure vs. Corrosion Behavior), Battery–Corrosion Joint Symposium on Fused Salt Corrosion, Electrodeposition (including symposia on Addition Agents and on Electrodeposited Magnetic Films), Electronics (Semiconductors), Electro-Organics, and Electrothermics and Metallurgy
(*See* pp. 133C-186C of August issue for complete program)

★ ★ ★

Los Angeles, Calif., May 6, 7, 8, 9, and 10, 1962
Headquarters at the Statler Hilton Hotel
Sessions probably will be scheduled on
Electric Insulation, Electronics (including Luminescence, Semiconductors, Optical Masers, and Nonconventional Electron Emitters), Electrothermics and Metallurgy (including a Symposium on Thermodynamics and Kinetics of Gas-Condensed Phase Reactions at High Temperatures), Industrial Electrolytics, and Theoretical Electrochemistry

★ ★ ★

Boston, Mass., September 16, 17, 18, 19, and 20, 1962
Headquarters at the Statler Hilton Hotel

★ ★ ★

Pittsburgh, Pa., April 14, 15, 16, 17, and 18, 1963
Headquarters at the Penn Sheraton Hotel

★ ★ ★

New York, N. Y., September 29, 30, and October 1, 2, and 3, 1963
Headquarters at the New Yorker Hotel

★ ★ ★

Toronto, Ont., Canada, May 3, 4, 5, 6, and 7, 1964
Headquarters at the Royal York Hotel

Papers are now being solicited for the meeting to be held in Los Angeles, Calif., May 6-10, 1962. Triplicate copies of each abstract (*not exceeding 75 words in length*) are due at Society Headquarters, 1860 Broadway, New York 23, N. Y., *not later than December 15, 1961* in order to be included in the program. *Please indicate on abstract for which Division's symposium the paper is to be scheduled, and underline the name of the author who will present the paper.* No paper will be placed on the program unless one of the authors, or a qualified person designated by the authors, has agreed to present it in person. An author who wishes his paper considered for publication in the JOURNAL should send triplicate copies of the manuscript to the Managing Editor of the JOURNAL, 1860 Broadway, New York 23, N. Y.

Presentation of a paper at a technical meeting of the Society does not guarantee publication in the JOURNAL. However, all papers so presented become the property of The Electrochemical Society, and may not be published elsewhere, either in whole or in part, unless permission for release is requested of and granted by the Editor. Papers already published elsewhere, or submitted for publication elsewhere, are not acceptable for oral presentation except on invitation by a Divisional program Chairman.

any way you measure

ANODE PERFORMANCE

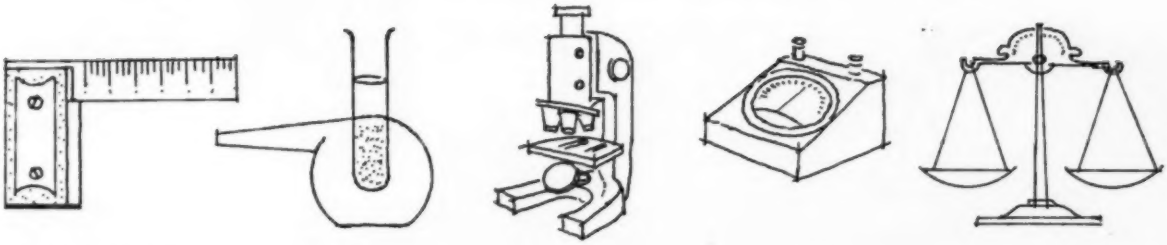

Structural and Dimensional Uniformity?

Chemical Stability of Treatments?

Uniform Texture?

Cell Voltage?

Pounds Consumed per ton of Chlorine Produced?

STACKPOLE

GraphAnode® ANODES

prove second to none for

Economical Chlorine Production

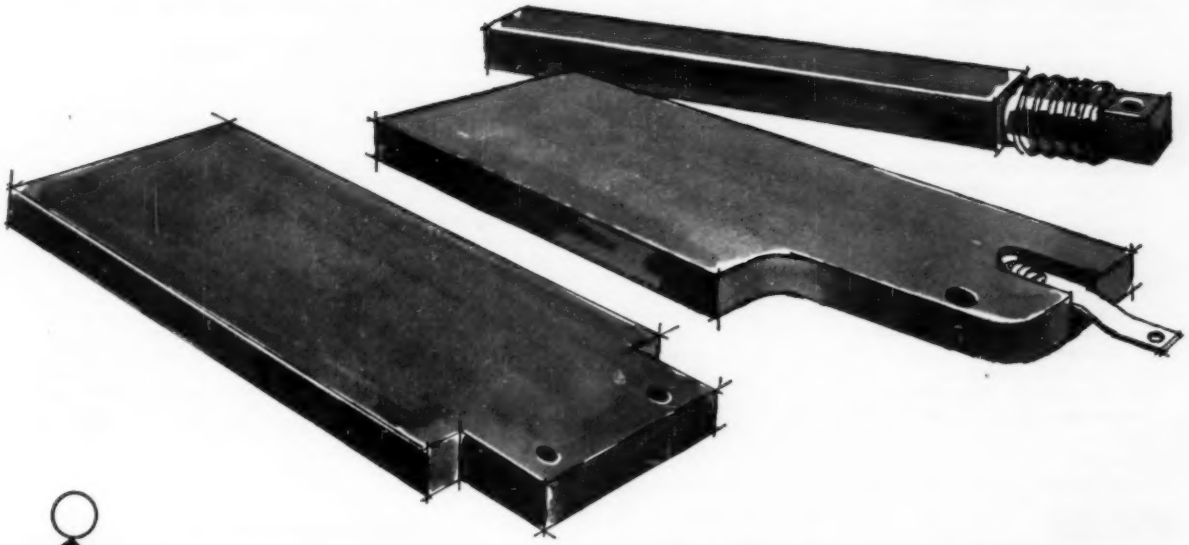

STACKPOLE CARBON COMPANY,
St. Marys, Pa.

CATHODIC PROTECTION ANODES • FLUXING & DE-GASSING TUBES • SALT BATH RECTIFICATION RODS • ROCKET NOZZLES • RISER RODS • GRAPHITE BEARINGS & SEAL RINGS • ELECTRODES & HEATING ELEMENTS • WELDING CARBONS • VOLTAGE REGULATOR DISCS • **"CERAMAGNET"®** CERAMIC MAGNETS • ELECTRICAL CONTACTS • BRUSHES FOR ALL ROTATING ELECTRICAL EQUIPMENT • AND MANY OTHER CARBON, GRAPHITE AND ELECTRONIC COMPONENTS.

SARGENT-SLOMIN ANALYZERS
are standard equipment in prominent laboratories

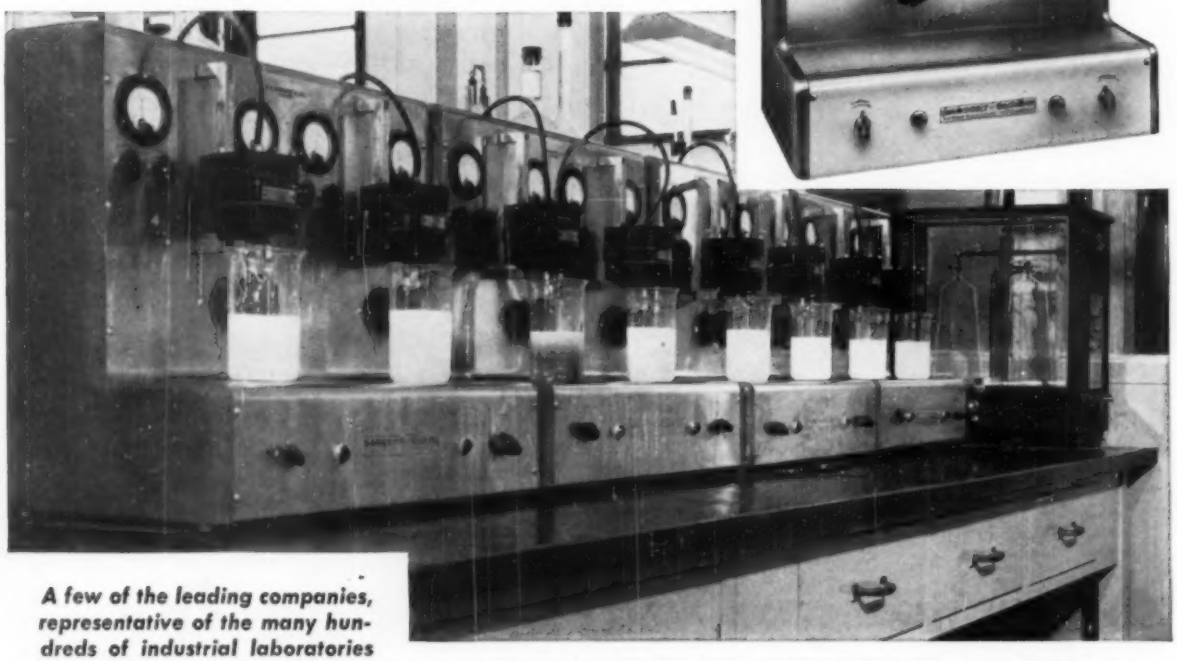

Photo Courtesy INTERNATIONAL HARVESTER COMPANY, Melrose Park, Illinois

A few of the leading companies, representative of the many hundreds of industrial laboratories using the Sargent - Slomin and Heavy Duty Analyzers for control analyses . . .

AMPCO METAL, Inc.
ANDERSON LABORATORIES
CALERA MINING COMPANY
EUREKA WILLIAMS COMPANY
THE FEDERAL METAL CO.
FORD MOTOR COMPANY
THE GLIDDEN COMPANY—Chemical, Metal and Pigment Division
HOT POINT CO.
HOWARD FOUNDRY COMPANY
INTERNATIONAL HARVESTER COMPANY
KENNAMETAL Inc.
McQUAY - NORRIS MANUFACTURING CO.
NATIONAL LEAD COMPANY, Fredericktown, Missouri
PIASECKI HELICOPTER CORPORATION
REVERE COPPER & BRASS INCORPORATED
THE RIVER SMELTING & REFINING COMPANY
SILAS MASON COMPANY
THE STUDEBAKER CORPORATION
THOMPSON PRODUCTS, INC.

Sargent-Slomin Electrolytic Analyzers are recommended for such electro analytical determinations as: Copper in—ores, brass, iron, aluminum and its alloys, magnesium and its alloys, bronze, white metals, silver solders, nickel and zinc die castings. Lead in—brass, aluminum and its alloys, bronze, zinc and zinc die castings. Assay of electrolytical copper, nickel and other metals.

Sargent analyzers are completely line operated, employing self-contained rectifying and filter circuits. Deposition voltage is adjusted by means of autotransformers, with meters indicating volts and amperes and controls on the panel. An easily replaceable fuse guards against circuit overload. Maximum D.C. current capacity is 5 to 15 amperes; maximum D.C. voltage available, 10 volts.

Sargent-Slomin Analyzers stir through a rotating chuck operated from a capacitor type induction motor, having a fixed speed of 550 r.p.m. with 60 cycle A.C. current or 460 r.p.m. with 50 cycle A.C. current. Motors are sealed against corrosive fumes and are mounted on cast metal brackets, sliding on ½" square stainless steel rods, permitting vertical adjustment of electrode position over a distance of 4". Pre-lubricated ball-bearings support the rotating shaft. All analyzers accommodate electrodes having shaft diameters no greater than 0.059 inch. Stainless steel spring tension chucks permit quick, easy insertion of electrodes and maintain proper electrical contact. Special Sargent high efficiency electrodes are available for these analyzers. Illustrated above is one model of the five types of Sargent-Slomin and Heavy Duty Analyzers.

S-29465 ELECTROLYTIC ANALYZER—Motor stirred, Two Position, 5 Ampere. With two adjustable heaters, pilot lights and control knobs. For operation from 115 volt, 50 or 60 cycle A.C. circuits.....**$590.00**

SARGENT *SCIENTIFIC LABORATORY INSTRUMENTS • APPARATUS • SUPPLIES • CHEMICALS*

E. H. SARGENT & CO., 4647 WEST FOSTER AVE., CHICAGO 30, ILLINOIS
DETROIT 4, MICH. • DALLAS 35, TEXAS • BIRMINGHAM 4, ALA. • SPRINGFIELD, N. J. • ANAHEIM, CALIF.

Gravity Field Effects on Zinc Anode Discharge in Alkaline Media

M. Eisenberg, H. F. Bauman, and D. M. Brettner

Lockheed Missiles and Space Division, Sunnyvale, California

ABSTRACT

Under conditions of zero-gravity such as may prevail in satellites and space vehicles the absence of free convection may represent a major problem in the use of some primary or secondary batteries. An experimental study was carried out on smooth zinc anodes in 30% KOH solutions in which constant current discharge at various current densities was carried out to the point of passivation. By use of three different orientations in the gravitational field, different modes of mass transfer were obtained. An extrapolation of the results for low current density and long duration runs (over 20 sec) led to three limiting current densities values for the three positions. These values were also calculated from theoretical equations using measured or estimated physical properties. The importance of free convection *vs.* diffusion was also demonstrated by means of incremental fixed current-time experiments which determined anode capacity to passivation. Physical properties of the system were measured and anodic dissolution studies were made to obtain the necessary data for calculations. The gravity field effects important in systems involving density gradients would become even more important under the influence of larger accelerations in space vehicles or missiles. These accelerations could produce sizable differences in the performance of porous zinc anodes.

The advent of space exploration and space flight gives rise to some interesting questions as to the effect that zero-gravity, or near zero-gravity, may have on the performance of primary and secondary batteries and of fuel cells in space vehicles. In an earlier study by Eisenberg (1), the effect of the absence of free convection resulting from the gravitational field of the earth was considered theoretically in regard to the mass transfer mechanism for a soluble anode such as zinc in alkaline media. Due to the unavailability of reliable physico-chemical data on alkaline zincate solutions, only approximate numerical examples were given at that time (1).

In view of the difficult problem of realizing gravity-free conditions in a laboratory, it was decided to study the effects of the gravity field by changing its orientation in respect to the concentration and density gradient in the vicinity of the working anodic electrode. Three different electrode orientations were chosen and used successfully for the purposes of this study. Although the effects of zero-gravity conditions on batteries and fuel cells may be manifold (*e.g.*, difficulties in phase separation, complications due to overcharge of cathode and/or anode, etc.), the experimental study was limited to the problem of absence of free convection in a battery. This convection is related to the density gradient resulting from a concentration buildup in the vicinity of a soluble anode.

Experimental Procedures

As discussed in the introduction, the simplest manner in which gravity field effects on the anode discharge mechanism could be studied under laboratory conditions was by a choice of three positions illustrated in Fig. 1.

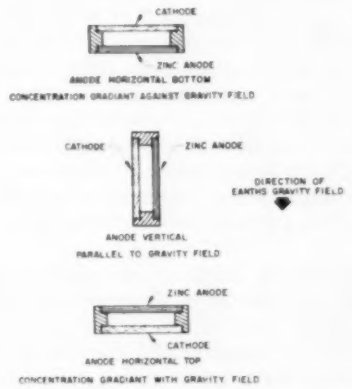

Fig. 1. Three orientations of the gravity field

Mass-transfer calculations require the knowledge of physical properties of the bulk electrolyte and the electrolyte in the vicinity of the working electrode. For the sake of simplicity, all properties were determined in 6.924M (30% by weight) potassium hydroxide solutions at room temperature. Essentially carbonate-free reagent grade potassium hydroxide was used. No efforts were made to remove any dissolved oxygen from the solutions.

Physical properties.—Viscosity and density measurements at 25°C were made of 6.924M KOH solutions saturated with ZnO in a constant temperature bath controlled to ±0.05°C. The clear supernatant solution was decanted and density and viscosity determined by conventional methods. Zinc analysis was carried out by titration with potassium ferrocyanide solution. In addition, density of pure 6.924M KOH (approximately 30% by weight) solution was measured.

Table I. Concentration studies on thin electrolyte layers near anode

Temperature, 24° ± 1°C; anode area, 73.6 cm²

Run No.	Sample collection technique	Current density, ma/cm²	Duration of run, min	Capacity, coulombs/cm²	Estimated anode layer density, g/cm³	Experimental zinc concentration in sampled layer, C_{av} m/l	Experimental zinc concentration in bulk solution, C_o m/l	Extrapolated interfacial zinc concentration, C_i m/l
S-7	Drip	163/81.5	15	—	1.350	0.94	—	—
S-8	Drip	81.5	25	1.225	1.349	0.94	—	—
S-9	Paper	81.5	25	1.225	1.351	0.95	—	—
S-10	Paper	81.5	25	1.225	1.353	0.99	—	—
S-11	Paper	81.5/27.1	48	—	1.379	1.42	0.450	2.39
S-12	Paper	81.5	45	2.200	1.388	1.58	0.474	2.69
S-14	Paper	81.5	53	2.590	1.395	1.89	0.584	3.20
S-15	Paper	81.5	15	0.734	1.373	1.33	—	—
S-16[a]	Bulk	81.5	235	1.150	—	—	1.69[c]	—
S-17[b]	Bulk	81.5	295	1.442	—	—	2.42[d]	—

[a] Volume of electrolyte = 260 cm³.
[b] Area = 36.8 cm²; volume of anolyte, 110 cm³.
[c] Density = 1.394 g/cm³.
[d] Density = 1.411 g/cm³.

It is known from the work of Dirkse (2) that zinc concentrations greater than those obtained by equilibrating ZnO with aqueous KOH can be produced by anodic dissolution in zinc alkaline solutions. After an initial attempt to obtain samples for determination of physical data by controlled syringe sampling methods proved unsatisfactory, a different approach was employed. A 6.35 x 5.7 cm sheet zinc anode (99.99%)[1] was clamped with a silver oxide cathode spaced on either side. After passage of the current for some time, the anode was removed from the cell and the dripping liquid film collected as a sample for analysis. The paper-collected samples (Table I) were from similar runs in which weighed filter paper was pressed against the anode, after its removal from the cell, to absorb the more adherent liquid.

Bulk electrolyte samples were secured from a galvanic cell, with stirred electrolyte with and without applied current from an outside source, and analyzed to obtain zinc concentrations possible at the anode interface without precipitation. A zinc sheet anode was suspended between two silver oxide cathodes which were replaced as discharged to permit long runs. The anode was changed when it became passive, and this run (S-16 in Table I) was stopped when a fresh anode passivated in less than a minute. An applied current run (S-17) required a porous cup surrounding the anode to prevent plating zinc on the cathode, and only the anolyte chamber was stirred. Anodes were replaced when area was lost by dissolution, and the run was stopped when the anolyte appeared cloudy. Samples were pipetted from the electrolyte or anolyte during the run for analysis at various times, and the final sample was also used for density measurement. Table I summarized the results of this work.

Constant current discharge.—Experiments with constant current discharge, until the onset of passivation on the anodic surface, were carried out at various current densities and for the three different positions as shown in Fig. 1. A Lucite cell, presented in Fig. 2, was employed. Initially, no care was taken to eliminate edge effects. Active area in this case was 34.2 cm² with the basic dimensions 6.35 cm high x 5.70 cm wide and the corners masked by the spacers. Later, for some experiments, special frames were made to assure uniform primary current distribution. These were 5.7 cm high and 5.0 cm wide with an active area of 28.5 cm². Experiments with the top horizontal positions were complicated by gas bubbles which were formed at the oxide cathode and rose to the top, *i.e.*, to the zinc anode surface. To prevent this, it was necessary to use fully charged cathodes and also to provide a nylon cloth diaphragm stretched over the cathode to retain there temporarily any gas bubbles in the lower (cathodic) compartment.

The zinc anode potential was measured with a standard Hg-HgO reference electrode. The electrodes were clamped in a frame with spacers, and a small diameter drawn polyethylene tube was introduced through a side hole in the Lucite frame. Cleaned high-purity zinc sheet (99.99%) was used as anodes. The circuit shown in Fig. 2 included a multichannel (Sanborn Type 350) recording oscillograph permitting simultaneous records of current, cell voltage, and anode polarization as measured by the reference electrode. The passivation time, t, was

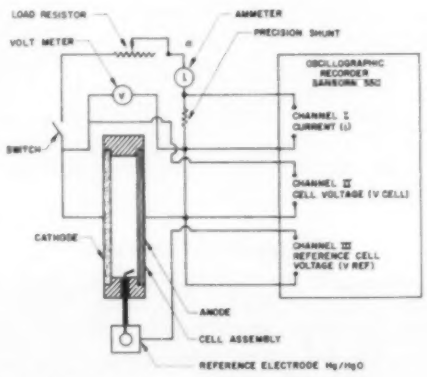

Fig. 2. Cell and circuit schematic diagram

[1] Horse Head Special-2, Mix-60, New Jersey Zinc Company, New York, N. Y.

Table II. Constant current discharge of smooth zinc anodes

Bottom position			Vertical position			Top position		
Run No.	Applied current density I, ma/cm²	Time to anode passivation t, sec	Run No.	Applied current I, ma/cm²	Time to anode passivation t, sec	Run No.	Applied current density I, ma/cm²	Time to anode passivation t, sec
148	88	278	202	146	607	113	219	161
152	88	251	203	146	587	140	234	17.9
161	88	435	201	160	335	141	234	15.6
171	88	571	200	160	321	142	234	18.9
150	117	129	124	175	115	206	234	228
153	117	104.6	125	175	57.1	112	248	79
162	117	182	126	175	94.8	208	248	430
170	117	152	127	175	53.8	137	263	14.3
151	146	58.8	128	175	54.1	138	263	12.3
154	146	55.4	174	175	229	139	263	13.9
155	175	39.8	175	175	224	135	292	9.8
156	175	39.7	180	181	71	136	292	9.9
157	204	26.8	181	190	44.4	166	292	15.0
158	204	27.8	178	190	131	164	350	11.0
159	234	25.4	183	192	59	215	365	8.0
160	234	28.6	179	199	46.6	213	380	12.0
169	234	21.5	119	234	23	212	410	7.0
146	263	16.1	120	234	24.8	205	439	6.1
147	263	17.3	121	234	23.6	187	490	4.0
168	320	12.6	173	234	28	204	555	3.4
221	424	6.5	117	263	18.5			
233	460	5.7	118	263	19.1			
232	550	4.25	182	280	18			
220	555	2.5	172	320	10.5			
			192	384	7.8			
			199	439	4.8			
			184	490	4.0			
			198	555	2.5			
			234	560	3.6			
			191	629	2.5			

determined as the time at constant current from the moment of closing the switch to the moment at which passivation occurred, as demonstrated by a sudden drop in the current and a large polarization. The results of these experiments given in Table II are plotted in Fig. 3.

Studies of limiting current density and anodic polarization by increasing current increments.—It was desirable to develop an experiment in which sufficient time would be made available for establishment of free convection conditions. Accordingly, a stepwise application of current for fixed periods of time was decided on. The experimental setup and material were essentially similar to that described above. The procedure, however, involved applying a predetermined program of currents in equal increments for equal amounts of time. At the same time, anode polarization was measured by subtracting from each anode potential at a given current the original zero current potential. The maximum current density just prior to the onset of passivation can then be designated as a quasi-limiting current density characteristic of a particular current-time history. Under these conditions different "limiting current" values should be obtained for the three individual positions. Experimental results on zinc anodes

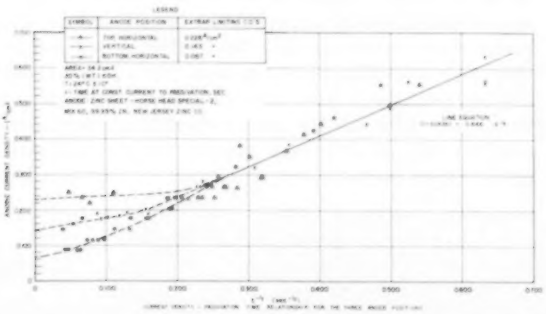

Fig. 3. Current density-passivation time relationship for the three anode positions.

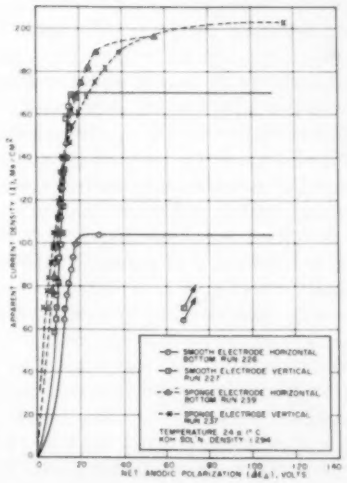
SMOOTH ELECTRODE HORIZONTAL BOTTOM RUN 226
SMOOTH ELECTRODE VERTICAL RUN 227
SPONGE ELECTRODE HORIZONTAL BOTTOM RUN 239
SPONGE ELECTRODE VERTICAL RUN 237

Fig. 4. Anodic polarization curves for zinc (1-min duration periods at each current density and approximately 6 ma/cm² increments).

Table III. Determination of "limiting current" by fixed current and time increments

Temperature 24° ± 1°C

Run No.	Anode type	Anode position	Step sequence, amp, 1 min each	Time to passivate, sec	Current density just prior to passivation, ma/cm²	Capacity to onset of passivation, coulombs/cm²
188	Smooth zinc sheet	Bottom	0.5, 0.8, 1.0, 1.2...	580	83.0	29.6
193		Bottom	0.5, 0.8, 1.0, 1.2...	602	90.0	31.4
196	Smooth zinc sheet	Vertical	2.0, 3.0...5.0, 5.5...	242	190.0	29.7
197		Vertical	2.0, 3.0...5.0, 5.5...	254	190.0	31.8
229		Top	2.0, 3.0...5.0, 5.5...	426	205.0	57.0
230		Top	2.0, 3.0...5.0, 5.5...	420	205.0	56.2
222	Smooth zinc sheet	Top	2.0, 2.2...5.0, 5.5...	1390	196.0	171.3
224		Top	2.0, 2.2...5.0, 5.5...	1801	234.0	258.0
231		Top	2.0, 2.2...5.0, 5.5...	1368	187.0	167.0
227		Vertical	2.0, 2.2...5.0, 5.5...	1172	170.0	132.0
228		Vertical	2.0, 2.2...5.0, 5.5...	1185	170.0	134.0
225		Bottom	2.0, 2.2...5.0, 5.5...	444	99.0	34.2
226		Bottom	2.0, 2.2...5.0, 5.5...	540	105.0	44.2
235	Commercial zinc sponge	Bottom	2.0, 2.2...5.0, 5.5...	942	175.0	114.3
239		Bottom	2.0, 2.2...5.0, 5.5...	1130	189.0	149.0
237		Vertical	2.0, 2.2...5.0, 5.5...	1160	203.0	155.5
238		Vertical	2.0, 2.2...5.0, 5.5...	1005	184.0	125.5

are shown in Table III and the net anode polarization values are plotted in Fig. 4.

Since it was expected that in the case of spongy zinc anodes the differences between the three positions would be minimized, additional experiments were also carried out for this case. The results of four runs with such spongy anodes are shown in Table III, in which the number of coulombs per unit area passed through the anode up to the moment at which passivation was achieved is also given.

Discussion

Physical properties of the electrolyte saturated with ZnO were necessary for mass transfer calculations. The density of 6.924M KOH at 25°C was found to be 1.2936 g/cm³. This solution became saturated with ZnO at a concentration of 0.690 moles/l and after saturation its density was 1.3360 g/cm³ and viscosity was 2.53 cps. From density data the densification coefficient α was calculated to be used later in the calculation of the Grashof numbers (see Nomenclature).

Zinc concentrations of 1.5 moles per liter (m/l) were obtained by Dirkse (2) by anodic dissolution studies. A knowledge of the higher zinc concentrations obtained by anodic dissolution is necessary for determining the interfacial concentration (C_i) used in calculations of the diffusion rate and of Grashof numbers required for free convection calculation. Because of the difficulty of measuring the interfacial concentration directly, a thin film of electrolyte on the anode was removed (by pressing with weighed filter paper) and analyzed for zinc to obtain an average concentration for the film. The zinc concentration in the bulk electrolyte was used with the average concentration of the film to extrapolate a value of C_i. Calculations from runs S-11 and S-12, Table I, give interfacial concentrations from 2.4 to 2.7 m/l of zinc and these results receive some verification from the bulk concentration obtained by long duration anodic dissolution (run 5-17, Table I). A value of 2.4 m/l was chosen for the interfacial concentration with corresponding values of density and viscosity. Interfacial densities were then calculated by adding to the experimentally measured bulk density a density correction calculated from the densification coefficient,

$$\alpha = 47 \text{ cm}^3/\text{mole}$$

(also derived experimentally), and the interfacial concentration according to a method described in Ref. (6). Examples of such calculations are shown in Table I for runs S-11 through S-14. Measurement of any diffusion coefficients was not attempted in this study since it represents a complex problem because of the changes in ionic species involving zinc after its dissolution (3-5).

Soluble reaction products from a working electrode usually cause density gradients in the electrolyte. The density differences result in natural or free convection flows in the electrolyte which depend on the magnitude of the acceleration forces affecting the system as well as its geometry. The over-all mass transfer rates near the limiting current density of an electrode should increase with the one-quarter or one-third power of the acceleration value (6).

Free convection can be established in a cell only after an initial time period which, depending on the rates and physical properties of the system, may range from seconds to minutes. Diffusion and migration are controlling mechanisms for mass transfer during this short time interval. For a situation in which ions generated at the anode diffuse away, time and current density are related by the following form (7) of the diffusion equation:

$$I = \left[\frac{n\mathbf{F}\Delta C\sqrt{D}}{\frac{2}{\pi^{1/2}}} \right] t^{-1/2} = n\mathbf{F}\frac{D}{\delta}\Delta C \qquad [1]$$

where ΔC is the concentration difference between the electrode surface and a point in the bulk (beyond

the boundary layer). The anodic dissolution of zinc is complicated by the formation of intermediate hydroxides of zinc and one or more forms of zincate ions (5). As is evident from anodic dissolution runs, equilibrium is reached slowly between these products. Landsberg (4, 5) correlated experimental results from the anodic dissolution of zinc in sodium hydroxide with the expression in the form

$$I - I_o = Bt^{-1/2} \qquad [2]$$

where t is the time to passivation, and B and I_o are constants, the latter increasing with the hydroxyl ion concentration in the electrolyte.

For runs in which passivation was reached in less than 20 sec, a straight line relationship could be established between I and $t^{-1/2}$. A least-squares fit of the data resulted in the following correlation:

$$I - 0.0636 = 0.846 \cdot t^{-1/2} \qquad [2a]$$

where the I value has a range of 0.25 to 0.60 amp/cm^2 and t has a range of 2.5-19 sec. A direct comparison with the corresponding values of Landsberg (5) (I_o = 0.0080 and B = 0.533) shows qualitative agreement but has limited significance because of his use of different electrolytes and concentrations.

Figure 3, which presents a correlation of the data in Table II, shows the importance of convection at current densities below 0.250 amp/cm^2 where time to passivation is more than 20 sec.

The three anode positions result in lines of different slope. These lines can be extrapolated to $t^{-1/2} = 0$ (*i.e.*, $t \to \infty$) to obtain a comparative limiting current density value for each of the positions. This would be the maximum current density at which no passivation would occur regardless of time. This is perhaps the only way in which a precise definition of the concept of limited current density can be given for an anode undergoing passivation, such as zinc in alkaline media. These values can then be related to predictions made for limiting current density from known theory.

The limiting rate of mass transfer for vertical electrodes can be represented (1, 6) by the following equation:

$$\mathrm{Nu}' = \frac{k_L L}{D} = 0.677\ (\mathrm{Sc} \cdot \mathrm{Gr})^{1/4} \qquad [3]$$

The over-all mass transfer coefficient, k_L, can be related to the applied current density. Thus,

$$\text{Rate} = k_L\ (C_i - C_o) = \frac{I(1 - t_i)}{n\mathbf{F}} \qquad [4]$$

(For definition of symbols see Nomenclature.)

Calculated values of the limiting current density I_L are compared with the extrapolated experimental I_L in Table IV. Diffusion equations discussed previously can be used to calculate limiting current densities for the case of the horizontal anode in the bottom position.

For the case of flat plate horizontal electrodes (*i.e.*, orthogonal to the gravitational field vector) the available theoretical background is far less satisfactory. A free convection study of a horizontal cathode facing upward in a copper sulfate-sulfuric acid electrolyte by Fenech (3) led to the following general correlations:

$$\mathrm{Nu}' = 0.129\ (\mathrm{Sc}^{1.1} \cdot \mathrm{Gr})^{1/3} \qquad [5]$$

Except for the estimated diffusion coefficient value, the following experimentally obtained or extrapolated physical properties were employed for mass transfer calculations:

$$\Delta C = C_i - C_o = C_s - 0 = 2.4 \cdot 10^{-3}\ \text{m/cc}$$
$$\rho_{av} = 1.350\ \text{g/cc}$$
$$\mu_{av} = 2.50 \cdot 10^{-2}\ \text{poise}$$
$$\alpha = 47\ \text{cm}^2\text{/mole}$$
$$D\ (\text{est}) = 0.33 \cdot 10^{-5}\ \text{cm}^2\text{/sec}$$
$$\text{Anode height (for vertical case)}\ L = 6.35\ \text{cm}$$

Calculated values for limiting current density for each of the cases studied are compared in Table IV with extrapolated correspondent experimental values obtained from Fig. 3.

For the horizontal convection case, the agreement in Table IV is poor. On the other hand, there are serious grounds for doubt as to the applicability of Eq. [5] to the case under study. It is known from heat transfer, for instance, on hot horizontal plates that the heat transfer coefficient for a given temperature differential is considerably higher for a horizontal plate facing upward than for one facing downward (8). Bearing the heat-mass-momentum transfer analogy in mind, one would expect that a relation properly describing the convective top horizontal case of this work (facing downward) would most likely also yield lower Nusselt and limiting current density values than those calculated from Eq. [5], a correlation obtained for the case of a cathode facing upward. It is also likely that the time required for the development of full convection is larger for the case of a horizontal electrode than for a vertical one. The result for the vertical

Table IV. Calculated and extrapolated experimental limiting current values

Smooth zinc anodes in 30% KOH at 25°C

Anode position	Mode of mass transfer	Equation	Nusselt number, Nu	Calc. lim. C.D. I_L, amp/cm^2	Extr. exptl. I_L, amp/cm^2
Top, Horizontal[a]	Free Convection, with Benard or turbulent type flow	[5]	1,326	0.319	0.228
Vertical	Free Convection, with parallel laminar or turbulent flow	[3], [4]	558	0.134	0.143
Bottom, Horizontal[b]	Pure Diffusion, unless disturbed	[2]	—	0.051	0.067

[a] Equation [5] may not apply to the anodic case (see Discussion).
[b] Calculated with an assumption of δ = 0.03 cm.

electrode calculated from Eq. [3] and [4] agrees satisfactorily with the experimental extrapolated value (Table IV).

Calculations for the bottom horizontal anode operating under undisturbed pure diffusion are much more complex. Diffusion theory as applied to an electrochemical process leads to the conclusion that, given sufficient time, every current density may become limiting unless other transfer processes are prevalent. The boundary-layer thickness, δ, defined by Eq. [1] is, of course, variable with time. Within a limited period of time one may, however, choose to calculate with an average value of the boundary-layer thickness, δ, over that period of time. It is possible to calculate for the system under study that within a period of 4 min, δ grows to a value of 0.03 cm. Since most of the runs rarely exceeded 10 min, it was convenient to adopt an average value of δ of 0.03 cm for the period. On the basis of this assumption and with the realization that the diffusion coefficient value, D, accepted for these calculations may be incorrect, a limiting current value of 0.051 amp/cm^2 was calculated as shown in Table IV. This compares with the experimental value of 0.067 amp/cm^2. It appears, therefore, that an average boundary-layer thickness of about 0.02 might be corresponding to the prevalent situation for runs up to 10 min.

In the conventional method for determining limiting current densities for a working electrode one usually applies ever-increasing currents and observes net electrode polarization until an extensive anodic polarization due to concentration polarization indicates the value of the limiting current. A simple consideration of the mass transfer problems suggests that the prior current-time history has a strong effect on the value of the current density at which passivation will take place in the case of an anodic process in which passivation by an oxide layer may become the limiting anodic process. Table III shows the results of such experiments on zinc anodes and allows a comparison of the electrode positions and of the size and spacing of the current increments. As would be expected, larger current increments allowed higher currents to be reached before the onset of passivation. With smooth electrodes, passivation occurred very abruptly, as shown by simultaneous drop of current and cell voltage and increase in anode polarization. The seven runs in Table III with smooth sheet zinc anodes for the three anode positions studied with the same initial program of current-time increments demonstrate the outstanding differences in the mass transfer mechanism due to the different orientations to the gravity field. This is shown by both the quasi-limiting current densities (*i.e.*, current density just prior to passivation) and by the total numbers of coulombs per unit area (*i.e.*, anode capacity values up to the onset of passivation). It was, of course, to be expected that under a current-time increment program the resulting quasi-limiting current density values would be higher than the extrapolated values of Fig. 3. This should be easily seen from the differences in definition and methods of determination. Impressive differences, however, are obvious between the bottom and the vertical positions of the order of 70%. The comparison of the capacity to the onset of passivation in terms of coulombs/cm^2 is even more impressive. For the same time-current program the vertical electrode (under free convection conditions) had a capacity four times as large as the horizontal bottom electrode (operating under pure diffusion).

While the relatively low ratio of true area to apparent area in the case of zinc sheet anode enabled the demonstration of these outstanding mass transfer differences, it was obvious that these differences would be minimized in the case of spongy zinc anodes because the high area ratio permits very large apparent current density values even in the case of pure diffusion. Results on such experiments are shown on commercial sponge zinc anodes and are given in Table III and Fig. 4. The passivation of a sponge zinc electrode is not abrupt. There is a gradual increase in anode polarization with a rising rate. The sponge zinc anode has a large true area, but its porous character results in wide differences in true current density over this area, particularly in depth of the electrode. The point of passivation is reached at different times at different points rather than abruptly as with smooth sheet anodes. The choice of position has a much smaller effect in the case of the sponge zinc anodes since most of the current is here carried by the interior surfaces of the electrode which are not exposed to the external convective flow operating on the outer surface.

It is important to realize that in these experiments the gravitational acceleration had only a value of 1 g and therefore the convective flow may have been insufficient to demonstrate the differences in the case of porous spongy anodes. No doubt under larger values of acceleration such as prevalent in missile flights this effect could be demonstrated much more clearly in the case of spongy anodes. In such cases, the orientation toward the vector of force of acceleration would have a significant effect on the transport processes and performance of spongy anodes.

Acknowledgment

The assistance of Dr. G. B. Adams, Jr. and Dr. H. P. Silverman with some of the density and viscosity measurements is gratefully acknowledged. This work was supported in part by Project NOrd 17017 and in part by the General Research program at Lockheed Missiles and Space Company.

Manuscript received Oct. 28, 1959; second revised manuscript received July 11, 1961. This paper was prepared for delivery before the Columbus Meeting, Oct. 18-22, 1961.

Any discussion of this paper will appear in a Discussion Section to be published in the June 1962 JOURNAL.

REFERENCES

1. M. Eisenberg, "Effect of Weightlessness on the Performance of Batteries and Fuel Cells," Proc. 12th Ann. Battery R&D Conference, U.S. Army Signal Lab. (Asbury Park, May 1958).
2. T. P. Dirkse, *This Journal*, **102**, 9 (1955).
3. E. J. Fenech, "Limiting Currents at Horizontal Electrodes under Free Convection Conditions," University of Calif. Rad. Lab. UCRL-3586 (Nov. 1956); *Electrochim. Acta*, **2**, 311 (1960).
4. R. Landsberg, *Z. phys. Chem.*, **206**, 291 (1957).

5. R. Landsberg and H. Bartelt, *Z. Elektrochem.*, **61**, 1162 (1957).
6. M. Eisenberg, C. R. Wilke, and C. W. Tobias, *This Journal*, **100**, 513 (1953).
7. C. W. Tobias, C. R. Wilke, and M. Eisenberg, *ibid.*, **99**, 359C (1952).
8. J. H. Perry, Chem. Eng. Handbook, 3rd ed., p. 474, McGraw-Hill Publishing Co., New York (1950).

NOMENCLATURE

B, constant expressed as the slope in equation of form $I - I_s = B \cdot t^{-1/2}$, amp/cm² sec$^{-1/2}$.
C_i, local concentration, moles/cm³.
C_o, bulk concentration moles/cm³.
C_s, saturation concentration, moles/cm³.
D, diffusion coefficient, cm²/sec.
$\mathbf{F}$, The Faraday, amp-sec/g-equivalent.
Gr, Grashof number, dimensionless $= \dfrac{g\alpha\Delta c L^3}{\nu} = \dfrac{g(\rho_i - \rho_o)\rho_{av} \cdot L^3}{\mu^2}$
g, acceleration of gravity, g-cm/sec².
I, current density, amp/cm².
I_L, limiting current density, amp/cm².
I_s, constant in equation, depending on conc. of alkali.
k_L, mass transfer coefficient, cm/sec.
L, height of vertical electrode, cm.
n, valence change of reacting ion, i.
N_D, mass transfer-dimensionless group for pure diffusion.
Nu', $\dfrac{k_L \cdot L}{D}$ = Nusselt number for mass transfer, dimensionless.
Sc, Schmidt number, dimensionless $= \dfrac{\nu}{D}$.
t, elapsed time to passivation, sec.
t_i, transference number of the potential determining ionic species, i.
α, specific densification coefficient, moles/cm³ $= \dfrac{1}{\rho}\left(\dfrac{d\rho}{dc}\right) T$.
δ, equivalent concentration film thickness, cm.
μ, viscosity, poise, g/sec-cm.
ν, kinematic viscosity, cm²/sec.
ρ, density, g/cm³.
ρ_{av}, arithmetic average density, g/cm³.
ρ_i, local film density, g/cm³.
ρ_o, bulk density, g/cm³.

A Model for Electrochemical Reaction Kinetics of Solid-State Phase Transformations in Reversible Electrodes

George T. Croft[1] **and Donald Tuomi**[2]

Thomas A. Edison Research Laboratory Division, McGraw-Edison Company, West Orange, New Jersey

ABSTRACT

An atomistic model is presented for the reversible oxidation-reduction of a compound, MX, which separates a metal, M, from an electrolyte containing anions X^-. The electrochemical film growth is assumed to depend on the presence of lattice imperfections. The detailed mass and charge transport mechanism is controlled by the particular set of exchange reactions at the M-MX and MX-electrolyte interfaces. If cation vacancies and holes are the relevant lattice and electronic imperfection, there are four possible sets of exchange reactions. Each set and the distribution of the overpotential across each interface determines a particular electrochemical mechanism.

This paper is a discussion of the reversible oxidation or reduction of a compound, MX, which separates the metal, M, from an electrolyte containing anions X^-. The compound MX contains both ionic and electronic defects, and these defects are involved in and play a dominant role in the exchange reactions at the metal-compound and compound-electrolyte interfaces. The defects also promote mass and electricity transport through the compound. The study of electrodes of this nature has been hampered by the lack of an adequate atomistic model for the electrochemical kinetics.

For example, consider the electrochemical processes occurring at the Cd negative electrode of the Ni-Cd cell. Models based on complex reaction sequences involving combinations of ion hydration, solution, and precipitation of the oxidized phase (1) are not in accord with the experimental facts. Recent data show that the kinetics of reversible electrochemical reactions, such as Ag/Ag_2O or $Cd/Cd(OH)_2$ where the Ag_2O and $Cd(OH)_2$ are adherent films on the base metal, must be considered as processes which take place by solid-state transport phenomena (2). The models used to explain Al and Ta oxidation apparently are not directly applicable.

In the range of reaction rates of interest to battery applications (overpotentials from 0 to 100 mv and current densities to 20 ma/cm²), the anodic oxidation of cadmium in alkaline electrolytes yields a coherent crystalline $Cd(OH)_2$ film on the metal. The color of this hydroxide ranges from pale yellow to brownish-red, in contrast to the normal white compound obtained by solution precipitation. Furthermore, the pale yellow samples are bleached white by exposure to x-rays. This fact indicates the presence of defects in the $Cd(OH)_2$ lattice. The electrochemically prepared $Cd(OH)_2$ is a p-type semiconductor and has a well-defined layer lattice crystal structure and cannot be classed as amorphous. The rate of oxidation as a function of overpotential has a maximum, a fact difficult to explain by solution mechanisms.

The $Cd\text{-}Cd(OH)_2$ electrodes are characterized by a unique reversible open-circuit potential which means the electrode reaction involves a readily reversible and large exchange current at both the $Cd\text{-}Cd(OH)_2$ and the $Cd(OH)_2$ electrolyte bound-

[1] Present address: Pitney-Bowes Inc., Stamford, Connecticut.

[2] Present address: Roy C. Ingersoll Research Center, Borg-Warner Corporation, Des Plaines, Ill.

aries. The reaction kinetics at each of these boundaries must be readily reducible to the reversible state without the introduction of irreversible steps. This qualification for Pb electrode kinetics has been noted by Beck, Lind, and Wynne-Jones (3).

The theory developed below specifically relates to an electrochemically formed compound MX which contains only cation vacancies as the ionic or lattice imperfection and holes as the electronic imperfection.

Theory

A discussion of electrochemical reaction kinetics subject to the condition of an MX covering layer on a metal M can be divided into three parts; namely: (*a*) the mechanism for mass and electricity transport through the compound, (*b*) the electrochemical exchange reactions at the metal-compound interface, and (*c*) the electrochemical exchange reactions at the compound-electrolyte interface.

The compound MX is considered to be a crystalline solid with an ordered crystal structure. The assumption is made that the transport of mass and electricity is promoted by the electronic and/or ionic imperfections present in the compound (4). [This is similar to the customary assumptions applied to the gas phase oxidation of metals with the formation of a protective layer (5).] A consequence of this assumption is that the electrochemical exchange currents at the two interfaces, metal-compound and compound-electrolyte, will involve the imperfections.

The first step in the formulation of the theory is to describe the interface electrochemical exchange processes as quasi-chemical "reactions" involving the lattice imperfections as reactants and products. The reactions are then described in terms of the band theory of solids, taking into account the curvature of the bands of a semiconductor-metal contact. It is then shown that the mechanism for mass and electricity transport, *i.e.*, growth rate, is controlled by the exchange reaction.

Interface electrochemical exchange reaction.— Since the electrode is reversible the half cell reaction is given by

$$M + X^- \rightleftharpoons MX + \epsilon \qquad [1]$$

This reaction must be expressed in terms of the exchange currents at the metal-compound and compound-electrolyte interfaces.

For definiteness and to simplify the discussion the compound MX shall be considered to contain cation vacancies, $\square^{\cdot}_{o}$; holes, p; and hole-vacancy pairs, $p/\square^{\cdot}_{o}$. The defects are described by the notation of Rees (6). The symbol $M^{\cdot}/\square^{\cdot}_{o}$ represents a metal ion, $M^{\cdot}$, located on its proper cation site, $\square^{\cdot}_{o}$, in the compound MX; but the symbol $M/\square_{m}$ is equivalent to a metal atom, M, on the proper metal site. A subscript "o" or "m" on the vacant site symbol means "a vacancy in the oxide or metal," respectively. The quantities $\square^{\cdot}$, p, $p/\square^{\cdot}$, etc., are considered as chemical entities subject to the law of mass action. The vacant cation site, $\square^{\cdot}_{o}$, has a net charge of minus one in a uni-uni valent compound, but the $\square_{m}$ in the metal would have a zero charge.[a]

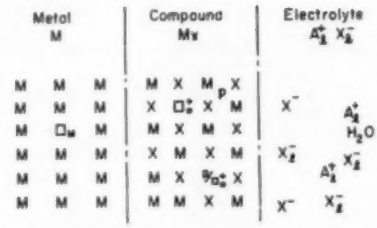

Fig. 1. Electrochemical system of metal M separated by compound MX from electrolyte-A^+, X^-. $\square_m$, lattice vacancy in metal; $\square^{\cdot}_{o}$, lattice vacancy in compound; p, hole in valence band; $p/\square^{\cdot}_{o}$, hole trapped on $\square^{\cdot}_{o}$.

The defects in the compound, MX, are in equilibrium with the metal, M, and with the aqueous electrolyte A^+_1 and X^-_1 as illustrated in Fig. 1. The subscript, 1, on X^- signifies that the ion is in the liquid phase. Additional limitations are now introduced: the mass transport through MX does not involve anion migration and the anion does not dissolve in the metal.

Plausible electrochemical exchange reactions at the metal-compound interface are

$$M/\square_m + \square^{\cdot}_{o} \rightleftharpoons M^{\cdot}/\square^{\cdot}_{o} + \square_m + \epsilon_m \qquad [2]$$

and

$$M/\square_m + p/\square^{\cdot}_{o} \rightleftharpoons M^{\cdot}/\square^{\cdot}_{o} + \square_m + p_o + \epsilon_m \qquad [3]$$

Exchange reaction [2] describes (see Fig. 2) the reaction of a metal atom from the metal with a cation vacancy in the compound MX to produce a vacancy and a free electron in the metal. Exchange reaction [3] is the reaction of a metal atom from the metal with a neutral hole-vacancy pair in the compound to produce a vacancy in the metal, a free electron in the metal, and a free hole in the compound valence band.

At the electrolyte side of the compound MX, a metal ion on a normal site can make a transition

[a] By definition a metal atom in a solid is a metal ion on metal site plus an electron, that is

$$M^{\cdot}/\square_m + \epsilon_m = M_{atom}$$

therefore

$$M^{\cdot} + \epsilon_m + \square_m = M_{atom}$$

showing that $\square_m$ is a neutral entity and simply represents a vacant lattice site in the metal.

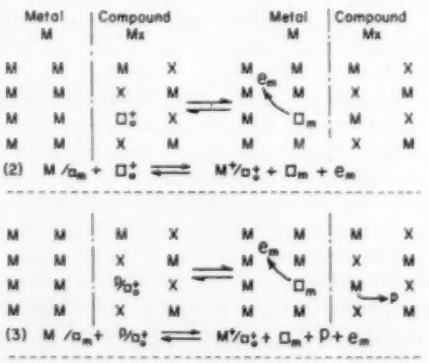

Fig. 2. Electrochemical exchange reactions at the metal-compound interface.

from an interior site to a surface or exterior site and create a cation vacancy in the compound. Thus the following reaction occurs:

$$M^{\cdot}/\square^{\cdot}_{\circ} \rightleftharpoons M^{\cdot}/\square^{\cdot}_{\circ} + \square^{\cdot}_{\circ} \qquad [4]$$

where the symbol $\square^{\cdot}_{\circ}$ describes a surface site located in the Helmholtz double layer. Alternatively, a metal atom, M, may make a transition from an interior site to an exterior site, according to the equation:

$$M^{\cdot}/\square^{\cdot}_{\circ} \rightleftharpoons M/\square^{\cdot}_{\circ} + p/\square^{\cdot}_{\circ} \qquad [5]$$

thus creating an interior hole-vacancy pair.

Once a metal atom or ion occupies an exterior site, reaction with an anion from the electrolyte can occur. The corresponding reactions are

$$M^{\cdot}/\square^{\cdot}_{\circ} + X^{-}_{i} \rightleftharpoons MX \qquad [6]$$

and

$$M/\square^{\cdot}_{\circ} + p + X^{-}_{i} \rightleftharpoons MX \qquad [7]$$

respectively.

Combining Eq. [4] with [6] and [5] with [7] the exchange reaction at the electrolyte side is

$$M^{\cdot}/\square^{\cdot}_{\circ} + X^{-}_{i} \rightleftharpoons MX + \square^{\cdot}_{\circ} \qquad [8]$$

if the metal ion combines with the anion from the electrolyte and

$$M^{\cdot}/\square^{\cdot}_{\circ} + p + X^{-}_{i} \rightleftharpoons MX + p/\square^{\cdot}_{\circ} \qquad [9]$$

if a metal atom combines with an anion from the electrolyte. The compound-electrolyte exchange reactions are illustrated in Fig. 3.

At equilibrium the exchange processes described by Eq. [2] and [3] and described by Eq. [8] and [9] are equivalent because the equilibrium

$$p + \square^{\cdot}_{\circ} \rightleftharpoons p/\square^{\cdot}_{\circ} \qquad [10]$$

is maintained throughout the compound. The combination of Eq. [10] with Eq. [2] and [8] yields the set [3] and [9], respectively. The equilibrium state is independent of the path as required by thermodynamics.

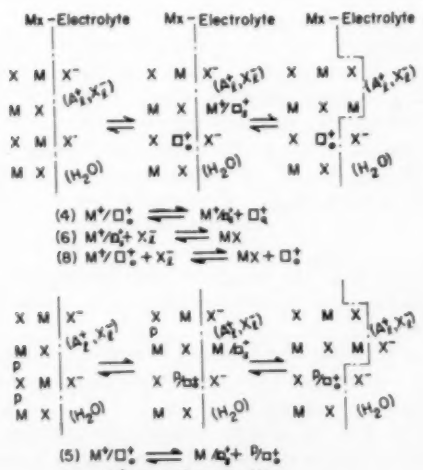
Mx – Electrolyte
Mx – Electrolyte
Mx – Electrolyte
(4) $M^{\cdot}/\square^{\cdot}_{\circ} \rightleftharpoons M^{\cdot}_{i} + \square^{\cdot}_{i}$
(6) $M^{\cdot}/\square^{\cdot}_{i} + X^{-}_{i} \rightleftharpoons MX$
(8) $M^{\cdot}/\square^{\cdot}_{i} + X^{-}_{i} \rightleftharpoons MX + \square^{\cdot}_{i}$
(5) $M^{\cdot}/\square^{\cdot}_{i} \rightleftharpoons M/\square^{\cdot}_{i} + p/\square^{\cdot}_{i}$
(7) $M/\square^{\cdot}_{i} + p + X^{-}_{i} \rightleftharpoons MX$
(9) $M^{\cdot}/\square^{\cdot}_{i} + p + X^{-}_{i} \rightleftharpoons MX + p/\square^{\cdot}_{i}$

Fig. 3. Electrochemical exchange reactions at compound-electrolyte boundary.

By adding Eq. [2] or [3] to [8] or [9] and using the Eq. [10] one obtains

$$M/\square_{m} + X^{-}_{i} \rightleftharpoons MX + \square_{m} + \epsilon_{m} \qquad [11]$$

which is the original half-cell reaction given by Eq. [1]. Thus the half-cell reaction is readily described in terms of the proposed exchange reactions occurring at the metal-compound and compound-electrolyte boundaries. *Furthermore, for a compound MX produced as a phase separating a metal M from the electrolyte ion X^{-}_{i} the half-cell reaction is formulated as a solid-state reaction not requiring solution of the cation during the reaction.*

Equations [2] through [9] express symbolically the net effect of exchange reactions at the boundaries. Thus far, exchange mechanisms have been formulated which are consistent with the half-cell reaction and with the imperfections in the compound. The relevance of the equations to electrochemical oxidation is shown more clearly by describing the boundary exchange reactions in terms of solid-state contact theory.

Exchange reactions and metal-semiconductor contacts.—The spatial distribution of imperfections and energy relationships in the compound corresponding to each of the above interface electrochemical exchange reactions are conveniently specified in terms of the band theory descriptions of semiconductor contacts.

Consider the initial state of semiconductor MX separated from the metal M by a short distance δ as shown in Fig. 4A. If the solids are now connected by an electronic conductor, the electrons will flow between the two materials until the electronic free energies are equal. As a result of charge transfer the surfaces of M and MX will become electrified. An electrostatic potential difference exists in the vacuum between a point just outside the metal surface and just outside the MX surface. This potential difference, neglecting surface states (7), is equal to the difference in thermionic work function for the two materials.

As the two surfaces are brought closer together more charge is induced on the surfaces. Just prior to contact the interface between the two materials is viewed as a dipole layer not unlike the Gouy-Chapman double layer. The charge on the metal resides on the surface because of the high density of electronic energy states (8). Because of the low density of allowed electronic energy states in the compound,

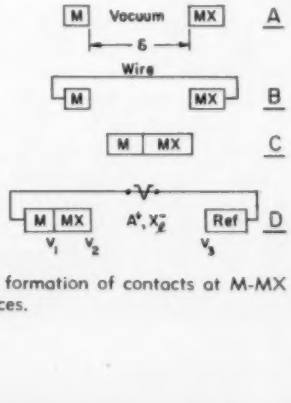

Fig. 4. The formation of contacts at M-MX and MX-electrolyte interfaces.

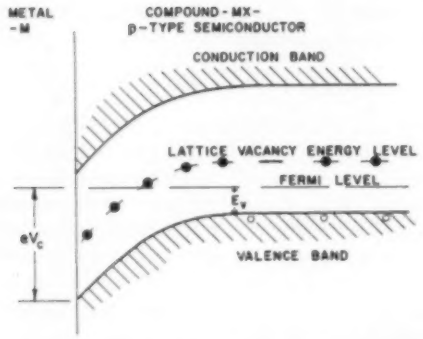

Fig. 5. Energy levels at the metal-compound interface for exchange reaction [2]. Open circle with a line through the center, vacant cation site; dash, vacancy-hole pair; open circle, free hole; V_c, electrostatic potential of top of valence band at the interface relative to the Fermi level for electrons; E_v, height of Fermi level above the valence band.

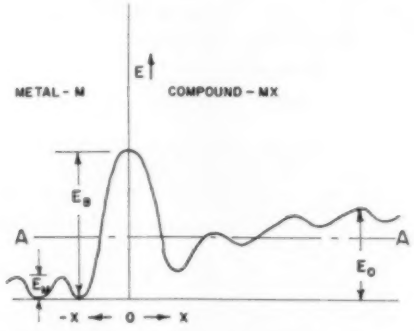

Fig. 6. Generalized energy vs. distance curve for a metal ion near the M-MX interface. The line A-A represents the Gibbs free energy of the metal ion at equilibrium. The upward slope to the right represents the effect of space charge in MX.

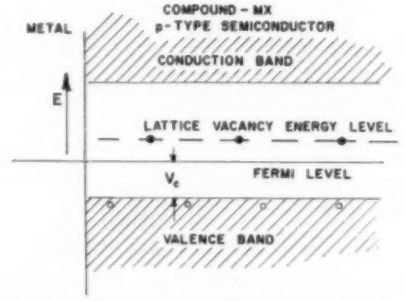

Fig. 7. Relative position of electron energy levels at the contact if there is no barrier to vacancy motion across the interface.

the charge here is distributed in depth between the surface and the bulk of MX.

Now, when contact is made between M and MX, atom and ion exchange can occur, for example, Eq. [2]. At the moment of contact the electronic charge carriers in M are equilibrated with the electrons in MX. However, as ionic exchange occurs across the interface the free energy of electrons in the one material will change relative to the other. As a result of this series of reiterative processes the metal ion in the metal and compound approaches an equilibrium state.

In Eq. [2] the exchange reaction between M and MX is with respect to metal ions and vacancies in the compound. Thus, after physical contact is made between M and MX, cation vacancies can exchange across the interface according to Eq. [2]. As cation vacancies flow either in or out of semiconductor MX, the density of electron trapping states in the surface region will change. This change will shift the Fermi level up or down with respect to the valence band edge E_{v_0} because the Fermi level depends on the density of hole-vacancy pairs in the compound, (see Fig. 5) (9).

At equilibrium the chemical potentials for electrons and metal ions are necessarily constant across the boundary. For a given temperature the Fermi level will have a unique value for each particular combination of M and defect structure compound MX. The downward curvature of the MX energy bands as shown in Fig. 5 implies the existence of a negative space charge at the M-MX interface with MX a p-type semiconductor.

The potential energy *vs.* distance as seen by the metal ion is of the general form shown in Fig. 6. The highest energy barrier, E_B, to vacancy migration between M and MX is a measure of the overpotential for the interface exchange current. If no energy barrier exists for metal ion (or vacancy) motion across the interface, then a space charge could not be maintained in the semiconductor near the M-MX interface because a distribution of charge can be maintained only by the application of external fields.

The electronic energy relationship according to band theory will be as shown in Fig. 7 if $E_m = E_B =$ E_v with no space charge in the semiconductor. This condition corresponds to a zero activation energy for the ion exchange across the M-MX interface. The model of Fig. 4 has a finite energy barrier to vacancy exchange. This electrode has therefore a finite activation energy associated with exchange reaction [2].

For the alternate exchange current description at the M-MX interface, Eq. [3] the exchange process is dominated by the motion of neutral hole-vacancy pairs. The transport of the hole-vacancy pair across the boundary into the metal releases a hole to the valence band of the oxide, removes a vacancy which had functioned as a hole trap, and releases an electron into the conduction band of the metal. Thus the hole space charge in the valence band of MX at the M-MX interface produces the energy barrier shown in Fig. 8 opposing the migration of positive metal ions into the semiconductor. If cation vacancies could be generated in the bulk of semiconductor MX, the resultant sites could capture the free holes and thereby reduce the space charge barrier.

Now consider the isolated interface of compound MX in contact with the electrolyte X^-_1. The physical situation corresponding to Eq. [8] and [9] is illustrated in Fig. 9A and B, respectively. Exchange reaction [8] can be considered to produce a less p-type or an n-type surface region by the transfer of a metal ion M^+ to a surface adsorbed state where combination with an anion X^-_1 occurs leaving a negatively charged vacancy in the interior region of MX.

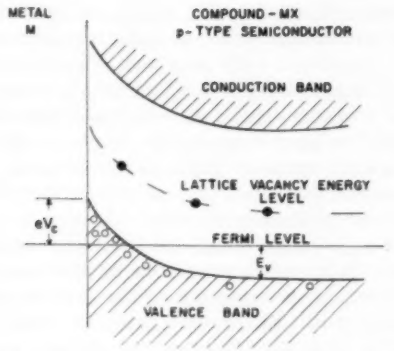

Fig. 8. Energy levels at the metal-compound interface for exchange reaction [3].

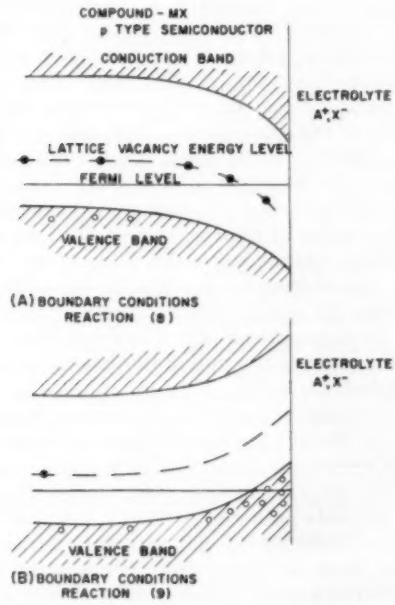

Fig. 9. Energy levels of compound-MX at the compound-electrolyte interface.

Alternatively the exchange could involve an anion X^- sorption on the MX surface displacing equilibrium [9] so that the surface density of holes in the valence band increases at the M-MX interface as shown in 9B. The charge distribution shown in Fig. 9A can be thought of as excess cations on the surface, but Fig. 9B shows a sorption of excess anion. If cation and anion surface concentrations were equal, a flat band potential would be obtained.

If the two interfaces M-MX and MX-X^-_1 are now placed back to back, the imperfection concentrations at the MX-X^-_1 boundary will equilibrate with imperfections generated at the other boundary. Thus, at equilibrium, the imperfections concentration in MX is related to the exchange processes at both boundaries. The system cannot be described without a detailed description of both exchange processes. The measured potential is the algebraic sum of the potential drops through the interfaces M-MX, MX-AX, AX to reference X as noted in Fig. 4D. The potential distribution at one boundary is influenced by the exchange reaction at the opposing boundary.

Boundary exchange reactions and transport properties.—The mechanism of mass and electricity transport in the compound MX is controlled by the particular combination of exchange reactions that occur at the phase boundaries. The strong influence of the terminal conditions on electron and mass exchange at phase boundaries on the transport properties through the intervening phase has been emphasized by Hebb (10) and by Wagner (11). The following discussion is an extension of their ideas (utilizing the concept of an electrochemical exchange current) to compounds undergoing growth or decomposition.

When the half-cell reaction, Eq. [1], is driven to the right by applying a potential, growth of compound MX occurs. The applied potential is dropped across the M-MX boundary, the bulk MX (an iR voltage drop) and the MX-electrolyte boundary. The potential drops across the interfaces cause unbalance of the exchange currents. These terminal conditions can be illustrated by considering the various combinations of exchange currents possible for the p-type semiconductor containing lattice vacancies.

For reaction [3] at the M-MX boundary the interface functions as a generator of holes and a sink for hole-vacancy pairs. For reaction [9] at the MX-electrolyte boundary the electrolyte-compound interface is a hole sink and a hole-vacancy pair generator. For the combination of [3] and [9] all of the electricity is transported by holes while the mass is transported by hole-vacancy pair diffusion from the electrolyte side to the metal side of MX. The compound transports charge as an electronic conductor. In contrast, since Eq. [2] provides a vacancy sink at the M-MX boundary, the combination of [2] with [8] provides a sink at the metal side for vacancies generated at the electrolyte side. Here both mass and electricity transport depend on vacancy motion. The compound now transports electricity as an ionic conductor.

The combination of reaction [3] with [8] leads to a hole source and a hole-vacancy sink at the metal side with a cation vacancy source at the electrolyte side. The kinetics of this case differs from the former case because the sink for imperfections is provided by recombination in MX. The holes injected at the metal side and the vacancies injected at the electrolyte side migrate toward one another carrying electricity through the compound. Ultimately they recombine near the electrolyte side to form hole vacancy pairs which diffuse back to replenish pairs removed at the metal side. Electrically the compound behaves as a mixed conductor in which charge transport is partially by vacancies and the remainder by holes.

The combination of [2] with [9] also involves mixed conduction except here the holes extracted at the electrolyte side and cation vacancies extracted at the metal side are replenished by the dissociation of hole-vacancy pairs created at the electrolyte side.

Methods for determining the exchange reactions.—The determination of the relevant combination of exchange currents for a particular electrode generally is not a simple process. The solid phases involve

a complex of mixed electronic and ionic conduction processes. For the particular electrode the terminal conditions for charge transport at the interfaces can and do impose stringent limitations on the possible reaction kinetics. The mechanism of mass and electricity transport in the isolated electrode does not necessarily reflect the properties expected from characterization of the isolated compound. Profound changes in transport properties can be imposed by the exchange currents existing at the boundary (10).

Some insight into the exchange reactions at the solid phase boundary M-MX is provided by considering the effect of changes in the terminal conditions on the charge transport through MX. If the compound MX is an ionic conductor for the terminal condition M-MX-M, then Eq. [2] is the relevant exchange reaction at the metal for either polarity. However, if MX is an electronic conductor, the exchange reaction may be given by Eq. [2] or [3]. Alternatively, if with the contacts Pt-MX-M the difficult direction of electronic current flow is for M positive (see Fig. 5); then the dominant exchange reaction is Eq. [2]. If the difficult direction of electronic current flow is for M negative (see Fig. 8); then exchange reaction [3] dominates. The electronic measurements should be made under conditions such that the imperfection distributions created during the electrochemical formation of MX on M are not altered.

The exchange reactions at the electrolyte side are determined by other methods. The complexity of the generalized surface electrical double-layer region makes difficult simple descriptions analogous to that for the metal-compound interface, particularly since detailed atomistic mechanisms are involved.

Several intuitive descriptions relating to the determination of the electrolyte boundary exchange currents are suggested by the equations. The quantity $(M^{\cdot}/\square^{\cdot}_{s})(X^{-}_{i})$ of Eq. [6] is directly related to the solubility product for MX. The symbol $(M^{\cdot}/\square^{\cdot}_{s})$ represents an $M^{\cdot}$ ion existing as a surface ion on the MX lattice. The surface density of these ions will depend on the exchange rate with the electrolyte; thus the solubility of MX in the electrolyte is relevant to the distribution of defect structure in the Helmholtz double-layer region.

If the compound MX is only an ionic conductor, the exchange reaction corresponds to [8]. For a soluble compound MX a high rate of $(M^{\cdot})$ exchange between the metal surface ion sites and the electrolyte would be expected. This, in turn, would contribute to a high probability for vacancy injection into the compound MX. For an insoluble compound MX which is an ionic conductor the entity $(M^{\cdot}/\square^{\cdot}_{s})$ could be interpreted as a metal ion on a surface site with a zero jump probability into the electrolyte. The electrolyte-MX exchange current for the X^{-} ions would, in effect, control the vacancy injection. On the other hand, if the compound MX is both an electronic conductor and not significantly soluble in the electrolyte, then [9] is the exchange reaction.

From a study of the variation in the space-charge distribution at the MX surface in contact with the electrolyte still further insight should be provided. Consider the boundary condition [8], the generation of vacant cation sites, $\square^{\cdot}_{s}$, in the oxide corresponds to the accumulation of a negative surface space charge associated with vacancies. The characterization of the behavior of this space charge with changes in the potential distribution at the boundary is dependent on the exchange current as well as the electric field intensity and polarity. For Eq. [8] the surface should at least be less p-type than the bulk phase as illustrated in Fig. 9A.

For Eq. [9] there exists an accumulation of holes in the surface region generated by the transition of metal from an interior site to the surface where it can react with X^{-}. Here a positive space charge would be generated within the surface region of compound MX as illustrated in Fig. 9B.

To maintain electrical neutrality at the compound-electrolyte interface a corresponding space charge of opposite sign must exist within the adjacent electrolyte volume. Thus, if the sign of the diffuse double-layer charge adjacent to the surface is established, inferences may be drawn about the character of the space charge distribution within the crystals. Studies of the electrokinetic characteristics of the system M-MX and MX interacting with an electrolyte involving X^{-}_{i} ions provides a source of data descriptive of the real system with its complex of variables. This includes the study of the zeta potential dependence on electrolyte composition for the system MX and M-MX^{-}. The sign of the zeta potential for a compound MX in contact with electrolyte is the same as the sign of the space charge in the inner Helmholtz layer.

The electrokinetic studies of ionic crystals as reviewed by Bolan (12) provide data relevant to surface ion exchange properties of crystals in contact with different composition electrolytes. The variation of the zeta potential of $BaSO_4$ with Ba^{++} ion or $SO_4^{=}$ ion concentration independent of the corresponding anion or cation may very well be directly related to the surface defect equilibria with the bulk crystals. The dependence of the $BaSO_4$ zeta potential on past crystallite history emphasizes the role defects play in such systems.

Discussion

Several mechanisms involving lattice imperfections have been outlined by which electrochemical film growth may proceed when the compound separates the metal substrate from the electrolyte. The detailed mechanism is controlled by the particular set of exchange reactions at the M-MX and the MX-electrolyte interfaces. If cation vacancies and holes are the relevant imperfections, there are four possible sets of exchange reactions. Each set and the distribution of the overpotential across each interface determines a particular electrochemical mechanism.

In terms of these concepts the electrochemical properties are explicitly associated with the substrate crystalline structure as well as that of the intermediate phase, MX. The electrode potential for this system is dependent on the properties of the composite system (taking into account lattice imperfections), rather than being simply related to the differences in the free energies of the isolated compounds and electrolyte. Differences in the electrode potential for

nominally identical materials may be interpreted as being caused by differences in types and concentrations of imperfections (13).

This theoretical study arose from attempts to explain the existence of a maximum in the rate of cadmium oxidation as a function of applied potential. The characteristic of passivation if the oxidation is forced by too high an anodic potential was difficult to reconcile with the observation that cadmium electrodes show relatively stable constant-current anodic overpotentials. This is particularly evident in the battery electrodes which are characterized by large effective exchange currents and small polarization overpotentials.

This dilemma was clarified by the concept of boundary exchange currents determining the defect concentration in the intermediate phase separating the metal from the electrolyte. Thus, depending on the distribution of the overpotential between the two boundaries and in the bulk phase, MX, a variable density of mass and charge carriers can be introduced into the system. Thus the ion diffusion rate in the $Cd(OH)_2$ as well as the electronic conductivity will be controlled by the particular exchange currents dominating the two interfaces and by the influence of the applied potential on these exchange currents. In general the change in the number of charge and mass carriers caused by dropping a fraction, α, of the overpotential, ϕ, across the interfaces is of the form $\exp \pm(\alpha e \phi/kT)$. The remaining potential $(1-\alpha)e\phi$ is the driving force for charge carrier motion through the intermediate phase. Since the rate of growth of the compound is proportional to the density of charge and mass carriers and also to the driving force, the rate, i, must be related to the overpotential by an expression of the form

$$i \alpha (1-\alpha) e\phi \exp \pm(\alpha e \phi/kT)$$

where e is the electronic charge, k the Boltzmann constant, and T the temperature. For the negative exponent this function gives curves of the form reported for Cd to $Cd(OH)_2$ and Ag_2O to Ag (2).

It is worth noting here the contribution of Grimley to the description of these complex systems (14). This study describes in detail the equilibrium properties of an electrolyte in contact with an ionic crystal containing lattice defects in thermal equilibrium. As a result of exchange reactions with the electrolyte a space charge of vacant sites can be generated near and in the surface region of the solid in contact with the electrolyte. The electrical double layer at the surface involves defects within the body of the crystal as well as the adsorption of ions on the surface. Grimley, in particular, notes that with a space charge of vacant sites the ion diffusion coefficient can depend on the position. A high density of vacancies would contribute to an increased ion diffusivity. As the crystallite size approaches the dimensions of the space charge region, below 10^{-4} cm, the rate of ion exchange between solid and electrolyte should increase because of the higher density of imperfections and the enhanced ion mobility.

For the more general case described here, at least two distinct electrochemical exchange reactions can contribute to the formation of two distinct space charge regions. As the compound grows from a thin film to a thick layer an initially overlapping space charge distribution, i.e, M-MX and MX-electrolyte, becomes separated as the film thickness increases. At some film thickness the properties should be controlled by the mass and charge transport through the intermediate region (2). At this stage, the characteristic electrochemical properties possibly may be directly related to the properties of the bulk phase prepared by electrochemical methods. Since the details of the mass and charge transport mechanism differ for different combinations of exchange current the electrochemical as well as other physical properties for thick films may provide data required to define the boundary exchange currents.

This theory can be generalized to apply to less crystalline or even amorphous materials. The concept is retained of exchange currents at the electrified M-MX and MX-electrolyte boundaries. The concept of the Helmholtz double layer is expanded to include the imperfections just inside the solid as illustrated in Fig. 3. The double layer is not a simple ideal surface with a layer of adsorbed ions. Furthermore, the surface defect structure which is propagated into the compound can be controlled by exchange reactions involving anionic as well as cationic defects.

The concept of structural defects can still be used to describe mass transport through the solid. In covalently bonded amorphous materials the simple lattice vacancy description must be altered to take into account the local site symmetry imposed on the motion of an atom from a covalent bonded proper site into a neighboring lattice vacant site. In general the oxidic compounds encountered in battery systems are covalently bonded and cannot be approximated as simple ionic or metallic systems; however, the concepts developed above for compound MX with slight modifications can be applied to amorphous materials.

Considering this complex model for the electrochemical processes involving simply an intermediate solid phase, between the reacting solid and the electrolyte, the existence of an extensive art for solid phase electrodes particularly in the battery field is not at all surprising. On the other hand, the relevant mechanisms must now be deduced for each electrode from a complex of observations. A simple model would not be expected to have a very broad range of physical reality. Clearly, only the initial steps have been taken toward a comprehensive description.

Acknowledgments

The authors are indebted to their colleagues at the T. A. Edison Research Laboratory and in particular to Drs. J. B. Johnson, A. Fleischer, and G. J. B. Crawford for many stimulating discussions and helpful criticism of the manuscript. The authors thank the members of the supporting staff for their assistance in preparing the manuscript and Dr. Donald W. Collier, Director of the T. A. Edison Research Laboratory, for permission to publish.

Manuscript received Nov. 14, 1960; revised manuscript received April 1, 1961. This paper was prepared for delivery before the Indianapolis Meeting, April 30-May 3, 1961.

Any discussion of this paper will appear in a Discussion Section to be published in the June 1962 JOURNAL.

REFERENCES

1. P. E. Lake and E. J. Casey, *This Journal*, **105**, 52 (1958); W. J. Muller, *Trans. Faraday Soc.*, **27**, 737 (1931).
2. G. T. Croft, *This Journal*, **106**, 278 (1959).
3. W. H. Beck, R. Lind, and W. F. K. Wynne-Jones, *Trans. Faraday Soc.*, **50** 147 (1954).
4. F. Seitz, "Phase Transformations in Solids," Chap. 4, 77-148, J. Wiley & Sons, Inc., New York (1951).
5. W. Jost, "Diffusion in Solids, Liquids, and Gases," Chap. IX p. 340-405, Academic Press, Inc., New York (1952).
6. A. L. G. Rees, Chemistry of the Defect Solid State," J. Wiley & Sons, New York (1954).
7. J. Bardeen, *Phys. Rev.*, **71**, 717 (1947).
8. L. P. Hunter, "Handbook of Semiconductor Electronics," Part I, sec. 2 and 3, McGraw-Hill Book Co., New York (1956); Charles Kittel, "Introduction to Solid State Physics," 2nd ed., Chap. 14, p. 383-400, John Wiley & Sons, Inc., New York (1956).
9. R. A. Hutner, E. S. Rittner, and F. K. DuPre, *Philips Research Rpts.*, **5**, 188 (1950).
10. M. H. Hebb, *J. Chem. Phys.*, **20** 185 (1952).
11. C. Wagner, *Z. Physik Chem.*, **B21**, 25 (1933).
12. J. A. V. Butler, Editor, "Electrical Phenomena at Interfaces," Chap. V. T. R. Bolan, 'Electrokinetic Behavior of Ionic Crystals,' Methuen and Co., London, (1951).
13. J. T. Stock, W. C. Purdy, and L. M. Garcia, *Chem. Rev.*, **58**, 611 (1958); W. J. Hamer, *J. Am. Chem. Soc.*, **57**, 10 (1935); W. J. Hamer and D. N. Craig, *This Journal*, **104**, 206 (1957).
14. T. B. Grimley, *Proc. Roy. Soc.*, **A201**, 40 (1950).

Investigation of the Electrochemical Characteristics of Organic Compounds

VIII. Hydrazine and Hydroxylamine Compounds

R. Glicksman

Semiconductor and Materials Division, Radio Corporation of America, Somerville, New Jersey

ABSTRACT

Electrochemical characteristics of various organic hydrazine and hydroxylamine derivatives are presented. Their use as anode materials in galvanic cells is considered. The anode potential of these compounds is dependent on the type and position of substituent groups in the molecule as well as the pH of the electrolyte. The effect of the first two factors on the anode potential is interpreted in terms of the electron density distribution in the molecule.

The ability of hydrazine to act as a powerful reducing agent has long been recognized as one of its outstanding chemical properties. Oxidation of hydrazine is readily effected in either acidic or alkaline solutions although the reactions are often involved. The normal oxidation product is nitrogen, but some ammonia or hydrazoic acid may appear (1).

The potentials for the following half-cell reactions involving hydrazine or the hydrazonium ions have been calculated and are shown below (2).

$$N_2H_5^+ + 2H_2O = 2NH_4OH^+ + H^+ + 2e^- \quad E^\circ = -1.42 \text{ v} \quad [1]$$

$$N_2H_4 + 2\,OH^- = 2NH_2OH + 2e^- \quad E^\circ_a = -0.73 \text{ v} \quad [2]$$

$$N_2H_5^+ = N_2 + 5H^+ + 4e^- \quad E^\circ = 0.23 \text{ v} \quad [3]$$

$$N_2H_4 + 4\,OH^- = N_2 + 4H_2O + 4e^- \quad E^\circ_a = 1.16 \text{ v} \quad [4]$$

The potential for the oxidation of hydrazine to hydroxylamine is very high and since no evidence has been presented to demonstrate that hydroxylamine is an oxidation product of hydrazine, reactions [3] and [4] appear the most plausible.

Similarly many of the organic derivatives of hydrazine are reported to be powerful reducing agents. In this paper, the electrochemical characteristics of various organic hydrazine compounds and related hydroxylamine derivatives are presented. Their use as anode materials in galvanic cells is also considered.

Experimental

A previously described technique (3) has been modified slightly (4) to measure the operating potential during current flow of the various organic hydrazine compounds. The technique consists in discharging a 0.5 g sample of the organic hydrazine derivative mixed with 0.05 g of Shawinigan acetylene black in a large volume of electrolyte at a constant current drain of 0.005 amp/g. The change in anode potential with time was measured with an L&N type K potentiometer using a saturated calomel reference electrode. Measured potentials were corrected for the IR drop associated with the apparatus and electrolyte by means of an oscillographic technique (5).

All half-cell potential data reported are referred to the normal hydrogen electrode and include a liquid junction potential. For the most of the measurements an aqueous 1.44*M* NaOH solution ($a_{OH^-} = 1$)[1] was used as the electrolyte, and a manganese dioxide bobbin wrapped in cheese cloth served as

[1] Calculated from the data given by Latimer (6).

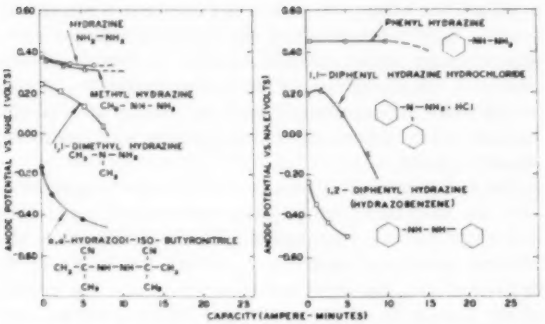

Fig. 1. Half-cell potential discharge curves of hydrazine and various N-substituted hydrazine derivatives discharged at a rate of 0.005 amp/g in 1.44M NaOH.

the cathode. In the study of the effect of pH on potential a manganese dioxide cathode was employed with the acidic $NH_4Cl-ZnCl_2-H_2O$ and the weakly basic $MgBr_2-H_2O$ [saturated with $Mg(OH)_2$] electrolytes.

Experimental Data and Discussion of Results

Hydrazine and N-substituted hydrazine derivatives as reducing agents.—Figure 1 shows half-cell potential discharge curves of hydrazine and various N-substituted hydrazine derivatives obtained by discharging these compounds at a rate of 0.005 amp/g[2] in 1.44*M* NaOH solution. In this electrolyte hydrazine operates at a potential of +0.35 v, a value considerably below that of its calculated reversible potential (Eq. [4]).

As one might expect from its close resemblance to hydrazine, methylhydrazine is a strong reducing agent and has an anode potential close to that of the parent compound. Phenylhydrazine, an N-substituted aryl derivative of hydrazine, is a stronger reducing agent than either hydrazine or methylhydrazine and operates at a potential 0.1 v more anodic than these compounds.

In agreement with its high anode potential, methylhydrazine reduces Fehling's solution. It is reported to produce nitrogen and the corresponding hydrocarbon when oxidized, probably through the intermediate formation of a derivative of diimide (7)

$$RNH-NH_2 \rightarrow RN=NH \rightarrow RH + N_2 \qquad [5]$$

Similarly, when phenylhydrazine is oxidized in a neutral solution with cupric sulfate (which is reduced to metallic copper) benzene and nitrogen are formed, probably via the diimide.

Figure 1 also shows discharge curves for symmetrical (RHN—NHR) and unsymmetrical (RRN—NH_2) alkyl and aryl disubstituted hydrazine compounds. Like the monoalkyl and monoaryl hydrazine derivatives, the unsymmetrical disubstituted hydrazines contain an $-NH_2$ group. However, as evidenced by the discharge curves of 1,1-dimethylhydrazine and 1,1-diphenylhydrazine hydrochloride, they operate at potentials 0.1-0.2 v less anodic than the monosubstituted hydrazine compounds.

The lower anode potentials of the unsymmetrical disubstituted hydrazines as compared to the monoalkylhydrazines are manifested in the fact that monoalkyl hydrazines reduce cold Fehling's solution and dialkylhydrazines when the solution is warmed (8).

This behavior is in agreement with the general observation that whenever any two atoms of the groups C, O, and N are joined and each holds a hydrogen atom, oxidation readily occurs. Thus, the alcohols, the hydroxylamines, and the hydrazines of type A below are not as readily oxidized as compounds of the type B (9).

Type A	Type B
R_3COH	R_2CHOH, RCH_2OH
R_2NOH	$RNHOH$, NH_2OH
R_2N-NH_2	$RNHNH_2$, NH_2NH_2

Generally, the oxidation of 1,1-disubstituted hydrazines leads to the formation of the corresponding tetrazenes. For example N,N-dialkylhydrazines are oxidized to symmetrical tetrazenes by mercuric oxide.

$$2(C_2H_5)_2N-NH_2 + 2\,HgO \rightarrow (C_2H_5)_2N-N=N-N(C_2H_5)_2 + 2\,Hg + 2H_2O \qquad [6]$$

In contrast, the symmetrical N,N′-disubstituted hydrazines, RNH-NHR, which have one available hydrogen on each of the nitrogen atoms, usually are converted to the azo compound by oxidation. Thus, 1,2-diphenylhydrazine in alcoholic alkali solution may be oxidized to azobenzene by air (10).

$$C_6H_5NH-NHC_6H_5 + O_2 \rightarrow C_6H_5N=NC_6H_5 + H_2O_2 \qquad [7]$$

Discharge curves of α,α′-hydrazodi-iso-butyronitrile and 1,2-diphenylhydrazine indicate that these compounds are considerably weaker reducing agents than the substituted hydrazine compounds which contain an $-NH_2$ group.

Half-cell potential discharge curves of various para substituted phenylhydrazine compounds discharged at a rate of 0.005 amp/g in 1.44*M* NaOH solution are shown in Fig. 2. These data illustrate the effect of para substituted groups on the anode potential of phenylhydrazine. It is seen that the introduction into the molecule of an electron repelling group such as $-CH_3$ raises the potential and that the addition of an electron attracting —Br or

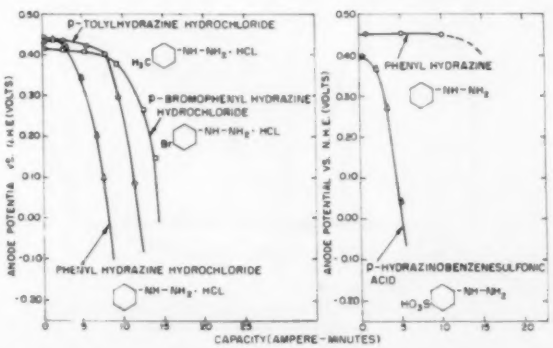

Fig. 2. Effect of substituted groups on the anode potential of phenyl hydrazine discharged at a rate of 0.005 amp/g in 1.44M NaOH.

[2] Liquid compounds were discharged at a rate of 0.005 amp/ml.

$-SO_3H$ group lowers the potential of the parent phenylhydrazine compound. However, the effect on potential, which ranges from 0.01 to 0.05 v for these substituents, is small.

Essentially, the influence of the electron repelling $-CH_3$ group is to increase the electron density in the vicinity of the oxidizable hydrazine group which decreases its affinity for electrons and renders it a stronger reducing agent. Conversely, the electron attracting $-Br$ and $-SO_3H$ groups decrease the electron density near the oxidizable hydrazine group and increase its affinity for electrons, which results in a compound that has a lower anode potential. This same effect has been noted previously for aromatic hydroxy and amino compounds (4).

The higher potential of phenylhydrazine as compared to phenylhydrazine hydrochloride is believed due to the lower pH in the vicinity of the phenylhydrazine hydrochloride electrode as a consequence of the acidic HCl group. The effect of pH on potential is described in another section of this paper.

The half-cell potential discharge curves of phenylhydrazine hydrochloride and various heterocyclic hydrazine compounds shown in Fig. 3 illustrate the effect of aromaticity on the anode potential. It is seen that the substituted hydrazine compounds having the strongly aromatic quinoline and benzothiazole rings operate at lower anode potentials than phenylhydrazine hydrochloride. This effect is attributed to the lower electron density in the vicinity of the oxidizable hydrazine group for the more strongly aromatic hydrazinoquinoline and hydrazinobenzothiazole compounds. Low electron density, a consequence of the resonance and inductive effects in these compounds, increases the affinity of the hydrazine group for electrons and renders it a weaker reducing agent. Similarly the higher anode potential of 3-hydrazinoquinoline dihydrochloride as compared to 2-hydrazinoquinoline is attributed to the higher electron density in the 3-position of quinoline than in the 2-position.[8]

[8] The unequal electron density distribution in quinoline is also a consequence of the resonance and inductive effects operating in this compound.

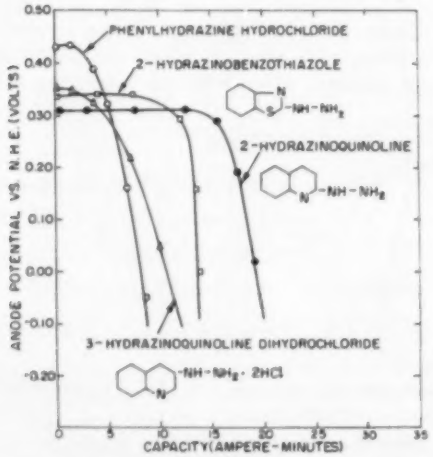

Fig. 3. Effect of aromaticity on the anode potential of organic hydrazine derivatives discharged at a rate of 0.005 amp/g in 1.44M NaOH.

Thus the effect of added groups and aromaticity on the anode potential of aromatic hydrazine compounds can be explained readily in terms of the electron density distribution in the molecules. These results are in agreement with previous results obtained from other organic oxidizing and reducing agents (4, 11-14).

Acyl derivatives of hydrazine as reducing agents. —Like the monosubstituted hydrazines, acyl derivatives of the hydrazines ($RCONHNH_2$) are reducing agents in that they reduce Fehling's solution and can be oxidized quantitatively by potassium iodate in acidic solution. The oxidation has the characteristic four electron change per hydrazine group (15).

Figures 4 and 5 show half-cell potential discharge curves of various acyl derivatives of hydrazine obtained by discharging these compounds at a rate of 0.005 amp/g in 1.44*M* NaOH electrolyte. From the curves it may be seen that the acid hydrazides operate at lower anode potentials than the monosubstituted hydrazines. The effect of substituted groups and their position in the molecule on the anode potential of benzhydrazide is demonstrated by the discharge curves of the three nitrobenzhydrazide isomers shown in Fig. 4. In agreement with the fact that the $-NO_2$ group is electron attracting and decreases the electron density to the greatest extent in the ortho and para positions, benzhydrazide operates at more anodic potentials than the nitrobenzhydrazide compounds, while m-nitrobenzhydrazide has a higher anode potential than its ortho and para isomers.

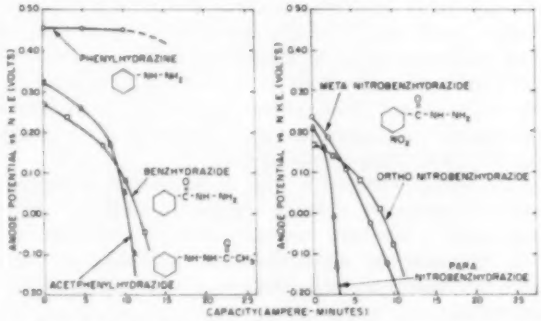

Fig. 4. Half-cell potential discharge curves of various acyl derivatives of hydrazine discharged at a rate of 0.005 amp/g in 1.44M NaOH.

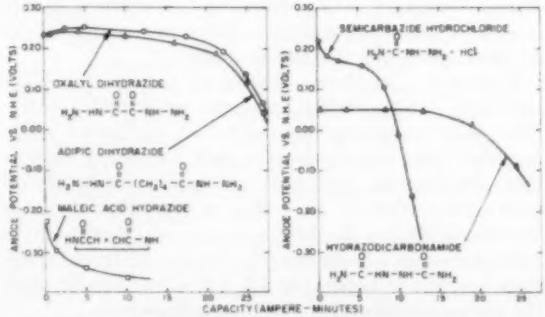

Fig. 5. Half-cell potential discharge curves of various acyl derivatives of hydrazine discharged at a rate of 0.005 amp/g in 1.44M NaOH.

Figure 5 shows that both the oxalyl and adipic dihydrazides have anode potentials close to that of benzhydrazide, and that they are considerably stronger reducing agents than maleic acid hydrazide, which can be considered as a cyclic diacyl derivative of hydrazine. As with the other substituted hydrazine compounds, the symmetrically disubstituted maleic acid hydrazide compound operates at considerably lower potentials than the hydrazide compounds which contain an $-NH_2$ group. This type of behavior is further illustrated by the lower operating potential of hydrazodicarbonamide as compared to semicarbazidehydrochloride.

Semicarbazide, a hydrazine derivative of urea, behaves in a manner similar to the acid hydrazides and hydrazines in that it reacts quantitatively with oxidizing agents. In its reaction with iodine, one molecule of semicarbazide reacts with four atoms of iodine by this probable equation (16)

$$H_2N\text{-}NHCONH_2 + 2I_2 + H_2O \rightarrow N_2 + CO_2 + NH_4I + 3HI \quad [8]$$

The lower potential of semicarbazide as compared to phenylhydrazine is in agreement with the observations that semicarbazide is more stable in air and less rapidly attacked by iodine than is phenylhydrazine.

Hydroxylamine derivatives as reducing agents.—Half-cell potential discharge curves of hydroxylamine and some of its organic derivatives obtained by discharging these compounds at a rate of 0.005 amp/g in 1.44 *M* NaOH are shown in Fig. 6. It is seen that under these conditions of discharge hydroxylamine hydrochloride operates at a potential of +0.30 to +0.35 v, a potential considerably lower than the theoretical value (1) shown below.

$$NH_3OH^+ = \tfrac{1}{2}N_2 + 2H^+ + H_2O + e^- \quad E^\circ = 1.87 \text{ v} \quad [9]$$

$$2NH_2OH + 2\,OH^- = N_2 + 4H_2O + 2e^- \quad E^\circ_s = 3.04 \text{ v} \quad [10]$$

$$2NH_3CH^+ = N_2O + 6H^+ + H_2O + 4e^- \quad E^\circ = 0.05 \text{ v} \quad [11]$$

$$2NH_2OH + 4\,OH^- = N_2O + 5H_2O + 4e^- \quad E^\circ_s = 1.05 \text{ v} \quad [12]$$

The alkyl or aryl derivatives of hydroxylamine occur as O-derivatives (α) or N-derivatives (β). The N-alkyl derivatives are more powerful reducing agents than the O-alkyl derivatives as evidenced by the fact that β-methylhydroxylamine (CH_3NHOH) reduces Fehling's solution while α-methylhydroxylamine (NH_2OCH_3) does not (17). This type of behavior is in agreement with the observed discharge curves of N-hydroxybenzenesulfonamide and methoxyamine hydrochloride.

Also shown in Fig. 6 are discharge curves for various oximes of the general formula RR′C = NOH. In these organic derivatives of hydroxylamine the two hydrogen atoms are replaced by a divalent radical. The discharge curves of these three typical oxime compounds indicate that they are considerably weaker reducing agents than the parent hydroxylamine compound. The stronger reducing activity of NH_2OH as compared to RR′C = NOH and NH_2OR compounds is in agreement with the previously stated observation that whenever any two atoms of the groups C, O, and N are joined, and each holds a hydrogen atom, oxidation occurs readily.

Effect of pH on the anode potential of hydrazine and hydroxylamine.—From Eq. [1-4] and [9-12] it is seen that hydrogen ions are involved in the oxidation of hydrazine and hydroxylamine. Thus the electrode potentials of these compounds should be pH dependent. Accordingly, the half-cell potential discharge curves of hydrazine sulfate and hydroxylamine sulfate presented in Fig. 7 show that the ease of oxidation and the anode potential generally increase with increasing pH.

It is also seen that little or no capacity is obtained from hydrazine sulfate in the $MgBr_2$(pH = 8-9) and NH_4Cl-$ZnCl_2$(pH = 4.5) electrolytes, while it operates at an efficiency of 33% in the strongly basic NaOH(pH = 14) solution. This may be due to the fact that, although hydrazine is capable of undergoing self-oxidation and reduction in both alkaline and acid solution according to the following over-all equation

$$3N_2H_4 \rightarrow N_2 + 4NH_3 \quad [13]$$

this reaction does not occur extensively in alkaline medium but does in acid solution (18). Similarly, hydroxylamine is unstable with respect to decomposition into ammonium ion and nitrous oxide (2).

$$4NH_3OH^+ = N_2O + 2NH_4^+ + 3H_2O + 2H^+ \quad [14]$$

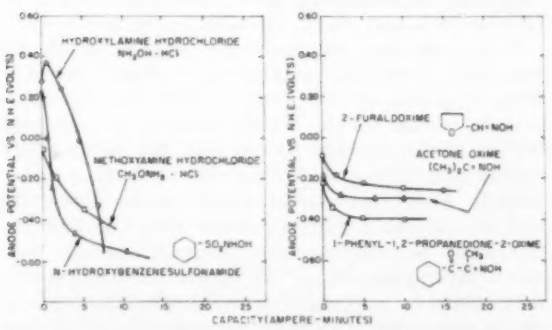

Fig. 6. Half-cell potential discharge curves of hydroxylamine and various organic hydroxylamine derivatives discharged at a rate of 0.005 amp/g in 1.44M NaOH.

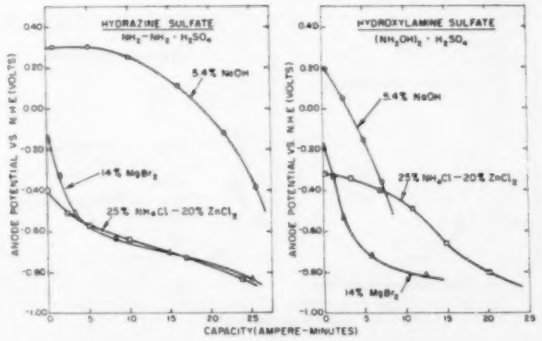

Fig. 7. Effect of pH on the anode potential of hydrazine sulfate and hydroxylamine sulfate discharged at a rate of 0.005 amp/g in various aqueous electrolytes.

However, the reaction is favored by alkali, as the equation indicates.

Although poor electrode efficiencies have been obtained from hydrazine sulfate and hydroxylamine sulfate under the aforementioned conditions of discharge, Lingane and Jones (19) have oxidized hydrazine quantitatively to nitrogen in neutral or acid medium at a platinum anode using controlled potential methods. Similarly, hydroxylamine dihydrochloride in 1*M* NaCl was oxidized at a platinum anode with a current efficiency of 100%, 82% of which was oxidized to nitrous oxide, 17% to nitrate ion, and 1% to nitrous acid.

Hydroxylamine and its organic derivatives as oxidizing agents.—According to Latimer (2) the potential for the hydroxylamine-ammonium ion couple is

$$NH_3OH^+ + 2H^+ + 2e^- = NH_4^+ + H_2O \quad E^\circ = 1.35 \text{ v} \qquad [15]$$

This value would indicate that hydroxylamine is a powerful oxidizing agent, but actually its rate of reduction is slow with many powerful reducing agents.

Figure 8 shows half-cell potential discharge curves of hydroxylamine sulfate, N-hydroxybenzenesulfonamide, and various organic oxime compounds obtained by discharging these compounds as cathodes at a rate of 0.005 amp/g in 250 g/l $MgBr_2 \cdot 6H_2O$ electrolyte. Although hydroxylamine sulfate and N-hydroxybenzenesulfonamide provide very little capacity as cathodes, they do operate at higher cathode potentials than the organic oximes.

Typical oxime compounds such as benzaldoxime, acetone oxime, and 2,4- pentanedionedioxime are found to operate at cathode potentials which are too low to be measured by the present technique. The higher cathode potentials of the 1-phenyl-1,2-propenedione-2-oxime and 1,2,3-cyclohexenetrionetrioxime compounds shown in Fig. 8 are attributed to the electron attracting C = O and C = NOH groups adjacent to the oxime group. The effect of these groups is to decrease the electron density in the vicinity of the reducible oxime group, thus increasing its affinity for electrons and rendering the compound a stronger oxidizing agent.

Coulombic capacities of hydrazine and hydroxylamine derivatives.—Table I presents theoretical

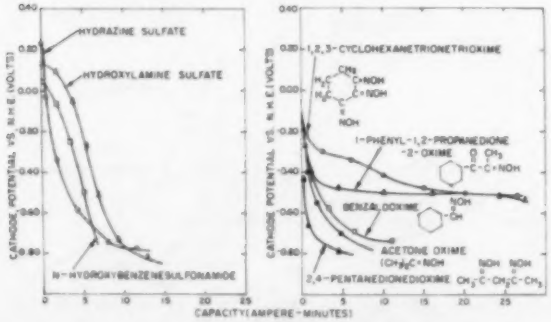

Fig. 8. Cathodic half-cell potential discharge curves of various organic hydroxylamine and oxime derivatives discharged at a rate of 0.005 amp/g in 250 g/l $MgBr_2 \cdot 6H_2O$ electrolyte.

Table I. Theoretical capacities and electrode efficiencies of various hydrazine and hydroxylamine derivatives

Anode material	Electron change	Capacity, amp-min/g Theoretical	Experimental*	Efficiency, %
Zinc	2	49.2	44.3	90.0
Magnesium (AZ10 Alloy)	2	132.0	53-86	40-65
Hydrazine	4	201.0	—	—
Methylhydrazine	4	140.0	—	—
Phenylhydrazine	4	59.3	—	—
Hydrazine sulfate	4	49.5	16.4	33.1
Phenyl hydrazine hydrochloride	4	44.4	6.3	14.2
p-hydrazinobenzenesulfonic acid	4	34.1	4.0	11.7
p-tolylhydrazine hydrochloride	4	40.3	10.1	25.1
p-bromophenyl hydrazine hydrochloride	4	28.8	13.2	45.8
2-hydrazinobenzothiazole	4	41.3	13.5	32.7
3-hydrazinoquinoline dihydrochloride	4	27.7	8.5	30.7
2-hydrazinoquinoline	4	40.1	18.3	45.6
Benzhydrazide	4	47.2	10.5	22.2
p-nitrobenzhydrazide	4	35.5	2.5	7.0
o-nitrobenzhydrazide	4	35.5	9.1	25.6
m-nitrobenzhydrazide	4	35.5	5.8	16.3
Oxalyl dihydrazide	8	109.0	27.5	25.2
Adipic dihydrazide	8	73.8	27.2	36.9
Semicarbazide hydrochloride	4	57.6	10.1	17.5
Hydrazodicarbonamide	2	27.2	26.7	98.2
Hydroxylamine sulfate	2	19.6	3.0	15.3
Hydroxylamine hydrochloride	2	46.2	3.2	6.9
N-hydroxybenzenesulfonamide	2	18.6	0.7	3.8

* Experimental capacity based on a 0.2 v drop in potential as end potential.

capacities and electrode efficiencies of various hydrazine and hydroxylamine derivatives calculated from the half-cell discharge data in Fig. 1-7. The experimental capacities were measured on the basis of a 0.2 v drop in potential from initial as the end potential, whereas the theoretical capacities were computed by means of Faraday's law using the electron change shown in the table. Also included in Table I are comparable data for conventional zinc and magnesium anodes when discharged in NH_4Cl-$ZnCl_2$ and $MgBr_2$ electrolytes, respectively.

It is seen that the electrode efficiencies of the monoaryl hydrazine compounds range from 12-46% as compared to a value of 33% for hydrazine sulfate in the 1.44*M* NaOH solution. In general higher efficiencies are found with the bicyclic hydrazinoquinoline and hydrazinobenzothiazole compounds which operate at lower anode potentials and are probably more insoluble than the phenylhydrazine derivatives. Such behavior suggests that some decomposition of the hydrazine compounds takes place by air oxidation in the alkali solution, a result consistent with previous experiments on the stability of hydrazine in alkali solution (20). Like the hydrazine derivatives, the organic hydrazides, with the exception of p-nitrobenzhydrazide, oper-

ate at efficiencies of 16-37% assuming a 4 electron change per hydrazino group. Of the compounds tested, the best electrode efficiency was found for hydrazodicarbonamide, which is oxidized quantitatively with a 2 electron change to azodicarbonamide.

The organic hydrazine derivatives do not compare favorably with inorganic materials on the basis of theoretical and experimental coulombic capacities. In addition, the anode potentials of the more strongly reducing organic hydrazine derivatives range from +0.25 to +0.45 v, values considerably lower than the anode potentials of 1.3 v for magnesium in aqueous magnesium bromide solution, and 0.7 and 1.3 v for zinc in acidic and strongly alkaline solutions, respectively. Liquid hydrazine itself is a more attractive anode material than any of its organic derivatives on the basis of its theoretically high capacity (201 amp-min/g) and operating potential of +0.35 v in alkali electrolyte. However, for hydrazine to compete with other liquid, gaseous, or solid primary cell anodes, higher efficiencies than those attained from the solid hydrazine compounds tested must be realized.

For the three compounds tested, the hydroxylamine derivatives had electrode efficiencies ranging from 4-15%, values considerably lower than those of the hydrazine derivatives. On this basis, together with their low theoretical capacities, the hydroxylamine derivatives do not show promise for use as anode materials in primary cells.

Acknowledgment

The author wishes to acknowledge support of this research by the Power Sources Division of the U. S. Army Signal Research and Development Laboratory under Contract Number DA-36-039-sc-78048.

Manuscript received April 18, 1961; revised manuscript received June 27, 1961. This paper was prepared for delivery before the Houston Meeting, Oct. 9-13, 1960.

Any discussion of this paper will appear in a Discussion Section to be published in the June 1962 JOURNAL.

REFERENCES

1. T. Moeller, "Inorganic Chemistry," pp. 580-585, John Wiley & Sons, Inc., New York (1952).
2. W. M. Latimer, "Oxidation Potentials," 2nd ed., pp. 97-100, Prentice-Hall, Inc., Englewood Cliffs, N. J. (1952).
3. C. K. Morehouse and R. Glicksman, *This Journal*, **103**, 94 (1956).
4. R. Glicksman, *ibid.*, **108**, 1 (1961).
5. R. Glicksman and C. K. Morehouse, *ibid.*, **102**, 273 (1955).
6. Ref. (2) p. 354.
7. N. V. Sidgewick, "The Organic Chemistry of Nitrogen," pp. 378-384, Oxford University Press (1937).
8. V. von Richter, "Organic Chemistry," Vol. I, p. 203, Elsevier Publishing Co., Inc., New York (1944).
9. C. W. Porter and T. D. Stewart, "Organic Chemistry," p. 111, Ginn and Co., New York (1943).
10. J. H. Walton and G. W. Filson, *J. Am. Chem. Soc.*, **54**, 3228 (1932).
11. R. Glicksman and C. K. Morehouse, *This Journal*, **105**, 299 (1958).
12. R. Glicksman and C. K. Morehouse., *ibid.*, **106**, 288 (1959).
13. R. Glicksman and C. K. Morehouse, *ibid.*, **106**, 741 (1959).
14. R. Glicksman and C. K. Morehouse, *ibid.*, **107**, 717 (1960).
15. W. R. McBride, R. A. Henry, and S. Skolnik, *Anal. Chem.*, **25**, 1042 (1953).
16. P. D. Bartlett, *J. Am. Chem. Soc.*, **54**, 2853 (1932).
17. F. C. Whitmore, "Organic Chemistry," 2nd ed., p. 182, D. Van Nostrand Co. Inc., New York (1951).
18. L. F. Audrieth and B. Ackerson, "The Chemistry of Hydrazine," p. 117, John Wiley & Sons, Inc., New York (1951).
19. J. J. Lingane and S. L. Jones, *Anal. Chem.*, **23**, 1798 (1951).
20. E. J. Cuy and W. C. Bray, *J. Am. Chem. Soc.*, **46**, 1786 (1924).

Correction

In the paper by Albert Mark "Single Crystal Silicon Overgrowths" which was published in the September 1961 issue of the Journal, the photograph, Fig. 8, p. 884, is by H. J. Yearian.

Cathodic Behavior of Iron Single Crystals and the Oxides Fe_3O_4, Gamma-Fe_2O_3, and Alpha-Fe_2O_3

C. D. Stockbridge,[1] P. B. Sewell,[2] and M. Cohen

National Research Council, Ottawa, Canada

ABSTRACT

The cathodic behavior of iron, Fe_3O_4, γ-Fe_2O_3, and α-Fe_2O_3 have been investigated in the borate/HCl buffer solution of $pH = 7.6$. The hydrogen overpotential on iron is found to vary on surfaces of different crystallographic orientation and with changes in the surface microstructure. The immersion potentials and cathodic reduction behavior with regard to reduction potential and current efficiency of the three oxides are sufficiently different to allow unambiguous distinction to be made between the oxides. Of the two cubic oxides, Fe_3O_4 is reduced with an apparent current efficiency of less than 17%, whereas the apparent current efficiency for γ-Fe_2O_3 is greater than 60% at a reduction potential some 300 mv more positive than that for Fe_3O_4. Air exposure of Fe_3O_4 causes the transformation of up to 25Å of the surface layer to γ-Fe_2O_3. This technique of cathodic reduction is suitable for both qualitative and quantitative measurements of thin oxide films on iron.

Previous study (1) has established that α-Fe_2O_3 is reduced quantitatively at high current efficiency (95-105%) when present as a film on iron cathodes in the borate/HCl buffer solution of pH 25°C = 7.65. The experimental work described in this paper arose out of a desire to extend the utility of cathodic reduction for characterizing and measuring the quantities of oxide(s) formed on iron at low temperatures when only thin layers are present. Having developed a method of electropolishing to prepare chemically clean, "atomically smooth" iron surfaces (2), which in the case of single crystals are covered with a thin layer of oriented cubic oxide less than 25Å thick, we were particularly anxious to characterize and measure this oxide by its cathodic behavior.

Throughout the experimental work on the cathodic reduction of very thin oxide films on electropolished iron highly reproducible potential/time curves of two types were obtained. The iron surface had either (i) a relatively positive potential on immersion into the solution and was covered with a protective film which did not disappear unless reduced by an impressed cathodic current or (ii) the surface had a more negative immersion potential, being covered with a nonprotective film which was reduced with or without impressed current. At first these curves had little obvious connection with the iron found in solution on ceasing cathodic treatment and bore less than expected similarity to those found by Allen (3) for thin cuprous oxide films or by Hoar and Stockbridge (4) for thin cuprous sulfide films. Furthermore, single crystal iron surfaces gave an unexpected type of reduction curve with a potential/time minimum, which was sensitive in magnitude and shape to the substrate orientation. These results indicated that a more complete potential/current study of iron and iron oxide surfaces was obligatory to further understanding of the constant current potential/time reduction curves of the thin oxide films on iron. This work is described below.

[1] Present address: Bell Telephone Laboratories, Whippany, N. J.
[2] N.R.C. Post-doctorate Research Fellow.

Table I. Materials used in cathodic studies of iron and its oxides

Specimen	Treatment
"Ferrovac E" sheet	Reduced in flowing H_2/H_2O for 1 week at 1250°C.
Iron single crystals (112), (117), (115)	Strain annealed from "Ferrovac E," from Dept. of Mines and Technical Surveys, Ottawa.
Iron single crystals (011), (001), (112)	Strain annealed from "Super Hiperm."
Fe_3O_4 crystal	Natural crystal used as received from Bell Telephone Laboratories.
γ-Fe_2O_3, powder	As received from Dr. Epelboin, Dept. of Physics, Sorbonne, Paris.

Experimental

Table I lists all the materials used. All the iron specimens were electropolished by the method reported fully elsewhere (2). Immediately after polishing the surfaces were generously washed with a jet of methyl alcohol distilled off CaO, dried by tapping with lens tissue to prevent evaporation chilling, and mounted in the stainless steel clamp shown in Fig. 1a. When mounted and air exposed the edges and lead-in wires or tails of all specimens were masked from contact with solution by a covering of paraffin wax applied with an artist's brush. The cathodic behavior of waxed specimens was the same as for nonwaxed specimens. This suggests that the bare surfaces were not contaminated by the wax and that edge effects do not play an important role in reduction experiments. However, surface areas of waxed specimens are more accurately defined and hence apparent current density values more reliable.

The waxed specimen and clamp were then put in the cell (Fig. 1) and deoxygenated nitrogen passed for 1 hr with T_1, T_2, and T_3 open. The cell having

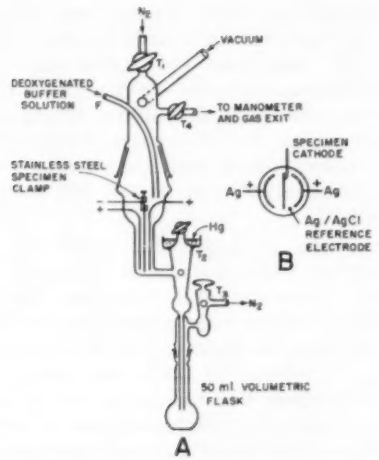

Fig. 1. Cathodic reduction cell

been purged of oxygen, T_3 and T_5 were closed, T_4 opened, and approximately 13 ml of deoxygenated borate/HCl buffer (1) admitted via F to cover the specimen and other electrodes in the cell. After measuring the zero applied current potential (immersion potential), current from a 90-v dry battery was passed between the specimen as cathode and two flat symmetrically placed silver/silver chloride anodes via a large external resistance and a calibrated microammeter. All cathode/solution potentials were measured against an internal silver/silver chloride wire which extended the length of the specimen about 3 mm away. Potentials were measured using a Keithley d-c indicating amplifier of input resistance $> 10^{12}$ ohms, connected to a Brush Recorder Mark II. All quoted potentials are on the hydrogen scale.

After cathodic treatment of generally 1000 sec, the solution in the cell was dumped via T_5 into a 50 ml volumetric flask which contained 1 ml iron-free concentrated HCl. The cell was flushed once with fresh buffer solution, current being applied continuously.

Iron content of dumped buffer solutions was measured colorimetrically using the thioglycollic acid complex (5). With 5 cm path length cells the calibration curve indicated a sensitivity of 0.2 μg iron per 50 ml solution. Reagent grade chemicals specially selected for the absence of iron, and water of less than 10^{-6} mhos were used. No iron was detected when the buffer solution was passed through the cell, provided it had been adequately rinsed with 10*N* HCl and conductivity water.

Results

Iron.—The polarization curves of Fig. 2 were obtained from electropolished iron specimens, which had been examined by reflection electron diffraction after polishing. Surfaces were shown to be chemically clean and extremely smooth but covered with a thin film of oriented cubic oxide (2, 6). The surface oxide was removed by cathodic reduction by passing a current of 15 μa/cm^2 in fresh buffer solutions for two periods of about 1000 sec. For each recorded value of E_H (hydrogen scale),

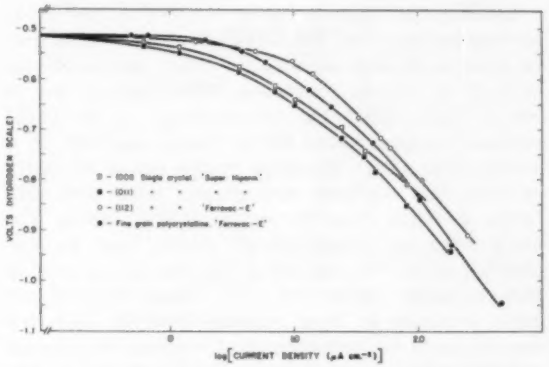

Fig. 2. Cathodic polarization of electropolished iron samples following cathodic reduction of the surface oxide.

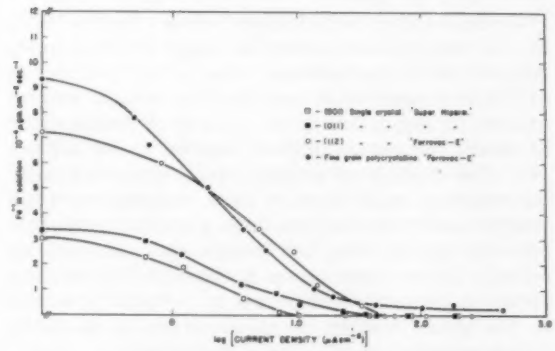

Fig. 3. Corrosion of iron during cathodic polarization experiments.

current was passed for 1000 sec and the solution then analyzed for iron. When these analyses are plotted as a rate of solution of iron against log applied current density (Fig. 3) they show unambiguous cathodic protection of the iron single crystal specimens. Polycrystalline iron is not completely protected at any of the applied current densities, presumably due to grain boundary effects.

An important observation of these experiments is that the hydrogen overpotential on iron surfaces is markedly dependent on substrate orientation for the very smooth surfaces prepared by electropolishing. However, on any one crystal face, the overpotential varies widely for small changes in surface microstructure. If an electropolished (001) surface is oxidized at 200°C to develop about 100Å oxide, and this oxide then is cathodically reduced, the overpotential on the resulting iron surface is about 100 mv more positive than on the initial surface at the same apparent current density. From Fig. 2 it can be shown that a rise of 100 mv on the (001) surface could be attributed to a change in the true surface area by about 3 which would give an effective current density of 5μa/cm^2. However, an increase of surface roughness factor to 3 from about 1.1 for electropolished iron (7) is not suggested by electron diffraction. Reflection diffraction patterns from the resulting (001) surface still exhibit marked refraction streaking indicating little change in surface microstructure (6).

Etching experiments on an electropolished (112) surface indicate that the change in overpotential may be associated with some factor other than a change in surface area or roughness. After etching for 30 sec in 0.05% HNO_3 the overpotential on the (112) surface becomes about 80 mv more negative. It is known that HNO_3 develops micro facets of (001) on iron, and electron micrographs show that such facets develop after 30 sec in 0.05% HNO_3. The more negative overpotential might thus be explained, since the original (112) surface is now in fact composed entirely of (001) facets without any great increase in true surface area. In both the case of cathodic reduction and etching the change in overpotential would appear to be related to the development of facets of different orientation as well as a change in the number and nature of active sites on the surface.

α-Fe_2O_3.—The polarization curve for α-Fe_2O_3, Fig. 4, was obtained using the outer layer of oxide formed on polycrystalline iron after heating at 417°C in oxygen at 19 mm Hg. The weight gain of oxygen corresponded to the growth of 8000Å oxide of which the outer 5300Å is known to be α-Fe_2O_3 (8). This oxide was probably cracked during cooling exposing small areas of Fe_3O_4 and possibly iron, which would depress the true potential curve especially during the last stages of reduction of α-Fe_2O_3. It has been shown previously (1) that the apparent reduction efficiency of α-Fe_2O_3 prepared in the above manner is of the order of 95-105% over a wide range of current densities.

An attempt to study the cathodic behavior of α-Fe_2O_3 powder dispersed on a conducting rubber substrate was unsuccessful due to interference of breaks in the powder layer which exposed rubber and the supporting metal.

Fe_3O_4.—The polarization curve for Fe_3O_4 in Fig. 4 was recorded using a natural "single crystal" of magnetite. Electron diffraction examination of the specimen indicated that it was not a well developed single crystal, but an aggregate of highly oriented small crystallites together with a considerable amount of randomly oriented material. The surface was rough on the atomic scale as the diffraction patterns were due entirely to transmission of electrons through projecting asperities. Prior to polarization experiments the crystal was cathodically treated for two periods of 1000 sec in fresh buffer solution, as it has been found that surface layers of magnetite transform to γ-Fe_2O_3 with air exposure.

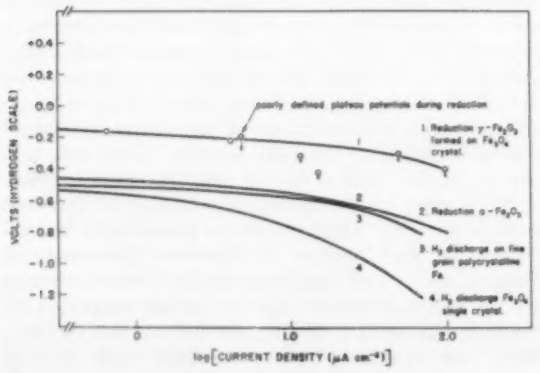

Fig. 4. Experimental polarization curves for cathodic reactions on iron and iron oxides.

From the iron found in solution during polarization experiments, the apparent reduction efficiency of Fe_3O_4 in this form is found to be very small. For current densities between 10 and 100 $\mu a/cm^2$ it is less than 5%.

When present as a thin film grown on iron by dry oxidation, Fe_3O_4 is reduced at higher current efficiencies. These experiments suggest that the apparent reduction efficiency depends on the thickness of the oxide and the amount of bare iron exposed by cracking or preferential reduction. Similar results have been obtained from oxides on both single crystal and polycrystalline specimens. Due to difficulty in reproducing oxide films of identical structure, the apparent reduction efficiency of thin Fe_3O_4 films on iron varies from 8% to 17% when reduced at 15 $\mu a/cm^2$. It had been demonstrated previously that the reduction efficiency of thicker Fe_3O_4 films was lower than this (9). These apparent efficiencies are based on the amount of Fe^{++} found in solution, but may be in error due to some complete reduction of magnetite to iron metal.

γ-Fe_2O_3.—A powder sample of γ-Fe_2O_3 was dispersed on rubber on iron and rubber on platinum. While not giving unambiguous potential/current curves, the oxide underwent cathodic reduction at apparent current efficiencies in the range of 40-60%. The most significant factor was that the reduction occurred from 100 to 300 mv more positive than the potentials associated with the reduction of any of the other oxides, whether as powders, films, or crystals.

It will be shown in the next section that when magnetite is exposed to air its surface layer is converted into a material which behaves electrochemically like γ-Fe_2O_3. The polarization curve labelled γ-Fe_2O_3 in Fig. 4 was obtained from the reduction of this material formed on a magnetite crystal repeatedly exposed to air for 15 min.

The reduction of γ-Fe_2O_3 at high current efficiency and at potentials much more positive than those associated with Fe_3O_4 or α-Fe_2O_3 has been confirmed from oxidation studies on iron single crystals (6). When an electropolished (116) iron surface is oxidized at 200°C, 20 mm O_2 for 2 hr, a highly oriented cubic oxide film some 120Å thick is developed. The electron diffraction pattern from this material is that of a cubic oxide either Fe_3O_4 or γ-Fe_2O_3. On cathodic reduction, an outer layer some 70Å thick is removed at about 60-80% current efficiency before the potential reaches a steady negative value about $E_{ss} = -0.70$ v. This negative plateau corresponds to the potential at which Fe_3O_4 films on iron are reduced. Furthermore, the reduction efficiency along this plateau is about 17%, and the electron diffraction pattern still shows highly oriented cubic oxide. Finally, after the inefficient removal of some 40Å of Fe_3O_4, the potential rises to a steady value about 100 mv more positive than the Fe_3O_4 plateau. At this new potential negligible iron is found in solution, and the electron diffrac-

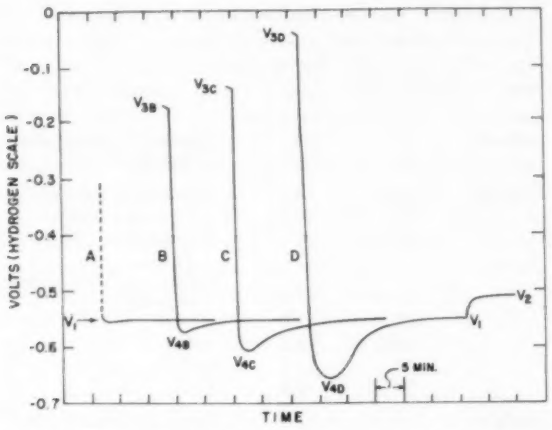

Fig. 5. Cathodic reduction of air formed oxide films on the (112) surface of iron. A, 15-min exposure to nitrogen in reduction cell; B, 2-min air exposure; C, 17-min air exposure; D, 90-min air exposure.

tion pattern after exposure to air is that of the smooth iron crystal substrate covered with a thin film of air-formed oxide.

There can be little doubt that the cubic oxide which is reduced at high current efficiency and at a high positive potential is γ-Fe_2O_3.

Effect of Air Exposure

Iron.—An electropolished iron surface which has been treated cathodically to remove the thin oxide film formed during preparation reacts with oxygen to form a reducible cubic oxide with an immersion potential of up to 500 mv positive to the zero current potential after cathodic treatment. Figure 5 shows the behavior of a surface parallel to the (112) crystal plane, as a result of air exposure for varying intervals. The initial reduction curve after electropolishing is similar to curve D and the steady potential reached at 15 μa/cm^2 is V_1. On removing applied current, the potential rises to V_2. The electrolyte is now dumped and the specimen allowed to dry in the cell in a flow of purified nitrogen. When fresh electrolyte is introduced and current at 15 μa/cm^2 applied, the potential immediately falls, as for curve A, to the value V_1 characteristic of hydrogen discharge on this iron surface. However, if the specimen is exposed to air after condition V_1 is reached, then the cathodic behavior is illustrated by curves B, C, and D. These exhibit a more positive immersion potential V_2 and a negative minimum V_4 as the oxide is cathodically reduced. The time required to reach the steady hydrogen overvoltage and the immersion potential both increase with time of air exposure. Curves B, C, and D indicate clearly that the air-formed film on iron can be detected readily by this method.

The cathodic behavior of iron single crystal surfaces exposed to air varies with crystallographic orientation. Interpretation of these reduction curves is discussed fully elsewhere (6).

α-Fe_2O_3.—In contrast to iron and magnetite, the immersion potential of air-exposed α-Fe_2O_3 and the zero current potential of cathodically treated α-Fe_2O_3 are the same, $E_H = -0.46$ v. This establishes that no reaction involving a phase change occurs on air exposure and that the effect of physically bound oxygen is small.

Table II. Effect of air exposure on immersion potential of magnetic crystal

Length of air exposure	E_H (immersion) zero current
Months	+0.27
~40 days	+0.20
24 hr	−0.01
15 min	−0.02
20 min (moist with MeOH)	−0.23
2 min	−0.26
0 min	
(20 min N_2)	−0.54

Fe_3O_4.—Magnetite which has been exposed to air after cathodic reduction acquires a more positive immersion potential with continued exposure as shown in Table II. This change suggests that the surface layer of Fe_3O_4 has been transformed to γ-Fe_2O_3.

Both the extent and perfection, as regards coverage, of the transformation of Fe_3O_4 to γ-Fe_2O_3 apparently increase with time. Figure 6 shows the cathodic reduction curves obtained with different times of air exposure of a magnetite crystal. Iron analyses of solutions after cathodic reduction point to the formation of 5.3 μg/cm^2 of γ-Fe_2O_3 (about 100Å) in 24-hr air exposure, and to 2.1 μg/cm^2 of γ-Fe_2O_3 (about 40Å) in 2-15 min. However the surface of the Fe_3O_4 crystal was rough so that these figures indicate the maximum extent of transformation which is probably less by a factor of 3 or 4.

Table III lists results obtained by re-exposing to air the visible oxide formed on iron at 200°C which had been reduced cathodically long enough to remove the outer layer of γ-Fe_2O_3. These results on much smoother oxide surfaces suggest that the underlying Fe_3O_4 reformed 14 ± 8Å γ-Fe_2O_3 in 20-hr air exposure and about 25Å in 100 hr. With longer air exposure, up to 200 hr, the γ-Fe_2O_3 was sufficiently thick and compact (few microflaws) that at zero applied current the characteristically high immersion potential $E_H = 0.0$ v was observed and a low rate of solution 2.3 x 10^{-4} μg Fe/cm^2/sec measured.

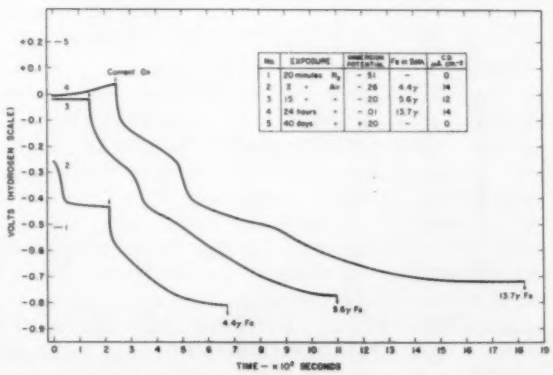

Fig. 6. Cathodic reduction of air-formed films on magnetite

Table III. Formation of γ-Fe_2O_3 on magnetite on iron

Air exposure after reduction, hr	E_H (immersion)	C.D. $\mu a/cm^2$	E_H (final)	Iron loss $\mu gFe/cm^2$ Solution analysis	Wt. loss
2	—	208	−0.88	0.35 ± 0.03	
20	—	30	−0.72	0.50 ± 0.03	0.5 ± 0.2
20	−0.10	2.0	−0.58	0.80 ± 0.02	0.9 ± 0.2
20	−0.22	0.66	−0.54	0.51 ± 0.02	0.4 ± 0.2
96	−0.08	6.5	−0.65	0.82 ± 0.03	0.7 ± 0.2
100	−0.08	0.34	−0.55	0.87 ± 0.03	

When γ-Fe_2O_3 is formed on Fe_3O_4 on iron as a cracked film, the system gives a well-defined cathodic reduction curve as a result of autoreduction, Fig. 7. Two well-defined potential plateaus are observed which agree closely with the values for the cathodic reaction on Fe_2O_3 and Fe_3O_4 at low current densities on the polarization curves, Fig. 4. The over-all "auto reduction" reaction may be represented by:

$$Fe \rightarrow Fe^{++} + 2e \qquad [1]$$

$$Fe_2O_3 + 3H_2O + 2e \rightarrow 2Fe^{++} + 6\,OH^- \qquad [2]$$

If γ-Fe_2O_3 is reduced at 100% efficiency by this process, then 2/3 of the total iron in solution at the end of the wave BC will be from γ-Fe_2O_3. From the total iron in solution at D, and the measured rate of solution of Fe_3O_4 on the plateau CD, the iron at point C is measured as 1.8 $\mu g/cm^2$, corresponding to a γ-Fe_2O_3 film about 32Å thick. However, if the autoreduction reaction is only 50% efficient, the thickness of γ-Fe_2O_3 is found to be 24Å. The thickness of γ-Fe_2O_3 on air-exposed magnetite estimated in this manner agrees favorably with values found by reducing with impressed current.

γ-Fe_2O_3.—The behavior of γ-Fe_2O_3 on air exposure is at present unknown since it has not been possible to prepare thick compact layers of γ-Fe_2O_3 suitable for such experiments. It has been shown in Table II that thin films of γ-Fe_2O_3 on Fe_3O_4 tend to acquire a more positive immersion potential with continued air exposure, but to what extent this is merely an approach to the immersion potential of stoichiometric γ-Fe_2O_3 is unknown. Some experiments with γ-Fe_2O_3 powder as a compact and as a powder on rubber on platinum indicate that the immersion potential may be as positive as $E_H = +0.5$ v.

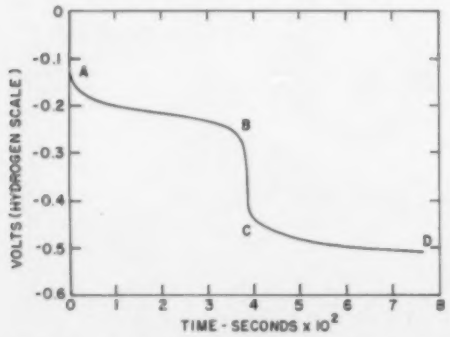

Fig. 7. Autoreduction of a thin air-formed film of γ-Fe_2O_3 on Fe_3O_4 on iron.

Table IV. Apparent reduction efficiencies of iron oxides

Material	App. reduction efficiency, %	Current density $\mu a/cm^2$	Remarks
α-Fe_2O_3	90	20	Oxide on polycrystalline iron. Ref. (1).
	95	10	
γ-Fe_2O_3	62	10.5	Powder on conducting rubber on iron.
	52	10.5	
	63	15	Air-formed film on Fe_3O_4.
			Oxide on iron single crystals
	61	13.5	(001)
	80	15.5	(001)
	72	11.5	(011)
	98	16.5	(112)
Fe_3O_4	1	15	Single crystal Fe_3O_4
	6	10	Single crystal Fe_3O_4
	1.5	20	Single crystal Fe_3O_4
			Thin film on iron single crystals
	8	18	(112)
	10	12	(011)
	17	15	(001)
	7	15	(001)

Discussion

Electron diffraction evidence suggests that much of the surface of electropolished iron is smooth on the atomic scale; however, the detailed microstructure and the distribution and nature of surface defects cannot be determined. Further, the curved polarization curves in the low current density region do not permit calculation of Tafel line parameters, so that the rate-determining step in the hydrogen discharge reaction cannot be estimated. As a result it is not possible to correlate the observed variation of hydrogen overpotential on the different single crystal faces with the crystallography of the surface in question. However, these results indicate that overpotential measurements on single crystal surfaces of known orientation and microstructure should lead to a more detailed understanding of the mechanism of hydrogen discharge on metals.

Experimental results show that the hydrogen overpotential on iron may vary by about 0.2 v. The observed final potential in a reduction analysis after all oxide has been reduced will thus depend on the resulting microstructure of the surface and may be more positive or more negative than the reduction potential of Fe_3O_4 as a thin film.

The markedly different cathodic behavior of Fe_3O_4 and γ-Fe_2O_3 enables these two materials to be distinguished even when present as very thin films on iron. Reflection electron diffraction experiments do not permit this distinction when the materials are present in the finely crystalline state usually developed at temperatures below about 200°C. Air-formed films have been identified previously by stripping followed by annealing to increase the particle size (10). This technique is not always practicable, and the film may be subject to change due to the treatment. The reduction potentials of Fe_3O_4 and γ-Fe_2O_3 are not always unambiguous as they may occur as mixed potentials when the oxides are present in thin nonuniform films. The reduction

potential of γ-Fe_2O_3 may appear more negative when γ-Fe_2O_3 is present as a thin film on Fe_3O_4 or iron. However, for Fe_3O_4 the reduction potential may appear more positive or more negative, depending on the microstructure of the underlying partly exposed iron surface. When the oxides are not clearly defined by potentials then they may be identified by measurement of the apparent reduction efficiencies. Table IV records the apparent reduction efficiencies of the oxides, for the current density range 10-20 $\mu a/cm^2$ which has been found most satisfactory for reduction analysis. The wide scatter in the values for γ-Fe_2O_3 is due to the difficulty of selecting an end point for the γ-Fe_2O_3 reduction when present as a thin film on Fe_3O_4. In all cases the figure represents a minimum value. Furthermore, it is considered by some authors that the oxides Fe_3O_4 and γ-Fe_2O_3 are the end members of a continuous series of cubic solid solutions, so that compounds exhibiting intermediate electrochemical behavior may be present in some experiments. The very high positive potentials may be associated with an oxygen rich (cation deficient) γ-Fe_2O_3.

Manuscript received Jan. 18, 1961.
Any discussion of this paper will appear in a Discussion Section to be published in the June 1962 JOURNAL.

REFERENCES

1. H. G. Oswin and M. Cohen, *This Journal*, **104**, 9 (1957).
2. P. B. Sewell, C. D. Stockbridge, and M. Cohen, *Can. J. Chem.*, **37**, 1813 (1959).
3. J. A. Allen, *Trans. Faraday Soc.*, **48**, 273 (1952).
4. T. P. Hoar and C. D. Stockbridge, *Electrochim. Acta.*, **3**, 94 (1960).
5. F. D. Snell and C. T. Snell, "Colorimetric Methods of Analysis," Vol. 2, p. 319, D. Van Nostrand Co. Inc., New York.
6. P. B. Sewell, C. D. Stockbridge, and M. Cohen, *This Journal*, **108**, 933 (1961).
7. H. H. Uhlig and T. L. O'Connor, *J. Chem. Phys.*, **61**, 402 (1957).
8. E. J. Caule, K. H. Buob, and M. Cohen, *This Journal*, **108**, 829 (1961).
9. K. H. Buob, A. F. Beck, and M. Cohen, *This Journal*, **105**, 74 (1958).
10. D. E. Davies and U. R. Evans, *J. Chem. Soc.*, **1956**, 4373.

An Electrometric and Electron Diffraction Study of Air-Formed Oxide Films on Iron

P. B. Sewell,[1] C. D. Stockbridge,[2] and M. Cohen

National Research Council, Ottawa, Canada

ABSTRACT

Oxide films formed at room temperature on iron single crystals and polycrystals have been investigated by electron diffraction and electrochemical methods. The structure of the oxide is found to vary from an Fe_3O_4 type material at the metal/oxide interface to a γ-Fe_2O_3 type material at the oxide/gas interface. The detailed nature of this film varies with the crystallographic orientation of the iron substrate, the mode of formation, and the time of subsequent air exposure. In all cases examined the oxide forms as a highly oriented, compact array of microcrystals of lateral extension less than 30Å. The mean thickness of the film lies within the range of 10-25Å.

The thickness of the thin oxide film which forms on iron as a result of oxygen exposure has been estimated by gravimetric (1, 2), optical (3, 4), and electrochemical (5) methods. It is generally found that the mean film thickness is of the order of 10-30Å, depending on surface pretreatment, oxygen pressure, and time of exposure.

Gravimetric experiments by Gulbransen (1) on hydrogen reduced polycrystalline iron indicate about 15Å of oxide following 6-min exposure to oxygen at 15 cm pressure. Exposure of such specimens for several days (2) resulted in the development of some 29Å determined for a surface roughness factor of unity ($\rho = 1$). As recent measurements on the roughness factor for hydrogen reduced iron (6) give $\rho = 1.22$, the mean thickness of the above films is slightly less than indicated.

These gravimetric results compare favorably with the optical studies of Winterbottom (3) on bright annealed carbonyl iron. About 20Å of oxide was found after 1 hr air exposure, increasing to some 25-40Å after many days. More recent optical polarization experiments by Andreeva (4) indicate 10-19Å of oxide on iron immediately after exposure to air at 40-45% humidity at 25°C. This film increased to 15-23Å after 24 hr and remained constant for 30 days.

Hancock and Mayne (5) used an electrometric method to estimate the film thickness on hydrogen-reduced iron after 48-hr air exposure and found about 26Å assuming $\rho = 1$. Their somewhat higher value of 40Å for pickled iron would suggest a somewhat larger value for ρ on these samples.

While the above methods of investigation provide valuable quantitative estimates of the mean oxide thickness they do not serve to identify the film. Further information regarding the composition of the oxide, its particle size, and epitaxial relationships between the oxide and the metal may best be obtained by the method of electron diffraction. Transmission and reflection electron diffraction studies on a wide variety of iron substrates have provided

[1] N.R.C. Post-doctorate Research Fellow.

[2] Present address: Bell Telephone Laboratories, Whippany, N. J.

much useful information concerning the nature of the oxide film. In general it has been established that the air-formed film is a cubic oxide similar to Fe_3O_4 or γ-Fe_2O_3 (7). The particle size is about 15-30Å so that the film gives rise to diffuse haloes on polycrystalline specimens and diffuse spots when formed as a highly oriented film on single crystal substrates (8). A simple development of the stoichiometric structures of γ-Fe_2O_3 or Fe_3O_4 does not appear to be favored. Haase (8) and Dankov and Shishakov (9) have reported that diffraction patterns from thin films formed at low oxygen pressures indicate that iron cations do not occupy sites expected in the normal structure for γ-Fe_2O_3 and Fe_3O_4. Dankov and Shishakov (9) suggest that the oxide structure varies from the metal/oxide interface to the oxide/gas interface from a pseudowüstite structure containing 2 2/3 iron atoms for every 4 oxygen atoms, through to a structure closely resembling γ-Fe_2O_3. Haase (8) has made observations on the oxidation of very smooth single crystal films by the reflection method and finds that the oxide formed at room temperature and 1 mm O_2 gives spot intensities in agreement with Fe_3O_4 or γ-Fe_2O_3. However room temperature oxidation at 10^{-5} mm pressure produced an oxide with abnormal spot intensities although the lattice parameter was measured as $a = 8.40 \pm 0.01$Å in agreement with Fe_3O_4. A structure was proposed which requires that no cations occupy the allowed tetrahedral positions of the spinel structure, thus resembling the pseudowüstite structure suggested by Dankov and Shishakov. An oxide of varying composition was not proposed by Haase for the air formed film at room temperatures although his results do not exclude such a possibility.

Due to the marked influence of the initial surface oxide film on the subsequent oxidation behavior of iron (10), an attempt has been made to characterize this film more fully by a combined electron diffraction and electrochemical investigation. In previous publications (11, 12), the technique of cathodic reduction in an oxygen-free solution has been described and the observed electrochemical characteristics of the oxides α-Fe_2O_3, γ-Fe_2O_3, and Fe_3O_4 reported. These results are now used in conjunction with electron diffraction information to analyze the highly reproducible cathodic behavior of single and polycrystalline iron oxidized at room temperature.

By making electron diffraction observations on surfaces before and after cathodic reduction experiments, information has been obtained regarding the surface topography of the iron substrate and the nature of the oxide film. Furthermore, electron diffraction from smooth electropolished surfaces enables foreign contamination products to be detected readily. Throughout these experiments surfaces have been free from detectable traces of contaminants from the electropolishing bath, rinsing solvents, and cathodic reduction solutions.

Experimental

Electron diffraction and cathodic reduction experiments have been carried out on fine grained ferrovac E sheet, coarse grained ferrovac E prepared by hydrogen annealing (13), and large strain-annealed single crystals. Information relating to the strain-annealed single crystals is listed in Table I. The large surface of the strip crystal is near parallel to the crystal plane specified, and the surface area of this plane available for cathodic reduction experiments is indicated. In all cases iron specimens were prepared initially using the electropolishing conditions described previously (13).

Details of cathodic reduction in the oxygen-free HCl-borate buffer of pH = 7.6 have been fully reported elsewhere (11, 12). Experiments performed in the cell described by Oswin and Cohen (11) and that described by Stockbridge *et al.* (12) gave the same results within the limits of experimental error. For convenience, mean oxide film thicknesses have been calculated assuming $\rho = 1$ for electropolished iron rather than the value $\rho = 1.12$ recently reported (6). All potentials are referred to the standard hydrogen electrode.

Electron Diffraction Results

After electropolishing, iron surfaces may be described as "atomically smooth" as evidenced by marked refraction elongation effects observed in all iron patterns. On such surfaces the oxide film formed during electropolishing and subsequent air exposure is detected readily. A more complete discussion of refraction elongation effects was reported earlier (13).

For electropolished fine grain polycrystalline iron the iron semirings appear as broad bands as seen in section (b) of the composite photograph, Fig. 1. When such a surface is etched, these bands sharpen

Table I. Information on iron single crystals

Crystal No.	Near surface plane	Material	Dimensions, mm	Major surface area, cm²
211058-C	112	Ferrovac E	35 × 6.5 × 1	5.0
270559-B	112	Ferrovac E	33 × 7 × 1	4.6
270559-D	112	Ferrovac E	51 × 6.5 × 1	6.6
211058-E	117	Ferrovac E	38 × 6 × 1	4.6
140759-A	011	Super Hiperm	51 × 9 × 0.5	9.2
210859-A	001	Super Hiperm	50 × 9 × 0.5	9.0

	C	Mn	Si	S	Cr	Ni	Al	P	Others
Ferrovac E	0.007	0.0002	0.002	0.0015	0.0002	0.0009	0.0005	0.003	—
Super Hiperm	0.005	0.05	0.05	0.012	<0.06		—	0.012	0.15

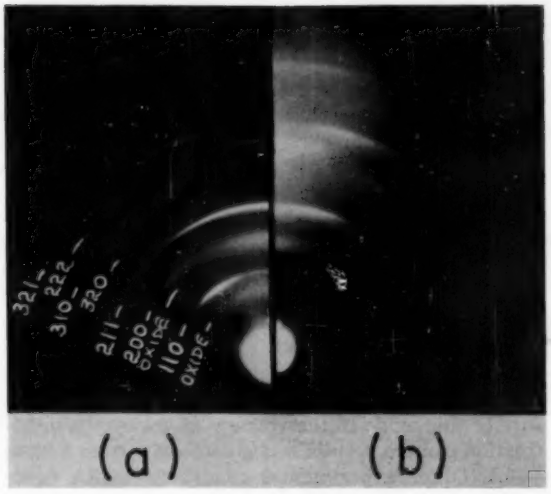

Fig. 1. Composite photograph showing reflection electron diffraction photographs from fine grained polycrystalline ferrovac E iron sheet having rolling orientation (a) etched following electropolishing; (b) as electropolished. The strong iron lines are indexed.

as seen in section (a) of Fig. 1 and are measured as the characteristic pattern of α-Fe. The air-formed oxide on the etched sample appears as two diffuse haloes, the origin of which has been described previously (7) as being primarily due to the broadening of the (113) and (440) reflections in a Fe_3O_4-like structure. On the electropolished surface only one halo is observed, that corresponding to the (440) oxide reflection. The absence of the inner halo may be due to internal reflection effects which can occur on such smooth surfaces or the result of absorption of this very low angle maxima within the film. The halo pattern suggests that the oxide is either amorphous or composed of randomly oriented microcrystallites. However, the study of iron single crystals shows conclusively that the oxide is crystalline and exhibits a well-developed epitaxial relationship with the substrate metal. (Diffuse halo patterns from overgrowths on polycrystalline substrates should thus be interpreted with caution.)

Electron diffraction patterns from coarse grained iron samples were similar to the above, but individual spots could be resolved on the semirings due to iron. Refraction elongation of these spots toward the shadow edge of the photograph was clearly visible. A diffuse halo from the oxide was again visible.

Typical electron diffraction patterns from electropolished iron single crystals are seen in Fig. 2 and from a cathodically reduced specimen in Fig. 3. The thin oxide film formed during electropolishing and subsequent air exposure is readily detected and appears in all instances as a system of diffuse spots.

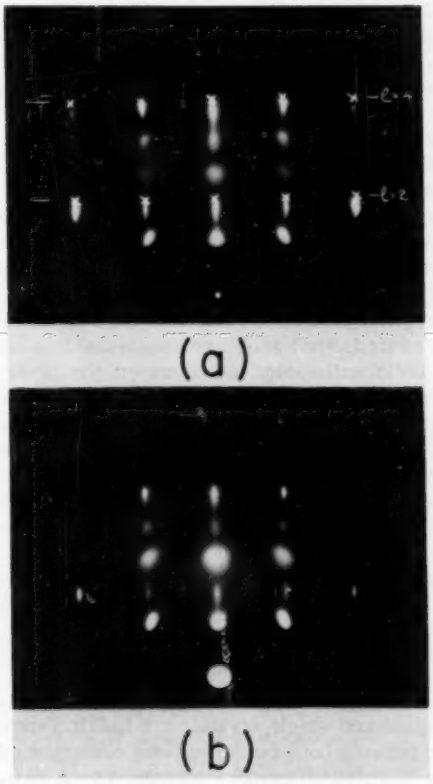

Fig. 2. Reflection electron diffraction patterns of electropolished iron single crystal; (001) surface, [$\bar{1}$10] azimuth. Elongated iron reflections originate at points (x) on the layer lines l = 2 and l = 4. Diffuse spots arise from oriented oxide film. (a) 10 min after electropolishing; (b) a further 66-hr exposure in desiccator.

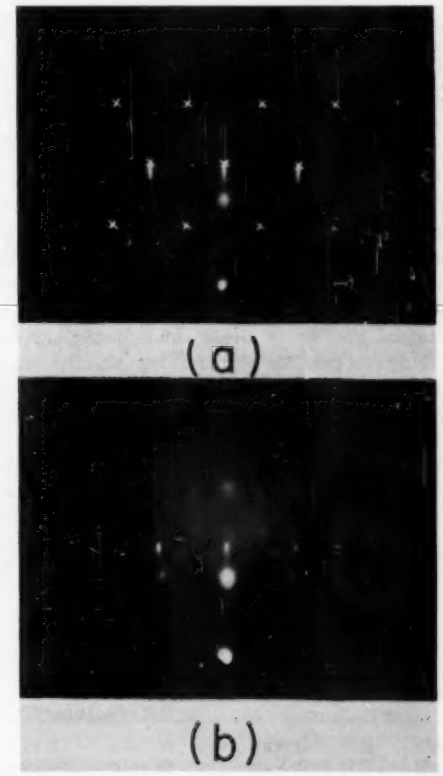

Fig. 3. Reflection electron diffraction pattern from electropolished iron single crystal following cathodic reduction; (112) surface from [11$\bar{1}$] azimuth. Iron reflections originate at points (x). Diffuse spots arise from oriented oxide film. (a) 10-min air exposure; (b) a further 460-hr exposure in desiccator.

Table II. Observed oxide orientations on electropolished iron surfaces

Iron surface plane	Parallel oxide plane	Parallel axes in contact planes iron	oxide
(001)	(001)	[010]	[$\bar{1}$10]
(112)	(110)	[$\bar{1}$11]	[1$\bar{1}$0]
(011)	(111)	[$\bar{1}$11]	[1$\bar{1}$0]*
			[$\bar{1}$10]
(117)	As for the (001)		

* Pattern appears twinned in the (111) oxide plane.

Table III. Iron single crystal. (112) surface

Variation of lattice parameter a of air-formed oxide*

Plate No.	Surface preparation	a, Å
13 plates	E.P., air exp., 5-15 min	8.26 ± 0.03
190559/1	E.P., exp. in E.D.C., 5 min	8.27 ± 0.04
190559/2	E.P., exp. in E.D.C., 30 min	8.26 ± 0.03
190559/3	E.P., exp. in E.D.C., 60 min	8.27 ± 0.04
190559/4	E.P., exp. in E.D.C., 120 min	8.32 ± 0.04
190559/5	E.P., exp. in E.D.C., 240 min	8.32 ± 0.03
200559/1	E.P., exp. in E.D.C., 22 hr	8.38 ± 0.04
5 plates	E.P., and E.P. plus C.R., exposure to air from 17-48 hr	8.39 ± 0.04
230659/2	E.P., 1½ hr at 200°C, in	
230659/3	vacuum 10^{-5} mm Hg	8.38 ± 0.03
3 plates	E.P. plus C.R., air exp., 10 min	8.32 ± 0.04

E.P.—Electropolished
C.R.—Cathodically reduced
E.D.C.—Vacuum of electron diffraction camera

* At room temperature, 25°C.

This diffuse nature of the oxide spots is due to a combination of several effects, namely, (i) small particle size, (ii) mis-orientation, and (iii) refraction effects. Contributions from each of these causes are difficult to separate, however the particle size can be shown to be less than about 30Å.,

Epitaxial growth of these small oxide crystallites is well developed on all surfaces studied; the observed relationships are listed in Table II. For the (112) and (001) surfaces the mean oxide lattice parameter may be measured in terms of the iron substrate pattern by the method of "sideline" measurements (8). It is emphasized that the lattice parameter a quoted for the oxide in Tables III and IV represents an average value determined from measurement between the centers of the diffuse oxide spots. Since it is believed that the oxide composition may vary from the metal/oxide interface to the oxide/gas interface, the oxide parameter quoted merely represents the average value for such a structure. However, since all patterns have been measured using the same technique, the variation in a does indicate a change in the nature of the oxide film.

Table IV. Iron single crystal. (001) surface

Lattice parameter a of air-formed oxide at 25°C

Plate No.	Surface preparation	a, Å
210859/1	E.P., air exposure: 10 min	8.34 ± 0.03
210859/2	E.P., air exposure: 10 min	8.29 ± 0.03
240859/1	E.P., air exposure: 66 hr	8.36 ± 0.08
240859/2	E.P., air exposure: 66 hr	8.34 ± 0.04
270859/1	E.P., plus C.R., exp., 10 min	8.33 ± 0.04
270859/2	E.P., plus C.R., exp., 10 min	8.32 ± 0.04

Results of measurements on several (112) surfaces are recorded in Table III. From 13 experiments where diffraction patterns were recorded within 5 min of electropolishing, the parameter observed is $a = 8.26 \pm 0.03$Å. This value is low for either γ-Fe_2O_3 (8.32-8.34) or Fe_3O_4 (8.39) and indicates that a cation or anion deficient oxide, most probably the former, is developed during electropolishing. Exposure of this oxide in the vacuum of the electron diffraction camera results in a change of a from 8.26 to 8.38Å. Other experimental conditions which favor the reaching of equilibrium conditions within the film give rise to oxide parameters between the values for γ-Fe_2O_3 and Fe_3O_4. This is to be expected if the resultant film has a composite structure varying between these two extremes. Even after 400 hr air exposure following cathodic reduction the oxide film is thin enough to allow a pattern from the iron substrate to be observed (see Fig. 3b).

The lattice parameters observed for the oxide film on the (001) iron surface are recorded in Table IV. For this surface an abnormally low value is not observed following electropolishing. In general the mean lattice parameter is between 8.32 and 8.39Å suggesting a composite film of γ-Fe_2O_3 and Fe_3O_4. Once again the pattern from the iron substrate is easily observable, even after an air exposure of 66 hr (Fig. 2b).

Measurement of the oxide patterns on the (011) surface is complicated by the apparent twinning of the oxide in the (111) plane. The nonsymmetrical nature of the pattern from the (117) surface makes use of the sideline technique difficult.

A point of particular interest regarding the diffuse oxide spots is that they are considerably displaced from their anticipated positions on the layer lines parallel to the shadow edge. This suggests that the oxide, although finely crystalline, forms a very smooth surface at the oxide/gas interface allowing refraction effects to occur. As there is no strong diffraction evidence of transmission diffraction from the oxide, the number of oxide particles projecting above the general level of the smooth surface must be very small. (A more detailed report on the analysis of diffraction patterns from iron single crystals is in preparation.)

Cathodic Reduction Results

Cathodic reduction experiments on both polycrystalline and single crystals are highly reproducible, as regards both potentials and coulombs passed. It was also found possible to interrupt a reduction run by dumping the solution for analysis at various times and replacing with fresh solution, without exposing the sample to air. The total iron found in solution after a continuous run is equal to the sum of the increments obtained in an interrupted run, within

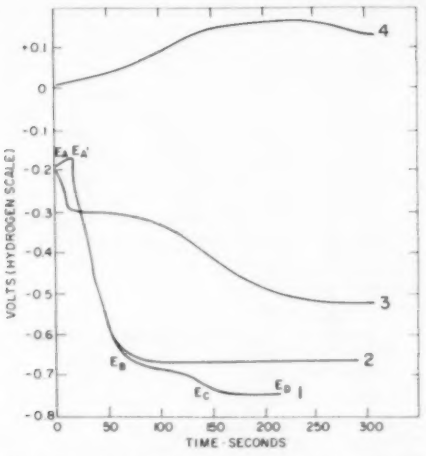

Fig. 4. Cathodic reduction curves of electropolished polycrystalline iron: 1, electropolished and 5-min air exposure; 2, electropolished and 5-sec etch in 0.05% HNO_3; 3, electropolished and 15-min air exposure (no applied current); 4, electropolished and 120-hr air exposure (no applied current).

the limits of the experimental error. It was thus possible to determine the apparent current efficiency over various segments of the cathodic reduction curve. In all cases current efficiency is calculated from the coulombs passed and the amount of Fe^{++} in solution, with the assumption that all Fe^{++} in solution is produced by the reduction of Fe^{+++} in the oxide. This point will be discussed more fully later.

Polycrystalline iron.—A typical cathodic reduction curve for a freshly electropolished sample is shown by curve 1, Fig. 4. After observing the initial immersion potential E_A and the behavior with no applied current E_A-$E_{A'}$, a current of about 14 $\mu a/cm^2$ is passed. The potential rapidly becomes more negative, passing through an ill-defined inflection between $E_{A'}$ and E_B, and a high apparent current efficiency of 70-100% is measured from the iron found in solution at E_B. Between E_B and E_C the remaining oxide is reduced at a much lower efficiency (about 10%) and finally on the plateau E_C-E_D, hydrogen discharge is the predominant reaction.

Comparing the potentials and apparent reduction efficiencies with the results published for the iron oxides in this solution (12), the high immersion potential E_A and the high reduction efficiency between $E_{A'}$ and E_B are characteristic of γ-Fe_2O_3. The low reduction efficiency on the plateau between E_BE_C and the potential of −0.65 to −0.70 v would indicate that the oxide at the oxide/metal interface behaves like Fe_3O_4.

Table V. Cathodic reduction of polycrystalline iron

Exposure time, min	c.d., $\mu a/cm^2$	E_A, v	E_D, v	Fe loss, μg Fe/cm²	Apparent* thickness, Å
Coarse grained iron, electropolished and air exposed:					
15	14	−0.30	−0.72	0.20	6
15	14	−0.07	−0.75	0.29	8.5
15	14	−0.18	−0.66	0.36	10
Coarse grained iron, E.P., etched 0.05% HNO_3 30 sec:					
15	17	−0.18	−0.66	0.52	15
15	17	−0.29	−0.69	0.47	13.5
15	17	−0.34	−0.69	0.49	14
Fine grained iron, electropolished air exposed:					
5	14	−0.14	−0.66	0.34	10
1200	13	−0.02	−0.61	0.42	12

* Thickness of oxides reduced to give Fe^{++} in solution.

Table V lists results obtained with several specimens and gives a reducible oxide thickness of 8 ± 2Å on electropolished iron exposed to air for 15 min, assuming that all the oxide is reduced to ferrous ion. When iron is etched in 0.05% HNO_3 following electropolishing the reduction curve is modified slightly as shown in curve 2, Fig. 4. The final hydrogen overpotential is more positive as a result of a micro-etch structure on the iron (12), and the end point of the reduction of the oxide is not clearly defined. Since the rate of solution of iron has been measured at these constant potentials, the iron in solution due to the reduction of the oxide film can be estimated. About 13 ± 1Å is found after the specimen has been etched after electropolishing and air exposed some 15 min. This 5-sec etch does not roughen the surface sufficiently to change the refraction effects on electron diffraction.

With prolonged air exposure following electropolishing, changes in the nature of the oxide film can be observed by studying the behavior of specimens in the buffer solution with zero applied current. After some 15-min air exposure, when the immersion potential is about −0.2 v, the outer oxide film (presumably γ-Fe_2O_3) undergoes autoreduction giving a well-defined potential inflection as shown in curve 3, Fig. 4. Both the immersion potential and the plateau potential are well above the hydrogen potential for this solution and correspond to the potentials for the cathodic reduction of γ-Fe_2O_3, the anodic reaction being iron dissolution. With over 120 hr exposure, the immersion potential was, and remained above 0.0 v for over 50 min as shown in curve 4, Fig. 4. The oxide in this case did not autoreduce, suggesting that a sufficiently pore-free but very thin layer of γ-Fe_2O_3 can protect iron from corrosion ($>5.0 \times 10^{-5}$ μg Fe/cm²/sec) in this solution for some considerable period of time.

Single crystals.—These cathodic reduction experiments are of particular interest since they provide information on both the cathodic behavior of oxide films on iron single crystals and the variation of hydrogen overpotential with crystallographic orientation (12). The cathodic reduction curves are highly reproducible for specimens of similar crystallographic orientation having the same method of surface preparation, but vary considerably with (*a*) surface treatment and (*b*) crystallographic orientation. For this reason it is convenient to discuss the results of these experiments individually.

(112) Crystals.—Cathodic reduction curves obtained following electropolishing from the three separate (112) type of single crystals listed in Table I are shown in Fig. 5. In general there is a high immersion potential E_A at zero applied current followed by a rapid (but not instantaneous) potential drop E_A-E_B when current is passed. The apparent reduction efficiency is found to be high during this period and

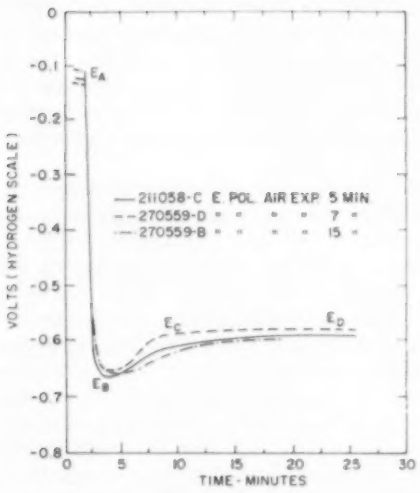

Fig. 5. Cathodic reduction curves of electropolished surfaces of 3 different iron crystals having (112) orientation.

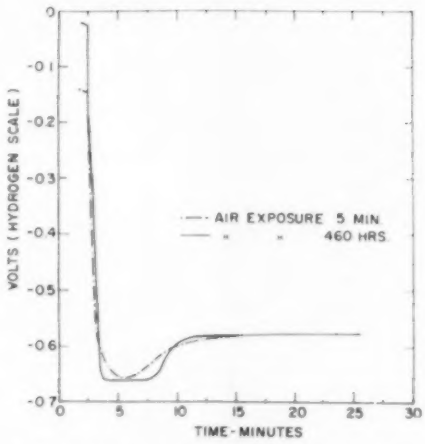

Fig. 6. Cathodic reduction curves of air-formed oxide films on the cathodically reduced surface of an electropolished (112) crystal.

together with the high immersion potential suggests the presence of an outer layer which behaves like γ-Fe_2O_3. The potential arrest at E_B is characteristic of the slow reduction of Fe_3O_4 and is followed by a slow drift more positive from E_B to E_C and then a steady potential E_C-E_D characteristic of the hydrogen overpotential on the smooth (112) surface. During the period E_B-E_C iron appears in solution at relatively low current efficiencies of about 10%, and on the plateau E_C-E_D the low rate of solution has been reported previously (12).

Table VI lists the results of reduction experiments on (112) surfaces. After electropolishing followed by 5-15 min air exposure an average of 0.58 ± 0.15 μg Fe/cm^2, due to the reduction of the oxide, is found in solution. This corresponds to a total thickness of 17 ± 4Å as γ-Fe_2O_3 or Fe_3O_4. The shape of the potential time curve suggests that the film is not of uniform composition, but consists of an outer layer of γ-Fe_2O_3 overlying a trace of Fe_3O_4. The effect of air exposure on a cathodically reduced specimen is shown in Fig. 6. The cathodic reduction curve after 5 min is very similar to that of an electropolished specimen, both having immersion potentials in the γ-Fe_2O_3 range. After a long period of exposure, during which the average lattice parameter approaches 8.39Å, there is an increase in the immersion potential and an increase in the length of the Fe_3O_4 plateau. This indicates that there is probably some thickening of the oxide. This is born out by the increase in the relative intensity of the oxide spots as compared to the iron spots shown in Fig. 3. Samples which have been etched for 30 sec in 0.05% HNO_3 behave essentially the same as the cathodically reduced specimens.

(001) Crystal.—The cathodic behavior of the (001) crystal surface shown in Fig. 7 is somewhat different from that for the (112) surface. A high immersion potential E_A is observed, followed by a rapid change negative when the current is applied. After a slight arrest at E_B, the potential becomes more negative to reach a point E_C and then drift slowly more positive to a steady value E_D. By interrupting the se-

Table VI. Cathodic reduction of (112) single crystal

Exposure time, min	c.d., μa/cm^2	E_A, v	E_D, v	Fe loss, μg Fe/cm^2	Apparent thickness, A
Electropolished and air exposed:					
5	14.0	—0.11	—0.58	0.50	14.5
5	12.5	—0.11	—0.59	0.51	14.5
5*	14.0	—0.13	—0.59	0.60	17.0
5	12.5	—0.14	—0.58	0.74	21.0
5	12.5	—0.15	—0.58	0.43	12.5
7*	13.4	—0.13	—0.57	0.70	20.0
15*	12.0	—0.12	—0.61	0.50	14.5
15	14.5	—0.14	—0.56	0.70	20.0
1320 (vac.)	14.0	—0.09	—0.58	0.78	22.5
Electropolished, cathodically reduced then air exposed:					
17	12.5	—0.15	—0.55	0.46	13
20	13.5	—0.10	—0.58	0.60	17
Etched 30 sec 0.05% HNO_3 then air exposed:					
5	14.0	—0.10	—0.65	0.40	11.5

* See cathodic reduction curves, Fig. 5.

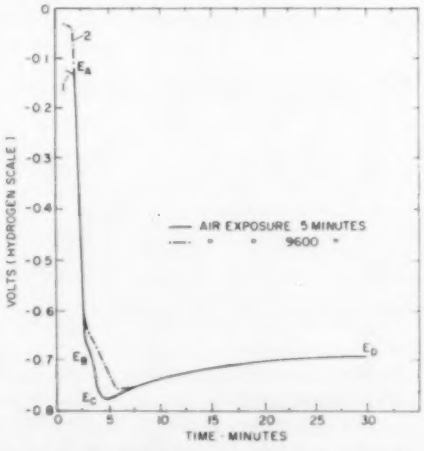

Fig. 7. Cathodic reduction curves of oxide on electropolished surface of (001) iron crystal.

Table VII. Cathodic reduction of (001) and (011) single crystals

Exposure time, min	c.d., μa/cm^2	E_A, v	E_D, v	Fe loss, μg/cm^2	Apparent thickness, Å
(001) crystal: E.P. and air exposed:					
5*	14.5	−0.13	−0.71	0.20	6
5	14.2	−0.15	−0.71	0.20	6
5	13.5	−0.12	−0.71	0.24	6.5
30	14.5	−0.09	−0.65	0.23	6.5
9600*	14.7	−0.04	−0.68	0.35	10
(001) crystal: E.P., cathodically reduced and air exposed:					
10	14.2	−0.10	−0.71	0.15	4.5
10	14.7	−0.10	−0.71	0.15	4.5
20	14.5	−0.10	−0.68	0.25	7
(011) crystal: E.P. and air exposed:					
15	14.4	−0.08	−0.71	0.45	13
30**	12.2	−0.06	−0.71	0.27	7.5
9600	14.7	+0.04	−0.70	0.33	9.5
(011) crystal: E.P., cathodically reduced and air exposed:					
5**	12.6	−0.18	−0.71	0.17	5
4400**	12.6	−0.05	−0.71	0.22	6.5

* See cathodic reduction curves Fig. 7.
** See cathodic reduction curves Fig. 8.

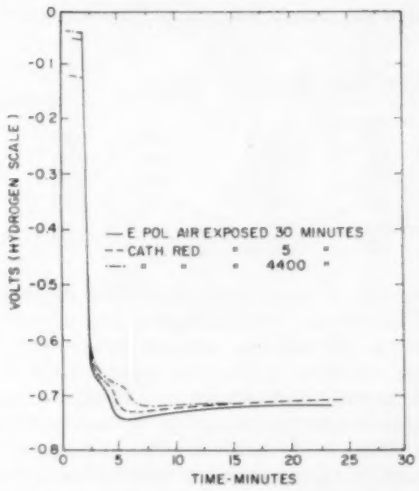

Fig. 8. Cathodic reduction curves of air formed oxide films on surface of (011) iron crystal.

quence at points E_B, E_C, and E_D and analyzing for iron, it is found that most of the iron (about 0.2 μg/cm^2) passes into solution between E_A and E_B. During the period E_B-E_C only some 0.02 μgm/cm^2 is found and between E_C-E_D no further change is detected suggesting that iron is neither plating out from solution nor passing into solution. The small amount of iron found in solution corresponds to 0.2 μg/cm^2 or a mean thickness of about 6Å (see Table VII).

The intensity of the oxide pattern in electron diffraction photographs suggests an oxide film similar in thickness to that on the (112) surface. It seems likely that during the period E_B-E_C-E_D an oxide is being reduced directly to iron (5), the mechanism probably being influenced by the epitaxial relationship between the iron substrate and the oxide. For such small amounts of iron, corresponding to 1 or 2 layers in the (001) plane, it has not been possible to detect such direct reduction by electron diffraction. Exposure to air for 160 hr causes some change in the cathodic reduction results as shown in curves 1 and 2 of Fig. 7. As with the (112) crystal the immersion potential is increased. There is also a shift in the lower part of the curve, accompanied by a larger amount of Fe^{++} in solution. This would indicate that there has been some thickening of the film, and this is also shown by the increased intensity of the oxide reflections in the electron diffraction pattern (Fig. 2b).

(011) Crystal.—The cathodic behavior of the (011) crystal for oxide films formed under three different conditions is shown in Fig. 8. The general form of the curves is similar to those for the (001) crystal, however E_C is less negative and E_D is more negative than with the (001) crystal. The length of the arrest potential for these curves indicates the relative amounts of Fe_3O_4 like material developed in these oxides. The film formed following air exposure of a cathodically reduced surface contains more Fe_3O_4 than the film formed during electropolishing although the mean thickness is about the same.

The small amounts of iron found in solution following reduction experiments on the (011) surface are recorded in Table VII. Again there is the possibility that the last traces of oxide are reduced directly to metal.

(117) Crystal.—Reduction of the oxide developed on the (117) crystal during electropolishing is illustrated by Fig. 9. The general behavior is similar to other crystals showing a slight arrest at about −0.68 v. The final hydrogen overpotential is more positive than for the (001) and (011) surfaces. Results of reduction experiments listed in Table VIII, indicate about 10Å of reducible oxide following electropolishing.

Oxidation at 200°C

Evidence obtained from the cathodic reduction of oxide films formed on iron single crystals at 200°C, 20 mm O_2 for 2 hr, has supported our interpretation of the reduction curves for thin films. For the (117) crystal gravimetric measurements indicate that such

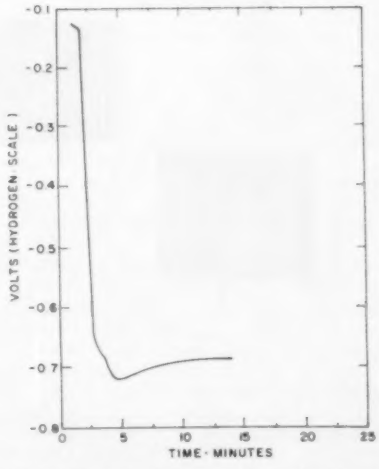

Fig. 9. Cathodic reduction curve of oxide film on electropolished surface of (117) iron crystal following 5-min air exposure.

Table VIII. Cathodic reduction of (117) single crystal

Exposure time, min	c.d., μa/cm²	E_A, v	E_D, v	Fe loss, μg/cm²	Apparent thickness, A
E.P. and air exposed:					
5	14	—0.15	—0.68	0.30	8.5
5	14	—0.15	—0.68	0.24	7
15	15.8	—0.12	—0.66	0.49	14
90	11.7	—0.06	—0.67	0.34	10
E.P. etched 60 sec 0.05% HNO_3, air exposed:					
30	12.0	—0.15	—0.66	0.37	10.5

an oxide film is about 120Å thick. The cathodic reduction curve can be interrupted and current efficiencies for the various portions determined. Furthermore, electron diffraction examination of the oxide is possible at the various stages of reduction.

A typical result for the (117) surface is shown in Fig. 10. At point A, following 200°C oxidation, the diffraction pattern consists of diffuse spots characteristic of the spinel structure Fe_3O_4 or γ-Fe_2O_3. Between A and B the oxide is reduced with a current efficiency of about 80% indicating the removal of some 70Å of γ-Fe_2O_3. On plateau B-C iron passes into solution with a current efficiency of 10-20%, and the reduction of about 40Å Fe_3O_4 is indicated. This is confirmed by electron diffraction observations on the plateau B-C which show a somewhat sharper spot pattern of cubic oxide together with weak reflections from the underlying iron. During the period CD a small amount of iron passes into solution as the last traces of Fe_3O_4 are reduced. The diffraction pattern on the final plateau shows elongated spots from the smooth iron substrate and weak diffuse spots characteristic of the air formed film.

The similarity of the reduction curves for very thin oxide films and those formed at 200°C is best illustrated by the results on the (112) crystal, Fig. 11. Curve 1 represents the reduction of the oxide on a freshly electropolished (112) surface while curve 2 is from the reduction of an oxide film some 80Å thick formed by oxidation at 200°C. Both exhibit the same general character having (i) a period AB during which γ-Fe_2O_3 is efficiently reduced, (ii) a potential plateau BC at which Fe_3O_4 is inefficiently reduced, and (iii) a rise CD to a steady potential for hydrogen evolution on base iron. The two phase nature of the thin oxide film is clearly established.

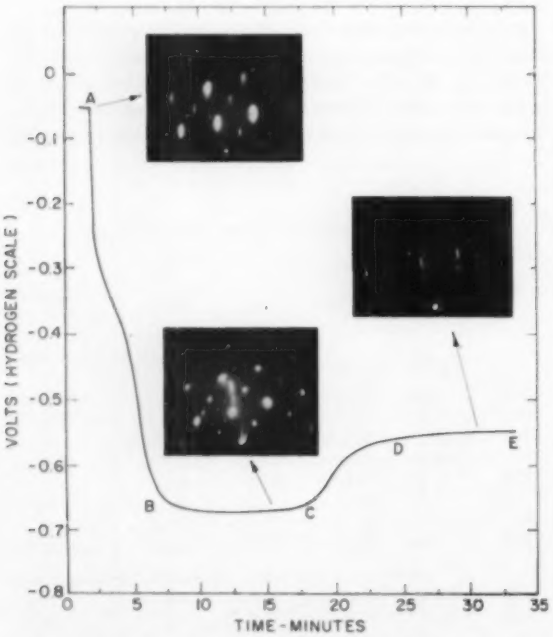

Fig. 10. Cathodic reduction curves of 120Å oxide film on (117) iron crystal showing electron diffraction observations on surface at various stages of reduction.

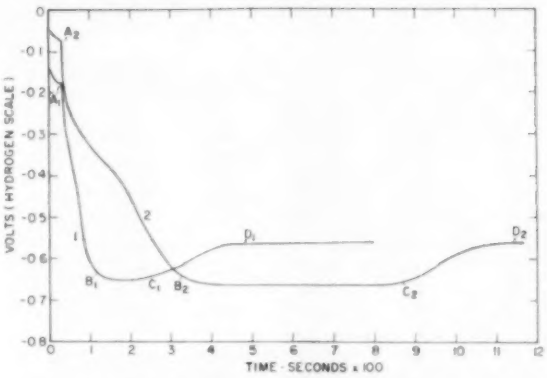

Fig. 11. Comparison of cathodic reduction curves of oxide film on (112) surface of iron. 1, electropolished and 10-min air exposure; 2, electropolished, followed by oxidation at 200°C for 2 hr in 20 mm oxygen. Total oxide thickness about 80Å.

Discussion

Both electron diffraction observations and cathodic reduction experiments support the view that the composition of the air-formed oxide films on electropolished iron, lightly etched iron, and cathodically reduced iron vary from the metal/oxide interface to the oxide/gas interface. An immersion potential much more positive than the hydrogen equilibrium potential and the high current efficiency during the early part of the cathodic reduction indicate that the outer section of the oxide resembles γ-Fe_2O_3 on top of an inner section of Fe_3O_4 like material. With an oxide film as thin as the air-formed film it seems unlikely that two discrete structures exist, but rather that the oxide has a varying cation concentration from the metal to the air interface. In all cases the oxide is cubic.

The structure of the air-formed film is dependent on the underlying orientation of the iron, method of preparation, and exposure conditions and time. In the case of (112) crystals electropolished iron exposed for short times to air or a vacuum has an oxide with a low lattice parameter (8.26) which could correspond to the presence of a cation-deficient γ-Fe_2O_3. This is probably due in part to the strongly oxidizing conditions of electropolishing. The lattice parameters of the oxide on the other orientations after electropolishing all lie between those of γ-Fe_2O_3 (8.32) and Fe_3O_4 (8.39). Specimens of all orientations exposed to air after cathodic reduction to bare metal or light etching in very dilute HNO_3 have cubic oxides with the intermediate lattice parameter. On

long time exposure to air the intensity of the oxide spots relative to the iron spots increased, indicating some thickening of the oxide. In no cases were the iron spots completely obscured, indicating that the films at room temperature, even after long time exposure, were no more than 25Å thick.

On exposure to vacuum at room temperature all the oxides approach Fe_3O_4 in composition. This process can be accelerated by heating at 200°C *in vacuo*. The outer layer of γ-Fe_2O_3 is probably reduced by migration of iron into its lattice. It would appear that one can have a cubic oxide with a cation concentration varying from Fe_3O_4 to cation deficient γ-Fe_2O_3.

There is a definite epitaxial relationship between the metal and the oxide. These are shown in Table II. The growth rates of the oxide on the various orientations is probably partly dependent on different energy barriers associated with the different epitaxy between the metal and the oxide. This may account for the low lattice parameter observed with the (112) but not the other orientations. The diffuseness of the oxide spots indicate that, although there is a high degree of preferred orientation, the particle size is of the order of 30Å. The oxide also appears to have the same degree of flatness as the metal substrate.

The electrochemical measurements confirm and amplify the above observations. As would be expected from previous work (12) the oxide at the air interface is always γ-Fe_2O_3. This is shown by the high immersion potential and the initial high current efficiency for cathodic reduction. This immersion potential is considerably higher than the equilibrium hydrogen potential for this de-aerated solution and is probably related to the $Fe_2O_3 \rightarrow Fe^{++}_{(sol'n)}$ reaction. The exact immersion potential varies with initial preparation and time of exposure to air and is probably associated with the cation concentration (and hence activity) of the oxide and the perfection of the oxide. In all cases after initial cathodic reduction the potential drops to the characteristic Fe_3O_4 potential. The final potential for hydrogen evolution is dependent on the orientation of the substrate iron.

Some indication of the characteristics of the oxide film can be obtained by a more detailed study of the cathodic reduction results. Most of the ferrous ion produced by cathodic reduction appears in the time required for the potential to reach the Fe_3O_4 potential. This would mean that the apparent thicknesses quoted in the tables is the thickness of a γ-Fe_2O_3 like oxide. At the magnetite potential there are three possible reactions: (*a*) some production of Fe^{++}, (*b*) some reduction directly to iron, and (*c*) some hydrogen evolution. The production of Fe^{++} from magnetite in these very thin films appears to be very inefficient. The observed number is 10% and this may include small residual amounts of γ-Fe_2O_3. Detailed examination of the (001) and (011) surfaces showed that after the point E_s (Fig. 7 and 8) practically no further Fe^{++} was formed from the oxide. The continued change in potential probably corresponds to the direct reduction of Fe_3O_4 to iron. The strength of the oxide diffraction patterns from the (001) crystal indicates that the films are considerably greater than the reducible 5Å of oxide. Other work in the laboratory gives an estimate of about 40% current efficiency for the reduction of thin films of Fe_3O_4 to metal in this solution. Using this number one can obtain an estimate of total thickness of the air-formed film; this is shown for the various specimens in Table IX. These numbers are approximations and do not imply a discrete boundary between the γ-Fe_2O_3 and Fe_3O_4. As pointed out earlier by Haase the oxide next to the metal is probably slightly cation excess, and the indication from this work is that the oxide next to the air is cation deficient.

Table IX. Total thickness of air-formed oxide films

Orientation	Preparation	Air exposure, min	γ-Fe_2O_3, Å	Fe_3O_4, Å	Total, Å
Coarse Grain Polycrystal	E.P.	15	8	5	13
112	E.P.	15	17	10	27
112	E.P. + C.R.	17	15	10	25
001	E.P.	5	6	13	19
	E.P.	9600	10	10	20
011	E.P.	30	8	12	20
011	E.P. + C.R.	5	5	8	13
011	E.P. + C.R.	4380	6.5	10	17
117	E.P.	5	8	12	20

The thicker films formed at higher temperatures show a more discrete plateau for the γ-Fe_2O_3 reduction. The diffraction pattern after complete reduction also shows some rings due to reduction to iron of the somewhat thicker Fe_3O_4.

The thickness of oxide formed on polycrystalline iron is approximately the same as that reported by Hancock and Mayne (5). However, they assumed incorrectly that all of the film was γ-Fe_2O_3. Stripping the film for identification, as was done by Davies and Evans (14), would give an erroneous result because exposure of the underlying thin magnetite layer to air would oxidize it to γ-Fe_2O_3.

Manuscript received Jan. 18, 1961. Preliminary results of this investigation were presented at the Columbus Meeting, Oct. 18-22, 1959.

Any discussion of this paper will appear in a Discussion Section to be published in the June 1962 JOURNAL.

REFERENCES

1. E. A. Gulbransen, *Trans. Electrochem. Soc.*, **81**, 327 (1942).
2. E. A. Gulbransen, *ibid.*, **82**, 375 (1942).
3. A. B. Winterbottom, *J. Iron. Steel Inst.*, **9** (1950).
4. V. V. Andreeva, *Trudy Inst. Fiz.-Khim., Akad. Nauk S.S.S.R.*, No. 6, Novye Metody Fiz.-Khim. Issledovanii, **1957**, No. 2, 79-98. (C.A.)
5. P. Hancock and J. E. O. Mayne, *J. Chem. Soc.*, **1958**, 4167.
6. T. L. O'Connor and H. H. Uhlig, *J. Chem. Phys.*, **61**, 402 (1957).
7. H. R. Nelson, *J. Chem. Phys.*, **5**, 252 (1937).
8. O. Haase, *Z. Naturforsch*, **11a**, 46 (1956).
9. P. D. Dankov and N. A. Shishakov, *Zhur. Fiz. Khim.*, **23**, 1031 (1949).
10. D. E. Davies, U. R. Evans, and J. N. Agar, *Proc. Roy. Soc.*, **A225**, 443 (1954).
11. H. G. Oswin and M. Cohen, *This Journal*, **104**, 9 (1957).
12. C. D. Stockbridge, P. B. Sewell, and M. Cohen, *ibid.*, **108**, 928 (1961).
13. P. B. Sewell, C. D. Stockbridge, and M. Cohen, *Can. J. Chem.*, **37**, 1813 (1959).
14. D. E. Davies and U. R. Evans, *J. Chem. Soc.*, **1956**, 4373.

The Formation of Porous Oxides on Metals

II. Tungsten and the Paralinear Rate Law

W. B. Jepson[1] and D. W. Aylmore[2]

Department of Chemistry, University of Exeter, England

ABSTRACT

The accepted mechanism of paralinear oxidation that an inner, compact layer of oxide forms at a parabolic rate and transforms to an outer, porous layer at a linear rate has been tested in the case of tungsten. Samples were oxidized at 750° and 800°C for increasing times, and the amount of porous oxide present on each sample was estimated by the method of krypton sorption. The rate of porous oxide formation is not constant, but instead decreases with time to reach an almost constant value so that the results are not in accord with the paralinear model. A similar conclusion is reached by metallographic examination of the partially oxidized samples. Results for the oxidation at 600°C are used to illustrate the difficulty of testing the paralinear rate equation by an analysis of kinetic data alone.

The kinetics of the oxidation of tungsten have been investigated by a number of workers (1-7). At low temperatures (below about 500°C) the metal oxidizes at a parabolic rate while at high temperatures (700°-1000°C), the oxidation is paralinear,[3] the rate decreasing with time to reach a constant value, that of the linear rate.

Webb, Norton, and Wagner (3) have explained the paralinear oxidation of tungsten in terms of a model similar to that used by Loriers (9, 10) to interpret the oxidation of cerium and of uranium. It was supposed that a metastable modification of one of the intermediate oxide phases of tungsten was formed at a parabolic rate as a continuous oxide layer (adherent to the metal) and this in turn oxidized at a linear rate to tungstic oxide, in a form porous to gaseous oxygen.

In a previous paper (11) (hereafter referred to as Part I), it was shown both by surface area and by density measurements that the oxide scale formed during the nonprotective oxidation of a number of metals, including tungsten, is in fact porous to oxygen gas. In the present work, improved techniques have been used to estimate the rate of formation of the porous oxide scale and thus make a direct test of the paralinear model as applied to tungsten.

Theory of Paralinear Oxidation

The generally accepted model (3, 12) of paralinear oxidation is that at a given time there are two distinct oxide layers on the metal (Fig. 1). It is supposed that the inner compact layer is formed at a parabolic rate and transforms to the outer porous layer at a constant rate so that:

$$\frac{dy}{dt} = \frac{a}{y} - b \qquad [1]$$

$$\frac{dz}{dt} = fb \qquad [2]$$

where y and z are the weights of combined oxygen per unit area at time t in the inner and outer layer, respectively; f is the ratio of the oxygen content per gram-atom of metal in the outer layer to that in the inner layer; a is one-half the parabolic rate constant, and fb is the linear rate constant (3). If the thickness of the "room temperature" film is neglected and if it is assumed that both [1] and [2] apply from zero time, we have after integration

$$\frac{a}{b}\ln\left(1 - \frac{b}{a}y\right) + y + bt = 0 \qquad [3]$$

$$z = fbt \qquad [4]$$

The total weight gain w at time t is given by

$$w = y + z \qquad [5]$$

and typical curves of y, of z, and of w are shown in Fig. 2. It will be noted that as oxidation proceeds,

[1] Present address: Metallurgy Division, Atomic Energy Research Establishment, Harwell, Didcot, Berks, England.

[2] Present address: Division of Pure Chemistry, National Research Council, Ottawa, Canada.

[3] The term "paralinear" appears to have been used first by McKewan and Fassell (8).

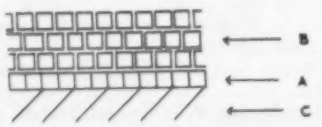

Fig. 1. Illustrating the inner compact layer of oxide (A) and the outer, porous layer of oxide (B) which are believed to be present on the metal (C) during paralinear oxidation.

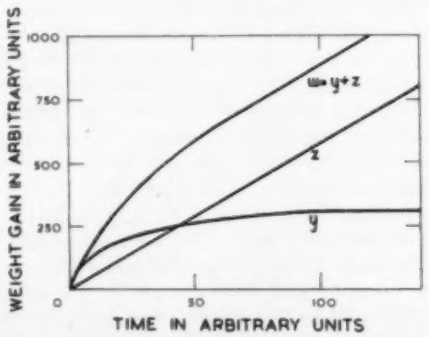

Fig. 2. Illustrating the curves for the rate of growth on the inner and outer oxide layers. The curves of y and of z against time are calculated from Eq. [3] and [4], respectively; the curve of w against time is calculated from Eq. [5].

the rate of thickening of the inner layer progressively decreases and its thickness tends to a limiting value.

$$y_{max} = a/b \quad [6]$$

so that the rate of oxidation (dw/dt) tends to the constant value fb. The thickness (in units of weight gain per cm²) of the inner layer at time t is given by

$$y = w - fbt \quad [7]$$

The evidence for the above model (Fig. 1) has been based on the whole (3, 9, 13) on the conformity of kinetic data to Eq. [5] with y and z given by Eq. [3] and [4], respectively. Now conformity of kinetic data to a particular rate equation does not in itself constitute a proof that the mechanism on which the rate equation is based is in fact operating. For paralinear oxidation, there appear to be two ways in which the model can be tested: (a) the thickness (*i.e.*, y) of the inner compact layer can be estimated from metallographic sections and compared with the value calculated from the kinetic data and Eq. [7]; (b) the weight (z) of the outer, porous layer can be measured and should, according to Eq. [4], increase linearly with time.

Webb, Norton, and Wagner (3) used method (a) and obtained reasonable agreement (within a factor of 2) between the calculated value of y and the value as measured by metallographic and x-ray methods. In the present work a series of samples has been oxidized for progressively increasing times at 750° and at 800°C and the amount of porous oxide present on each measured both by the method of krypton sorption (14, 15) and from metallographic sections.

Provided that the oxide scale does not sinter after it has been formed then, for unit area of geometrical surface, the surface area S is proportional to the weight z of combined oxygen in the porous layer

$$S = Az \quad [8]$$

so that a plot of S against t should be linear. In Eq. [8], A is a constant.

Experimental

The tungsten was obtained from the Tungsten Manufacturing Company Ltd. (England) as samples measuring 20 x 9 mm which had been hot-sheared from 0.8 mm thick sheet; the main impurity was iron (0.05% max.) with only traces of other elements. As will be discussed later, surface preparation of the tungsten surface by abrasion on emery led to exfoliation of the metal on oxidation with an attendant increase in effective geometrical area. Accordingly, prior to oxidation, each as-received sample was etched in an aqueous solution of potassium ferricyanide and caustic soda for 5 min, washed with water and then acetone (16).

The samples for the surface area measurements and metallographic studies were prepared by oxidation at 750° and 800°C in oxygen at 1 atm pressure on a thermal balance (17), a fresh sample being used for each measurement. The temperature was measured on a calibrated chromel-alumel thermocouple and the furnace controlled to ± 6°C with a Cambridge temperature controller. In order to avoid the uncertainty in the zero of time at the start of each run (the shortest oxidation time was 10 min), each sample was lowered into the hot zone of the reaction chamber at the beginning of each run and raised into the cold zone at the end of the run.

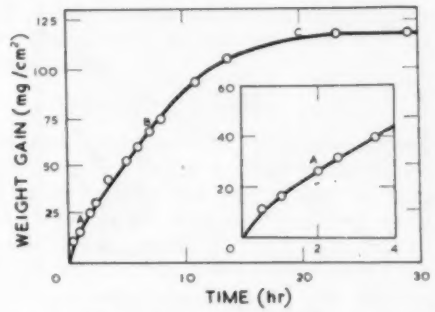

Fig. 3. Oxidation of tungsten at 800°C in oxygen at atmospheric pressure. The sample was oxidized to completion.

The surface area of each oxidized sample was measured by the method of krypton sorption using a technique (15) which had been developed for the measurement of small absolute areas (the areas ranged from 500 to 2000 cm²). The reproducibility varied from about 4% for 500 cm² to about 1% for 1000 cm² and above.

In order to obtain more accurate kinetic data for a test of the fit to Eq. [3], several additional runs were made at 600°C and at 0.1 atm pressure on a vacuum microbalance (18, 19). For these measurements, tungsten foil of a different batch from that described above was used; the impurities amounted to less than 0.1% with molybdenum (0.02%) as the main impurity.

Results and Discussion

Kinetics.—The curve corresponding to the oxidation of a sample to completion is shown in Fig. 3 as the weight gain in mg/cm² against the time in hours. The rate of oxidation decreases with time over the branch OA to become constant along AB in agreement with the findings of other workers (3); the linear branch AB however persisted for only about 7 hr (corresponding to 60% of the metal having been oxidized) after which the rate slowly decreased with time (branch BC) until all the metal had been oxidized. It is likely that this falling off in rate is due to a decrease in the geometrical area of metal undergoing oxidation.

The samples for the surface area measurements were prepared by oxidizing a series of tungsten samples for increasing times at each of the temperatures 750° and 800°C. Because of the small surface areas of the samples oxidized for only short times, two samples were used to obtain the first three experimental points on each of the curves (see Fig. 4, 800°C). The individual weight gains were found to fall on a reasonably smooth curve and the linear rates were 4.5 mg/cm² hr and 9.9 mg/cm² hr at 750° and 800°C, respectively, with corresponding values of y_{max} (intercept of linear

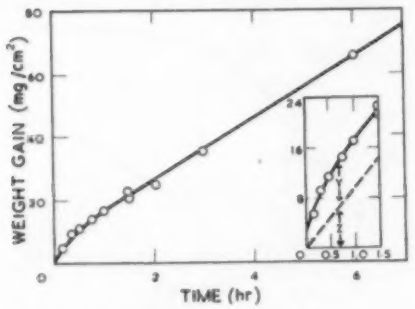

Fig. 4. Oxidation of tungsten at 800°C in oxygen at atmospheric pressure. Each experimental point corresponds to the oxidation of a fresh sample.

branch with the weight gain axis): 5.1 mg/cm² and 6.8 mg/cm², respectively.

In order to provide kinetic data for analysis, two runs were carried out at 600°C on a vacuum microbalance; here it was possible to measure the weight gain more accurately than on the thermal balance and avoid the complication of the area of metal significantly decreasing during oxidation (the linear rate was reached at a weight gain smaller than that at the higher temperatures). Readings were taken at 1-min intervals from 2-13 min, at 2-min intervals from 13-21 min, and at 5-min intervals from 21-125 min; the weight gain was measured to ± 1.3 μg/cm² which meant that the relative error varied from 3% for the first point to slightly more than 0.1% for the final point.

The kinetic data thus obtained (Fig. 5) were analyzed (20) by calculating the rate of oxidation (dw/dt) at each tabular point by means of the approximate relation

$$h\frac{dw}{dt} = \Delta_o' - \frac{1}{6}\Delta_o''' \qquad [9]$$

where h is the interval and Δ_o' and Δ_o''' are the first and third central differences, respectively. The rate of thickening (dy/dt) of the barrier film was next calculated from the relation

$$\frac{dy}{dt} = \frac{dw}{dt} - \frac{dz}{dt} \qquad [10]$$

where the linear rate (dz/dt) was read off from the oxidation curve (Fig. 5). The plot of (dy/dt) against $1/y$ (Fig. 6) demonstrates the difficulty of

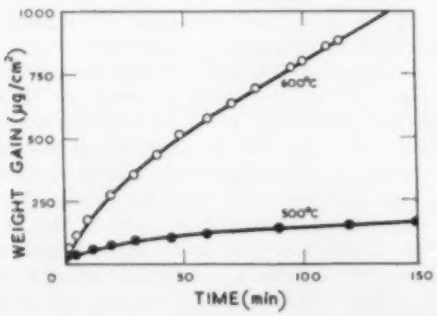

Fig. 5. Oxidation of tungsten at 500° and 600°C in oxygen at 0.1 atm pressure

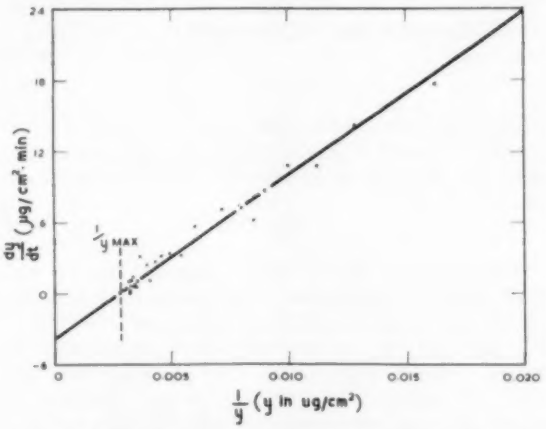

Fig. 6. Oxidation of tungsten at 600°C in oxygen at 0.1 atm pressure. The conformity of the data with Eq. [1] is tested by plotting (dy/dt) against 1/y. Note that the point furthest away from the origin corresponds to 2-min oxidation only. The value of $1/y_{max}$ is shown as the vertical line on the graph.

making a rigorous test of the paralinear rate equations (which contain two disposable constants) from kinetic data alone. In addition to the considerable scatter of the individual points from the best straight line, the range over which Eq. [1] can be tested is seen to be restricted on the one hand by the value of $1/y_{max}$ (note the crowding of of the experimental points) and on the other, by the experimental difficulty of obtaining data for the early stages of the oxidation (the point furthest away from the origin corresponds to 2-min oxidation).

Surface Areas

The surface area of each of the samples oxidized at 750° and 800°C was measured by the method of krypton sorption; the results for 800°C are shown in Fig. 7 where the surface area per unit area of geometrical surface (S) is plotted against the time of oxidation (t). It is clear that S does not increase linearly with time as required by Eq. [4] and [8], but instead increases at a rate which decreases with time to become almost constant. A curve similar in shape to that shown in Fig. 7 was obtained for the samples which had been oxidized at 750°C.

The similarity between the shapes of the curves of w and of S against time (compare Fig. 4 with

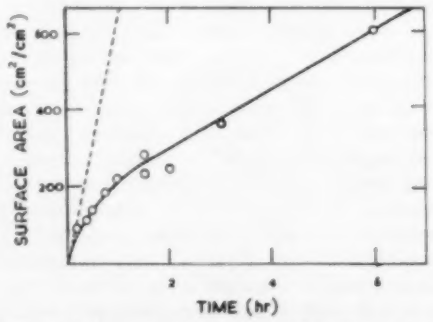

Fig. 7. Oxidation of tungsten at 800°C. The surface area per cm² of metal surface is plotted against the time of oxidation. Samples are the same as those in Fig. 4. The broken line represents the slope of the curve at zero time.

Fig. 7) suggests that the weight of porous oxide at a given time is not proportional to z (Eq. [4]), but is instead approximately the same as the total weight gain w; in other words, the weight of combined oxygen in the barrier film is small compared with w. If this supposition is correct, a plot of S against w should be linear, and reference to Fig. 8 will show that this condition is true for the first few points on the curve. Since both oxidation temperatures lie above the Tammann temperature (11) of tungstic oxide (one-half the melting point or 730°C), the subsequent deviation from the relation

$$S = Bw \qquad [11]$$

is probably to be interpreted in terms of the oxide scale sintering after it has been formed, a process which will result in an increase in the average crystallite size of the oxide with a corresponding reduction in its surface area. The constant B in Eq. [11] can be identified with S_m°, the slope of the curve of S against w at zero weight gain. The values of S_m°, expressed in terms of specific surface (surface area of oxide per unit weight) are 0.379 m^2/g and 0.290 m^2/g at 750° and 800°C, respectively.

It might be argued that the initial linearity of the curve of S against w (Fig. 8) at 750° and 800°C is fortuitous and that, in the absence of sintering, the surface area would increase linearly with time (Eq. [8]) as required by the paralinear model. To test the latter possibility, the kinetics of the sintering process in the absence of oxidation were measured by heating a sample of tungstic oxide (that formed by complete oxidation of the metal at 750°C) in oxygen at 800°C for increasing periods of time, the specific surface S_m of the oxide being measured after each period of heating. Over 16 hr, S_m decreased from 0.123 m^2/g to 0.0867 m^2/g, and the data were found to conform to the relation

$$1/S_m = Ct^{1/3} + D \qquad [12]$$

with $C = 0.09$ $g/m^2\ hr^{1/3}$; D is a constant identified below.

Now if the paralinear model is correct, S_m° the specific surface of the oxide in the absence of sintering is given by the product of the slope of the curve of S against t at zero time (Fig. 7) and the linear rate constant; at 800°C, $S_m^\circ = 1.34$ m^2/g. If we make the reasonable assumption that the relation [12] is valid for specific surface areas up to S_m°, we have

$$D = 1/S_m^\circ \qquad [13]$$

After 2-hr oxidation at 800°C, the weight of porous oxide according to the paralinear model (Eq. [2]) will be 95 mg/cm^2 and in the absence of sintering would have an area of 1280 cm^2/cm^2; insertion of the derived values of S_m° and C in Eq. [12] and [13] shows that after 2 hr heating at 800°C this area would only decrease to 1100 cm^2/cm^2 compared with the value of 300 cm^2/cm^2 read off from the experimental curve. Furthermore, the actual decrease in area due to sintering will be considerably less than 180 cm^2/cm^2 because the calculation has been simplified by overestimating the sintering time. Since in order to obtain conformity between the measured and calculated values of S the rate of sintering (as expressed in terms of the parameter C) would have to be some twentyfold greater than that obtained experimentally, it is clear that the nonlinearity of the curve of S against t cannot be explained in terms of sintering alone. In other words, the experimental results are not in accord with the model of paralinear oxidation.

Metallographic Examination of Oxidized Samples

Each of the samples which had been oxidized at 800°C was examined metallographically; for this purpose, each sample was mounted between two strips of mild steel, cast in "Araldite D" resin, sectioned, and one-half abraded to Grade 00 emery and finally polished with 6μ and then 1μ diameter diamond paste.

According to Eq. [7], the weight of combined oxygen in the barrier film should represent 77% of the measured weight gain on the sample which had been oxidized for 10 min at 800°C. Correspondingly, the thickness of the barrier film should be 30μ [using the x-ray density of 7.33 g/cm^3 for tungstic oxide (21)] and that of the outer, porous layer 11μ [taking a value of 5.8 g/cm^3 for the density of porous tungstic oxide (11)]. Microscopic examination of the sample failed to confirm these predicted values, thus a barrier film could not be detected while the measured thickness of the distinct yellow porous oxide, 38μ, was found to be in reasonable agreement with the value of 47μ calculated from the *total* weight gain.

Confirmation of the conclusions drawn from the surface area measurements was obtained by measuring the thickness of the porous oxide layer on sections of each of the samples which had been oxidized at 800°C (see Fig. 4); the results, shown graphically in Fig. 9, again demonstrate that the rate of thickening of the porous oxide layer is not constant from the start, but at first decreases with time.

Although it was not possible to detect a barrier film by microscopic examination of any of the sections, some evidence for such a film was provided by flexing a partially oxidized sample when the yellow oxide flaked away in parts to reveal a dark-blue film adhering to the metal. The film was, however, extremely thin since light scratching revealed

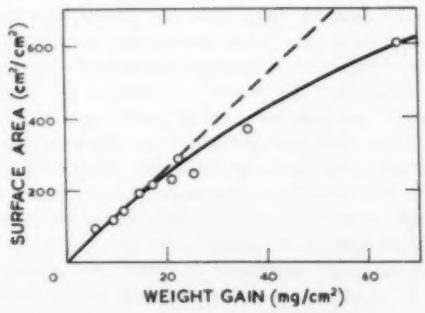

Fig. 8. Oxidation of tungsten at 800°C. The surface area per cm^2 of metal surface is plotted against the weight gain per cm^2. Samples are the same as those in Fig. 4.

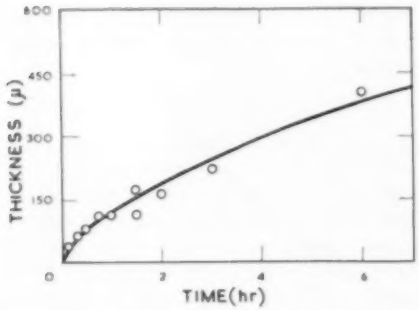

Fig. 9. Oxidation of tungsten at 800°C. The thickness of the oxide scale as determined from metallographic sections, is plotted against time. Samples were the same as those in Fig. 4.

the bright metal below. A dark blue substrate was noted by Webb, Norton, and Wagner (3).

A number of abraded tungsten samples were also oxidized at 800°C on the thermal balance; while some of these oxidized in a similar manner to the etched samples, the majority gave a characteristic S-shaped curve (7) over which the rate of oxidation first decreased, was constant, and then increased with time (Fig. 10). Microscopic examination of sections of a number of samples which had oxidized in this manner showed that the increase in rate at *X* (Fig. 10) could be attributed to exfoliation of the metal with an attendant increase in the geometric area available for oxidation. Once cracking of the specimen has begun, the continuation of the process will be favored by the compressive stress set up at the base of the crack by the increase in volume associated with the conversion of metal to oxide (Pilling-Bedworth ratio 3.35:1).

Finally, the micrographs in Fig. 11, which correspond to the samples oxidized at 800°C, illustrate the remarkable "edge-effect" which is obtained during the oxidation of tungsten (3, 4, 7).

Oxidation Mechanism

The experimental results described in the previous sections would appear to show conclusively that the accepted model of paralinear oxidation cannot be used to describe the oxidation kinetic of tungsten. Thus:

1. The rate of formation of porous oxide is not constant from the start (cf. Eq. [2]) but instead

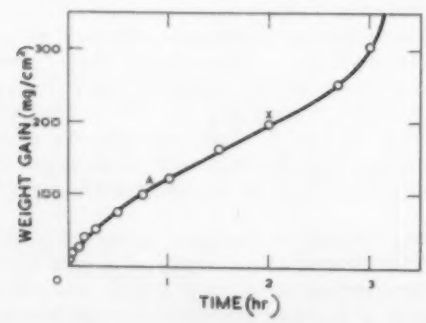

Fig. 10. Oxidation of tungsten at 800°C in oxygen at atmospheric pressure. The deviation from the linear rate at X is due to exfoliation of the metal.

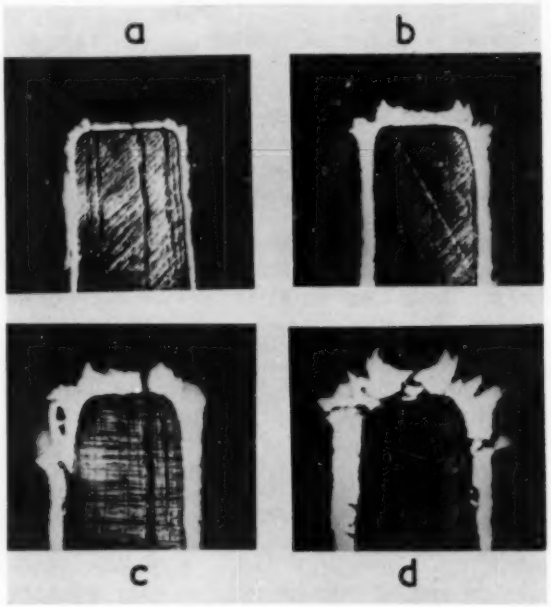

Fig. 11. Sections of samples oxidized at 800°C showing the "edge-effect." The samples were the same as those in Fig. 4, (a) 10 min; (b) 20 min; (c) 30 min; and (d) 45 min. Polarized light, X30.

decreases with time to reach an almost constant value (Fig. 7 and 9);

2. The thickness of the barrier film is considerably less than the predicted value (cf. Eq. [3]). A barrier film could not be detected on any of the sectioned samples while the measured thickness of the outer porous layer on the least oxidized sample at 800°C is in reasonable agreement with that calculated from the *total* weight gain.

Since the bulk of the oxide layer is porous in that the amount of combined oxygen in the barrier film is small compared with w, the evidence for the existence of such a film is necessarily indirect and must be based on the visual observation of the dark-blue substrate referred to above.

Regarding the true oxidation mechanism of tungsten, it is suggested that as in the model of paralinear oxidation the linear rate reflects the situation where the rate of thickening of the barrier film is equal to its rate of cracking to form the porous oxide so that the thickness of the barrier film is constant. The decrease, on the other hand, to the linear rate (branch OA, Fig. 3) cannot now be explained in terms of a decreasing contribution to the weight gain by virtue of the barrier film thickening (see Fig. 2); first, the weight of combined oxygen in the barrier film is itself very small, and second, the rate of formation of porous oxide is decreasing with time. Presumably over the branch OA, the barrier film is thickening at a greater rate than that at which it is cracking to form the porous oxide and the increasing path for ionic diffusion [the barrier film probably thickens by anionic diffusion (2)] causes the rate of oxidation to decrease. If this model is correct, the rate of cracking of the barrier film must depend on its thickness which seems reasonable.

An interesting feature of the early stages of the oxidation of tungsten is the absence of a rate transition, or breakaway, which if it occurred would denote the development of cracks in a hitherto protective oxide layer (22). The runs at 500° and 600°C on the microbalance (Fig. 5) clearly show that the rate of oxidation decreases from the start.

It finally remains to discuss the specific surface results themselves. If it is assumed (11) that the oxide is composed of equal sized cubelets, the values of $S_m°$ at 750° and 800°C correspond to particle sizes of 2.2 x 10⁴Å and 2.8 x 10⁴Å, respectively. That the average crystallite size of the oxide at 800°C is greater than that at 750°C may be interpreted in terms of the fact that the barrier film is more plastic at the higher temperature and can thus deform to a greater extent before developing cracks and transforming to the outer, porous oxide.

These measurements are now being extended to the oxidation of niobium and tantalum, and it is hoped to present the results in a later paper.

Acknowledgments

It is a pleasure to thank Dr. S. J. Gregg for his interest in this work and Mr. J. A. Baker who carried out most of the surface area measurements. The authors are also grateful to the U.K. Atomic Energy Authority for their support of this work.

Manuscript received Nov. 7, 1960; revised manuscript received June 20, 1961.

Any discussion of this paper will appear in a Discussion Section to be published in the June 1962 JOURNAL.

REFERENCES

1. E. A. Gulbransen and W. S. Wysong, *Am. Inst. Mining Met. Engrs.*, **175**, 611 (1948).
2. V. I. Arkharov and Yu. D. Kozmanov, *Akad. Nauk S.S.S.R.*, **2**, 131 (1957).
3. W. W. Webb, J. T. Norton, and C. Wagner, *This Journal*, **103**, 107 (1956).
4. J. P. Baur, D. W. Bridges, and W. M. Fassell, Jr., *ibid.*, **103**, 266 (1956).
5. V. A. Arslambekov and K. M. Gorbunova, *Doklady Akad. Nauk. S.S.S.R.*, **119**, 294 (1958).
6. V. A. Lavrenko and I. N. Frautvitch, *Akad. Nauk. Ukrain S.S.S.R.*, **6**, 42 (1958).
7. E. A. Gulbransen and K. F. Andrew, *This Journal*, **107**, 619 (1960).
8. W. McKewan and W. M. Fassell, Tech. Report No. VII, February 1952, Institute for the Study of Rate Processes, Utah.
9. J. Loriers, *Compt. rend.*, **229**, 547 (1949).
10. J. Loriers, *ibid.*, **231**, 522 (1950).
11. D. W. Aylmore, S. J. Gregg, and W. B. Jepson, *This Journal*, **106**, 1010 (1959).
12. E. W. Haycock, *ibid.*, **106**, 771 (1959).
13. E. W. Haycock, *ibid.*, **106**, 764 (1959).
14. R. A. Beebe, J. B. Beckwith, and J. M. Honig, *J. Am. Chem. Soc.*, **67**, 1554 (1945).
15. D. W. Aylmore and W. B. Jepson, *J. Sci. Inst.*, **38**, 156 (1961).
16. C. J. Smithells, "Metal Reference Book," p. 290, Butterworths Scientific Publications, London (1955).
17. S. J. Gregg and W. B. Jepson, *J. Inst. Metals*, **87**, 187 (1958-59).
18. E. A. Gulbransen, *Rev. Sci. Inst.*, **15**, 201 (1944).
19. D. W. Aylmore, S. J. Gregg, and W. B. Jepson, *J. Inst. Metals*, **88**, 205 (1959-60).
20. L. J. Comrie, "Chamber's Six-Figure Mathematical Tables," p. 544, W. & R. Chambers, London (1949).
21. G. Anderson, *Acta Chem. Scand.*, **7**, 154 (1953).
22. J. V. Cathcart, J. J. Campbell, and G. P. Smith, *This Journal*, **105**, 442 (1958).

Effect of Reynolds Number on Corrosion of Copper by Sulfuric Acid

I. Cornet, E. A. Barrington,[1] and G. U. Behrsing[2]

University of California, Berkeley, California

ABSTRACT

Corrosion of electrolytic tough-pitch copper pipe was determined in aerated 2.1*N* sulfuric acid at 30°C. A closed loop circulating system was used, with 1 in., ¾ in., and ½ in. diameter test sections. There was a gradual increase of corrosion rate with increasing Reynolds number in the laminar flow regime, Re $<$ 2100; a rapid increase in corrosion rate with increasing Reynolds number in the low turbulent flow regime, Re 2100 to 10^4; and a relatively constant corrosion rate due to polarization at Reynolds number $>10^4$. Reynolds number as a corrosion parameter permitted useful generalizations and comparisons with published heat and mass transfer correlations.

When copper is subjected to corrosion by sulfuric acid, particularly in the presence of oxygen, it is found that the corrosion rate may be a function of the relative velocity of the acid and metal. It is the purpose of this investigation to elaborate on the effect on corrosion of flow regime as characterized by Reynolds number.

The system copper-sulfuric acid has been selected for many reasons. Copper displays a constant rate of dissolution with time in a nonoxidizing acid such as sulfuric acid containing oxygen as a depolarizer. The mechanism of the corrosion process in this case is characterized by the transport of dissolved oxygen to the local cathode elements on the surface of the metal.

The net reaction for the over-all corrosion process is generally considered to be (1, 2, 3)

[1] Present address: Shell Oil Company, Martinez, California.

[2] Present address: Lawrence Radiation Laboratory, University of California, Berkeley, California.

$$2Cu + O_2 + 4H^+ = 2Cu^{++} + 2H_2O \quad [1]$$

Several assumptions exist with regard to the rate-determining step. Hill (4), Weeks and Hill (3), and Robertson *et al.* (5) consider the rate-determining step to be

$$2Cu + H^+ + O_2 = 2Cu^+ + HO_2^- \quad [2]$$

followed by the decomposition reaction

$$HO_2^- + 2Cu^+ + 3H^+ = 2Cu^{++} + 2H_2O \quad [3]$$

Katz (6) and Lu and Graydon (2) have postulated rate-controlling reactions which involve atomic oxygen.

Some of these mechanisms are open to question, but this paper is hardly the place to resolve such problems. Although the various investigators have different ideas regarding which reaction step is rate determining in the corrosion process, they do agree that the dissolution rate of copper in dilute sulfuric acid is dependent on and directly proportional to the concentration of dissolved oxygen in solution (7, 1, 2, 8, 9).

In addition to the dependence of the corrosion reaction on the oxygen concentration, the dissolution rate of copper is also strongly influenced by the depolarizing action of the cupric ions at the metal surface

$$Cu + Cu^{++} = 2Cu^+ \quad [4]$$

followed by the oxidation of the cuprous ions (6, 1, 2). The cupric ion, over a wide range of concentration, is an effective cathode depolarizing agent in the solution of copper in dilute aerated sulfuric acid solutions. The dissolution of copper is catalyzed by a product of the corrosion reaction and is therefore autocatalytic. The process is a complex one in which two parallel reactions are apparently superposed, the solution of copper by the action of oxygen as well as the action of the cupric ions. The rate of formation of oxide films on the copper surface is also lowered substantially by the addition of cupric ions to the acid solution and decreases with increasing cupric ion concentration (6).

In solutions with constant corrosion rate the oxygen mechanism is the primary one, and the reduction process of the cupric ions is either very small or does not take place at all. Such is the case with dilute sulfuric acid as corrosive agent when the copper ion concentration is very low.

Of the many variables affecting the rate of corrosion of copper in aerated dilute sulfuric acid such as temperature, acid volume, concentration of copper, sulfate and hydrogen ion and dissolved oxygen, acid velocity and sample area (7, 1, 2, 5) only the latter two parameters were varied in this study, while the other variables were maintained essentially constant.

Early investigation of the effect of velocity on the corrosion of copper in dilute sulfuric acid containing oxygen using a stirring technique by Whitman and Russell (9) showed that higher velocities caused increased corrosion, but the increase in corrosion rate could not be explained by diffusion considerations alone. The results therefore led to the proposal of protective film formation. In a more recent study Lu and Graydon (2) found that increased velocity had little effect on the corrosion rate, and they predicted that a chemical reaction rather than diffusion was the controlling factor in the corrosion process.

The work of Kinevsky (1) and Krasilshchikov and Andreeva (10) on the other hand points to diffusion as the controlling factor in the dissolution of copper by aerated dilute sulfuric acid.

Whatever the controlling physical mechanism of the corrosion system may be, the important role played by oxygen in the dissolution process is such that in many cases its presence is the determining factor in the entire corrosion reaction. Experimental results obtained by using a rotation technique have little value in predicting corrosion for the case of flow in pipes. The manner in which the oxygen is brought to the walls of the pipe must be considered. The effect of flow conditions on the availability and transfer of dissolved oxygen and other processes involved in corrosion reactions have been evaluated on the basis of certain hydraulic concepts of fluid mechanics (11).

When a real fluid flows in a tube two distinct flow regimes may be observed: laminar and turbulent. Friction and viscous forces result in the establishment of flow gradients. Thus the velocity of flow varies from the wall, where liquid molecules are at rest, to the center of the tube, where flow velocity is a maximum. When flow is laminar (also called viscous or streamline in corrosion literature) the velocity distribution is parabolic, the average velocity is approximately 0.5 the maximum velocity, and the laminar boundary layer which starts at the wall extends to the center of the tube. At a higher flow rate the flow becomes turbulent; streamlines lose their identity, the laminar boundary layer at the wall becomes very thin, decreasing in thickness with increasing velocity; and the average velocity becomes more nearly equal the maximum velocity, and turbulent mixing may be thought of as wiping the boundary layer (12). The flow is conveniently characterized by Reynolds number, $Re = vd\rho/\mu$ where v is velocity, d diameter, ρ mass density, and μ viscosity. Transition from laminar to turbulent flow in a tube occurs at $Re \sim 2100$, but for different geometries this transition occurs at different Reynolds numbers. Frictional resistance, heat transfer rates, and mass transfer rates are altered as hydrodynamic flow changes, not necessarily at equal pace.

The effect of hydrodynamic flow on corrosion has been appreciated for years (13, 14, 15, 16, 17, 18, 19, 20, 21, 22, 23), but quantitative illustrations have been few indeed. Fortunately there have been theoretical analyses published in recent years on laminar boundary layer flows with surface reactions (15), and these will point the way for future research. A rigorous analysis requires consideration of continuity, dynamic, energy and stoichiometric equations (24, 25, 15, 26).

Apparatus

The industrially important case of flow through pipes was selected for this study.

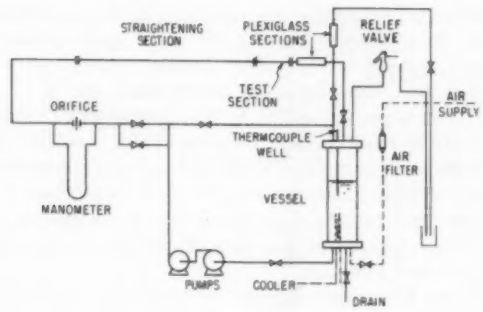

Fig. 1. Equipment diagram

The corrosion apparatus used was essentially the same as the one designed by Barrington (27), Fig. 1. However, a few necessary modifications had to be incorporated in order to facilitate the development of laminar flow at low Reynolds numbers (28). Details of the apparatus are available in references (27, 28).

The construction of the apparatus is such that temperature, oxygen concentration, fluid velocity, pipe size, and corrodent concentration may be varied independently. The corrosion rates may also be determined by different methods such as electronic or radioactive tracer techniques after minor alterations of the present equipment.

Test section.—The material tested was American Brass Company alloy 100, also known as electrolytic tough pitch copper, a type widely used in the United States. A representative analysis of this material is: copper 99.95%; gold, silver, arsenic, antimony, bismuth, tin, lead, iron, nickel, selenium, tellurium, sulfur, each less than 0.002%.

Specimens were prepared from hard-drawn, unannealed solid round stock and were machined to nominal Schedule 80 pipe sizes of ½-, ¾-, and 1-in. The actual internal diameters of the pipe sections were 0.532, 0.746, and 0.952 in., respectively, matching the internal diameters of the corresponding straightening as well as outlet sections on both ends of the specimen. Test sections were 4 in. long.

A short time before each run the test specimen was carefully polished with 3/0 grade emery paper to remove oxides and other corrosion products. After polishing, the test section was washed with distilled water, acetone, and absolute ethyl alcohol and dried in air. A single specimen of each pipe size was sufficient for all runs.

Test system.—The test system is shown in Fig. 1. The equipment is essentially a closed loop circulation system of unplasticized polyvinyl chloride (PVC) pipe, fittings, and valves. The pumps, each capable of delivering 25 gpm at 25 ft of head or 10 gpm at 37 ft, use Buna-N rubber for pump body, impeller, and diaphragm. Impeller shafts are stainless steel with a rubber coating. Only one pump is used for the flow rates at low Reynolds number.

An orifice and manometer system provides for metering. The Plexiglas orifice is sharp edged with a beveled downstream edge, located between flanges in such a way as to minimize turbulence due to variations in the direction of flow (29).

The straightening section of PVC pipe preceding the test section is 66 in. long and is adapted to the test loop by a reducing flange for the ½ and ¾-in. pipe sizes. It is supported by aluminum angle for rigidity. The 7-in. long outlet section following the test section is made of Plexiglas and is also adapted to the test loop by a reducing flange. It was necessary to employ a transparent outlet section to make sure that no air bubbles were trapped in the top portion of the pipe during low flow rates. The entrance and exit sections allow the establishment and maintenance of the flow through the test section. The inlet length is sufficient to establish laminar flow for Reynolds numbers below 2100 in the present apparatus.

The sulfuric acid solution passes through the test section or by-passes it to enter a pressure vessel made of 8-in. PVC pipe. In this vessel a cooler made of ½ in. Hastelloy C tubing removes the heat generated by the pump and friction. The Hastelloy C cooler and the mercury in the manometer are the only metals in the circulation system other than the copper test section. The copper-constantan thermocouple is in a Pyrex tube containing oil.

Experimental Procedure

General.—The corrosion of copper pipe by aerated dilute sulfuric acid depends on acid velocity, pipe size, temperature, and dissolved oxygen, hydrogen ion, and copper ion concentration. The purpose of the experimental work was to study two of the corrosion parameters: pipe diameter and acid velocity. Temperature and oxygen concentration were held constant. The hydrogen ion concentration varied but slightly between test runs. Variations in the copper ion concentration were also slight and had no measurable effect on the corrosion rate for concentrations encountered in this investigation. The acid volume varied approximately 1% during each run due to sample removal; however, this variation had a negligible effect.

Corrosive liquid.—The acid solution was prepared from reagent grade concentrated sulfuric acid and distilled water. The hydrogen ion concentration for all test runs was $2.13 \pm 0.02N$ as determined by titration. Aerated sulfuric acid of this strength readily attacks copper (30, 6).

The copper ion concentration in the corrosive liquor was kept always below 7.16×10^{-4} g/l. Concentrations of this order have been shown (31) to have no measurable effect on the corrosion rate. Experimental results also indicate no increase in corrosion rate due to increasing copper ion concentration.

A technique was developed to neutralize the aerated acid sample without loss of dissolved air prior to the Winkler analysis for oxygen. The oxygen content obtained, 5.3 ppm, indicated over 90% saturation, based on application of Henry's law to solubility data published (32).

The acid was mixed in 8.4 liter batches and syphoned into the vessel through the sample tap. The average total acid volume in the system was about 32 liters.

Procedure.—The corrosive fluid was aerated for 1 hr before each run by circulating it through the inner loop of the corrosion apparatus while air was bub-

bled into the vessel. The relief valve was held open during this period. The saturation period also provided time for the fluid to attain a temperature of 86 ± 2°F (30°C), the value used for all runs.

After the acid was aerated, the copper specimen with the freshly prepared surface was installed and the fluid diverted through the test section loop. Flow was controlled by the bypass valve and the valves downstream from the test section. A visible level was maintained in the vertical Plexiglas section after all the air in the horizontal section had been displaced by the acid.

The initial fluid sample was taken after ½ hr, when the corrosion process had essentially reached steady state. Thereafter, samples were removed every 1½ hr during the test runs of lower velocity and every hour during the runs with higher velocity for the extent of the run, 4½ or 3 hr, respectively.

Copper content of the acid solution was analyzed by the spectrophotometric procedure determined in a Beckman Model B spectrophotometer with a set of four matched cells, using dithizone reagent (33). A plot of the corrosion in milligrams of copper *vs.* time in hours for the four samples of each run resulted almost always in a straight line, the slope of which was determined by the method of least squares. The corrosion rate in milligrams per hour, which was represented by the slope, was multiplied by a factor to obtain the rate in mg/dm²/day (mdd).

Additional test runs were made with the ½-in. pipe at Reynolds numbers of 600, 6000, and 60,000 after saturating the acid with pure oxygen for 3 hr to confirm that oxygen concentration and diffusion were indeed the rate controlling factors in the corrosion of copper by sulfuric acid.

Results and Discussion

Results of this investigation are presented in different ways to illustrate some of the advantages of considering Reynolds number as a parameter in corrosion. In Fig. 2 corrosion rate is shown as a function of Reynolds number. In the laminar flow regime, Re < 2100, the corrosion rate increases slowly with increasing Reynolds number. Between Reynolds numbers of 2000 and 3500 the data show a rapid increase in corrosion rate with increasing Reynolds number. It is believed that the experimental region of Reynolds number of 3500 to 10,000 did in fact represent turbulent flow, for reasons to be discussed shortly. To suppress transition flow and resultant scatter in data, flows below Re = 2100 were approached by opening the valves to maintain laminar flow; flows above Re = 2100 were approached by closing valves to maintain already established turbulent flow. The data presented here, for ½-, ¾-, and 1-in. pipe, appear to fit the curves within limits that are normal in heat transfer, mass transfer, and fluid flow experiments. These data show no persistent effect of pipe diameter on corrosion rate; they permit generalization; and they show a change in the corrosion rate when the flow changes from laminar to turbulent above Re = 2100.

Above Reynolds number 10,000 the corrosion rate approaches a constant, probably due to polarization. Here presumably both the anodic and cathodic reaction rates are controlled by a limiting rate of electron transfer. The activation energy of the discharge process becomes controlling (34). Supplying pure oxygen instead of air does not change the corrosion rate appreciably under these conditions, demonstrating that the corrosion rate is no longer determined by the access of oxygen to the solid-liquid interface. Halpern (35) found the rate of corrosion of copper in aqueous ammonia was proportional to oxygen pressure to a value dependent on the ammonia concentration. Unfortunately the present investigation maintained constant acid concentration and gives no indication of the possible effect of varying the acid concentration.

In Fig. 3 the corrosion rate is presented as a function of velocity. In the laminar regime the data do not warrant more than one generalized curve. This is reasonable because the exponent shown in Table I is 0.23 for Reynolds number and therefore for the product of velocity and diameter. For the range of diameters used, diameters raised to the 0.23 power are not experimentally separable. However, in the turbulent regime, for Reynolds number 2100 to 10⁴ the exponent of Reynolds number is 0.68, and the diameters raised to this power are experimentally distinguishable. At a given velocity in this regime, the corrosion rate will then depend on the diameter, and three separate lines are shown. After polarization the corrosion rates are again not distinguishable for the different diameters studied.

The use of dimensionless groups such as Reynolds number is of long standing in fields such as fluid flow, heat transfer, and mass transfer (36, 37). In recent years the use of dimensionless groups has become well established in electrochemistry (38, 26, 39). Relationships commonly presented include Nu =

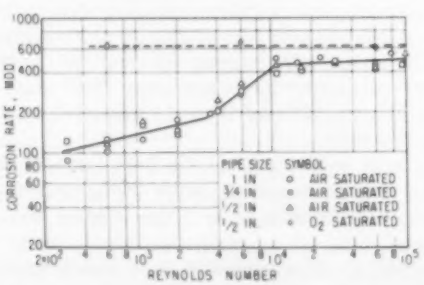

Fig. 2. Correlation curve of corrosion rate vs. Reynolds number (corrosion of copper pipes by 2.1N H_2SO_4 at 86°F).

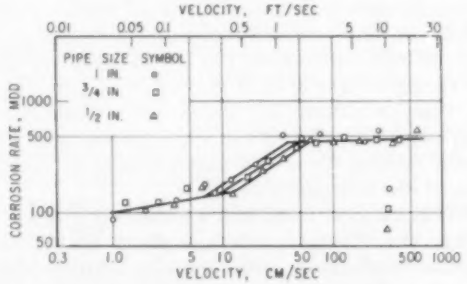

Fig. 3. Corrosion rate—Velocity curve (corrosion of copper pipes by 2.1N H_2SO_4 at 86°F).

Table I. Corrosion rates for the different flow rates

Flow regime	Corrosion rate, mdd	Average deviation, %	Maximum deviation, %
Laminar flow (Re = 300-2100)	$28.27\ Re^{0.280}$	12.1	20.7
Low turbulent flow (Re = 3500-11,000)	$0.78\ Re^{0.902}$	7.7	13.6
High turbulent flow (Re = 11,000-100,000	$270.4\ Re^{0.051}$	8.4	15.1

$B(Re)^a(Pr)^b$ where the constant B and exponents a and b are determined experimentally (40, 36). Correlations between heat transfer and mass transfer permit the use of Nusselt or Sherwood numbers, and Prandtl or Schmidt numbers. Such correlations help one to understand and to predict corrosion rates.

For example, a common correlation in turbulent heat transfer is $Nu = 0.023\ Re^{0.8}\ Pr^{0.33}$ where Nu is Nusselt number, Pr is Prandtl number, and Re is Reynolds number (41). The Prandtl number plays the same role in heat transfer as the Schmidt number in mass transfer (36). In mass transfer (36) Nusselt number is defined as $Nu = jd/D\Delta C$, where j is the mass transfer coefficient, d is diameter, D is the diffusion coefficient, and ΔC the concentration change. Up to $Re = 10^4$, the corrosion rate of copper observed in this investigation is determined by the cathodic rate of reduction of oxygen; therefore j, D, and ΔC should refer to oxygen. The rate of oxidation of copper at the anode must be proportional to the rate of reduction of oxygen at the cathode (unless other chemical species are being oxidized or reduced at the same time). Since in this study the change in copper concentration with time was analyzed, and not the change in oxygen concentration with time, it appeared reasonable to use the corrosion rate of copper as j for Nu, using D_{O_2} and ΔC_{O_2} for the denominator. The expression for Nu involves moles of diffusing species, rather than equivalents, so the use of j for copper instead of j for oxygen should involve a proportionality constant which depends on the mechanism of the rate controlling reaction. If 1 mole of oxygen is reduced to give 4 moles of cuprous ion, there will be a factor of 4; if the mole of oxygen reduced gives 2 moles of cupric ion there will be a factor of 2. This assumes that the solution analysis accounts for all copper oxidized, and no substantial adherent copper oxide is formed.

The present investigation was performed with a single corrosive solution, 2.1N H_2SO_4, with a constant Schmidt number. Correlations in the literature differ somewhat on the relative importance of transfer of mass by momentum rather than by diffusion; the exponent of the Schmidt number therefore varies (42, 26). In this study an exponent of 0.33 was arbitrarily adopted.

In Fig. 4 is shown a plot of $Nu/Sc^{0.33}$ *vs.* Re, for different diameter pipes, paralleling the conventional heat transfer relation. Different diameters give different lines here because the corrosion rate, relatively constant at a fixed Re, must be multiplied by $d/D\Delta C$ to give a dimensionless Nusselt number. The data fit the lines drawn within 15%, again a reasonable agreement, particularly in view of the fact that mass transfer may be better correlated by raising Reynolds number to the 0.7 power rather than to the 0.8 power.

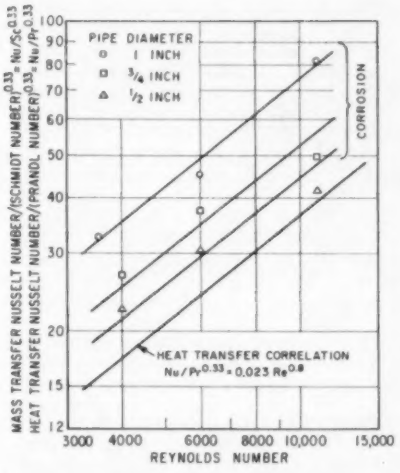

Fig. 4. Mass transfer correlation for turbulent flow (corrosion of copper pipes in aerated 2.1N H_2SO_4).

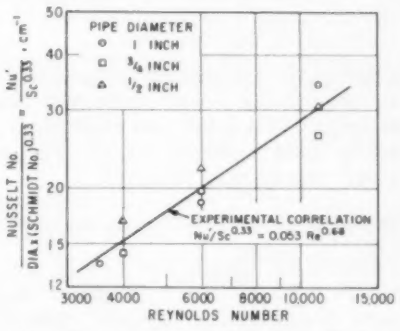

Fig. 5. Mass transfer correlation for turbulent flow

$$Nu' = \frac{\text{Corrosion Rate of Copper}}{\text{Diffusion Coefficient}_{O_2} \times \text{Concentration Gradient}_{O_2}}$$

(corrosion of copper pipes on aerated 2.1N H_2SO_4)

If the Nusselt number is multiplied by the reciprocal of the diameter one obtains Nu', a function with dimensions 1/cm, directly proportional to the corrosion rate. In Fig. 5 is shown a correlation of $Nu' = 0.053\ Re^{0.68}\ Sc^{0.33}$. The data fit this generalized line within a ±15% band, indicating that the effect of diameter on the corrosion rate was indeed not distinguishable in this study. Since all these data are for constant Schmidt number, no test of the exponent is feasible, but a correlation of $Nu = 0.079\ Re^{0.7}\ Sc^{0.356}$ has been established for mass transfer of a cylinder rotating about its axis (42). Both Fig. 4 and 5 are correlations for turbulent flow, as the exponents for Reynolds number show, indicating that the flow was probably turbulent in the experimental range Re 3500 to 10^4.

Correlations of mass transfer with heat transfer are not as well established for forced convection

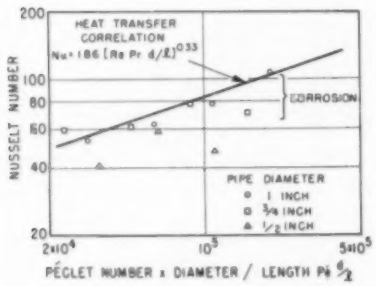

Fig. 6. Mass transfer correlation for laminar flow

$$Nu_m = \frac{0.5 \text{ Corrosion Rate of Copper} \times \text{Diameter}}{\text{Diffusion Coef.}_{O_2} \times \text{Conc. Gradient}_{O_2}}$$

Nu_h = heat transfer coef. x diameter/thermal conductivity; P'e = RePr for heat transfer = ReSc for mass transfer; Reynolds number = diameter x velocity x mass density/viscosity; Prandtl number = specific heat x viscosity/thermal conductivity; Schmidt number = viscosity/mass density x diffusion coefficient (corrosion of copper pipes in aerated 2.1N H_2SO_4).

laminar flow as for turbulent flow, especially for flow in tubes. Nevertheless a correlation was attempted between corrosion rates obtained experimentally and an empirical heat transfer relation. The equation selected (41) was

$$Nu = 1.86\ (RePr\ d/l)^{0.33}\ (\mu_{bulk}/\mu_{surface})^{0.14}.$$

The viscosity ratio was assumed to be unity. The product RePr is Péclet number, Pé. Since the present data were for constant Schmidt number, and Schmidt number for mass transfer processes corresponds to Prandtl number for heat transfer processes, this equation was evaluated for a range of Péclet numbers equal to ScRe for Sc = 419 and Re < 2100. The line drawn in Fig. 6 therefore is just a numerical solution for this empirical equation for laminar flow convective heat transfer. Superposed are the experimental data at these Péclet numbers. The Nusselt numbers for corrosion are defined as $Nu = 0.5\ jd/D\Delta C$, where j is taken as the corrosion rate of copper, moles/cm² sec; d is the diameter of the tube, cm; D is the diffusion coefficient for oxygen as based on Wilke (43), cm²/sec; and ΔC is the concentration difference of oxygen between the metal-liquid interface solution (assumed zero concentration) and the bulk of the liquid phase (assumed a constant concentration due to saturation with air). Although one point lies about 45% off the calculated curve, the other data points are within 30% of predictions. It should be observed that the empirical relationship for laminar convective heat transfer, $Nu = 1.86\ (RePr\ d/l)^{0.33}\ (\mu_{bulk}/\mu_{surface})^{0.14}$ emphasizes the effect of changes in viscosity μ at the solid-liquid interface (41). In mass transfer the rate of change in concentration as one approaches this interface becomes important. The first approximations discussed in this paper make no attempt to introduce such refinements, or even to introduce rigorous mathematical models and analyses.

Some limitations of the present study should be noted. In industrial tubular heat exchangers, impingement corrosion is generally prominent at the entrance end of the tubes; in this investigation flow entrance effects have been avoided. Cavitation and erosion effects have also been excluded.

Flow entrance effects have been avoided by having an entrance length of plastic pipe 66 in. long. This, however, has assured an entrance effect with respect to mass transfer. The corrosive fluid, entering the 4 in. long copper tube, will build up a laminar boundary layer in which the oxygen tension along the metal-liquid interface decreases from entrance of the copper test section to some point along the length where the oxygen tension approaches zero (except for the polarized condition at $Re > 10^4$). Correspondingly, the concentration of copper ion in this boundary layer changes from the bulk concentration C_o to a concentration $C_o + \Delta C$ where ΔC is the cuprous ion appearing as the oxygen is reduced. The test section is really too short to give a fully developed diffusion boundary layer. A better study would be to have a sufficient entrance length of copper tubing preceding a radioactive section of copper tubing; the rate of appearance of radioactive copper would then be a better measure of steady-state corrosion rate.

The present investigation has been confined to relatively smooth copper pipe in which protective film formation is not pronounced. This may explain why Reynolds number is a convenient parameter for correlations here. In contrast it has been stated that for rough steel pipes (in which protective corrosion films form diffusion barriers) Reynolds number is not a criterion of similarity (11).

The present investigation does enable one to understand inconsistencies in the literature on corrosion of copper in aerated sulfuric acid. Data taken under conditions where polarization existed would show no effect of increased velocity or Reynolds number. Data in the laminar regime would show little effect of velocity and Reynolds number. Judging by the short range of Reynolds numbers between the start of turbulent flow, $Re \sim 2100$, and the inception of polarization, $Re \sim 10^4$, it would be easy to run experiments in the turbulent flow regime in aerated sulfuric acid in which there was insufficient data to demonstrate any effect of Reynolds number. This would be particularly true at oxygen pressures above 1/5 atm.

Conclusions

The rate of corrosion of copper pipe in aerated 2.1*N* H_2SO_4 at 30°C is controlled by the transport of oxygen to the reacting surface at Reynolds number $< 10^4$.

At Reynolds number $> 10^4$ the corrosion rate is essentially constant, due to polarization effects.

At a given Reynolds number no significant effect of diameter on corrosion rate has been observed for the diameters studied: ½, ¾, and 1-in.

The rate of change of corrosion rate with increasing Reynolds number is different in laminar flow, $Re < 2100$, than in turbulent flow, $2100 < Re < 10^4$.

By use of Reynolds number and other criteria of similarity it is possible to obtain reasonable correlations of corrosion data with mass transfer and heat transfer relationships in the literature.

Acknowledgment

The assistance of Harry Eagles and Joseph De Costa is gratefully acknowleged. Grants from the Office of Naval Research have assisted two of the co-authors in their graduate studies.

Manuscript received Feb. 23, 1961; revised manuscript received June 26, 1961.

Any discussion of this paper will appear in a Discussion Section to be published in the June 1962 JOURNAL.

REFERENCES

1. A. I. Kinevsky, *J. Appl. Chem.* (*USSR*), **28** [10], 1088 (1955).
2. B. C. Y. Lu and W. F. Graydon, *Can. J. Chem.*, **32** [2], 153 (1954).
3. J. R. Weeks and G. R. Hill, *This Journal*, **103** [4], 203 (1956).
4. G. R. Hill, *ibid.*, **100**, 345 (1953).
5. W. D. Robertson, V. F. Nole, W. H. Davenport, and F. P. Talboom, *ibid.*, **105** [10], 569 (1958).
6. V. W. Katz, *Werkstoffe u. Korrosion*, **1** 303 (1953).
7. G. H. Damon and R. C. Cross, *Ind. Eng. Chem.*, **28** [2], 231 (1936).
8. R. P. Russell and A. White, *ibid.*, **19** [1], 116 (1927).
9. W. G. Whitman and R. P. Russell, *ibid.*, **17** [4], 348 (1925).
10. A. I. Krasilshchikov and V. A. Andreeva, *J. Phys. Chem.* (*USSR*), **20**, 1199 (1946).
11. A. J. Romeo, R. T. Skrinde, and R. Eliassen, *Proc. Am. Soc. Civil Engrs.*, **84** [SA4], 1702-1 (1958).
12. H. Schlichting, "Boundary Layer Theory," 1st ed., p. 402, McGraw-Hill Book Co., Inc., New York (1955).
13. F. N. Speller and V. V. Kendall, *Ind. Eng. Chem.*, **15** [2], 134 (1923).
14. I. Cornet, "A Short Course in Corrosion," p. 2, University of California (1953).
15. A. Acrivos and P. L. Chambré, *Ind. Eng. Chem.*, **49**, 1025 (1957).
16. A. C. Makrides, *This Journal*, **107** [11], 869 (1960).
17. A. C. Makrides and N. Hackerman, *ibid.*, **105**, 156 (1958).
18. A. C. Makrides, N. Komodromos, and N. Hackerman, *ibid.*, **102**, 363 (1955).
19. L. F. Epstein, *Chem. Eng. Prog. Symposium Ser.*, **53**, 67 (1957).
20. D. A. Frank-Kamenetskii, "Diffusion and Heat Exchange in Chemical Kinetics," 1st ed., Princeton University Press, Princeton (1955).
21. M. B. Abramson and C. V. King, *J. Am. Chem. Soc.*, **61**, 2290 (1939).
22. C. V. King, *ibid.*, **57**, 828 (1935).
23. C. V. King and W. H. Cathcart, *ibid.*, **59**, 63 (1937).
24. P. L. Chambré, *Appl. Sci. Res.*, Section A, **6**, 97 (1957).
25. P. L. Chambré, *ibid.*, **9**, 157 (1960).
26. C. W. Tobias, M. Eisenberg, and C. R. Wilke, *This Journal*, **99**, 359C (1952).
27. E. A. Barrington, M. S. Thesis in Engineering Science, University of California, Berkeley (1960).
28. G. U. Behrsing, M. S. Thesis in Engineering Science, University of California, Berkeley (1961).
29. J. K. Vennard, "Elementary Fluid Mechanics," 3rd. ed., John Wiley & Sons, New York (1954).
30. U. R. Evans, *J. Soc. Chem. Ind., London*, **43** [18], 127t (1924).
31. R. Glauner, *Z. physik. Chem. A*, **142**, 87 (1929).
32. G. Geffken, *Z. physik. Chem.*, **49**, 257 (1904).
33. E. B. Sandell, "Colorimetric Determination of Traces of Metals," 3rd ed., Interscience Publishers, New York (1958).
34. M. Stern, *Corrosion*, **18** [11], 775t (1957).
35. J. Halpern, *This Journal*, **100** [10], 421 (1953).
36. R. B. Bird, W. E. Stewart, and E. N. Lightfoot, "Transport Phenomena," 1st ed., cf. p. 648, John Wiley & Sons, New York (1960).
37. C. S. Lin, R. W. Moulton, and G. L. Putnam, *Ind. Eng. Chem.*, **45** [3], 636 (1953).
38. N. Ibl, *Electrochimica Acta*, **1**, 117 (1959).
39. C. S. Lin, E. B. Denton, H. S. Gaskill, and G. L. Putnam, *Ind. Eng. Chem.*, **43** [9], 2136 (1951).
40. C. V. King, in "The Surface Chemistry of Metals and Semiconductors," H. C. Gatos, Editor, p. 357, John Wiley & Sons, Inc., New York (1960).
41. F. Kreith, "Principles of Heat Transfer," 1st ed., International Textbook Co., Scranton (1958).
42. M. Eisenberg, C. W. Tobias, and C. R. Wilke, *Chem. Eng. Prog. Symposium Ser.*, **51** [16], 1 (1955).
43. C. R. Wilke, *Chem. Eng. Prog.*, **45** [3], 219 (1949).

NOMENCLATURE

C, concentration, g moles/cm^3.
C_o, concentration of copper ions in bulk of solution, g moles/cm^3.
ΔC, concentration change of copper ions, g moles/cm^3.
Cp, heat capacity, calories/g mole °C.
d, diameter of pipe, cm.
D, coefficient of diffusion, cm^2/sec.
h, heat transfer coefficient, calories/cm^2 sec.
j, mass transfer coefficient, g moles/cm^2 sec.
k, thermal conductivity, calories/sec cm^2 °C.
l, characteristic length, cm.
V, linear velocity of fluid, cm/sec.

Greek Symbols:

Δ, Incremental amount.
μ, dynamic viscosity, g/cm sec.
ν, kinematic viscosity, cm^2/sec.
ρ, density, g/cm^3.

Dimensionless groups:

Nu, Nusselt number, $jd/D\Delta C$ for mass transfer; hd/k for heat transfer.
Nu', Modified Nusselt number, $Nu' = Nu/d = j/D\Delta C$ for mass transfer, $(cm)^{-1}$.
Pé, Péclet number, RePr for heat transfer, ReSc for mass transfer.
Pr, Prandtl number, $Cp\mu/k$.
Re, Reynolds number, Vd/ν, $Vd\rho/\mu$.
Sc, Schmidt number, ν/D.

The Role of a Displacement Reaction in the Kinetics of Oxidation of Alloys

Roger L. Levin and J. Bruce Wagner, Jr.

Hammond Metallurgical Laboratory, Yale University, New Haven, Connecticut

ABSTRACT

The oxidation of some copper-zinc alloys and a copper-nickel alloy in pure oxygen at 700°C has been studied to determine the occurrence of a displacement reaction of the type

$$B^{+2} + 2e^- + AO = A^{+2} + 2e^- + BO$$

as proposed by C. Wagner. The formation of BO in the displacement reaction has been shown to occur by observing a change in the oxide scale by metallographic examination and by noting a change in the rate of oxidation as given by the parabolic reaction rate constant. A change in the oxidation rate for several samples was further emphasized by observing the rates during two periods of oxidation which were separated by an isothermal annealing period in an inert gas.

When a pure metal reacts with an oxidizing atmosphere at an elevated temperature, the kinetics may be described in terms of a parabolic rate equation when a compact oxide layer is formed and diffusion of ions and electrons through the layer is rate determining (1). The oxidation of an alloy can be considerably more complex. The thermodynamics of oxidation of the various alloy constituents, each with different activities, must be considered. The diffusion rates of the different species through the oxide, which may consist of more than one phase, will be different, and superimposed on these features may be a change in the structural and chemical composition of the oxide with time. Structural changes brought about by recrystallization which affect the oxidation kinetics have been studied on the oxide of a pure metal by Meijering and Verheijke (2) and on the oxide of an alloy by Sartell, Bendel, Johnston, and Li (3).

The role of a displacement reaction has received less attention. The effect of a displacement reaction on the kinetics of oxidation has been pointed out (4-6); however, the effect has not been correlated with chemical and structural changes which occur in an oxide under conditions involving an oxidation process interrupted by an isothermal anneal in an inert atmosphere. Such changes are of current theoretical and practical interest particularly for the development of oxidation resistant alloys for high-temperature use.

In order to demonstrate the role of a displacement reaction on the kinetics of an oxidation process, binary, one-phase alloys whose constituents differ widely in affinity for oxygen are the most convenient to use. Two such systems, the copper-zinc and copper-nickel systems, are considered, and for both alloys, the oxidation processes were carried out under one atmosphere of pure oxygen, at 700° and at 800°C, respectively.

Several investigators (7, 8) have determined the amount of copper oxide in the total oxide on brasses of various compositions oxidized under conditions similar to those above. Dunn (7) has shown that all brass alloys which have less than 76 wt % copper oxidize at virtually the same rate, and the oxide on these alloys consists of essentially pure zinc oxide (see Fig. 1). For these alloys, the diffusion of zinc to the surface through the metal and through the oxide is sufficiently rapid to keep pace with the oxygen reacted on the surface, and the parabolic mode of oxidation is followed approximately. This is shown in Fig. 2.

In brasses containing between 76 and 82% of copper, the amount of zinc capable of diffusing to the surface becomes less than the amount of oxygen absorbed, and as a result the amount of copper in the oxide increases with the formation of cuprous oxide. The oxidation of these brasses does not follow the parabolic oxidation law.

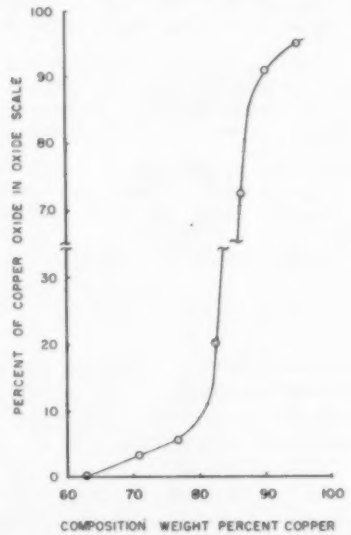

Fig. 1. Percentage of copper oxide in the oxide scale on brasses of various compositions oxidized in oxygen at 725°C. Note the break in the ordinate between 30 and 70%. (After Dunn)

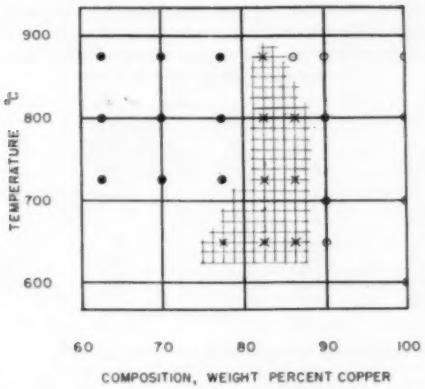

Fig. 2. Influence of temperature and composition on the form of the oxidation rate curve. •, Approximate conformity to the ideal oxidation law; X, wide departure from the ideal oxidation law; O, accurate conformity to the ideal oxidation law. (After Dunn)

Brasses which contain greater than 90% copper are shown to contain greater than 90% copper oxide in their oxides. With the remaining amount of zinc oxide either dissolved or as a finely dispersed mixture in the cuprous oxide, it is then expected that the oxidation rate is governed by the diffusion of cations and electrons across the composite oxide layer. The oxidation of these brasses with greater than 90% copper conform to the parabolic oxidation law. In experiments where the oxidation is carried out in pure oxygen, a very thin layer of cupric oxide may form on the outer oxide surface. This CuO layer does not appreciably affect the kinetics for the experiments described.

The deviations from parabolic behavior for certain brasses were attributed by Dunn to a sintering or recrystallization of the oxide, and to confirm his hypothesis, he performed the following experiments. Brass of an unspecified composition was oxidized at 725°C under the following conditions:

Experimental conditions	Change in weight, mg
1. Oxygen absorbed in 1 hr in pure O_2	9.42
2. Oxygen absorbed after 1 hr in O_2 followed by 2 hr in N_2 followed by 3 hr in O_2	9.8
3. Oxygen absorbed in 4 hr in O_2, uninterrupted	17.2

The 2-hr anneal in nitrogen greatly altered the kinetics of the oxidation reaction. Wagner (6) suggested that during the isothermal anneal a displacement reaction occurred where

$$Zn \text{ (in alloy)} + Cu_2O = 2Cu + ZnO \qquad [1]$$

During the oxidation of a hypothetical alloy AB, Wagner (4) has stated that such a displacement reaction is possible if the oxide BO, as shown in Fig. 3, has a greater affinity for oxygen, i.e., a lower standard free energy of formation, than the oxide AO. He has shown that under such conditions the oxide BO could be expected to grow, even though

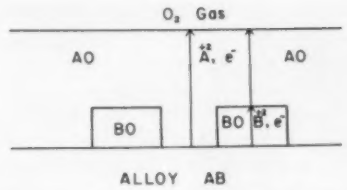

Fig. 3. Schematic cross section of the scale of an alloy AB with an outer layer of oxide AO and an inner two phase layer of oxides AO and BO. At the interface of oxides AO and BO, the displacement reaction

$$B^{+2} + 2e^- + AO = A^{+2} + 2e^- + BO$$

occurs so that oxide BO can grow even though it is not in contact with the oxidizing atmosphere. [After Wagner (4)]

it is not in direct contact with the oxidizing atmosphere, by the reaction

$$B^{+2} + 2e^- + AO = BO + A^{+2} + 2e^- \qquad [2]$$

The free energy of formation of ZnO is less than the free energy of formation of Cu_2O at 700°C. The values are (9)

$$\Delta G^\circ_{ZnO} = -60{,}540 \text{ cal/mole}$$

$$\Delta G_{Cu_2O} = -23{,}700 \text{ cal/mole}$$

Therefore one would expect that reaction [1] would proceed toward the formation of zinc oxide and free copper under the same conditions as those described above for the formation of the hypothetical oxide BO.

Because it is known that the diffusion of zinc ions is slower in zinc oxide than copper ions in cuprous oxide (10-12), a reasonable assumption is that, because of the marked differences in the structures of zinc oxide (hexagonal close-packed of the wurtzite type) and cuprous oxide (cubic), copper ions also diffuse more slowly in zinc oxide than in cuprous oxide. In addition, because cuprous oxide and zinc oxide are virtually immiscible, the diffusion of copper in zinc oxide is expected to be very small. If displacement reaction [1] occurs, the area of contact between the cuprous oxide and the metal alloy would be decreased by the formation of zinc oxide at the interface. Thus the avenues of rapid transit would be blocked, and a decrease in the oxidation rate would be expected to occur as the relatively impermeable envelope develops and increases in thickness. A change in the oxidation rate would be manifested as a change in K_p, the reaction rate constant, in the parabolic equation which may be written as

$$K_p = \frac{d}{dt}\left[\frac{\Delta m}{A}\right]^2 \qquad [3]$$

where $\Delta m/A$ is the weight gained per unit area, and t is the time.

Experimental Procedure

To check the proposed displacement reaction and to correlate a change in the oxidation rate with a change in the oxide structure, Cu-Zn alloys with wt % Zn = 30, 15, 10, and 5 were oxidized in oxygen and annealed in argon at 700°C. These

alloys were chosen because they are representative samples of the brasses which fall in the three regions shown in Fig. 1 and 2. Also, in order to show the generality of the displacement reaction to other systems, measurements were carried out on a 68% copper-32% nickel alloy oxidized in oxygen and annealed in argon at 800°C.

Specimens 1.15 × 0.5 in. were cut from 0.005 in. sheet.[1] These metal coupons were annealed in vacuum at a temperature between 375° and 400°C, depending on the composition of the alloy, in order to stabilize grain size and to prevent distortion of the sample during the period of oxidation. They were polished on emery paper through to 4/0, lapped on a wheel saturated with Linde A abrasive, and washed with methyl alcohol. The surface area was determined from micrometer measurements. The oxidation apparatus is the same as that described in an earlier paper by Pettit, Yinger, and Wagner (13).

The procedure followed for each oxidation run was to oxidize the sample in pure oxygen, at a flow rate of approximately 3 l/hr, for a period termed the "first oxidation period." For the samples undergoing continuous oxidation, this period constituted the entire process. In the interrupted oxidation experiments, the furnace was flushed with argon at the end of the first oxidation period, and the sample was held in a static atmosphere of argon for a determined period of time. The argon was purified by passing it through a furnace containing copper chips at 500°C and successively through tubes containing magnesium perchlorate, Ascarite, and magnesium perchlorate. At the end of the isothermal anneal, the argon was evacuated and the flow of oxygen was resumed during a second period of oxidation. All oxidation and annealing temperatures were the same for a particular run, and the temperature was controlled at ±¾°C by a L&N AZAR temperature controller. Curves of each run were plotted as $(\Delta m/A)^2$ *vs.* time to obtain K_p, the parabolic reaction rate constant.

In order to follow the changes in structure and composition of the oxide layers as a function of time, representative experiments were terminated and the samples were removed and mounted for metallographic examination.

Results and Discussion

Because a change in the kinetics of the oxidation reaction is reflected as a change in the parabolic reaction rate constant, it is possible to correlate these values of K_p qualitatively with the amount of zinc oxide or nickel oxide, as the case may be, present in the total oxide. The values of K_p for the oxidation of representative samples of brasses of various compositions in pure oxygen, at 700°C, both before and after a period of isothermal annealing in argon, are presented in Table I. Because the thickness of the zinc oxide layer is the rate-controlling step in the oxidation of these alloys, the differences in the values of K_p before and after the isothermal annealing periods of different lengths is a measure of the relative amount of zinc oxide formed and, hence, a measure of the extent to which the displacement reaction [1] occurs. Rhines and Nelson (14) have shown that where zinc oxide is associated with cuprous oxide on brasses, the zinc oxide is pink because of the presence of dissolved copper. This provides a means of visually identifying the zinc oxide which is formed with free copper according to the displacement reaction.

[1] The brass specimens were kindly furnished by the Chase Brass and Copper Company of Waterbury, Connecticut.

Table I. Parabolic reaction rate constant, K_p, is shown for representative brass samples before and after an isothermal anneal in an inert gas. The samples were oxidized in pure oxygen and annealed in argon at 700°C

Alloy, %Cu-%Zn	K_p for first oxidation period, g²/cm⁴-min	Length of isothermal anneal in inert gas, min	K_p for second oxidation period, g²/cm⁴-min
70-30	9.1×10^{-10}	—	—
85-15	1.4×10^{-8}*	60	1.0×10^{-9}
85-15	1.5×10^{-8}*	120	0.5×10^{-9}
90-10	3.8×10^{-9}	120	3.2×10^{-9}
95-05	5.0×10^{-9}	—	—

* The slope at the end of the first oxidation period.

A 70-30 brass follows the ideal parabolic oxidation law very closely (see Fig. 4). One would expect this agreement because, as indicated in Fig. 1, the oxide on a 70-30 brass consists of practically pure zinc oxide, with a maximum of approximately 3% cuprous oxide. X-ray diffraction analysis of the oxide from several 70-30 brass samples yielded no evidence of the occurrence of cuprous oxide in the oxide scale. Therefore, the oxidation rate of these brasses is controlled by the diffusion of cations and electrons across the relatively impermeable and essentially pure layer of zinc oxide.

Brasses containing 85% copper are representative of those which exhibit nonparabolic oxidation (see Fig. 5). From the graph of $(\Delta m/A)^2$ *vs.* time, it is seen that the value of the reaction rate constant decreases during the period of continuous oxidation. The cross section of this sample, shown at the end of the 3-hr oxidation period, in Fig. 6, illustrates the reason for this deviation. The dark oxide at the oxide-metal interface is actually "pink"

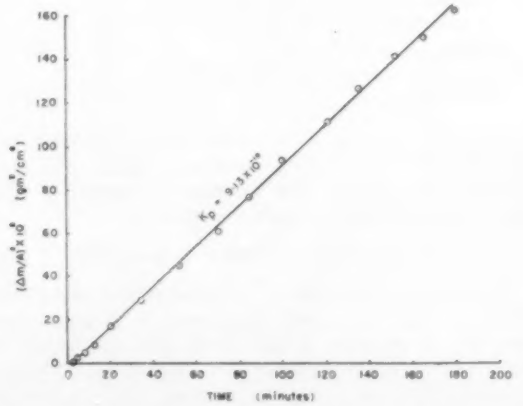

Fig. 4. Oxidation rate curve for a 70% Cu-30% Zn alloy oxidized in pure oxygen at 700°C.

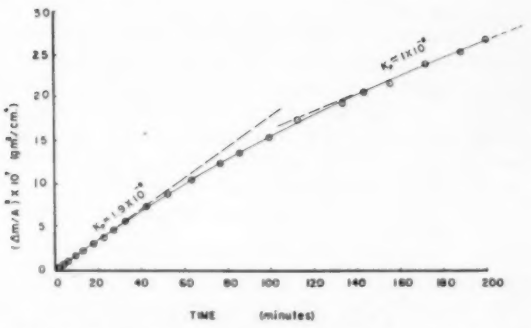

Fig. 5. Oxidation rate curve for an 85% Cu-15% Zn alloy oxidized in pure oxygen at 700°C.

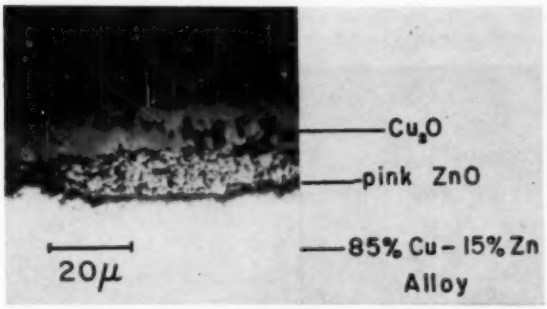

Fig. 6. Cross section of an oxide scale on an 85% Cu-15% Zn alloy oxidized for 200 min in pure oxygen at 700°C. The "pink" zinc oxide is shown as the dark oxide layer at the metal-oxide interface.

zinc oxide which is being formed by the displacement reaction during the period of continuous oxidation. As this layer of zinc oxide increases in thickness, the rate constant decreases from its initial value for the diffusion of cations across a composite oxide layer, toward the value of the reaction rate constant across a relatively pure zinc oxide layer, as given by the 70-30 brass.

Figures 7 and 8 show the oxidation curve and cross sections of an 85-15 brass which was oxidized initially for 90 min, isothermally annealed in cleansed argon for 1 hr to allow the displacement reaction to occur, and then followed by a second period of oxidation. After the 1-hr anneal there is a decrease in the slope[2] of the rate curve by a factor of 14. This is caused by the formation of a much thicker layer of zinc oxide during the period in the inert gas. Note also from the cross sections of the oxide of the same sample that in the regions where the zinc oxide layer is thick and coherent, as in Fig. 8(a), the total thickness of the oxide is less than in those regions where the zinc oxide structure remained in a dispersed state, in a copper-red matrix, as in Fig. 8(b). This further emphasizes the impermeable nature of a coherent envelope of zinc oxide. The structure shown in Fig. 8(a) represents the more typical found in these studies.

[2] The data were plotted as $(\Delta m/A)^2$ before anneal + $(\Delta m/A)^2$ after anneal = $(\Delta m/A)^2$ second oxidation period. The first term in this expression is a constant after the isothermal anneal.

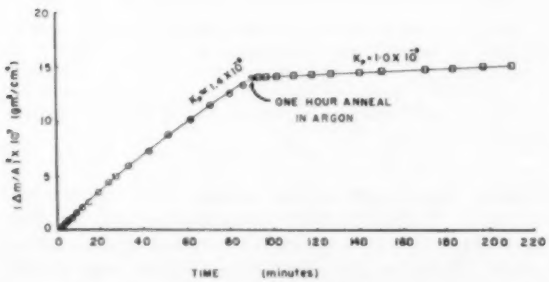

Fig. 7. Oxidation rate curve of an 85% Cu-15% Zn alloy oxidized in pure oxygen at 700°C, interrupted by a 1-hr isothermal anneal in argon.

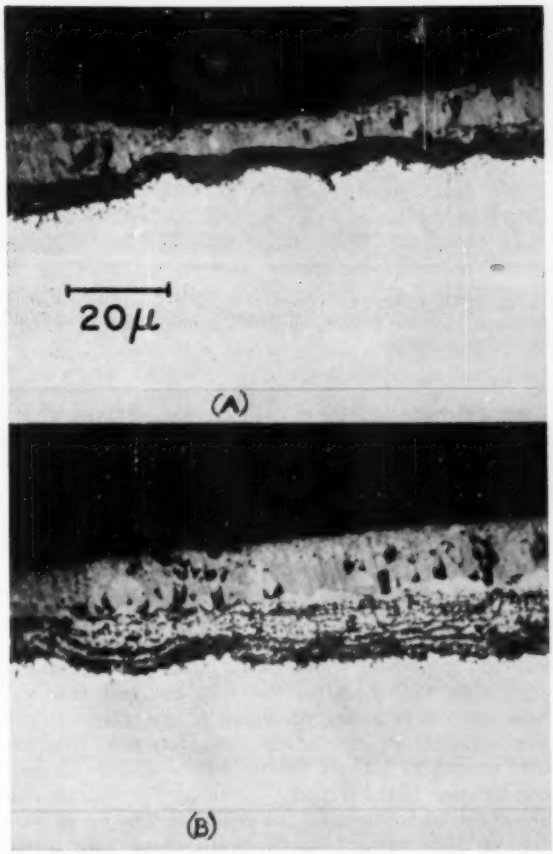

Fig. 8. Cross section of an oxide scale on an 85% Cu-15% Zn alloy after a 90-min first oxidation period followed by a 1-hr isothermal anneal in argon followed by a 60 min second oxidation period. (a) the pink zinc oxide layer is thick and coherent; (b) the pink zinc oxide structure remained in a dispersed state in a copper-red matrix.

The change in the reaction rate constant under similar oxidizing conditions, but after a 2-hr isothermal annealing period in argon, is shown in Table I. Note that after the 2-hr anneal K_p drops to half the value which was observed after the 1-hr annealing period. This difference is to be expected inasmuch as the oxidation rate is controlled by the thickness of the zinc oxide layer formed by the displacement reaction.

The alloys containing 90% or more copper follow closely the parabolic oxidation law under the conditions of continuous oxidation at 700°C. As previously mentioned and as shown in Fig. 1, the ox-

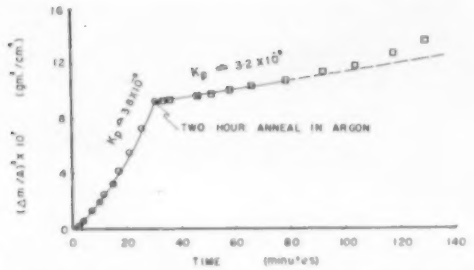

Fig. 9. Oxidation rate curve for a 90% Cu-10% Zn alloy oxidized in pure oxygen at 700°C, interrupted by a 2-hr anneal in argon.

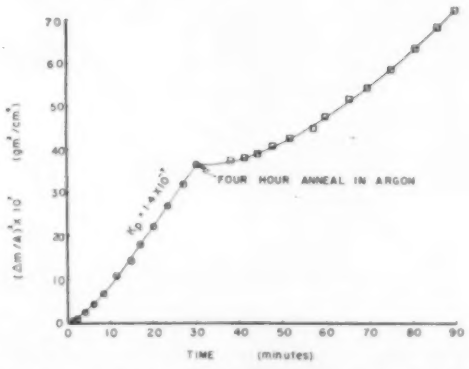

Fig. 10. Oxidation rate curve for a 62% Cu-38% Ni alloy oxidized in pure oxygen at 800°C, interrupted by a 4-hr anneal in argon.

ides formed on these alloys are composed of cuprous oxide and zinc oxide in approximately the same ratio as the copper and the zinc concentration in the alloy. From Table I it is seen that the value of the rate constant increases as the amount of cuprous oxide in the oxide layer increases, and it will approach a limiting value as given by the diffusion of copper ions across a pure cuprous oxide layer.

The oxidation curve for a 90-10 brass, interrupted by a 2-hr isothermal anneal in argon, is shown in Fig. 9. After the displacement reaction was allowed to occur, the value of the rate constant decreased by a factor of about 11, less than that for the oxidation of an 85-15 brass under similar conditions, but certainly significantly enough to show the occurrence of the reaction. The cross section of this oxide showed particles of zinc oxide dispersed in a copper-red matrix.

Recently Sartell, Bendel, Johnston, and Li (3) studied the oxidation of 62% copper-38% nickel alloy. They suggested that the formation of a nickel oxide phase was due to an inward diffusion of oxygen.

Because the displacement reaction was shown to occur in the absence of oxygen in copper-zinc alloys, a test was made to determine if this reaction, and similar results, could be duplicated for a copper-nickel alloy. The standard free energy of formation of nickel oxide is, at 800°C, 10,700 cal/mole less than that for cuprous oxide, and the diffusion of nickel ions through nickel oxide has been shown (15) to be slower than the diffusion of copper ions through cuprous oxide.

A 62% copper-38% nickel alloy was made following the procedure of Sartell, *et al.*, and the samples were prepared and oxidized at 800°C in the same manner as that for the copper-zinc samples previously discussed, except, because of a smaller difference in the standard free energy of formation of the two oxides, a 4-hr isothermal anneal in argon was utilized. The initial period of oxidation was purposely kept short (30 min) in order to restrict virtually all of the displacement reaction to the annealing period, in order to emphasize its occurrence more vividly.

A curve of the oxidation rate and a cross section of the oxide before and after the isothermal anneal are shown in Fig. 10 and 11. Although the value of K_p is not constant during the second period of oxidation, but rather tends, ultimately, toward the value of K_p for the first oxidation period, the fact that there is a change in the slope is indicative of some change in the oxide structure. In Fig. 11(a), the cross section of the oxide at the end of the first period of oxidation is seen to consist of three distinguishable layers. The outer black layer is a thin

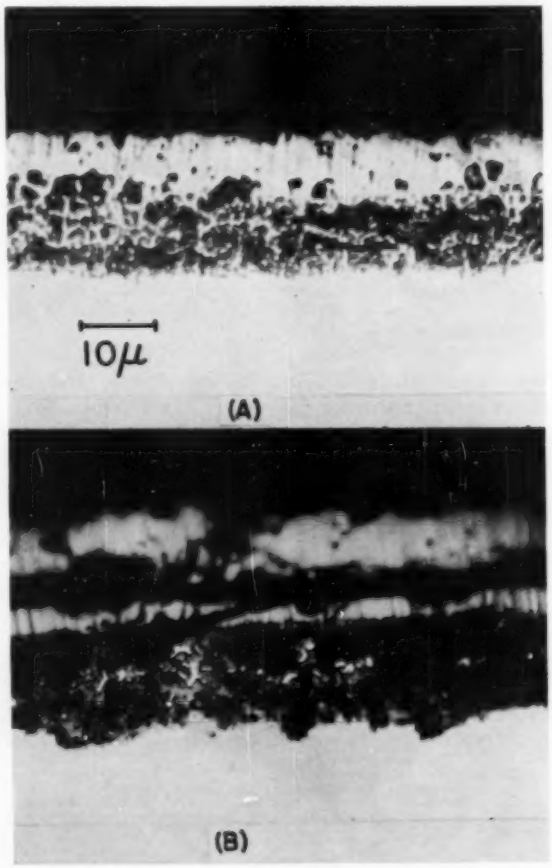

Fig. 11. Cross section of an oxide scale on a 62% Cu-38% Ni alloy (a) after 30-min oxidation in pure oxygen at 800°C, and (b) after 30-min oxidation in pure oxygen followed by a 4-hr isothermal anneal in argon at 800°C. Note the particles of free copper formed as a consequence of the displacement reaction.

film of cupric oxide which forms by the oxidation of cuprous oxide. The middle oxide layer is cuprous oxide, and the oxide at the metal-oxide scale interface is a cuprous oxide-nickel oxide layer which has a dark orange tint indicating the presence of free copper in solution in the oxide. This dark oxide layer forms, in a manner analogous to the formation of the "pink" oxide layer on the Cu-Zn alloys, by the displacement reaction

$$\text{Ni (in alloy)} + Cu_2O = NiO + 2Cu \qquad [4]$$

which has occurred during continuous oxidation by the outward diffusion of cations and electrons. Any structural changes which may have occurred in the thin cupric oxide layer during this short period of oxidation have not been considered.

The oxide cross section after a 4-hr isothermal anneal in argon is shown in Fig. 11(b). Microscopic examination reveals numerous areas of free copper in a matrix of nickel oxide, both of which were formed by the occurrence of the displacement reaction to a large extent during the period in the inert gas. It is noted that the interface between the composite oxide and the cuprous oxide did not shift via the displacement reaction during the anneal, and it is believed that because of the porosity in the inner layer, the nickel ions were unable to migrate to the cuprous oxide layer. The difference in specific volumes of cuprous oxide (23.9 cm^3/mole) and nickel oxide (9.9 cm^3/mole) provides a possible explanation for the porosity.

Summary and Concluding Remarks

A displacement reaction has been shown to occur during the oxidation of alloys in which the values of the free energies of formation of the oxides of the individual constituents are different. The displacement reaction was manifested as a change in the parabolic reaction rate constant, which was shown to decrease as the more impermeable oxide layer was formed. It was shown that by interrupting the oxidation process and by allowing the displacement reaction to occur during an isothermal annealing in an inert atmosphere the rate of subsequent oxidation was greatly diminished.

Acknowledgments

The authors wish to thank Professor Carl Wagner for his advice. This work was supported by a grant from the Union Carbide Metals Company and by a contract with the U.S. Atomic Energy Commission. One of the authors (R.L.L.) is a U.S. Navy Advanced Scientific Program Scholar.

Manuscript received April 24, 1961. This paper was prepared for delivery before the Detroit Meeting, Oct. 1-5, 1961.

Any discussion of this paper will appear in a Discussion Section to be published in the June 1962 JOURNAL.

REFERENCES

1. C. Wagner, *Z. physik Chem.*, **B21**, 25 (1933).
2. J. L. Meijering and M. L. Verheijke, *Acta Met.*, **7** [5], 331 (1959).
3. J. A. Sartell, S. Bendel, T. L. Johnston, and C. H. Li, *Trans. A.S.M.*, **50**, 1047 (1958).
4. C. Wagner, *This Journal*, **103**, 627 (1956).
5. F. Maak and C. Wagner, *Werkstoffe u. Korrosion*, In press.
6. C. Wagner, "High Temperature Properties of Metals," p. 93, American Society for Metals, Cleveland, Ohio (1951).
7. J. S. Dunn, *J. Inst. Metals*, **46**, 25 (1931).
8. K. W. Froelich, *Z. Metallkunde*, **28**, 368 (1936).
9. J. P. Coughlin, Bureau of Mines, Bulletin 542.
10. R. Linder, *Act Chem. Scand.*, **6**, 457 (1952).
11. E. A. Secco and W. J. Moore, *J. Chem. Phys.*, **26**, 942 (1957).
12. G. W. Castellan and W. J. Moore, *ibid.*, **17**, 41 (1949).
13. F. Pettit, R. Yinger, and J. B. Wagner, Jr., *Acta Met.*, **8**, 617 (1960).
14. F. N. Rhines and B. J. Nelson, *Trans. A.I.M.E.*, **156**, 171 (1944).
15. M. T. Shim and W. J. Moore, *J. Chem. Phys.*, **26**, 802 (1956).

Composition and Thickness Effects on Magnetic Properties of Electrodeposited Nickel-Iron Thin Films

Irving W. Wolf

Electronics Laboratory, General Electric Company, Syracuse, New York

ABSTRACT

Thin films of nickel-iron have found use in the fabrication of magnetic memories for information storage in computers. These memories have the advantage of very high speed switching. Use is made of a magnetic field during deposition to align the magnetic axes in the film in one direction so that the film exhibits a single "easy" axis of magnetization. Thus an "induced" anisotropy is established. In this work, effects of thickness (500-6000Å) and composition (~60% Ni-100% Ni) on the anisotropy field, H_k, as well as on wall coercive force, H_c, and easy direction disturb, H_{cD}, are presented. Evidence for stress interaction with magnetization and some data on substrate roughness are given.

With an increasing demand for higher speed memories for computers, there has developed an increasing interest in the magnetic thin films of iron-nickel codeposits. The first work reported in this area, by Blois (1) in 1955, has been followed by a large number of investigations of applied and basic nature and in the construction of operating memories. The work of Blois was concerned with

vapor-deposited films, and much of the investigative work has concerned itself with such films. However, in 1957, magnetic anisotropy in electrodeposited nickel-iron films similar to that observed in vapor-deposited films was reported (2). Since that time, development effort in electrodeposition has produced films whose properties are similar to those of vapor-deposited films in many ways, but, in general, the process has a somewhat higher degree of reproducibility (3, 4).

When these iron-nickel films are deposited in a magnetic field of sufficient strength, an anisotropy is induced in the plane of the film, such that the magnetization "prefers" to lie along the axis parallel to this field. The geometric demagnetizing force constrains the magnetization to lie in the plane of the film. It will lie in only one of two directions unless influenced by outside fields. Thus two stable magnetic states are present. These states can be designated as 0 and 1 and the film thus used to store information.

It has also been established (5) that the magnetization can be made to switch from one state (direction along the preferred axis) to the other by a "coherent rotation" rather than by the film's breaking up into a number of domains the way other magnetic materials have been observed to behave. This "rotation" switching mode is many times faster than the "domain wall" mode and is thus the means whereby fast memory elements can be operated.

Magnetic parameters.—The magnetic properties of a film which are of primary interest for magnetic memory application are the H_{cD}, easy axis disturb, and H_k, and the anisotropy field.

The easy axis disturb, H_{cD}, is measured by applying a field along the preferred, also called "easy," axis in the direction opposite to that in which the magnetization lies. When the field becomes sufficiently large, disturbance of the magnetization in the film will occur, so that small domains will form in which the magnetization is in the direction of the applied field. Thus the beginning of domain wall switching will have occurred. When this field is increased to the point where half the film has switched the value of the field at this point is called the coercive force, H_c.

If, however, a field is applied perpendicular to the preferred axis, a rotation of the magnetization as a whole will occur. This rotation is, ideally, reversible, and the angle of magnetization from its rest position will increase with increasing applied field until this angle, ideally, reaches 90°. At this field intensity, called the anisotropy field, H_k, the magnetization lies in the direction of the applied field and will remain so until the applied field is once again reduced.

Measurements

In this work values of the parameters H_{cD}, H_c, and H_k, the easy axis disturb, the coercive force, and the anisotropy field, respectively, were measured for samples of electrodeposited films of various Ni to Fe ratios and of varying thicknesses by hysteresigraph techniques. (Note: This method of measuring H_k does not necessarily yield the same results as those obtained from the more physically meaningful torque data.) The samples, all ¼ in. square, were deposited on a gold substrate which had been sputtered on a glass base (Corning No. 1 microscope cover slide, 0.007 in. thick). The measurements are made with a hysteresigraph at 1 kc. The preparation and measurement procedures have been described in earlier reports (2, 6, 7).

In order to vary the Ni to Fe ratio in the plate, the ratio of the two ions in the bath (sulfate-chloride type) was varied.

The plate composition *vs.* bath composition characteristic was determined by examining plates from various baths by means of x-ray fluorescence from the plates. The relative strength of the K_α lines of iron and nickel were related to their relative concentrations and, using this relationship, samples were analyzed.[1]

A plot of % Ni in the plate *vs.* g/l of Fe^{++} in the solution (61.5 g/l Ni^{++}) is given in Fig. 1 for 1000Å thick samples.

Thickness measurements were not made for individual samples, but an assumption of a constant plating current efficiency was used over the entire range of composition. As a justification for this assumption, it might be pointed out that the measured saturation magnetizations were within experimental error of expected values. However, precise measurements were not made of individual sample areas and, as a result, random thickness variations of up to 10% could be expected.

The possibility of ion depletion during deposition causing a varying iron-nickel ratio as plating progresses was examined by testing film composition as a function of thickness. The films were examined by x-ray fluorescence as mentioned above.[2] Results for three compositions 93%, 82%, and 63% Ni indicated no variation for the first two within experimental error (1%) but a gradual increase of several per cent for Ni for the latter from 500 to

[1] In this work, the K_α ratios of salts prepared by dissolving the films were compared with those of salts of known Ni to Fe ratios.

[2] Both films and dissolved-film salts were analyzed.

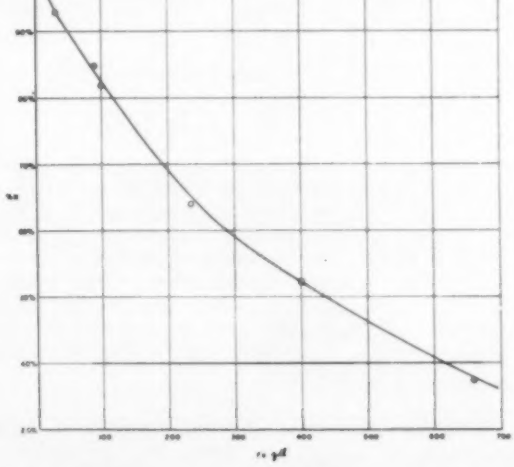

Fig. 1. Plate composition vs. Fe content of plating solution for 1000Å samples.

Table I. Easy axis disturb, H_{CD} in oersteds vs. composition and thickness

Composition wt % Fe	Thickness	500A	1000A	1500A	2000A	3000A	4000A	5000A	6000A
	0	19.6	20	18	18.8	22.8	20	25	
		19							
		19							
	5	4.4	4.8	5.3	4.7	4.4	4.8	6.5	
		4.9	5.6						
	9	4.0	4.0	4.6	3.9	3.7	3.6	4.1	4.4
	12	2.6	2.6	2.5	2.5	1.7	1.0	1.3	0.8
	13.5	3.6	2.7			1.8			
		3.3	3.1						
	15	3.0	2.3	1.6	1.3	0.9	0.8	0.6	0.4
		3.0	2.2		1.2		0.6		0.4
	17	2.8	2.0	1.2	1.1	0.6	0.5	0.4	0.3
	20	3.4	1.7	1.6	0.9	0.6	0.4		0.35
	23	3.4	1.7						
		3.1	1.9	1.1	0.9	0.6	0.5		0.35
	28	4.7	1.6	1.2	1.0	0.6	0.4		
		6.0	1.6						
	35	7.6	2.6	1.4	1.0	0.9	0.8		0.7
		7.5	2.5						
		7.0	2.0						
		6.0	1.9						
	53	10.0	3.0	2.0	1.5	1.2			
		8.3	2.5	2.1					
	66	7.6							

5000A. The results reported in the tables are not corrected for this variation since it occurs in the Fe rich region where the variation of magnetic properties with composition are slow and since the effect is relatively small.

Results

In general square hysteresis loops were obtained for samples measured in the preferred direction for *all* compositions when the thickness of the sample was 1000Å or less. The linearity or reversibility of the transverse "loop" did vary with composition for the range of compositions exceeding ~ 82% nickel, (zero magnetostriction) becoming less linear as the nickel content increased up to 90-95% but more linear as pure nickel was approached. This variation did not occur with the "iron rich" samples, less than ~ 82% nickel.

Typical hysteresigrams are given in Fig. 2 for 1000Å thick samples of the compositions 47, 83, and 100% Ni. The extent of linearity in the transverse direction is not shown because, in order to standardize the procedure for H_k measurement, a low drive had to be used.

As the film became thicker, the loops in the preferred direction became less square, the degree of this "shearing" varying with composition.

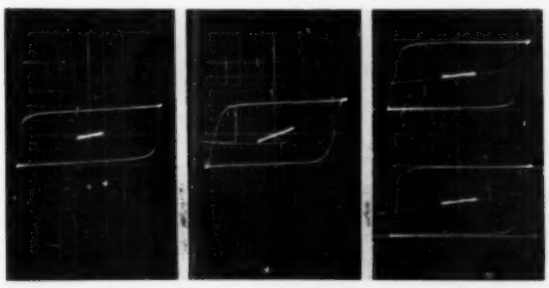

Fig. 2. Typical hysteresis loops for 1000Å samples: (left) 100% Ni, H = 26.8 oe; (center) 83% Ni, H = 3.4 oe; (right) 47% Ni, H = 3.8 oe.

Tables I, II, and III contain the H_{CD}, H_c, and H_k data for samples of the various compositions (47-100% Ni) thicknesses (500-6000Å). An indication of loop "shearing" can be obtained by taking the ratio H_{CD}/H_c for any desired sample, since the H_{CD} is approximately the abscissa value for the knee of the loop.

Discussion

Calculations (8) and observations (9, 10) of the effect of thickness on H_c, reported in the literature led to an expectancy of a logarithmic relationship of the form, $H_c = At^{-B}$, for the case of permalloy composition near zero magnetostriction (approximately 82%). In this equation, A and B are constants and t the film thickness. Lloyd and Smith (8) reported a dependency of A on the substrate roughness and B with plating conditions (and presumably composition).

That B varies with composition for a given substrate and plating condition can be seen in Fig. 3

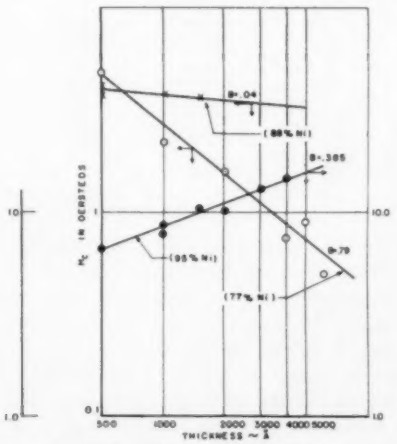

Fig. 3. Coercive force vs. thickness

Table II. Easy axis coercive force, H_c, in oersteds vs. composition and thickness

Composition wt % Fe	Thickness	500Å	1000Å	1500Å	2000Å	3000Å	4000Å	5000Å	6000Å
	0	22	25	24.8	23	27	23	27	
		22	21						
		22	21						
	5	6.5	8.0	10.2	10.1	13.3	14.5	13.9	
		6.5	8.6						
	9	4.9	5.3	6.2	6.7	7.1	8.2	8.6	12.6
	12	3.4	3.7	3.6	3.8	4.1	6.1	6.0	10.5
		3.5	3.7		3.7		5.3		9.8
	13.5	4.9	3.4			3.7			
		4.2	3.9						
	15	4.1	3.0	2.7	2.4	2.1	2.0	2.0	2.8
		3.4	3.3		2.7		2.5		3.0
	17	3.5	2.9	2.4	2.0	1.7	1.6	1.2	3.6
	20	4.3	2.2	1.6	1.3	0.9	0.7		0.5
	23	5.0	2.5	1.6	1.4	0.9	0.7	0.6	
		4.6	2.7						
	28	9.9	3.0	2.0	1.6	1.0	0.9	0.7	
		11	3.0						
	35	11.2	3.8	2.9	1.8	1.3	1.0	1.1	
		11.6	3.7	3.3					
		11.7	4.2	3.3					
		11.6	3.4						
	53	12.0	3.5	2.7	1.9	1.5			
		10.0	3.0	2.7					
	66	9.0							

Table III. Anisotropy field, H_k, in oersteds vs. composition and thickness

Composition wt % Fe	Thickness	500Å	1000Å	1500Å	2000Å	3000Å	4000Å	5000Å	6000Å
	0	42	41	42.5	41.5				
		40	38						
		40	40						
	5	7.7	9.8	14.3	19.3	29	41		34.5
		8.0	10.3						
	9	5.3	5.4	6.9	9.3	9.9	15.1	19.8	28
					8.4				
	12	3.9	3.8	4.1	4.0	4.6	8.0	9.0	23
		3.5	3.7		4.0		7.7		19
	13.5	4.2	4.1			3.7			
		4.0	4.0						
	15	4.0	3.8	3.8	3.7	3.8	3.8	3.6	5.4
		3.8	3.9		3.9		3.7		6.4
	17	4.3	4.0	3.8	3.9	3.7	3.7	3.3	8.0
	20	5.1	3.8	3.7	3.8	3.9	3.6		5.4
	23	4.6	4.3	4.0	4.4	4.1	4.0	4.0	
		4.7	4.1						
	28	7.9	5.7	5.0	5.6	5.0	5.0	5.0	
		7.4	6.3						
	35	10.3	7.0	7.6	6.2	6.3	5.4	5.7	
		10.5	6.6						
		9.0	7.7						
		10.6	7.8						
	53	10.0	9.0		10.0	10.4			
		9.3	8.2						
	66	7.5							

where H_c *vs.* t is plotted at three different compositions. The value actually undergoes a sign change in the nickel rich region. A similar behavior of H_{CD} *vs.* thickness is shown in Fig. 4. However, for the latter case a break in the lines in the high 80% composition range is noted. This break occurs at about 2000Å for the 88% Ni films and may simply be due to the onset of loop "shearing" due to geometric demagnitizing influences (samples are ¼ in. squares) which is more evident when the other effects are small ($B = 0.04$).

As a parallel to the relationship for H_c, a like relationship is apparent for H_{CD}, *i.e.*, $H_{CD} = Ct^{-D}$.

Plots of the exponents B and D are given in Fig. 5. The dependency of B and D on composition and especially the radical changes that occur for the values in the neighborhood of zero magnetostriction point strongly to a stress dependent effect influenc-

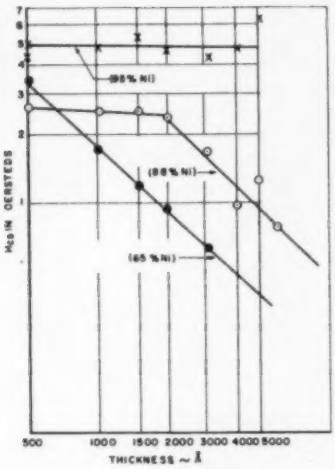

Fig. 4. Easy axis disturb field vs. thickness

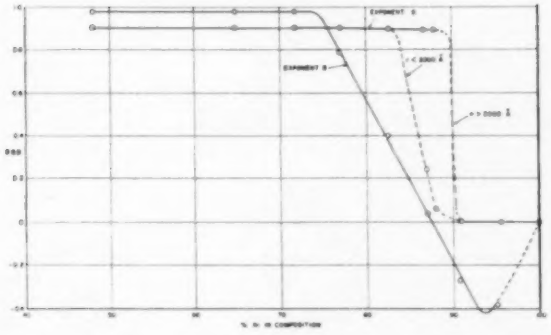

Fig. 5. Exponent B and D vs. $H_c = Ae^{-Bt}$ and $H_{cD} = Ce^{-Dt}$, respectively.

ing wall motion. Such an effect is in keeping with the mechanism described by Smith (10).

The value of B at 80% Ni composition can be interpolated as approximately 0.55. In view of the steepness of the curve at this point combined with the uncertainty of exact composition there is reasonable agreement with the value of 0.75 reported by Lloyd and Smith (8). The substrates were, of course, smoother than those used by Lloyd and Smith and, as a result, their value of A was higher.

An indication of the behavior of the values H_c and H_{cD} as functions of composition for one thickness are given in Fig. 6, where the values are plotted for 1000Å thickness. Although the exact curve shape changed with the thickness parameter, the general nature and in particular the approximate location of the flat minimum was similar for all thicknesses. This, of course, also points to the role of stresses in affecting H_c and H_{cD} values.

An unexpected but meaningful result was the observation of a dependence of H_k on thickness. This dependence is shown in Fig. 7 where H_k is plotted against thickness for three compositions.

It can be seen from Fig. 7 that the dependence of H_k on thickness cannot be formulated simply. However, the H_k does increase with thickness for nickel rich films (above 82% Ni) and decreases with thickness for iron rich films. The effect is smallest in the vicinity of zero magnetostriction. Thus a very strong argument for invoking an anisotropic stress mechanism in formulating a hypothesis for the anisotropy of these films has been presented. Such a mechanism has been proposed by Smith (11) which he has suggested as an effect which can be superimposed on the short range ordering effect. An additional indication is the composition dependence of H_k itself shown in Fig. 8 for 1000Å films. The minimum of H_k in the zero magnetostriction composition range is shown clearly.

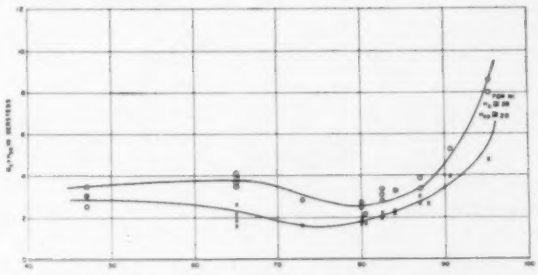

Fig. 6. H_c, H_{cD} vs. % Ni (1000Å thickness)

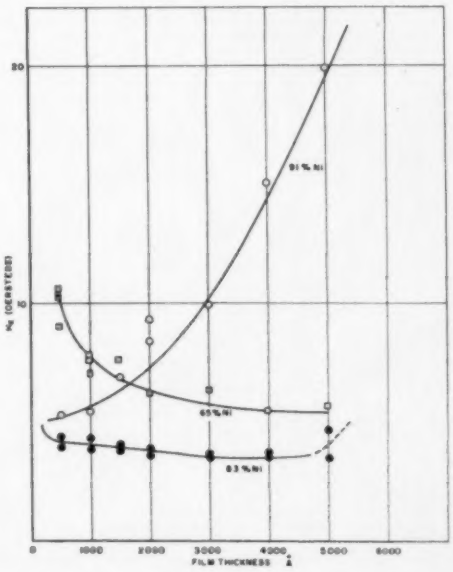

Fig. 7. Anisotropy field, H_k, vs. thickness

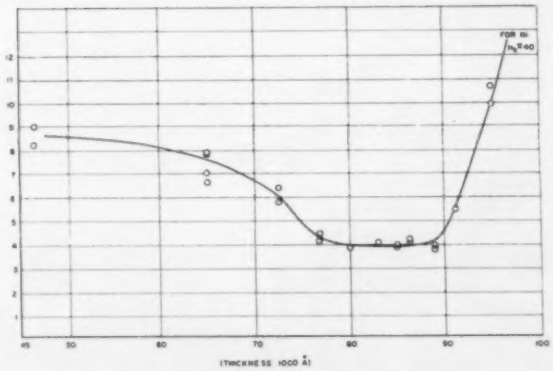

Fig. 8. Anisotropy field, H_k, vs. % Ni

Summary

Data for H_c, H_{cD}, and H_x for electrodeposited Ni-Fe films of thickness in the range 500-6000Å and for compositions above 47% Ni are given. These films were deposited on a very smooth substrate so that roughness effects were minimized. Analysis of the data strongly indicates a role of stress affecting both rotational and wall motion of magnetization.

Acknowledgments

The author wishes to express his appreciation to Mr. R. E. Schultz, Mr. G. Putman, Mrs. J. Harrington, and Mr. V. Popoff of the G. E. Electronics Laboratory for their invaluable aid in carrying out this study and to Dr D. Smith and Mr. J. Raffel of Lincoln Laboratory for their suggestions and interpretations relating to it.

This work was performed under the sponsorship of Lincoln Laboratory, a center for research, operated by Massachusetts Institute of Technology with the joint support of the U.S. Army, Navy, and Air Force.

Manuscript received April 14, 1961; revised manuscript received June 28, 1961. This paper was prepared for delivery before the Houston Meeting, Oct. 9-13, 1960.

Any discussion of this paper will appear in a Discussion Section to be published in the June 1962 JOURNAL.

REFERENCES

1. M. S. Blois, *J. Appl. Phys.*, **26**, 975 (1955).
2. I. W. Wolf, *Proc. Am. Electroplaters' Soc.*, **44**, 121 (1957).
3. C. D. Olson and A. Pohm, *J. Appl. Phys.*, **29**, 274 (1958).
4. I. Wolf and T. Crowther, *Proc. Electronic Components Conf.*, **1960**.
5. J. I. Raffel *et al.*, *Proc. IRE*, **49**, 155 (1961).
6. V. P. McConnell and I. Wolf, *Proc. Am. Electroplaters' Soc.*, **43**, 215 (1956).
7. I. W. Wolf, H. W. Katz, and A. E. Brain, *Proc. Electronic Components Conf.*, **1959**, 15.
7. L. Neel, *J. Phys. Radium*, **17**, 250 (1956).
8. J. C. Lloyd and R. S. Smith, *J. Appl. Phys.*, **30**, 274S (1959).
9. C. O. Tiller and G. W. Clark, *Phys. Rev.*, **110**, 583 (1958).
10. D. O. Smith, M.I.T. Lincoln Laboratory Report No. 53G-0047.

Electrodeposition of Molten Metals and Alloys from Glycerine Solutions

George L. Schnable

Lansdale Division, Philco Corporation, Lansdale, Pennsylvania

ABSTRACT

Various metals and alloys including In, In-Cd, In-Sn, In-Ga, Sn-Cd, and Sn-Zn are used in the fabrication of electrochemical transistors (SBT, MAT, MADT, SAT). These and metals and alloys such as Sn, Sn-Pb, Pb-Cd, Pb-Sb, and Cd-Zn have been electrodeposited in molten form on small wires and strips from glycerine solutions of metal halides. In contrast to conventional processes for electrodeposition of solid metals, deposition of molten metals can be very rapid since high current densities can be employed. Moreover it has been possible, at these high current densities, to deposit binary (or ternary) alloys of metals separated by over 0.6 v in the acidic electromotive series of the elements.

Recently techniques have been developed for extremely rapid electrodeposition of molten metals and alloys on the ends of small wires or strips. Various metals and alloys with liquidus temperatures up to about 270°C have been electrodeposited from plating solutions consisting of chloride or other halide salts dissolved in high-boiling, polar organic solvents such as glycerol (1-3). Metals and alloys which have been electrodeposited in molten form are smooth, dense, and nonporous, and are free of occlusions or nonmetallic plating bath constituents (4).

Since the plating solutions, which are acidic, have a fluxing action, the molten metals or alloys have a high surface tension which tends to minimize their surface area and influence their location. On wires held vertically during plating the molten deposit forms an ellipsoidal bead of metal or alloy at the end of the wire. The plating solutions are also effective fluxes for the base metal to be plated, for example, a nickel whisker wire, and thus result in good wetting of the wire by the molten deposit.

Transistor fabrication.—The technique of electrodepositing molten metals and alloys from glycerine solutions is particularly useful in production of uniform, high-reliability semiconductor devices, especially high-frequency transistors such as SBT, MAT, MADT, SAT. The electrode diameters of such transistors are very small, on the order of 0.1-0.2 mm. Consequently the weight of alloy used in fabrication of each electrode is frequently on the order of 10 μg. By electrodepositing a bead of the desired weight and alloy composition on the end of a fine wire, it is possible to handle readily extremely small alloy pellets on high-speed, automated equipment. In a subsequent operation to wire plating, the pellet is alloyed to an electrode dot of a micro-alloyed transistor (MAT or MADT). The coating of solution which remains on the electrodeposited bead of alloy as the plated whisker is withdrawn

from the plating solution serves as an effective flux during the simultaneous alloying and lead attachment operation.

Generally only a few seconds plating time is required to obtain the desired size of molten metal or alloy bead. Size is readily controlled by varying plating time, or in some cases, applied voltage. A typical micro-alloy pellet would be an ellipsoidal bead about 0.1 mm in diameter and 0.2 mm long deposited at the end of 0.05-mm nickel whisker wire. Approximately 2 sec is required to deposit a bead of In-Cd eutectic alloy having these dimensions.

Electrodeposition of molten metals and alloys.—Because such molten deposits are characterized only by composition and temperature, plating quality is unaffected by many of the variables which must be controlled carefully in conventional aqueous electroplating processes. Limiting current density, for example, is not limited by plating quality as with aqueous plating solutions where dendritic growths are formed at higher current densities. For this reason, extremely high current densities, on the order of 20 to 50 amp/cm^2, are frequently employed (3). Such current densities are considerably higher than those used in other commercial electrolytic processes (5) (metals are electrodeposited from aqueous solutions at current densities up to about 0.5 amp/cm^2; the cryolyte process for electrodeposition of aluminum employs current densities of about 1.5 amp/cm^2).

Three benefits result from the use of extremely high current densities. (*A*) Metals widely separated in the electromotive series of the elements can be readily codeposited. For example, indium ($E^\circ = -0.34$ v) and tin, which is considerably more noble ($E^\circ = -0.14$ v) than indium in the acidic electromotive series of the elements, are readily codeposited in approximately equal amounts. (*B*) Electrodeposition can be extremely rapid. It is possible to electrodeposit molten indium metal or indium alloys on a cathode surface at a rate on the order of several mm/min. (*C*) Local heating at the cathode during electrodeposition enables molten metals or alloys to be deposited from a bath operated at a temperature considerably lower than the liquidus temperature of the electrodeposited solder. For example, In-Cd alloy can be electrodeposited on 0.05-mm (2-mil) nickel wire immersed in a solution operated at about 70°C using 18 v for electrolysis. In this case the temperature at the cathode rose more than 50°C above the operating temperature of the bath (3).

The principle of employing local heating at the cathode so that the solution can be operated at a temperature considerably below the liquidus temperature of the electrodeposited metal or alloy is of interest in applications where long plating bath life or minimum fuming is desired.

Molten metals and alloys having liquidus temperatures up to about 270°C have been electrodeposited from glycerine solutions. Solutions for deposition of In, Sn, Bi, and alloys of In, Sn, Bi, Tl, Cd, and Pb have been developed. The In-Cd, In-Sn, In-Ag, Sn-Cd, Sn-Zn, Sn-Pb, Pb-Cd, and Pb-Sb plating solutions are intended to deposit alloys of approximately eutectic composition. The composition of the eutectic alloys (in percent by weight) and the melting point of the eutectics are (7): 75In-25Cd, 123°C; 52In-48Sn, 117°C; 97In-3Ag, 141°C; 68Sn-32Cd, 177°C; 91Sn-9Zn, 198°C; 63Sn-37Pb, 183°C; 83Pb-17Cd, 248°C; 89Pb-11Sb, 252°C; 83Tl-17Cd, 204°C; 83Cd-17Zn, 266°C; 60Bi-40Cd, 144°C. Pure indium, tin, and bismuth have melting points of 156°, 232°, and 271°C, respectively. The In-Ga plating solution was developed to plate indium containing about 0.5% Ga by weight. If ductile and malleable In-Ga alloys are desired, the solid solubility of Ga in In (about 0.75% Ga by weight) cannot be exceeded.

Experimental Results

Solution preparation.—Materials used in the preparation of baths for electrodeposition of low melting metals and solders are: glycerine, sp gr 1.25, minimum assay 95%; indium trichloride ($InCl_3$), anhydrous, fine powder; cadmium chloride ($CdCl_2$), anhydrous, powder, minimum assay 99%; zinc chloride ($ZnCl_2$), minimum assay 95%; ammonium chloride (NH_4Cl), granular; lead chloride ($PbCl_2$), anhydrous; silver chloride (AgCl); ammonium bromide (NH_4Br), granular; lead bromide ($PbBr_2$), anhydrous; cadmium bromide ($CdBr_2$), anhydrous; antimony trioxide (Sb_2O_3); ammonium chlorogallate, anhydrous; and stannous chloride ($SnCl_2$), anhydrous. Preparation and properties of ammonium chlorogallate (NH_4GaCl_4) have been described by Friedman and Taube (9). A homogeneous mixture of NH_4GaCl_4 and NH_4Cl having an assay of 60% as $GaCl_3$ (23.8% as Ga metal) is available commercially. Anhydrous gallium trichloride ($GaCl_3$) may also be used, although it is considerably more hygroscopic than ammonium chlorogallate and thus is less convenient to handle.

Stannous chloride ($SnCl_2$), anhydrous, is available commercially. Anhydrous stannous chloride has also been prepared by heating stannous chloride dihydrate ($SnCl_2 \cdot 2H_2O$) in a stream of hydrogen chloride gas.

All plating solutions were prepared by stirring the constituents at room temperature for ½ hr and then heating the resulting mixture, with constant stirring, at 140°C for 10 min to form a clear solution. Solutions used to deposit alloys with liquidus temperatures of 140°-200°C were subsequently heated to 160°C for 5 min; those for alloys with liquidus temperatures over 200°C were heated to 200°C for a few minutes to expel any excess water which might be present.

Electrodeposition of various solders.—Table I lists bath composition and operating conditions for electrodeposition of various metals and alloys on 0.05-mm (2-mil) nickel wire immersed 0.03-0.05 mm below the plane of the surface of the plating solution. In all cases a carbon anode was used.

As the operating temperatures and melting points in Table I indicate, it is not necessary for the operating temperature of the plating solution to be as high as the liquidus temperature of the metal or alloy being deposited. The use of very high cathodic current densities results in considerable local I^2R

Table I. Bath compositions and operating conditions for electrodeposition of various metals and alloys on 0.05-mm nickel wire immersed 0.03-0.05 mm below the surface of the plating solution

Metal or alloy electrodeposited	Solution composition, % by weight of constituents	Operating temp. of solution, °C	Applied voltage, carbon anode	Approx. composition of the electrodeposited alloy, % by weight	Eutectic composition, % by weight (7)	Melting point of eutectic alloy (7) (or of metal), °C
Indium	80 glycerine, 12 $InCl_3$, 8 NH_4Cl	160	18	100% In	(In)	156
Indium-cadmium	81.7 glycerine, 6.0 $InCl_3$, 1.7 $CdCl_2$, 10.6 NH_4Cl	140	24	In with 20 to 30% Cd	75 In-25 Cd	123
Indium-gallium	80.3 glycerine, 11.2 $InCl_3$, 0.5 NH_4GaCl_4, 8.0 NH_4Cl	140	15	In with about 0.5% Ga	—	—
Indium-tin	80 glycerine, 10 $InCl_3$, 2 $SnCl_2$, 8 NH_4Cl	140	18	In with 40 to 60% Sn	52 In-48 Sn	117
Indium-silver	Solution containing 80 glycerine, 12 $InCl_3$, 8 NH_4Cl, and saturated at 140°C with AgCl	140	18	In with on the order of 3% Ag	97 In-3 Ag	141
Tin	80 glycerine, 12 $SnCl_2$, 8 NH_4Cl	180	21	100% Sn	(Sn)	232
Tin-cadmium	81.6 glycerine, 6.0 $SnCl_2$, 4.2 $CdCl_2$, 8.2 NH_4Cl	160	22	Sn with 30 to 40% Cd	68 Sn-32 Cd	177
Tin-zinc	73.2 glycerine, 16.1 $SnCl_2$, 3.4 $ZnCl_2$, 7.3 NH_4Cl	155	18	Sn with about 10% Zn	91 Sn-9 Zn	198
Tin-lead	73 glycerine, 11 $SnCl_2$, 8.7 $PbCl_2$, 7.3 NH_4Cl	180	18	Sn with on the order of 40% Pb	63 Sn-37 Pb	183
Lead-cadmium	89.7 glycerine, 9 NH_4Cl, 1 $PbBr_2$, 0.3 $CdBr_2$	140	23	Pb with on the order of 20% Cd	83 Pb-17 Cd	248
Lead-antimony	91 glycerine, 8 NH_4Br, 0.9 $PbBr_2$, 0.1 Sb_2O_3	160	45	Pb with on the order of 10% Sb	89 Pb-11 Sb	252

heating in the vicinity of the cathode. When local heating is used, current density must be such that the temperature of the immersed surfaces of the cathode during electrolysis is above the liquidus temperature of the electrodeposited metal or alloy. If insufficient current density is used with a low bath operating temperature, dendritic growths or slushy plating forms at the cathode.

Under the conditions described in Table I, molten metals or alloys were plated with each solution. Because the surface area of the molten deposits increased rapidly during electrodeposition, sometimes by an order of magnitude, whiskers were plated using constant applied voltage, and plating conditions are described in terms of voltage applied between the cathode and a carbon anode rather than in terms of current density. At a constant applied voltage, total current drawn increases roughly at the same rate as the surface area of the molten deposit; thus, applying a constant voltage results more nearly in a condition of constant current density than would passing of a constant current during electrolysis.

In all experiments an inert carbon anode (spectroscopic graphite) was used. The anodes had an area sufficiently large that no appreciable polarization or local heating occurred at the anode during electrolysis.

Figure 1 shows a 0.05-mm nickel whisker on which a molten alloy was electrodeposited using one of the plating solutions listed in Table I. Figure 2 is a cross section of a plated whisker.

Wires ranging from 0.01 mm up to about 5 mm have been plated successfully with molten metal.

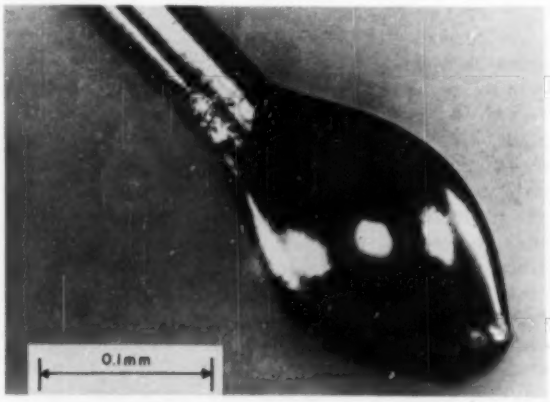

Fig. 1. Bead of In-Sn alloy electrodeposited in molten form on nickel wire.

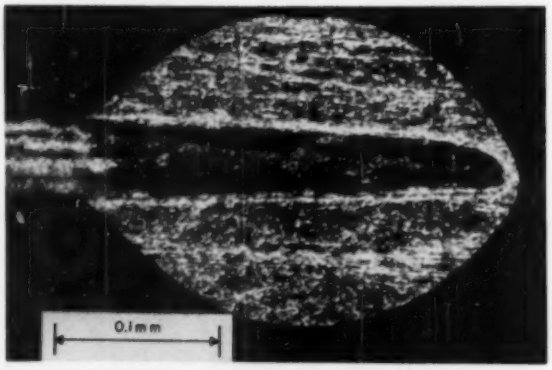

Fig. 2. Cross section of a plated whisker

Small parts such as strips, rods, or disks have also been plated with good results. The maximum size of metal droplet which can be electrodeposited on a wire or strip is determined by the density and surface tension of the molten metal or alloy. On 0.05-mm nickel wire maximum diameter for In-Sn alloy beads was about 0.5 mm. On large wires or rods, deposits can be obtained which are considerably thicker than can be obtained by a dip "tinning" operation, although the maximum over-all diameter may be only slightly larger than that of the original part.

Bath compositions, which were established empirically, generally result in the alloy composition listed only under the conditions described. However, it is relatively easy to determine the solution composition for electrodeposition of a desired binary alloy under a given set of plating conditions. If the binary system forms a eutectic, the required solution composition can be estimated from a plot of plating solution composition (moles of metal A/moles of metals A + B) vs. solidus and liquidus temperatures of the resultant alloys and consideration of the binary equilibrium diagram. This technique was used to estimate the composition of binary alloy systems for which a eutectic exists.

Alloy compositions were also determined by spectrographic techniques (10, 11). The compositions listed were generally determined at least three times with groups of 20 or more whiskers.

Ammonium chloride is added to lower the electrical resistivity of the plating solutions appreciably. In some cases the NH_4Cl also makes the solution a more effective flux for the base metal to be plated and for the molten alloy. Zinc chloride-containing solutions are particularly good fluxes with or without ammonium chloride.

The plating operation itself results in considerable stirring action at the cathode because (*a*) plating solution partially depleted of metal ions is less dense, (*b*) local heating causes convection currents, and (*c*) hydrogen evolution causes formation of a stream of small bubbles which rise and move away from the cathode, sweeping solution along with them. In some applications, however, mechanical agitation or stirring is beneficial in assuring reproducible size and shape of plated beads.

In some cases a small amount of compatible surfactant, for example 0.05% by weight of dodecyl benzene sodium sulfonate, is added to plating solutions to lower surface tension. The lower surface tension, by making the bubbles evolved at the cathode smaller, results in steadier plating currents and thus more reproducible plating rates.

After plating, the metal or alloy is rinsed with a dilute acetic acid or dilute hydrochloric acid solution. The solution must be acidic to prevent hydrolysis of metal salts with resultant formation of insoluble basic salts.

The influence of applied voltage on plating results can be illustrated by describing results obtained with the In-Ga plating solution listed in Table I, operated at 140°C. With 2 v applied between the 0.05-mm Ni cathode and a carbon anode, dendrites of solid indium are deposited at the cathode. With 8 v applied, a molten deposit is obtained; Ga content of the deposit is considerably less than the 0.5% which is obtained with an applied voltage of 15. Further increase in applied voltage beyond about 15 again results in lowering of the Ga content of the electrodeposited alloy. With 25 v applied, Ga content is significantly lower than with 15 v applied. Voltages much in excess of 30 can result in intermittent arcing. The In-Ga plating solution has a specific conductivity on the order of 0.0003 mho/cm at 25°C and about 0.03 mho/cm at 140°C. Solutions of lower conductivity begin to arc at higher voltages.

Cathode current efficiency of the In-Cd plating solution is roughly 20% (3). Current efficiency, and thus plating rate, is greater with tin plating solutions than with similar indium plating solutions.

Other plating solutions.—The list of metals and alloys which can be electrodeposited in molten form is by no means limited to those listed in Table I. Additional alloys which have been deposited in molten form from glycerine solutions include In-Cd-Ge, Tl-Cd, Cd-Zn, In-Sn-Ga, Sn-Ga, Sn-Cd-Ga, Sn-Cd-Zn-Ga, Bi-Cd, In-As, In-Sb, and others.

Chlorides are generally used in solution preparation, particularly because of the better availability of anhydrous chloride salts. Molten plating has also been obtained using halides other than chlorides, and occasionally those halides offer significant advantages over chlorides. Bromides, for example, are sometimes more soluble than the corresponding metal chlorides. In a few cases bromides, (or iodides) may be preferable because they are less volatile than chlorides. For example, if a Sn-Pb solder containing a few per cent arsenic were desired, the volatility of $AsCl_3$ (bp 130°C) would make a bromide-containing solution a more likely choice ($AsBr_3$ boils at 221°C).

Anode reactions may also change with change in the nature of the anion. With the glycerine solution containing $InCl_3$ and NH_4Cl, chlorine and oxygen are evolved at the anode, although the chlorine reacts to some extent with the solvent rather than being evolved as a gas. With bromides and iodides, more evolution of elemental halide occurs at the anode at a given electrolysis current. With the glycerine solution containing $SnCl_2$ and NH_4Cl, oxidation of the divalent tin to $SnCl_6^=$ occurs at the anode. The presence of appreciable amounts of $SnCl_6^=$ in a plating solution results in lowered cathode current efficiency.

In many cases the metal may exist in solution as an anionic chloride complex, such as the chlorogallate ion ($GaCl_4^-$). Use of a halide other than chloride would, in those cases, result in a change in the strength of the complex formation, and thus would result in a change in the current efficiency, or, with alloys, in the composition of the electrodeposited solder.

Occasionally volatilization of a higher valent metal chloride such as $SnCl_4$ might occur at the anode.

Conclusions and Discussion

Water content.—The term glycerine (rather than glycerol or 1,2,3-butanetriol) has been used

throughout this report since the plating solutions described normally contain a few per cent water. The glycerine used to prepare the solutions contains up to 5% water by weight; the salts used contain small amounts of water and absorb additional moisture during weighing and handling. Some water is lost during solution preparation. The residual moisture content is less in those solutions held at the highest temperatures during solution preparation. Generally the plating solutions are used under conditions where considerable volumes of room air pass over the surfaces of the solution. Thus it can be assumed that, at least after several hours at operating temperature, the heated plating solution has approached equilibrium with the room air in terms of water content.

Change in water content of glycerine solutions can cause a very profound change in the physical properties of the solutions. At room temperature the viscosity of glycerine containing 5% water (by weight) is only about one-third of that of pure glycerol. With the glycerine plating solutions described in Table I, viscosity is greatly dependent on water content. Similarly, because of reduced mobility of ions in more viscous solutions, electrical conductivity at room temperature is very dependent on water content of the solutions. At higher temperatures variation in the amount of water present in a glycerine plating solution has less influence on the viscosity of the solution. Moreover, the maximum amount of water which can be present in a glycerine solution decreases with increase in temperature. Therefore higher operating temperatures make the plating solutions less susceptible to the influence of variations in water content.

Alloy composition.—In most of the glycerine solutions for electrodeposition of molten alloys, several competing mechanisms occur at the cathode during electrolysis. Ordinarily, increase in current density in an alloy plating bath tends to increase the relative concentration of the less noble metal in the electrodeposited alloy. Thus increase in the voltage applied to these glycerine solutions, with resulting increase in the current density, ordinarily would be expected to increase the concentration of the less noble metal in the electrodeposited alloy. However, the very high current densities used during electrodeposition of molten alloys result in considerable local heating at the cathode. This local cathodic heating results in appreciable decrease in the viscosity of the plating solution in the vicinity of the cathode. [At 140°C, the viscosity of glycerol decreases roughly 2%/°C (12)]. Decrease in viscosity, which decreases polarization, favors plating of the more noble metal (13) since local depletion of the more noble metal ions is less likely to occur. Moreover, convection currents arising at the cathode as a result of local heating with accompanying decrease in solution density, and supplemented by bubbles of hydrogen evolved at the cathode and by decrease in density because of locally decreased metal ion concentration, tend to favor electrodeposition of the more noble metal (13).

Viscosity effects are particularly important with solutions where the minor constituent of the desired binary alloy is the less noble metal. With the solution for plating In-0.5% Ga alloy, for example, where $E^\circ = -0.34$ v for In and $E^\circ = -0.52$ v for Ga, changes in the viscosity of the solution result in changes in the polarization curve of In and thus can cause considerable change in the percentage of the total cathodic current which results in reduction of Ga ions to Ga metal. On the other hand, with a solution for deposition of Sn-5% Ag, where the major constituent of the alloy is the less noble metal, alloy composition would be expected to be influenced less by viscosity changes.

For most glycerol solutions for alloy plating, the effects of these two competing factors are not equal in magnitude, and thus the net result of changes in applied voltage is a change in alloy composition. With several solutions, such as the In-Ga plating solution operated at 20 v, increase in applied voltage results in decrease in the concentration of the less noble metal in the electrodeposited alloy. However, direction of change is not readily predicted and depends on the exact nature of plating conditions. Because the effects are opposite in direction, alloys having a composition within a desired range can be obtained using a relatively wide range of applied voltages, and thus magnitude of applied voltage is not particularly critical.

Bath life.—Bath life of glycerine solutions similar to those listed in Table I has been discussed by Certa *et al.* (3). The solutions described are stable for years at room temperature. In the absence of operating conditions in which depletion of one or more metal ion concentrations becomes significant, the principal limitation on bath life is increase in plating solution viscosity with time at operating temperature. The increased viscosity results in lower plating rates (at a constant applied voltage), and eventually results in significantly lower plating rates and/or erratic plating rates. Increased viscosity has been attributed to evaporation of glycerine and to condensation polymerization of glycerol to form polyglycerides (3).

Conclusions

The electrodeposition of molten metals and alloys from glycerine is an extremely versatile technique. Molten In, Sn, and Bi have been deposited in pure form, and alloys having In, Sn, Bi, Cd, Tl, or Pb as a principal constituent have been electrodeposited in molten form. Substantial percentages of Ag, Zn, Ga, Ge, As, or Sb have been codeposited with one or more of the above metals or alloy systems. Glycerine is a suitable solvent for baths for metals and alloys having liquidus temperatures up to about 270°C (the boiling point of glycerol is 290°C). Fused-salt systems have been developed for operation at temperatures above 200°C (4).

Metals separated by over 0.6 v in the electromotive series, such as Sn and Zn, have been codeposited without use of a complexing agent ($E^\circ = -0.76$ v for Zn and -0.14 v for Sn).

Several of the alloys described above are used in the fabrication of electrochemical type semiconductor devices, including Surface Barrier Transistors (SBT) (14-16), Micro Alloy Transistors (MAT)

(8), and Micro Alloy Diffused-base Transistors (MADT) (17-19). These devices are generally made on automatic lead attachment equipment in which the desired alloy is plated on the end of the wire and then the wire with alloy bead is bonded or microalloyed to the germanium device (15, 20). In the lead attachment operation the coating of plating solution which remains on the finished whisker as it is withdrawn from the plating solution serves as an effective flux during the subsequent bonding or alloying operation. Millions of high reliability transitors have been made using alloys electrodeposited in molten form.

The technique of plating molten metals or alloys on the ends of wires, rods, or strips is useful in fabrication of various electronic devices and components, especially miniature devices.

Acknowledgment

The author gratefully acknowledges the many co-workers who made contributions to the development of the solutions described above, including E. Zimmerman of the Research Division, who developed the In-Ga plating solution, A. Certa, T. Manns, H. Segal, J. Javes, W. Lilker, and W. Hillegas, Jr., of the Lansdale Division, who developed the various solutions for electrodeposition of eutectic alloys, and E. Murt, who developed spectrographic techniques for analysis of several of the alloys. It is a pleasure to acknowledge the cooperation and continued encouragement of R. Musa and C. Thornton. Appreciation is also expressed for the Special 1959 Glycerine Applications Award which was presented by the Glycerine Producers' Association to the research team consisting of A. J. Certa, T. J. Manns, and G. L. Schnable.

Manuscript received May 1, 1961. This paper was prepared for delivery before the Indianapolis Meeting, April 30-May 3, 1961.

Any discussion of this paper will appear in a Discussion Section to be published in the June 1962 JOURNAL.

REFERENCES

1. G. L. Schnable, U. S. Pat. 2,818,375, Dec. 31, 1957.
2. T. J. Manns and A. J. Certa, U.S. Pat. 2,818,374, Dec. 31, 1957.
3. A. J. Certa, T. J. Manns, G. L. Schnable, and H. S. Segal, *This Journal*, **106**, 690 (1959).
4. G. L. Schnable and J. G. Javes; *ibid.*, **105**, 84 (1958).
5. E. C. Potter, "Electrochemistry," p. 287, 310, Cleaver-Hume Press Ltd., London (1956).
6. W. M. Latimer, "The Oxidation States of the Elements and Their Potentials in Aqueous Solutions," 2nd ed., Prentice-Hall, Inc., New York (1952).
7. M. Hanson, "Constitution of Binary Alloys," McGraw-Hill Book Co., Inc., New York (1958).
8. A. D. Rittmann, G. C. Messenger, R. A. Williams, and E. Zimmerman, *IRE Trans. Electron Devices*, **ED-5**, 49 (1958).
9. H. L. Friedman and H. Taube, *J. Am. Chem. Soc.*, **72**, 2236 (1950).
10. E. M. Murt, *Appl. Spectroscopy*, **10**, 210 (1956).
11. E. M. Murt and J. C. Bready, *ibid.*, **15**, 1 (1961).
12. J. S. Segur, "Physical Properties of Glycerol and Its Solutions," in "Glycerol," C. S. Miner and N. N. Dalton, Editors, p. 284, Reinhold Publishing Corporation, New York (1953).
13. C. L. Faust, "Alloy Plating" in "Modern Electroplating," A. G. Gray, Editor, p. 64-97, John Wiley & Sons, Inc., New York (1953).
14. J. W. Tiley and R. A. Williams, *Proc. IRE*, **41**, 1706 (1953).
15. "Soldering Whiskers on Transistor Pellets," in "Production Techniques," J. Markus, Editor, *Electronics*, **29**, 270 (1956).
16. J. Roschen and C. G. Thornton, *J. Appl. Phys.*, **29**, 923 (1958).
17. C. G. Thornton and J. B. Angell, *Proc. IRE*, **46**, 1166 (1958).
18. C. G. Thornton, "Physical Design Concepts for Ultra-High Frequency Graded-Base Transistors," in "Solid State Physics in Electronics and Telecommunications," Vol. 2, p. 1122, M. Desirant and J. L. Michiels, Editors, Academic Press, Inc., London (1960).
19. G. L. Schnable and J. A. Hastings, Paper prepared for delivery at the Indianapolis Meeting, May 1-3, 1961.
20. "Automated Transistor Production," *Automation*, March, 1959.
21. E. M. Zimmerman, U. S. Pat. 2,931,758, April 5, 1960.

The Shape of Melt-Crystal Interfaces During Float Zoning of Silicon

Juergen H. Braun and Remo A. Pellin[1]

Pigments Department, E. I. du Pont de Nemours & Company, Inc., Wilmington, Delaware

ABSTRACT

The thermal environment of the interface of growth of a silicon crystal during float zoning is described. Depending on operating conditions, the interface between the melt and the growing crystal can be convex, near flat, or concave. The shape of the interface was made visible by slot doping of n-type silicon with an excess of boron dope to give a p-n junction between n-type crystal and p-type melt. This junction, outlining an interface, was decorated with a staining etchant.

Structural defects are generated in crystals grown from the melt by a mechanism which comes into play if the interface between the growing crystal and the melt is curved. Curvature of the isothermal surfaces, of which one coincides with the interface, causes a cold, peripheral annulus to contract over a hot, expanded core, or *vice versa*, depending on whether the growing crystal is convex or concave. In either case, thermal stresses result and, according to Billig

[1] Present address: Motorola, Inc., Phoenix, Arizona.

(1), Bennett and Sawyer (2), Dorendorf (3), and Lederhandler (4), relieve themselves into dislocations.

Shapes of the growing interface of silicon crystals in contact with the melt have been studied for the Czochralski process and were observed to be convex, as well as flat and concave. Tanenbaum *et al.* (5) and Billig (1) have observed traces of growing interfaces made visible as p-n junctions; Edwards (6) has described composition striations which follow the shape of the interface. Mullin (7) made pertinent observations of interfaces during the growth of indium antimonide crystals using tracer techniques.

A correlation between features of the interface and its thermal environment has been described for dendritic growth of germanium crystals from supercooled melt (8).

Temperature distributions in a silicon ingot have been analyzed theoretically for cross-sectional entrance of heat by Billig (1) and for peripheral heating by Akiyama, Yamaguchi, and Morishita (9).

In this publication results of studies of interface shape during float zoning of silicon are reported. The types of interfaces that were observed and the operating variables that control their shape are described. An attempt is made to identify these experimental variables with parameters of theoretical significance.

Experimental

Silicon ingots were float zoned by standard techniques in conventional equipment. Operating parameters were changed over wide ranges in an attempt to identify controlling variables in a minimum number of experiments.

Delineation of the shape of the floating zone was accomplished by slot doping of n-type silicon with an excess of boron to give a p-n junction between the n-type crystal and a p-type melt. The junction coincides with the interface between the molten zone and the growing crystal. The upper interface, between the molten zone and the feed stock, was delineated subsequently by a sudden freezeout of the p-type melt in contact with the n-type solid. The p-n junctions were decorated with an etchant that stains p-type silicon preferentially.

Float zoning.—Float zoning was carried out by techniques essentially as described by Hannay (10) in equipment of conventional and of custom design. Argon was used as ambient gas. Various types of induction coils were evaluated. The following operating parameters were investigated: rate of zone travel, rotation of seed, power input, and distance between seed and interface. Changes in operating conditions were made when the upper interfaces (between molten zone and feed stock) had progressed about 1 cm above the slot containing the boron dope for delineation of the interface.

Slot doping.—Silicon rods (19-22 mm in diameter), predoped to a resistivity of 0.05-2.0 ohm-cm n-type, were converted into single crystals. Boron dope was selected with 10^5-10^6 ppb boron, depending on the resistivity of the crystal. The amount of dope was calculated to give a 5-20 fold excess of p-type over n-type carriers in the molten zone. For 20 mm rod, this zone was assumed to weigh 10 g. Slots were cut into the crystal, spaced 5-10 cm apart and of the minimum size that would accommodate the slices of dope.

Standard techniques of float zoning were used to outline lower interfaces; both lower and upper interfaces were delineated by freezing out the zone shortly after the dope had melted. The bar was then dropped by about ½ cm and remelted for further zoning.

Delineation of interface.—The doped rods were sectioned, sanded, polished, and stained or etched to outline the interfaces as p-n junctions.

The rods were typed, cut into pieces 5-10 cm long for convenient handling, and sliced lengthwise. The faces were then sanded with 600 grit abrasive. For staining, they were polished with No. 6 and No. 1 diamond dust (4-8 μ and 0-2 μ, respectively).

The shape of the interface is revealed with least ambiguity by a staining etch proposed by Fuller and Ditzenberger (11). The etchant oxidizes and stains p-type silicon faster than n-type silicon. The solution consists of 0.2% concentrated nitric acid in concentrated hydrofluoric acid. The stain develops within 10-100 sec.

Features of the p-n junctions, as well as defects of the crystal, are revealed in greater detail by an etch proposed by Dash (12). A mechanical polish of the interface is not required, but the decorated interface is frequently less pronounced and more difficult to evaluate.

Results

Lower interfaces between growing crystal and floating zone were found to be near-flat, convex, or concave dependent on conditions of zoning. Characteristic shapes are shown in Fig. 1. Three types of convex[a] interfaces can be distinguished: cone shaped, resembling a blunt cone; interface shaped like an inverted dish with a flat peripheral annulus and a bulge in the center, and interfaces wave-shaped in cross section. Concave[a] interfaces resemble a flat depression. They are displaced less from planar than convex interfaces of cone and dish shape. Near-flat interfaces exhibit a wavelike pattern. Zoning with inadequate power supply gave interfaces that indicated a core of solid remaining unmolten.

The effect of zone travel is illustrated in Fig. 2. With increasing rate of zone travel, upper interfaces become more convex, lower interfaces less convex or

[a] Throughout this paper the designations convex and concave refer to the shape of the solid.

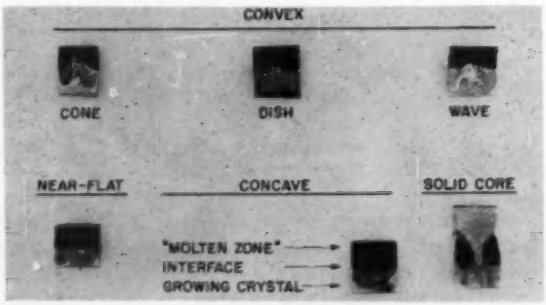

Fig. 1. Shape of interfaces, crystal melt

Table I. Shape of interfaces

Crystal, No.	Interface	Crystal diameter, mm	Seed rotation, rpm	Rate of zoning, cm/hr	Interfaces: Lower: Type	Lower: Displacement (1): Convex, % (2)	Lower: Displacement (1): Concave, % (2)	Lower: Relat. temp. gradient	Upper: Displacement convex, % (1)
49 (3)	a-d	20	0	8	D	22	<2	5	—
53	a-d	19	0	10	C (6)	44	<2	12	—
55	a	20	12	0	D	26	<2	6	—
	b		12	10	C	30	<2	7	—
	c		2	10	C	30	<2	7	—
	d, e		0	10	C	32	<2	8	70
58 (3)	a	20	0	15	C	34	<2	10	—
60	a	22	60	20	W	16	<2	4	—
61	a, b	22	60	20	W	14	4	4	—
	c, d		0	20	W	12	4	5	—
64	a-c	22	15	20	W-F	12	<2	3	—
66 (3)	a, b	22	30	19	W	12	12	5	—
68	a, b	22	15	5	C-D	22	<2	6	—
71	a	20	12	0	W	18	6	4	—
	b		12	9	C	36	<2	10	56
73 (4)	a	20	0	0	W	22	6	6	—
	b		0	11	—	—	—	—	50
	c		13	11	D	30	<2	7	42
	d		2	11 (5)	D	22	<2	6	52
	e		0	11 (5)	W	18	8	5	56
75	a	22	12	0	W	22	6	6	—
	b		12	10	W	22	<2	6	76
	c		0	10	W	22	<2	8	46
	d, e		0	10 (5)	W	22	6	7	44
77 (3)	a-c	22	10	12	D-W	24	<2	6	—
79	a,b	22	0	12	W	18	6	6	—
81	a	19	12	0	W	32	<2	7	—
	b	22	12	8	W	18	<2	4	32
	c		0	15	X	6	<2	—4	76
	d		0	30	X	16	10	—3	114
	e		0	60	S	—	—	—	—
83	a	22	0	5	W	20	<2	6	26
	b		0	10	W	28	10	6	38
	c, d		0	5	W	16	10	5	36
	e, f		0	25	W	26	4	5	92
85	a	22	12	0	W	22	4	—	—
	b		12	8 (5)	W	20	4	6	44
	c		0	15 (5)	F	<2	16	—	50
	d		0	30 (5)	X	<2	14	—4	80
	e		0	60 (5)	S	—	—	—	—
87 (3)	a	22	30	17	D-C	26	<2	6	—
89 (3)	a-c	19	30	20	C	32	<2	8	160
91	a	22	12	30	X	<2	14	—4	—
	b		0	38	X	<2	16	—4	—
	c	22	0	45	X	<2	16	—5	—
	d		0	60	S	—	—	—	—
93	a	22	12	0	W	22	6	—	—
	b		12	15	W	10	4	3	—
	c		12	18	F	10	6	3	—
	d		12	30	F	4	8	—4	—
	e		12	38	X	<2	14	—5	—
	f		0	45	S	—	—	—	—

Shape of Interfaces

(1) D, dish shape; C, cone shape; W, wave shape; F, near flat; X, concave; S, solid core.
(2) Vertical displacement from planar as percent of diameter.
(3) Modified induction coil and power unit.
(4) Radiation shield above coil.
(5) Increased power input.
(6) Core of n-type silicon projected from top of lower interface indicative of close proximity of lower and upper interface.

more concave. Slight asymmetry of the lower interfaces in Fig. 2 corresponding to rates of 15, 30, 45, and 60 cm/hr was caused by a distortion of the silicon bar during freeze-out at 7.5 cm/hr.

Zoning conditions and shapes of the interfaces obtained in a series of experiments are listed in Table I. Curvature of the interface is expressed in terms of vertical displacement from flat as per cent of radius. The type of interface, conical, dish, or wave-shaped, etc., is indicated by symbols. The column entitled "temperature gradient" gives relative thermal gradients for comparison. Not listed in Table I are several experiments in which modifications of the zoners were found to have little effect on the shape of the interface.

Discussion and Conclusions

The observations described above can be explained qualitatively and to some extent quantitatively, if

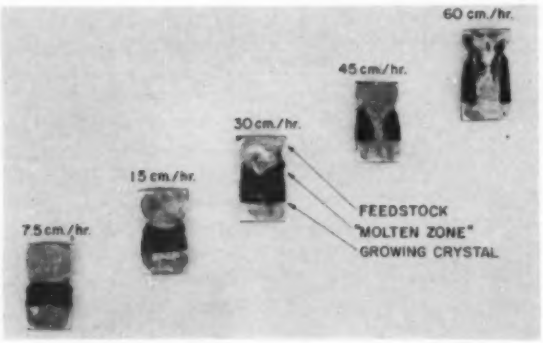

Fig. 2. Distortion of interface vs. rate of zone travel

one considers thermal properties and geometry of the silicon in conventional float zoning equipment.

Shape of interface.—Shape of the interfaces of the floating zone is controlled by 2 parameters: (*A*) The skin depth of high-frequency induction currents is sufficiently low under experimental conditions (about 1 mm at 4 megacycles) to consider the bar heated at the surface only. (*B*) The latent heat of fusion of silicon (11 kcal/mole) (13) contributes significantly to the heat balance of the system. At a rate of zoning of 30 cm/hr, crystallization releases 110 kcal/hr at the lower interface, while fusion consumes a corresponding amount of heat at the upper interface. These 110 kcal/hr are within the order of magnitude of the heat flow through each interface at stationary conditions, estimated at 300 kcal/hr from radiation loss, as well as power consumption and utilization.

The effects of these parameters combine to give shapes of interfaces illustrated in Fig. 3. The drawing shows traces of isothermal surfaces in the cross section of silicon rods skin-heated from high-frequency induction coils.

Coil and bar shown in Fig. 3A are stationary; isotherms above and below the coil, therefore, are approximately symmetric. Which isotherms coincide with the melting point, *i.e.*, from upper and lower interfaces, depends on the temperature level represented as determined by the balance between heat input and withdrawal. The shape of the interface under stationary conditions is, therefore, controlled primarily by the power input from the coil.

With an adequate supply of heat, a core of solid remains, and the interface corresponds to shape *a*. Marginal power input gives conical shapes *b*. Interfaces shaped like an inverted dish *c* are controlled by heat input; concave interfaces *e*, flat in the center with a slight peripheral upturn, should occur where heat loss is controlling, *i.e.*, where the peripheral heat loss by radiation and conduction exceeds the axial heat loss by conduction alone. An overlap of conditions at *c* and *e* should give wave-shaped isotherms *d*.

The latent heat of fusion of silicon has to be taken into account only when the zone is in motion. A plane of symmetry is no longer present. Interfaces become distorted as illustrated in Fig. 3B.

The latent heat of fusion, consumed at and supplied to the upper interface, causes it to become more convex, *b'* or *c'*. The lower interfaces, where heat is liberated and dissipated, become less convex, *b* or *c*, or more concave, *d* or *e* dependent on the shape of the corresponding interface at stationary conditions.

A quantitative consideration gives support to this interpretation. Displacement of the interface from flatness should not be a simple function of rate of zone travel if power input and rate both are controlling. Instead, the distortion of the zone shape, *i.e.*, the asymmetry of zone, should correlate with the rate of zoning. This, indeed, is the case, as illustrated in Fig. 4 where a measure of distortion is plotted against rate of zone travel.

Distortion is measured as the difference between displacement of upper and lower interfaces in per cent of radius and expressed as one-half of the measured value, *i.e.*, one half of the sum of the distortions of upper and lower interfaces. The plot shows that this expression is approximately proportional to the rate of zone travel. Pertinent data are given in Table II.

The mechanical transport of heat contributes to the asymmetry of the temperature distribution by increasing axial temperature gradients in the feed-

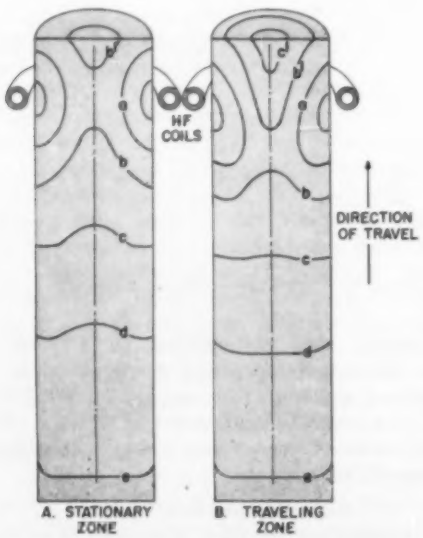

Fig. 3. Isothermic surfaces during float zoning

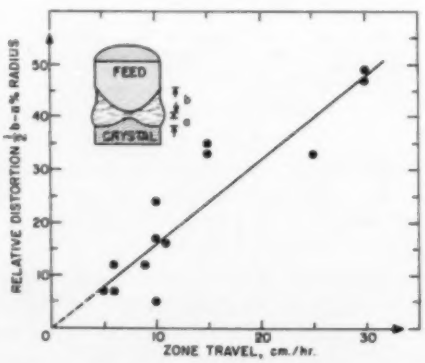

Fig. 4. Rate of zone travel, effect on interface

Table II. Rate of zoning vs. distortion of zone

Crystal	Interface	Rate of zoning, cm/hr	Displacement of interface, % of radius (1) Lower interface a	Upper interface b	Distortion of zone, % of radius (2) ½ (b-a)
55	d, e	10	32	70	19
71	b	9	36	56	10
73	c	11	30	42	12
75	b-e	10	22	56	17
81	b	7.5	18	32	7
	c	15	6	76	35
	d	30	16	114	49
83	a, c, d	5	18	32	7
	b	10	28	38	5
	e, f	25	26	92	33
85	b	7.5	20	44	12
	c	15	—16	50	33
	d	30	—14	80	47

(1) Vertical displacement from planar.
(2) Measure of asymmetry of zone.

stock and decreasing axial gradients in the growing crystal.

Rate of zone travel and power input had a much more pronounced effect on the shape of the interface than any of the other variables studied: rate of seed rotation, varied from 0 to 60 rpm, had no significant effect. The diameter of the bar, 19-22 mm, did not influence the shape of the zone noticeably. The distance between seed holder and zone and between the support of feedstock and zone did not appear to be significant. Design of the coil and zoning equipment affected the floating zone, but did not change the character of the response of the shape of the zone to the rate of zoning and the power input.

Temperature gradients.—Curvature of the interface from the growing crystal proves existence of radial temperature gradients essential to the generation of dislocations according to the theory introduced by Billig. Consideration of geometrical characteristics of the system reveal that this radial temperature gradient is proportional to the axial temperature gradient and the slope of the interface:

$$\frac{dT}{dr} = \frac{dT}{da} \times \frac{da}{dr} \qquad [1]$$

with dT/dr the radial temperature gradient, dT/da the axial temperature gradient, and da/dr the slope of interface. A derivation of the equation is given in Fig. 5.

RADIAL TEMPERATURE GRADIENT: $\frac{dT}{dr} \equiv \left(\frac{T_2 - T_1}{\Delta r}\right)_{\Delta r \to 0}$

AXIAL TEMPERATURE GRADIENT: $\frac{dT}{da} \equiv \left(\frac{T_2 - T_1}{\Delta a}\right)_{\Delta a \to 0}$

$$T_1 = T_2 - \frac{dT}{da} \times \Delta a$$

$$T_2 - T_1 = \frac{dT}{da} \times \Delta a$$

$$\frac{T_2 - T_1}{\Delta r} = \frac{dT}{da} \times \frac{\Delta a}{\Delta r} \quad \Delta r \to 0$$

$$\frac{dT}{dr} = \frac{dT}{da} \times \frac{da}{dr}$$

Fig. 5. Derivation of the radial temperature gradient

Relative radial temperature gradients, listed in Table I, were calculated using an equation for the "average radial temperature gradient"

$$\frac{\Delta T}{\Delta r} = C \times \frac{\Delta T}{\Delta a} \times \frac{\Delta a}{\Delta r} \qquad [2]$$

with $\Delta T/\Delta r$ the average radial temperature gradient, C the proportionality constant, $\Delta T/\Delta a$ the axial temperature gradient, and $\Delta a/\Delta r$ the slope of interface. Arbitrarily, the value of unity was assigned to the proportionality constant. The data have the dimensions of a temperature divided by a distance, but do not represent absolute values. They can, however, be used to compare the effects of operating variables on radial temperature gradients.

The radial temperature gradient exceeds the axial gradient only if the slope of the interface increases above 45°. In practice, inadequate power input to the zone leads to this condition.

The circumferential temperature gradient, a measure of the asymmetry of heat flow, can be derived similarly and expressed in analogous terms

$$\frac{dT}{d\alpha} = \frac{dT}{dr} \times \frac{dr}{d\alpha} \qquad [3]$$

$$\frac{dT}{d\alpha} = \frac{dT}{da} \times \frac{da}{dr} \times \frac{dr}{d\alpha} \qquad [4]$$

with $dT/d\alpha$ the circumferential temperature gradient, dT/dr, dT/da, da/dr, as in Eq. [1], and $dr/d\alpha$ the angular distortion of interface. The equations show that the peripheral temperature gradient is large only for large radial gradients combined with asymmetry of the zone.

Summary

Features of the interface between growing crystal and melt and between feed stock and melt during float zoning of silicon were made visible by a technique involving slot doping and decoration of the resulting p-n junctions by a staining etch.

Observations can be summarized as follows:

1. The interface of the growing crystal can be concave as well as convex. Several characteristic shapes of convex phase boundaries can be distinguished.

2. Rate of zone travel and power input into the zone control the shape of the interface. A near-flat interface of the growing crystal can be obtained by independent control of these variables.

3. Two primary parameters account for all observed shapes: (*a*) latent heat of fusion of silicon, and (*b*) skin heating characteristics of high-frequency induction.

Acknowledgments

The authors are indebted for counsel to numerous members of the Pigments Department technical staff, in particular, W. W. Greer, M. D. Jordan, and D. G. Kelemen. A. C. Mueller, Engineering Service Division, has contributed estimates of heat transfer characteristics. L. G. Hammond, C. B. Kelley, and L. A. Jesyk performed the experiments.

Manuscript received Feb. 13, 1961; revised manuscript received July 3, 1961. This paper was prepared for delivery before the Houston Meeting, Oct. 9-13, 1960.

Any discussion of this paper will appear in a Discussion Section to be published in the June 1962 JOURNAL.

REFERENCES

1. E. Billig, *Proc. Roy. Soc. London*, **A-235**, 37 (1956).
2. D. C. Bennett and B. Sawyer, *Bell System Tech. J.*, **35**, 637 (1956).
3. H. Dorendorf, *Z. Angew. Phys.*, **9**, 513 (1957).
4. S. R. Lederhandler, *J. Appl. Phys.*, **30**, 1631 (1959).
5. M. Tanenbaum, L. B. Valdes, E. Buehler, and N. B. Hannay, *ibid.*, **26**, 686 (1955).
6. W. D. Edwards, *Can. J. Phys.*, **38**, 439 (1960).
7. J. B. Mullin, Paper presented at the Chicago Meeting of The Electrochemical Society, May 1960.
8. A. I. Bennett, R. L. Longini, W. J. Smith, *ibid.*
9. K. Akiyama, J. Yamaguchi, and K. Morishita, Private communication.
10. N. B. Hannay in "Transistor Technology," F. J. Biondi, Editor, Vol. II, p. 9, D. Van Norstrand Co., Inc., Princeton (1958).
11. C. S. Fuller and J. A. Ditzenberger, *J. Appl. Phys.*, **27**, 550 (1956).
12. W. C. Dash, *ibid.*, **27**, 1193 (1956).
13. D. W. Lyon in "Rare Metals Handbook," C. A. Hampel, Editor, p. 383, Reinhold Publishing Corp., New York.

Characteristics of the {111} Surfaces of the III-V Intermetallic Compounds

III. The Effects of Surface Active Agents on InSb and the Identification of Antimony Edge Dislocations

M. C. Lavine, H. C. Gatos, and M. C. Finn

Lincoln Laboratory,[1] Massachusetts Institute of Technology, Lexington, Massachusetts

ABSTRACT

The effects of inorganic and organic surface active agents on the behavior of the InSb {111} surfaces in oxidizing etchants were investigated. It was found that specific adsorption of these agents leads to a decrease in the dissolution rate of InSb and pronounced changes in the microstructure of the {111} surfaces. In the presence of an organic sulfide it was possible to develop etch pits which were identified with Sb edge dislocations on the {111} surfaces. This result was verified by means of plastic deformation experiments. Electrical measurements at 78°K suggest that Sb dislocations serve as electron donors whereas In dislocations serve as electron acceptors.

In earlier communications (1-3) on III-V intermetallic compounds the differences in the chemical characteristics of the {111} surfaces terminating with group III atoms (A surfaces) and those terminating with group V atoms (B surfaces) have been discussed. The difference in behavior of the A and B surfaces has been attributed to the electronic configuration of the triply bonded A and B surface atoms (2). As a result of the difference in chemical reactivity of the triply bonded group III and group V atoms, it has been suggested (2) that only one of the two types of edge dislocations present in the III-V compounds is revealed on the A surfaces in the commonly employed oxidizing etchants. The dislocations revealed were shown to be those terminating in triply bonded A atoms. By altering the relative reactivities of the A and B atoms with the addition of surface active agents to oxidizing etchants, it has been possible to develop dislocations on the B surfaces as well (4). It has also been tentatively suggested (4) that both types of edge dislocations may be revealed in the case of InSb by the addition of aliphatic amines to an oxidizing etchant. In the present investigation Sb dislocations in InSb were developed and identified by employing suitable surface active agents. This identification was confirmed by experiments involving plastic deformation of InSb.

[1] Operated with support from the U. S. Army, Navy, and Air Force.

Experimental

Rate determinations.—Tetrahedral InSb samples bounded exclusively by In {111}[2] or Sb {111} surfaces were employed for the determinations of the dissolution rates. The surface active agents were added to an etchant consisting of 1 part 30% H_2O_2 + 1 part 48% HF + 3-8 parts H_2O, which hereafter will be referred to as the base etchant. This etchant was found very satisfactory in obtaining reproducible rates; however, other oxidizing solutions would probably serve as well. The dissolution rates (mg/cm^2/min) were determined from weight loss measurements (employing a commercial microbalance) and the geometric area of the samples. Generally the weight losses were between 5.0 and 250 mg for an average sample area of 3 cm^2 and time-periods up to 5 min. The rates remained constant for periods much longer than 5 min. The vigorous hydrogen evolution associated with the dissolution reaction provided effective agitation of the solutions (3). Consequently, no mechanical stirring was employed in these experiments.

Etching tests.—Wafers obtained by cutting perpendicular to the <111> growth axis of InSb single crystals were employed for observing microstructure

[2] It has become customary to designate the (111), ($1\bar{1}\bar{1}$), ($\bar{1}1\bar{1}$), and ($\bar{1}\bar{1}1$) set of planes as {111} or A(111); the ($\bar{1}\bar{1}\bar{1}$), ($1\bar{1}1$), ($\bar{1}11$) and ($11\bar{1}$) set of planes as {$\bar{1}\bar{1}\bar{1}$} or B(111). In the case of InSb they are designated as In(111) and Sb(111).

effects. The opposite sides of such wafers are In {111} and Sb {111} surfaces, respectively; thus, the effects of the surface active agents could be observed on both surfaces under identical etching conditions. The effects on the microstructure were established by (*a*) characterizing the surfaces in the base etchant; (*b*) etching in the base etchant containing the surface active agent; and (*c*) re-etching in the base etchant. Following each etching operation the surfaces of the wafer were replicated on Fax-film, then ground with 1600 mesh (10μ) garnet powder. The replicas provided a permanent record of the surfaces and afforded a direct means of establishing the effect of the particular surface active agent. Regrinding between successive etchings assured an identical starting surface since cold-work damage affects the microstructure obtained on the surface (2). All etching tests, unless stated otherwise, were performed at room temperature.

Because the organic sulfide present in the base etchant does not wet the InSb surfaces uniformly, it was found that for best results the sample must be immersed prior to etching in a wetting agent such as sodium lauryl sulfate solution.

Deformation tests.—Sample bars of the shape and orientation shown in Fig. 1 were obtained from InSb single crystals grown in the <110> or <100> directions. In bending, each sample was rested on two graphite blocks 18 mm apart and a load was applied through two steatite knife edges 6 mm apart. If bending about the [110] axis introduces an excess of In dislocations, bending about [110] axis (90° to the first bend axis) introduces an excess of Sb dislocations (5). Bending of the samples was performed in air at temperatures ranging from 280° to 300°C. Heating above 300°C (without bending) leads to marked changes in the electrical properties of this material (6). The amount of oxide formed under these conditions was removed by etching and had no effect on the properties studied. Before and after bending, the samples were ground, etched, and replicated in the manner described above. Electrical measurements to determine mobility and majority carrier concentration were made before and after bending. Control samples carried only through the heating cycle were also measured before and after heating.

Results and Discussion

Exploratory experiments.—It was reported earlier (4) that the addition of aliphatic amines to a mixture

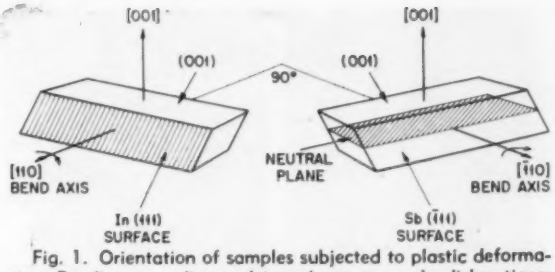

Fig. 1. Orientation of samples subjected to plastic deformation. Bending according to I introduces excess In dislocations; bending according to II introduces excess Sb dislocations.

of HF + HNO_3 + CH_3COOH substantially decreased the dissolution rate of the Sb surfaces of InSb while the rate of the In surfaces was essentially unaltered. It was further found that In dislocations (and possibly Sb dislocations) are revealed on the In and Sb surfaces in the presence of these amines. Only In dislocation etch pits appear, and only on the In surfaces, when these amines are not present. The effect of the amines was attributed to their preferential adsorption on the Sb surface atoms.

In the present work the effect of several inorganic and some organic surface active agents on the dissolution rate and the microstructure of InSb {111} surfaces was studied by employing the base etchant: H_2O_2 + HF + H_2O. Some typical results are shown in Table I. It is seen that the heavy cations, Ni^{++}, Co^{++}, and Cr^{+++}, do not alter the etching rate of the Sb surfaces and have a relatively small effect on the In surfaces. Of all active agents tested, only Cr^{+++} ions and butylthiobutane alter significantly the microstructure of the {111} surfaces as will be discussed below.

Effect of Chromic Ions

The chromic ions developed dislocation etch pits on the Sb surface only at low angle boundaries. Figure 2 shows a sequence of photomicrographs of parallel and corresponding sample fields on the indium (a) and on the antimony (b) surface. Ia and Ib are the fields after etching in the base etchant. IIa and IIb show the effect of the addition of 1% Cr^{+3} [as $Cr_2(SO_4)_3$] to the etchant. While the In surface is substantially unaffected (IIa), a low angle boundary is now developed on the Sb surface (IIb) as a series of etch pits with trails. The photomicrographs IIIa and IIIb of Fig. 2 show the same fields after etching at 0°C in modified CP4 (Table I) containing n-amylamine. This etchant develops In dislocations on both In and Sb surfaces.

Table I. Effect of surface active agents on the dissolution rate of InSb {111} surfaces

Etchant	Temp, °C	Rate	
		In{111}	Sb{111}
Base etchant*	25	11 mg/cm²/min	17 mg/cm²/min
Base etchant + $NiSO_4$(1% Ni^{++})	25	8 mg/cm²/min	18 mg/cm²/min
Base etchant + $CoSO_4$(1% Co^{++})	25	8 mg/cm²/min	18 mg/cm²/min
Base etchant + $Cr_2(SO_4)_3$(1% Cr^{+++})	25	9 mg/cm²/min	17 mg/cm²/min
Base etchant + n-butylthiobutane (0.4%)	25	3 mg/cm²/min	6 mg/cm²/min
Modified CP4**	4	0.5$_1$ mg/cm²/sec	7.8 mg/cm²/sec
Modified CP4 + n-amylamine (0.3%)	4	0.4$_4$ mg/cm²/sec	0.4$_8$ mg/cm²/sec
Modified CP4 + sodium stearate (0.05%)	2	0.3$_9$ mg/cm²/sec	0.3$_6$ mg/cm²/sec

* Base etchant in parts by volume: 1 30% H_2O_2 + 1 48% HF + 8 H_2O.
** Modified CP4 in parts by volume: 2 conc. HNO_3 + 1 48% HF + 1 glacial CH_3COOH.

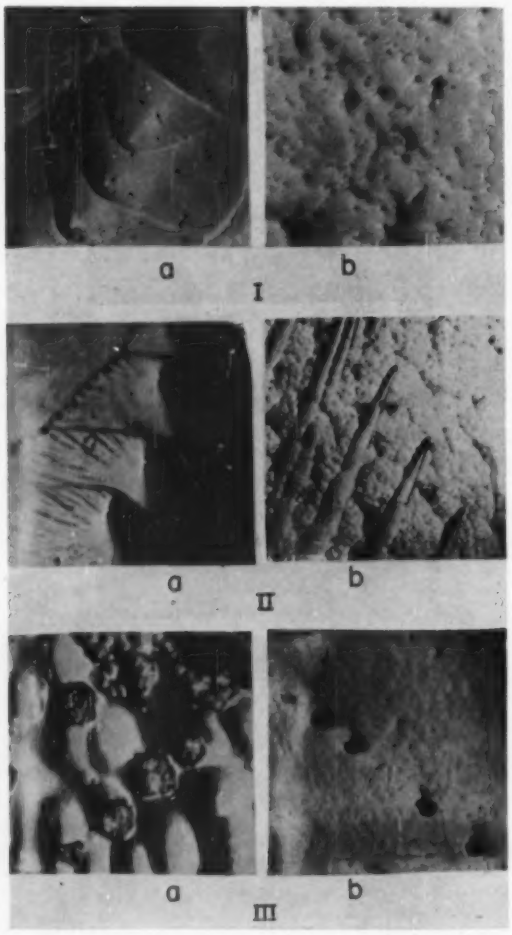

Fig. 2. In {111} and Sb {111} surface of an InSb wafer etched under various conditions. The In surface is marked in all instances (a) and the Sb surface is marked (b). The (a) and (b) sample fields are parallel and corresponding. Etching took place in: I, (a and b) base etchant (see Table I); II, (a and b) base etchant + 1% Cr^{+++} as $Cr_2(SO_4)_3$; III, modified CP4 (see Table I) + 0.3% n-amylamine at 0°C. 300×. All magnification before reduction for publication.

Chromic ions do not alter significantly the dissolution rates of the In or Sb surfaces (Table I). Similarly they are without effect on the microstructure of the In surfaces. They do, however, reveal low angle boundaries on the Sb surfaces of InSb. Considering the model proposed for the electronic configuration of the In and Sb surface atoms (2) (Fig. 3) and the chemistry of complex ions, it is not surprising that these ions do not adsorb on the In surfaces to an extent which would alter the etching behavior. On the other hand, the Sb surface atoms have a dangling bond with an unshared pair of electrons, and thus adsorption of the positively charged complex ions becomes quite plausible. In dilute solutions of chromic salts the complex ion $[Cr(H_2O)_6]^{+3}$ is formed having a very small dissociation constant. In the presence of halides, complexes of the type $[CrX_y(H_2O)_{6-y}]^{+(3-y)}$ may also be formed although the aqua complex is the most likely species present.

Although the mechanism involved is not understood at this time, adsorption of the above ions manifests itself only at the low angle boundaries. The trails associated with the dislocation etch pits on the Sb surfaces (Fig. 2-IIb) are analogous to those observed by Dash in silicon (7) which were attributed to the segregation of vacancies or impurities along the dislocation path. A similar origin is proposed for the trails observed in the case of InSb.

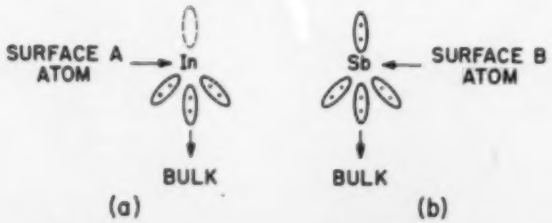

Fig. 3. Atomic model of the In and Sb atoms of the {111} surfaces.

Effect of n-Butylthiobutane ($C_4H_9SC_4H_9$)

Dissolution.—As shown in Fig. 4, the apparent activation energy for the dissolution of the In and Sb surfaces in the base etchant is 9 and 7 kcal/mole, respectively. These values are indicative of a diffusion controlled process. The observed differences in the diffusion controlled rates and in the apparent activation energies of the two surfaces in the same etchant are attributed to differences in their true areas as discussed extensively elsewhere (3). In the presence of the n-butylthiobutane, the room temperature dissolution rate of the In surfaces decreased by a factor of approximately four and the rate of the Sb surfaces decreased by a factor of three (Table I). As shown in Fig. 4, the apparent activation energy for dissolution changes somewhat in the case of the In surfaces, but the process remains under diffusion control upon addition of n-butylthiobutane. In the case of the Sb surfaces, however, the apparent acti-

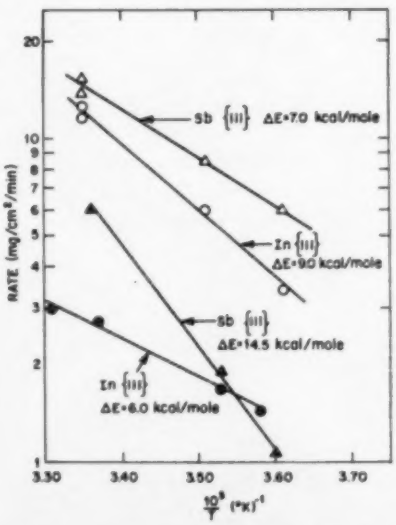

Fig. 4. Temperature dependence of the dissolution rates of the InSb {111} surfaces. o and △ base etchant (see Table I); • and ▲ the base etchant + n-butylthiobutane.

vation energy for dissolution increases to the value of 14.5 kcal/mole which is indicative of an activation controlled process.

The above effect on the dissolution process is believed to be the result of the adsorption of the oxidation product of n-butylthiobutane on the In and Sb surfaces. In the presence of peroxides, the alkyl sulfides (R-S-R) are oxidized to the corresponding sulfoxides with the oxygen atom covalently bonded to the sulfur:

$$R\text{-}\ddot{S}\text{-}R \xrightarrow[H_2O_2]{[O]} R\text{-}\overset{\overset{O}{\uparrow}}{\ddot{S}}\text{-}R$$

In acid (HX) solutions the sulfoxides form salts which correspond to two tautomeric forms depending on whether the H^+ attaches itself to the sulfur or to the oxygen atom:

$$R\text{-}\overset{\overset{O}{\uparrow}}{\ddot{S}}\text{-}R \xrightarrow{HX} \left[R\text{-}\overset{\overset{O}{\uparrow}}{\ddot{S}}\text{-}R\right]^+ X^- \quad (I)$$

$$\left[R\text{-}\overset{\overset{O}{\uparrow}}{\ddot{S}}\text{-}R\right]^+ X^- \quad (II)$$

It has been shown (8) that, in these compounds, the sulfur has the sp^3 tetrahedral coordination. Thus, it is likely that the tautomeric form II with an unshared pair of electrons can be covalently adsorbed on the In surface atoms which have no electron-dangling bonds (*c.f.* Fig. 3).[3] Adsorption of the sulfoxide on the In surfaces is quite extensive as evidenced by the pronounced decrease of the dissolution rate. On the other hand, the positively charged ions of either tautomeric form can adsorb on the Sb surface atoms which have an unshared pair of electrons. A similar explanation (4) has been advanced for the adsorption of ammonium ions $[RNH_3]^+$ on Sb surfaces.

In the presence of butylthiobutane the dissolution of the Sb surface becomes activation controlled although the values of the dissolution rates are comparable to those of the In surfaces under the same experimental conditions. However, in the case of the In surface the dissolution process is under diffusion control. The observed activation energy of 14.5 kcal/mole is apparently associated with the probable reduction of the sulfoxide on the Sb surfaces.

Microstructure.—With n-butylthiobutane added to the base etchant, pits appear on the In as well as on the Sb surfaces. Successive grinding-etching operations showed that these pits are associated with edge dislocations. However, they do not correspond to the dislocation etch pits which are developed by the base etchant and which have been shown to be associated with In dislocations. Typical results are shown in Fig. 5. Photomicrographs Ia and IIa depict the identical field on an indium surface etched in the base etchant (Ia) and in the base etchant containing

[3] The probability for electrons to be present in the group III atom dangling bond is taken to be extremely small.

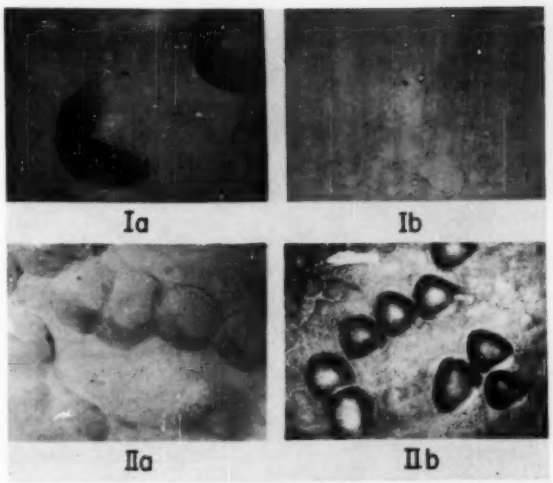

Fig. 5. In {111} and Sb {111} surface of an InSb wafer. Ia and Ib are the In and Sb surface respectively etched in the base etchant; these sample fields are parallel and corresponding. IIa and IIb are the In and Sb surface respectively etched in the base etchant + 0.4% butylthiobutane; these sample fields are parallel and corresponding. Fields Ia and IIa are the same as are Ib and IIb. 300X.

n-butylthiobutane (IIa). Photomicrographs Ib and IIb show the parallel and corresponding field on an antimony surface etched in the base etchant (Ib) and in the base etchant containing n-butylthiobutane (IIb). It is seen from Fig. 5 that there is no correspondence between the etch pits shown on Ia and those shown on IIa. Notice that a few individual In dislocation etch pits are present in Ia. However, on etching in the base etchant containing n-butylthiobutane, arrays of pits are developed on both surfaces. The pits in Figures 5-IIa and 5-IIb are associated with edge dislocations as evidenced by the one to one correlation in these figures. It is believed that these new etch pits are associated with Sb edge dislocations. This conclusion will be further verified below.

The fact that no In dislocation etch pits develop on these surfaces in the presence of butylthiobutane is attributed to the strong adsorption of the sulfoxide on the In atoms of the dislocation line intersecting the surface. Thus, the necessary condition for the formation of pits is not met; *i.e.*, the etching rate along the dislocation line does not exceed the rate on the overall surface.

The formation of Sb dislocation pits on In and Sb surfaces can best be visualized with the help of the models shown in Fig. 6. They illustrate the atom arrangement of an Sb dislocation intersecting an In surface (Fig. 6-I) and an Sb surface (Fig. 6-II). In Fig. 6-I the terminal dislocation atom is triply bonded and lies in the layer below the In surface atoms which are also triply bonded. In the sulfide etchant the room temperature dissolution rate of the Sb surface is greater than that of the In surface by more than a factor of two (Table I). Since the rate-determining step in the dissolution of the III-V compounds is associated with the reactivity of the outermost surface atoms (4) it can be concluded that here also the triply bonded Sb atoms are more reactive

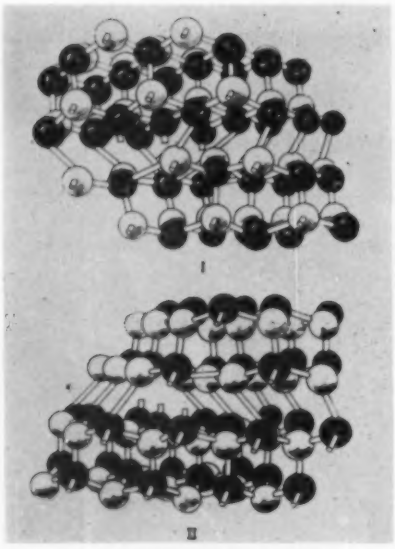

Fig. 6. Atomic model of an Sb dislocation intersecting an In {111} surface (I) and an Sb {111} surface (II) of InSb. Surfaces are defined by the atoms with the protruding bonds.

than the corresponding triply bonded In atoms. This difference in reactivity would favor attack along the Sb dislocation and lead to etch pit development. In the case of Fig. 6-II where an Sb dislocation intersects an antimony surface, the terminal dislocation atom is only doubly bonded and lies in the triply bonded Sb surface layer. The doubly bonded atom is more reactive than the triply bonded atoms. Thus, it will be the first to react exposing adjacent triply bonded In atoms which would be expected to be less reactive than the triply bonded Sb atoms as pointed out above. However, this would be the case only if the sulfoxide were to adsorb on the exposed In atoms adjacent to the terminal dislocation atom. It is reasonable to believe that effective adsorption on these recessed atoms is not probable due to steric hindrance. Thus, dissolution along the dislocation in this case would proceed more nearly at the rates found in the absence of the sulfide. Indeed, the pits on the Sb surface are deeper than those developed on the In surface by at least a factor of two. This difference can be seen by comparing Figures 5-IIa and 5-IIb. At the same magnification, the bottoms of the Sb surface pits are not resolved while the shallow pits of the In surface are entirely in focus.

Identification of antimony dislocations.—Plastic deformation of InSb provided a means for the unambiguous identification of Sb dislocations. Referring to Fig. 1, bending of a pair of samples with the orientations shown will give an excess of In dislocations in one case and an excess of Sb dislocations in the other. Several samples, bent to a radius of about 30 cm, were etched to test the specificity of each etchant. Typical results are shown in Figs. 7 to 14. In these figures sample areas were chosen in the vicinity of the neutral plane. In Fig. 7 to 10 indium dislocations (positive) have accommodated the sign of the bending moment. It can be seen that the samples etched in the base etchant (Fig. 7) and the modified CP4 +

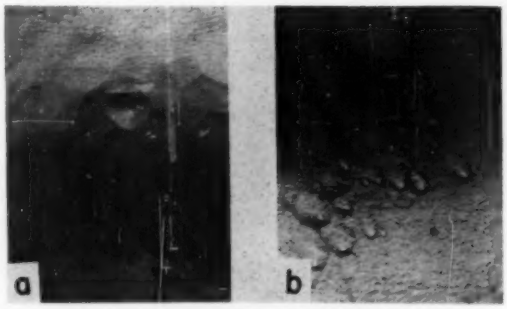

Fig. 7. In {111} surface before (a) and after (b) plastic deformation leading to the introduction of excess In dislocations (Fig. 1-I). The base etchant (Table I) was employed. 300X.

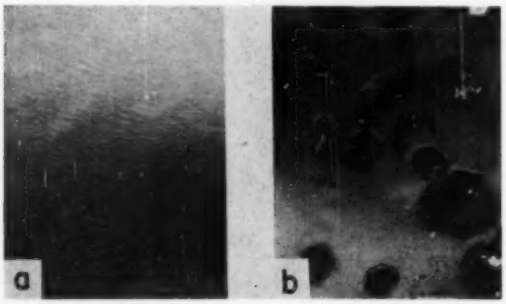

Fig. 8. Sb {111} surface before (a) and after (b) plastic deformation leading to the introduction of excess In dislocations (Fig. 1-I). Etchant employed: modified CP4 (Table I) + 0.3% n-amylamine. 300X.

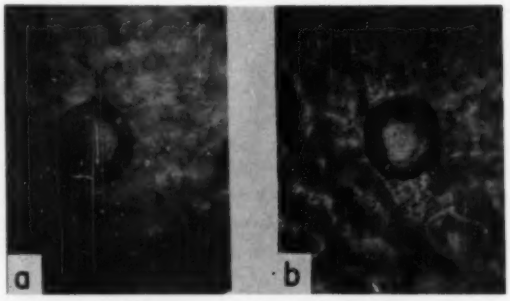

Fig. 9. In {111} surface before (a) and after (b) plastic deformation leading to the introduction of excess In dislocations (Fig. 1-I). No change in etch pit density is revealed. Etchant employed: the base etchant (Table I) + 0.4% n-butylthiobutane. 300X.

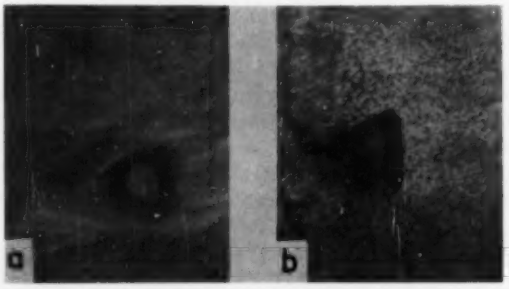

Fig. 10. Sb {111} surface before (a) and after (b) plastic deformation leading to the introduction of excess In dislocations (Fig. 1-I). No change in etch pit density is revealed. Etchant employed: the base etchant (Table I) + 0.4% n-butylthiobutane. 300X.

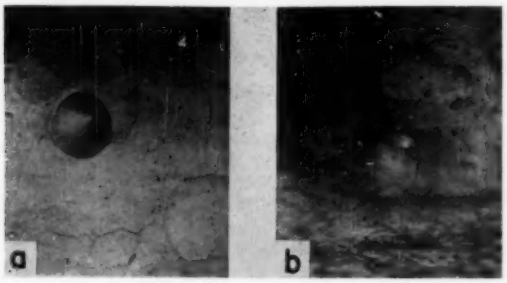

Fig. 11. In {111} surface before (a) and after (b) plastic deformation leading to the introduction of excess Sb dislocations (Fig. 1-II). No change in etch pit density is revealed. The base etchant (Table I) was employed. 300X.

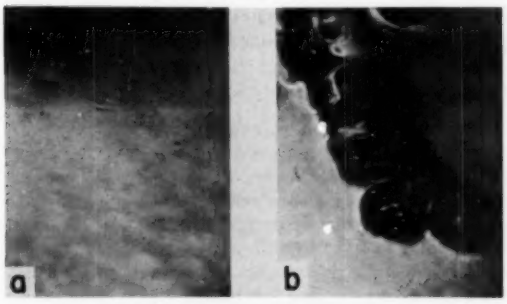

Fig. 12. Sb {111} surface before (a) and after (b) plastic deformation leading to the introduction of excess Sb dislocations (Fig. 1-II). Etchant employed: modified CP4 (Table I) + 0.3% n-amylamine. 300X.

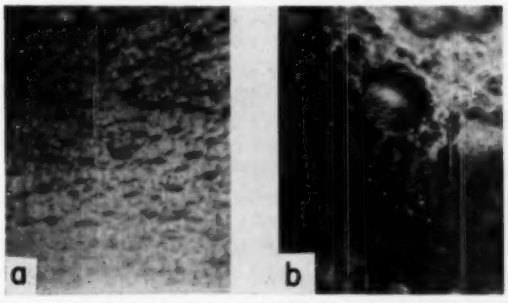

Fig. 13. In {111} surface before (a) and after (b) plastic deformation leading to the introduction of excess Sb dislocations (Fig. 1-II). Etchant employed: the base etchant (Table I) + 0.4% n-butylthiobutane. 300X.

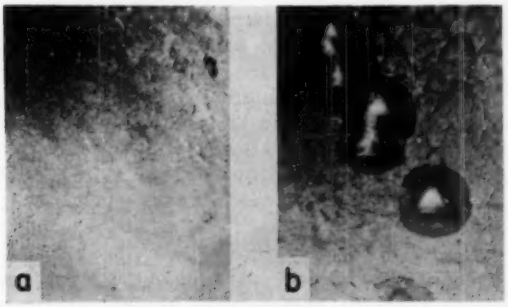

Fig. 14. Sb {111} surface before (a) and after (b) plastic deformation leading to the introduction of excess Sb dislocations (Fig. 1-II). Etchant employed: the base etchant (Table I) + 0.4% n-butylthiobutane. 300X.

n-amylamine (Fig. 8) after bending show an increase in etch pit density with the etch pits lined up in traces of the {111} slip planes. Etching in the base etchant + n-butylthiobutane reveals no increase in etch pit density after bending. (Fig. 9 and 10.)

In Fig. 11 to 14 the Sb dislocations are positive with respect to the bending moment (Fig. 1-II). Employing the same etchants as in Fig. 7 to 10, a marked difference in behavior is observed. In Fig. 11 there is no increase in dislocation density after bending. Figure 12 shows an increase in the density of pits on the Sb surface after bending. A similar behavior was observed in the In surface employing the same etchant as in Fig. 12. Thus, (on the basis of Fig. 8 and 12) the previous suggestion (4) that both types of pits are developed in the presence of aliphatic amines is verified. With the sulfide etchant the density of pits increases after bending as shown in Fig. 13 and 14. Thus, recalling that the base etchant reveals only In dislocations (Fig. 7 and 11) and in view of the fact that in the presence of n-amylamine both types of dislocations are revealed, it becomes apparent from Fig. 9-10 and Fig. 13-14 that n-butylthiobutane in the base etchant develops only Sb dislocations.

Measurements of the Hall coefficient and resistivity at 78°K were performed on InSb samples before and after bending. It was found (9) that, in many instances, introducing an excess of In dislocations on bending according to Fig. 1-I leads to a decrease in electron carrier concentration; introducing an excess of Sb dislocations on bending according to Fig. 1-II leads to an increase in the electron carrier concentration. In all cases, the electron mobility of the samples was decreased significantly after bending. Control samples carried only through the heating cycle exhibited no change in their electrical properties. These results, although qualitative in nature, indicate that In dislocations act as electron acceptors whereas Sb dislocations act as electron donors. They are entirely consistent with the model proposed for the electronic configurations of the triply bonded In and Sb atoms (Fig. 3) on the {111} surfaces and along a dislocation line of an edge dislocation.

Summary

Surface active agents present in an oxidizing etchant have pronounced effects on the microstructure of the In {111} and Sb {111} surfaces of InSb. Chromic aqua complex ions develop etch pits associated with In edge dislocations at low angle boundaries on the Sb surface. Organic sulfides such as n-butylthiobutane uniquely develop etch pits associated with Sb edge dislocations on both the In and the Sb surfaces. A simple atomic model has been employed to describe this effect. Plastic deformation experiments verified the identity of the dislocation etch pits developed in the presence of organic sulfides. Electrical measurements on plastically deformed samples with an excess of In or an excess of Sb dislocations suggest that In dislocations serve as electron acceptors and Sb dislocations serve as electron donors. This is in accord with the model proposed in these studies for the electron configuration of the triply bonded group III and group V atoms.

Manuscript received April 5, 1961; revised manuscript received June 5, 1961. This paper was prepared for delivery before the Houston Meeting, Oct. 9-13, 1960.

Any discussion of this paper will appear in a Discussion Section to be published in the June 1962 JOURNAL.

REFERENCES

1. M. C. Lavine, A. J. Rosenberg, and H. C. Gatos, *J. Appl. Phys.*, **29**, 1131 (1958).
2. H. C. Gatos and M. C. Lavine, *This Journal*, **107**, 427 (1960).
3. H. C. Gatos, M. C. Lavine, and E. P. Warekois, *ibid.*, **108**, 645 (1961).
4. H. C. Gatos and M. C. Lavine, *J. Phys. Chem. Solids*, **14**, 169 (1960).
5. J. D. Venables and R. M. Broudy, *J. Appl. Phys.*, **29**, 1025 (1958).
6. K. F. Hulme, R. R. E. Memorandum, 1581 (1959).
7. W. C. Dash, *J. Appl. Phys.*, **29**, 705 (1958).
8. H. Gilman, "Organic Chemistry," 2nd ed., vol. 1, p. 421, John Wiley & Sons, Inc., New York (1948).
9. H. C. Gatos, M. C. Finn, and M. C. Lavine, *J. Appl. Phys.*, **32**, 1174 (1961).

Polarography and Voltammetry in Dimethylsulfoxide

I. M. Kolthoff and T. B. Reddy[1]

School of Chemistry, University of Minnesota, Minneapolis, Minnesota

ABSTRACT

An exploratory voltammetric study of several acids, some representative metal ions, a few quinones, and oxygen has been made in the solvent dimethylsulfoxide (DMSO). Perchloric, sulfuric, and hydrochloric acids were found to be monoprotic strong acids in DMSO. Cobalt(II) and nickel(II) are reduced irreversibly at the dropping mercury electrode with large overpotentials indicating strong solvation. Polarograms of quinones showed two cathodic waves of unequal height in the absence of proton donor. The effect of proton donor on the polarograms of quinones was studied. The mechanism of the reduction of quinones in DMSO is discussed. Rotated platinum and rotated mercury pool electrodes can be used to advantage in DMSO.

Because of the unusual physical and chemical properties of dimethylsulfoxide (DMSO), an exploratory study was made of polarography and voltammetry in this solvent. On the basis of its physical properties (Table I) and its chemical structure, DMSO may be expected to exhibit similarity with water in some respects and with acetonitrile (1-3) in others. DMSO has a very low vapor pressure and is a liquid at room temperature; however, it is moderately viscous. The dielectric constant is rather high for an organic solvent and the liquid is strongly associated as shown by the high value of Trouton's "constant." The molecule is pyramidal (5) and highly polar. DMSO contains nonbonded electron pairs and should function as a base.

Nonaqueous polarography has been reviewed by Gutman and Schöber (4). Sears, Lester, and Dawson (6) have shown that a number of uni-univalent electrolytes are fully dissociated in DMSO. Due to greater solvation, the equivalent conductances of cations are significantly lower than those of anions of the same charge and comparable size. Using chronopotentiometry, Iwamoto (10) studied the oxidation of iodide in DMSO. At a platinum electrode in 0.1*M* sodium perchlorate, the oxidation proceeds by the same two-step process observed in acetonitrile (2, 11). Gutman and Schöber investigated the polarographic reduction of ten alkali and alkaline earth ions, six other metals as halides or organo-metallic species (12), and several tetra alkyl ammonium ions (13). Data on the solubility of some electrolytes in DMSO have been reported (14).

In the present work, polarograms of several acids, cobalt(II), nickel(II), and sodium have been determined. Current-voltage curves of some acids were also made at a rotated platinum wire electrode (RPtE). The polarographic waves of cobalt(II) and nickel(II) were irreversible with acute maxima even in very dilute solutions. Therefore current-voltage curves were also run at a rotated mercury pool electrode (RMPE). At this electrode smooth waves were observed which allowed a first approximation of $E_{1/2}$ (16). The mechanism of the polarographic reduction of benzoquinone, tetrachloroquinone, and duroquinone has been studied in the presence and absence of proton donor. Information on the acidic properties of DMSO has been deduced from this work. The polarography of oxygen was investigated briefly.

[1] Present address: Bell Telephone Laboratories, Murray Hill, New Jersey.

Table I. Physical properties of DMSO

Molecular weight		78.13
Melting point		18.4°C (6)
Boiling point		189.0°C (6)
Viscosity	(25°C)	1.96 cps (6)
Dielectric constant	(25°C)	46.7 (7)
Specific gravity	(25°C)	1.096 (6)
Heat of vaporization	(25°C)	12.64 kcal/mole (8)
Vapor pressure	(30°C)	0.60 mm mercury (8)
Trouton's constant		29.5 (6)
Dipole moment		3.9 debyes (9)

Experimental

DMSO (Stepan Chemical Company, Chicago) was shaken overnight with freshly heated and cooled Woelm chromatographic grade alumina in a sealed container. The liquid was then siphoned off by suction into a distilling flask. It was distilled over

alumina through a 20-in. column packed with porcelain saddles at a pressure of a few mm of mercury. A first fraction, amounting to about 10% of the total, was rejected and a second fraction, of about 80%, was collected. This second fraction was subjected to the same procedure twice or until the specific conductivity was 2×10^{-8} ohm^{-1} cm^{-1} and the water content 0.01% by weight or less as determined by the Karl Fischer titration method. The procedure of Sears, Lester, and Dawson (6) cannot be recommended because refluxing with calcium oxide or barium oxide causes extensive decomposition of the solvent. Removal of all the decomposition products was not possible.

Materials.—Anhydrous sodium perchlorate (G. F. Smith Chemical Company) was dried at 130°C *in vacuo* prior to use. Tetraethylammonium perchlorate was prepared by a slightly modified version of the procedure used previously (1). Another product was prepared according to the directions of Knecht (17) from perchloric acid and tetraethylammonium bromide.

Tetraethylammonium bisulfate of 100% purity was supplied by Dr. M. K. Chantooni of this laboratory.

G. F. Smith Chemical Company nickel(II) perchlorate hexahydrate and cobalt(II) perchlorate hexahydrate were brought to constant weight in a desiccator over magnesium perchlorate. Eastman Kodak benzoquinone, hydroquinone, and tetrachloroquinone were purified by sublimation. Eastman Kodak Company quinhydrone was recrystallized from 50% glacial acetic acid and dried in a desiccator. Duroquinone was supplied by Professor L. I. Smith.

Solutions of sulfuric acid were obtained by adding drop-wise Dupont reagent grade concentrated sulfuric acid to DMSO cooled in an ice bath. Hydrogen chloride was prepared by allowing reagent grade sodium chloride to react with concentrated sulfuric acid. The gas was slowly bubbled into DMSO which was cooled in an ice bath. Ice-cooling of the solvent is necessary to prevent decomposition of DMSO. Perchloric acid solutions in glacial acetic acid were added to DMSO to give solutions of perchloric acid in DMSO. Direct addition of 72% perchloric acid to DMSO caused a small explosion.

Eastman Kodak Company 40% aqueous technical grade trimethylbenzylammonium hydroxide was diluted with DMSO to obtain a 0.106*N* solution as standardized against potassium acid phthalate. This solution contained about 2.5% water.

Aerosol OT (sodium dioctylsulfosuccinate; American Cyanamid Company) was tested as a polarographic maximum suppressor.

Reagent grade chemicals were used where not otherwise noted.

Electrodes.—The DME used for most of this work had an m value of 1.03 mg/sec. and an open circuit t value of 6.02 sec. The mercury pool electrode (RMPE) has been described previously (15). The platinum electrode consisted of a piece of platinum wire about 1 cm long sealed into the end of a glass tube. The mercury electrode was rotated at 120 rpm and the platinum electrode at 600 rpm.

Table II. Polarization limits (vs. SCE) in DMSO

Supporting electrolyte	Electrode	Anodic limit vs.SCE	Cathodic limit
0.1*M* $NaClO_4$	DME	+0.25	−1.90
0.1*M* Et_4NClO_4	DME	+0.25	−2.80
0.1*M* $NaClO_4$ or Et_4NClO_4	RPtE	+0.70	−1.85
0.1*M* $NaClO_4$	RMPE	+0.3	−1.9

Recording polarograph.—A L&N Electrochemograph Type E was used to record all current-potential curves. The average current was corrected for iR drop by determining the average resistance with an Industrial Instruments Type RC-1B bridge.

Cells.—The two types of cells used have been described elsewhere (1, 17). With both cells an aqueous SCE with agar-potassium chloride salt bridge dipped into an isolated compartment to prevent contamination with water or electrolyte in the microelectrode compartment.

Nitrogen.—All solutions were deaerated with high-purity Linde nitrogen.

Temperature.—Polarographic and voltammetric measurements with acids were performed in a thermostat at 30°C. Other measurements were made at 25° or room temperature.

Results

The limits of anodic and cathodic polarization at the DME and RPtE in DMSO are given in Table II.

The electrocapillary curve in 0.1*M* sodium perchlorate is shown in Fig. 1. The maximum occurs near −0.3 v; the curve is somewhat distorted as compared to that in aqueous solution.

Acids at the DME.—A polarogram of 8.9 m*M* perchloric acid in 0.1*M* sodium perchlorate exhibits a small but unusual maximum on the rising portion of the wave (Fig. 2). This type of maximum is frequently encountered in DMSO. The reduction of perchloric acid is irreversible and the diffusion current constant (I) was found to be 1.3 at 30°C. The $E_{1/2}$ was determined by interpolating on the normal sigmoid shape of the wave and found to be −1.06 v. The limiting current is well defined, diffusion controlled, and proportional to the concentration of perchloric acid.

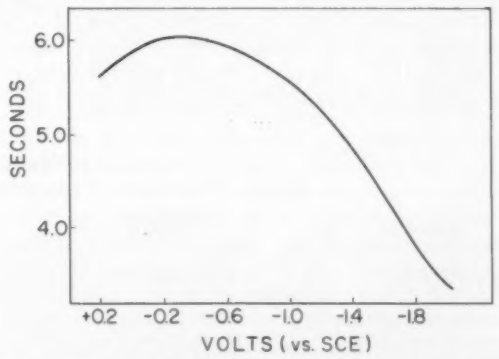

Fig. 1. Electrocapillary curve in deaerated 0.1M sodium perchlorate.

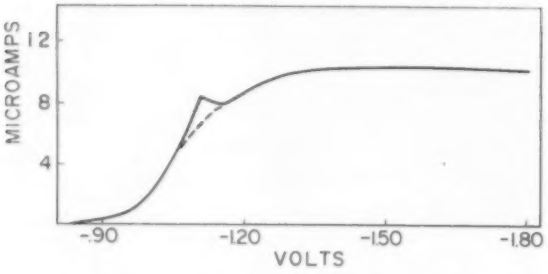

Fig. 2. Polarogram of 8.9 mM perchloric acid in 0.1M sodium perchlorate. $E_{1/2} = -1.06$ v.

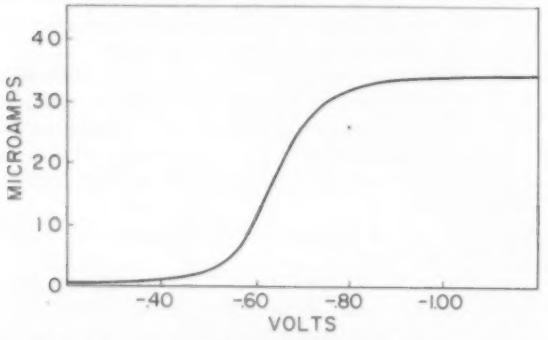

Fig. 3. Current-potential curve at RPE for 0.90 mM perchloric acid in 0.1M sodium perchlorate.

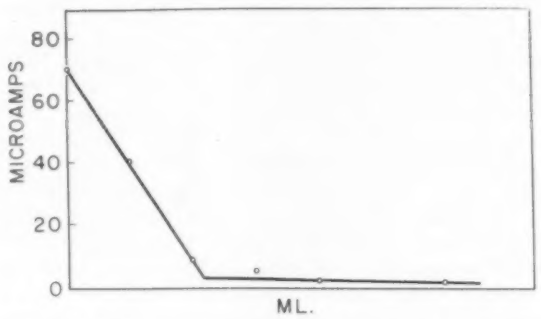

Fig. 4. Amperometric titration curve of 11 ml of 8.15 mM hydrochloric acid in 0.09M tetraethylammonium perchlorate with 0.106M trimethylbenzylammonium hydroxide at RPtE with E = −1.00 v.

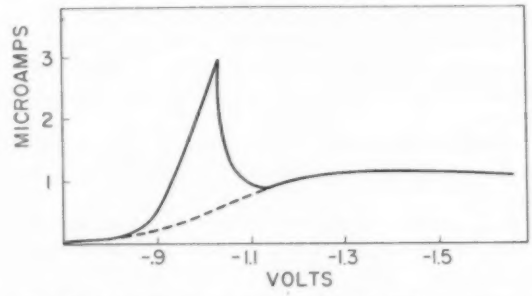

Fig. 5. Polarogram of 5 x 10^{-4}M nickel(II)perchlorate in 0.1M sodium perchlorate. $E_{1/2}$ is ca. −1. v.

The polarography of some acids is described in Table III.

Acids at RPtE.—Well-defined (Fig. 3) and identical current-potential curves in solutions of perchloric, sulfuric, and hydrochloric acid in 0.1*M* sodium perchlorate were observed at this electrode with $E_{1/2} = -0.67 \pm 0.02$ v. Use of this can be made for the amperometric titration of a dilute solution of a strong acid in DMSO. The current at $E = -1.00$ v was measured and correction made for the dilution effect. (Fig. 4)

Cobalt(II) and nickel (II).—Polarograms of the perchlorates of these metals in 0.1*M* sodium perchlorate exhibit pronounced sharp maxima even in very dilute solutions (Fig. 5). No surface-active substance has been found which completely eliminates the maxima. In the presence of 0.5% Aerosol OT, the maxima were greatly reduced but not eliminated. However, this maximum suppressor also reduces the diffusion current. By interpolation the $E_{1/2}$ of nickel was estimated to be −1.0 and that of cobalt −1.4 v. Well-defined waves without maxima were observed at the RMPE (120 rpm) which has the additional advantage over the DME that it yields much greater diffusion currents at the same concentration than does the DME. A voltammogram of 1 x 10^{-4} *M* nickel(II) (Fig. 6) showed a diffusion current of 7.5 μa, while a 5 x 10^{-4} *M* nickel(II) solution gave a diffusion current of only 1.1 μa at the DME. Apparent half-wave potentials of nickel and cobalt at the RMPE were −1.08 and −1.39 v (*vs.* SCE), respectively. The RMPE is comparable to the rotated mercury electrode of Lee (16) in which a ring of mercury in a Teflon well is rotated at high speeds. Lee has derived an equation which gives the variation of the half-wave potential with rate of voltage scanning. Delahay (19) noted that, with conventional polarographic rates of scan (0.2 v/min), the observed $E_{1/2}$ will be only a few hundredths of a volt more negative at the rotated electrode than at the DME. This also holds true for the RMPE, at which the half-wave potentials for nickel and cobalt were found of the same order of magnitude as at the DME.

Sodium.—A well-defined polarographic wave was obtained from a dilute solution of sodium perchlorate in 0.1*M* tetraethylammonium perchlorate with

Table III. Polarography of some acids in DMSO

Substance	Supporting electrolyte	$E_{1/2}$, v	Observations
Sulfuric acid	0.1*M* Et_4NClO_4	−1.06	Maximum, ill-defined; one-electron wave by comparison with $HClO_4$
Hydrogen chloride	0.1*M* Et_4NClO_4	−1.08	Maximum, one-electron wave
Sodium bisulfate	0.1*M* Et_4NClO_4	—	Sodium wave only
Tetraethylammonium bisulfate	0.5*M* Et_4NClO_4	−2.5	Drawn-out wave
Acetic acid	0.1*M* Et_4NClO_4	ca. −2.3	Intense maximum

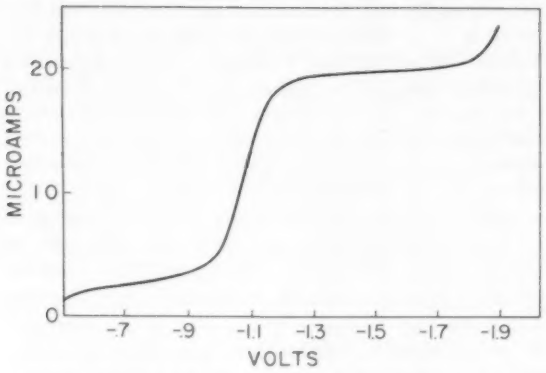

Fig. 6. Current-potential curve at the RMPE for 1 x 10^{-4}M nickel(II)perchlorate in 0.1M sodium perchlorate. Apparent $E_{1/2} = -1.08$ v.

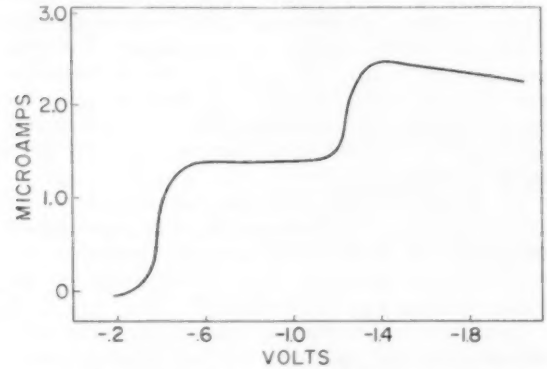

Fig. 7. Polarogram of 5.5 x 10^{-4}M benzoquinone in 0.1M tetraethylammonium perchlorate. First wave: $E_{1/2} = -0.396$ v; second wave: $E_{1/2} = -1.24$ v.

$E_{1/2} = -2.07$ v, in good agreement with the value −2.06 reported by Gutman and Schöber (12). The wave is nearly reversible.

Quinones.—In 0.1*M* tetraethylammonium perchlorate in DMSO, the polarograms of benzoquinone and quinhydrone are identical, showing two cathodic waves of unequal height. Quinhydrone shows no anodic wave. Figure 7 shows the polarogram of 5.5 x 10^{-4}*M* benzoquinone in 0.1*M* tetraethylammonium perchlorate. The $E_{1/2}$ values were −0.40 and −1.24 v, respectively. The first wave corresponds essentially to a one-electron reversible step (v.i.) while the second wave is irreversible. The current and potential on the rising portion of the first wave have been measured with the L&N Electrochemograph and Student Potentiometer. A plot of log $(i_d - i)/i$ against $-E$ (corrected for iR drop) yielded a straight line of slope 0.062 as against a theoretical slope of 0.059 for a reversible one-electron reduction at 25°C. Upon successive additions of proton donor, like 0.01*M* hydrochloric, 0.01*M* acetic acid, or water in DMSO, the second wave shifted to more positive potentials until only one wave with a maximum was observed. The height of this wave was found equal to the sum of the two waves found in the absence of acid. Duroquinone in a concentration of 3.9 x 10^{-4}*M* in 0.1*M* tetraethylammonium perchlorate also gave two waves with $E_{1/2}$ values of −0.73 and −1.53 v. The first wave is virtually reversible while the second wave is irreversible. Again, the second wave height was found less than the first and the diffusion current on the second wave decreased with increasing negative potential. A 8.3 x 10^{-4}*M* tetrachloroquinone solution in 0.1*M* tetraethylammonium perchlorate gave two waves of equal height with $E_{1/2}$ at +0.08 v and −0.73 v. Both waves are irreversible.

Oxygen.—In 0.1*M* sodium perchlorate saturated with oxygen gas, a very ill-defined wave was obtained starting at −0.65 v and reaching a diffusion current of 21 μa at −1.20 v. The wave was distorted by the appearance of a maximum and by erratic drop formation. In dilute solutions of oxygen, the maximum was eliminated and the drop time variation became only slightly erratic. Two drawn-out waves were observed with $E_{1/2}$ equal to −0.72 and −1.13 v, respectively. The ratio of wave heights, corrected for drop time effect, was 1.53. In 0.1*M* sulfuric and in a buffer composed of 0.1*M* ammonium acetate −0.1*M* acetic acid only one wave was observed with $E_{1/2}$ of −0.39 and −0.37 v, respectively.

Discussion

Polarographic studies substantiate the conclusion that DMSO is a good solvent for cations by virtue of the presence of a lone pair of electrons. This property accounts for the fact that the half-wave potentials of cobalt and nickel in DMSO (−1.4 and −1.0 v, respectively) are close to those in water (−1.4 and −1.1 v) and considerably more negative than those in acetonitrile [−0.65 and −0.33 v (2)], in which solvent nickel yields a reversible wave and cobalt a nearly reversible wave. The strong solvation of nickel and cobalt in DMSO is also evident from the intense red color of cobalt(II) perchlorate hexahydrate in dilute solutions as well as the green color of nickel(II) perchlorate hexahydrate in DMSO. Coordinated water is replaced by DMSO in this solvent. This conclusion is substantiated by the work of Cotton and Francis (9), Schlafer and Schaffernicht (20), and Meek, Straub, and Drago (21) who have isolated a large number of coordination compounds containing DMSO as ligand, including $[Co(DMSO)_6](ClO_4)_2$ and $[Ni(DMSO)_6](ClO_4)_2$. These were prepared by dissolving the hexahydrates in DMSO and removing the solvent under vacuum. In agreement with these results is the experimental fact that DMSO is a much stronger base than acetonitrile, its basic strength being of the same magnitude as that of water. Perchloric, sulfuric (K_1), and hydrochloric acids are completely dissociated in DMSO since these acids all give the same polarographic wave. In acetonitrile the latter two acids are considerably weaker than perchloric (3). The second dissociation constant of sulfuric acid is abnormally smaller in organic solvents than in water, and the same effect is observed in DMSO in which the constant was determined spectrophotometrically with indicators and found to be 8 x 10^{-10} (22). The weak acid character of the bisulfate ion accounts partly for the fact that no second wave of sulfuric acid is observed even in 0.1*M* tetraethylammonium perchlorate. In addition, the negative charge of the bisulfate ion makes it difficult for

this ion to approach the strongly negatively charged mercury drop close enough to give reduction of the proton. Only in 0.5*M* tetraethylammonium perchlorate, at which concentration the electrical double layer is greatly compressed, did the tetraethylammonium bisulfate give a drawn-out wave with an $E_{1/2}$ of about −2.5 v.

The diffusion coefficient of the hydrogen ion in solutions of strong acids was calculated from its relation with the diffusion constant: $I = 607\ n\ D^{1/2}$. At 30°C, D was found equal to 4.4×10^{-6} cm^2 sec^{-1}. From the relation:

$$D = \frac{RT}{F^2}\lambda_o$$

λ_o was found to be 17 at 30°. This compares with a value of 14.4 given for potassium ion in DMSO at 25°C (6). The Walden product, $\eta\lambda_o$, is calculated to be 8.6×10^{-4} cps cm^2 sec^{-1} while in water at 30°C it is 93.4×10^{-4} cps cm^2 sec^{-1}. The proton diffusion mechanism in DMSO is clearly different from that in water.

The polarographic behavior of quinones and oxygen provides evidence that DMSO is a much weaker acid than water and approaches acetonitrile as far as proton donating properties are concerned. The polarography of quinones in weakly acidic solvents has been studied by Wawzonek and co-workers (23) who used acetonitrile and N,N-dimethylformamide (DMF) and by Given *et al.* (24-27) who employed DMF. The results obtained in DMSO are similar to those obtained in the other two solvents. Hoijtink and co-workers (28, 18) have presented a general mechanism for the two-electron reduction of organic compounds at the DME. In a relatively acidic solvent, HS, like water, acetic acid, or formic acid, the reduction mechanism is:

$$R + e \rightarrow R^{\cdot-}$$

$$R^{\cdot-} + HS \rightarrow RH^{\cdot} + S^-$$

$$RH^{\cdot} + e \rightarrow RH^-$$

$$RH^- + HS \rightarrow RH_2 + S^-$$

Hoijtink and co-workers have shown that the electron affinity of $RH^{\cdot}$ is always greater than that of R. Therefore whenever $R^{\cdot-}$ can be protonated, the product $RH^{\cdot}$ is immediately reduced at the same potential as R. This results in a single two-electron reduction wave such as is observed for quinones in water.

In solvents like DMF, DMSO, or acetonitrile which are very weakly acidic, the reduction mechanism for quinones is:

$$R + e \rightharpoonup R^{\cdot-} \qquad \text{(first wave)}$$

$$R^{\cdot-} + e \rightharpoonup R^= \qquad \text{(second wave)}$$

$R^=$ diffuses into solution where:

$$R^= + HS \rightharpoonup RH^- + S^- \qquad \text{(slow)}$$

$$RH^- + HS \rightharpoonup RH_2 + S^- \qquad \text{(slow)}$$

The result is a double wave since $R^{\cdot-}$ is reduced at a more negative potential than R. Limited protonation of $R^{\cdot-}$ by the solvent and its disproportionation and dimerization may account for the fact that the first wave is larger than the second one. In addition, repulsion before further reduction of the negatively univalent charged radical by the electrode at potentials cathodic to the electrocapillary maximum is also possible. The addition of a proton donor to a solvent which is weakly or nonacidic may have two effects on the reduction mechanism of quinones. If $R^{\cdot-}$ reacts with the proton donor, the $RH^{\cdot}$ formed is reduced at the same potential as R, and the height of the first wave increases at the expense of the second until the latter disappears. If $R^=$ reacts with the proton donor but $R^{\cdot-}$ does not, the rate of the reaction: $R^- + HA \rightleftharpoons RH^- + A^-$ becomes potential-determining, and a shift of the second wave to more positive potentials occurs on addition of proton donor. This latter effect is that noted in DMSO.

A quinone-hydroquinone electrode will function as a reversible pH electrode only in those solvents which are acidic enough to react rapidly with the semiquinone radical. In such solvents a reversible two-electron reduction wave is observed. For the reasons mentioned, quinhydrone at the DME or at a platinum electrode does not function as a pH electrode in DMSO.

No anodic wave of hydroquinones is observed in DMSO. Wawzonek and co-workers (23) have stated that ionization of the hydroquinone is necessary before oxidation can occur. This is in accord with the mechanistic concepts of Hoijtink.

Qualitatively, the polarography of oxygen is comparable to that of quinones, and the wave has characteristics similar to that in acetonitrile (3) and N-methylacetamide (17). The difference in wave heights is undoubtedly caused by factors similar to those causing this effect in the reduction of quinones. A more detailed study of oxygen reduction is necessary before it can be stated which radicals or ions are involved.

DMSO should be useful as a solvent for organic polarography. It dissolves nearly all organic compounds and has the advantage over DMF of lower toxicity. From the analytical point of view it offers no advantages over water in the polarography of inorganic compounds.

Acknowledgment

The junior author wishes to thank the General Electric Educational and Charitable Fund for the award of an Edwin Rice, Jr., Fellowship for 1958-59. Partial financial support of this work was received from the United States Air Force Office of Scientific Research of the Air Research and Development Command, under Contract No. AF 49(638)519. Reproduction in whole or in part is permitted for any purpose of the United States Government.

Manuscript received March 3, 1961. This paper was prepared for delivery before the Detroit Meeting, Oct. 1-5, 1961.

Any discussion of this paper will appear in a Discussion Section to be published in the June 1962 JOURNAL.

REFERENCES

1. I. M. Kolthoff and J. F. Coetzee, *J. Am. Chem. Soc.*, **79**, 870 (1957).

2. I. M. Kolthoff and J. F. Coetzee, *ibid.*, 1852.
3. J. F. Coetzee and I. M. Kolthoff, *ibid.*, 6110.
4. V. Gutman and G. Schöber, *Angew. Chem.*, **70**, 98 (1958).
5. O. Bastiansen and H. Viervoll, *Acta Chem. Scand.*, **2**, 702 (1948).
6. P. G. Sears, G. R. Lester, and L. R. Dawson, *J. Phys. Chem.*, **60**, 1433 (1956).
7. R. A. Hovermale and P. G. Sears, *ibid.*, 1579.
8. T. B. Douglas, *J. Am. Chem. Soc*, **70**, 2001 (1948).
9. F. A. Cotton and R. Francis, *ibid.*, **82**, 2986 (1960).
10. R. T. Iwamoto, *Anal. Chem.*, **31**, 955 (1959).
11. A. I. Popov and D. H. Geske, *J. Am. Chem. Soc.*, **80**, 1340 (1958)
12. V. Gutman and G. Schöber, *Z. anal. Chem.*, **171**, 339 (1959).
13. G. Schöber and V. Gutman, *Monatsh.*, **90**, 897 (1959).
14. J. Kenttämaa, *Suomen Khemistilehti*, **B33**, 180 (1960).
15. I. M. Kolthoff, A. Anastasi, and B. H. Tan. *J. Am. Chem. Soc.*, **80**, 3235 (1958).
16. T. S. Lee, *ibid.*, **74**, 5001 (1952).
17. L. A. Knecht, Ph.D. Thesis, University of Minnesota (1959).
18. G. J. Hoijtink, *Rec. Trav. Chim.*, **73**, 895 (1954).
19. P. Delahay, *"New Instrumental Methods in Electrochemistry,"* Interscience Publishers, New York (1954).
20. H. L. Schlafer and W. Schaffernicht, *Angew. Chem.*, **72**, 618 (1960).
21. D. W. Meek, D. K. Straub, and R. S. Drago, *J. Am. Chem. Soc.*, **82**, 6013 (1960).
22. I. M. Kolthoff and T. B. Reddy, Results to be published elsewhere.
23. S. Wawzonek, R. Berkey, E. W. Blaha, and M. E. Runner, *This Journal*, **103**, 456 (1956).
24. P. H. Given, M. E. Peover, and J. Schoen, *J. Chem. Soc.*, **1958**, 2674.
25. P. H. Given and J. Schoen, *ibid.*, 2680.
26. P. H. Given and M. E. Peover, *ibid.*, **1960**, 385.
27. P. H. Given and M. E. Peover, *ibid.*, 394.
28. G. J. Hoijtink, J. van Schooten, E. de Boer, and W. Y. Aalbersberg, *Rec. Trav. Chim.*, **73**, 355 (1954).

The Application of an X-Y Pulsed Measuring System to Polarization Studies

I. The Hydrogen Reaction on Platinum

Clifton H. Presbrey, Jr. and Sigmund Schuldiner

United States Naval Research Laboratory, Washington, D. C.

ABSTRACT

The X-Y pulsed measuring system developed at the Naval Research Laboratory by Haas and Harris was modified and used in the study of electrochemical systems. By means of a versatile pulse generator and a modified double sweep oscilloscope, a highly flexible system giving accurate control of pulse rise time, repetition rate, length, amplitude and delay makes it possible to determine the electrokinetic parameters of fast reaction steps. An investigation of the hydrogen reaction on platinum in acid solution resulted in a quantitative separation and determination of solution resistance, charge on the double layer, and the discharge/ionization reaction step.

In the spring of 1959 the authors learned of the technique of Haas and Harris (1) for plotting instantaneous values of voltage across a circuit element against the current flowing through it at any given time after the application of a step function in the form of a variable-width pulse. The plot is developed as the locus of a series of increasing or decreasing current-voltage values at any set time after the initiation of each pulse of a recurrent series. It is displayed on an oscilloscope screen where it can be recorded photographically. This measurement and method of presentation appeared capable of providing information on electrode processes hitherto unavailable or at best available only with laborious effort. This paper presents the suggested application, describing the equipment used and the results obtained from an investigation of the hydrogen reaction on platinum. This technique has thrown new light on an old subject and promises to offer a powerful tool for electrochemical studies.

Instrumentation

Circuit design.—The original system described by Haas and Harris (1) was modified somewhat in adapting it for use with an electrolytic cell. The original circuit used a "measuring resistor" in series with the sample under test, and the voltage across this resistor was fed into the oscilloscope vertical amplifier as a measure of the sample current. A portion of the pulse applied across the sample and measuring resistor was fed into the oscilloscope horizontal amplifier (superimposed on the regular time base) as a measure of the voltage across the sample. This is true, only of course, to the degree that the measuring resistance is insignificant compared with the sample resistance. Since our electrolytic cell resistance was only a few ohms, our "measuring resistor" in this case would have to be less than 0.01 ohm for reasonable accuracy in the oscilloscope presentation. Since this value is a little difficult to work with, we reversed the signal inputs to the oscilloscope and fed

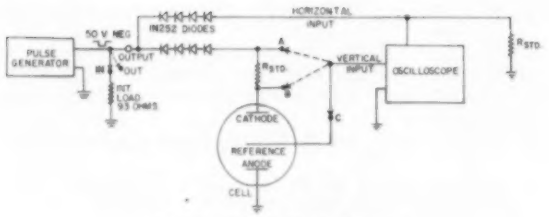

Fig. 1. Circuit block diagram

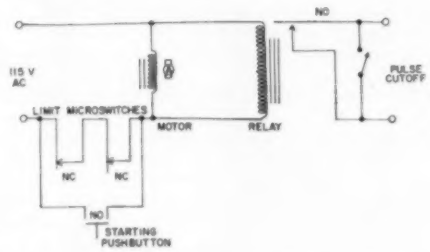

Fig. 2. Motor drive circuit for pulse generator amplitude control including pulse cutoff relay.

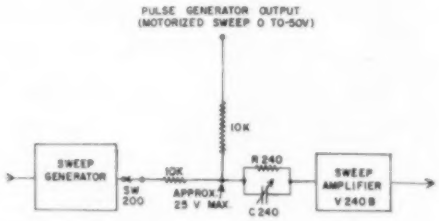

Fig. 3. Modification of Tektronix Model 535 oscilloscope sweep amplifier circuit to permit introduction of external signal.

the cell voltage directly to the vertical amplifier. The portion of the pulse fed into the horizontal amplifier then becomes a measure of the cell current if the series resistance is large compared to the cell resistance. The same accuracy would require a resistor value of 100 ohms or larger. This is easily obtained and measured.

The revised circuit diagram is given in Fig. 1. The cell current

$$I = (V_A - V_B)/R_{std}$$

where V_A and V_B are the voltages at points A and B and R_{std} is the current-setting resistor. Thus accurate values of cell current and voltage are obtained from voltage measurements made with a calibrated oscilloscope. In practice, the current calculation was made for the maximum applied pulse voltage, and thus the scale of the horizontal axis of the oscilloscope presentation was established for a given combination of maximum voltage and R_{std}. Inspection of Fig. 1 shows that the voltage developed across the entire electrolytic cell is measured at B while that of the anode alone is measured at C by means of a reference electrode. Cathode voltage is measured by taking the entire cell voltage at B while using an anode which is so large that it is unpolarized during current flow. However, in the case of either anode or cathode measurements the counter electrode is unpolarized.

Figure 1 shows four IN252 diodes connected in series with the cell circuit. These were required in order to reduce the minimum cell current to a negligible value. Thus a reduction to 10^{-5} amp was effected with a loss of only 2.4 v or 5% of the maximum available pulse amplitude.

Four more IN252 diodes are shown connected to the pulse generator output in series with a resistance to ground equal to the R_{std} value in the cell circuit. This duplication of the cell circuit equalizes the starting times of the vertical and horizontal oscilloscope input voltages, preventing the introduction of nonlinearity or heel at the start of the X-Y trace. It was necessary to switch the 93 ohm internal load into the output circuit of the pulse generator in order to avoid excessive voltage build-up (and consequent high minimum cell current) under no-signal conditions when the high forward breakdown resistance of the diodes constitutes the only output circuit load. (The output step attenuator load was not used because maximum output was required.)

A set of relay contacts was connected in the plate supply lead of the pulse-forming unit of the generator so that the maximum pulse can be removed immediately from the cell circuit at the end of an increasing-amplitude sweep. This is done as shown in Fig. 2 by connecting the relay coil in parallel with the motor driving the pulse amplitude control to give the necessary voltage sweep. A manually operated switch shorts these contacts when testing or when operating at fixed amplitudes. Also shown in Fig. 2 are the minimum and maximum limit microswitches installed on the drive mechanism and the starting pushbutton. The motor was provided with an automatically reversing clutch.

Figure 3 shows the minor modification that was made to the Model 535 Tektronix oscilloscope used for this project, to provide the horizontal amplifier input needed for our purpose. With the aid of the 5X Sweep Magnifier switch, a 50-v pulse applied at the 10,000 ohm resistor gives a horizontal displacement to the sweep of about 7½ cm. At this point we found that a positive pulse applied to the positive-going sweep caused a bad overlap in the display. Fortunately, the use of a negative pulse solved this problem, but at the same time completely reversed the presentation. "Normal" display was then restored by reversing the polarity of the connections to the oscilloscope plates.

Description of equipment.—The pulse generator used in this setup is the Model 3450 C manufactured by Electro-Pulse, Inc. It was chosen for its excellent, wide-range specifications, but it had one outstanding deficiency which had to be overcome for this application, namely, it lacked a suitable continuously variable output amplitude control. Considerable experimental work was carried out before a solution to this problem was found. The original circuit provided a constant-impedance, step-attenuator, coarse amplitude control at the output terminal supplemented by a continuously-variable fine or "fill-in" control which covered the range between attenuator steps by changing the supply voltage to the pulse-forming circuitry. It was found that the range of action of the fine control could be extended to almost 100% amplitude and still hold a usable square pulse at lengths

up to approximately 10 μsec. Longer pulses suffered deterioration due to overshoot that could be corrected at a given amplitude but not throughout the amplitude range. The cathode-follower output stage of the pulse-forming unit appeared to be a likely control point and it turned out that a potentiometer substituted for the cathode resistor provided the desired control of long pulses (10-1000 μsec) although it seriously affected the rise time of shorter pulses. Hence, for pulses up to 10 μsec the amplitude fill-in control was driven, whereas for longer pulses the potentiometer which was substituted for the cathode resistor was used.

A General Radio Model 908-P1 clock-motor dial-drive unit operating at 4 rpm was mounted on a supporting bracket and used to drive the pulse-amplitude controls. The starting pushbutton, limit microswitches, and pulse cutoff relay were also mounted on this bracket.

The oscilloscope used to display the desired plot must have a triggered sweep and a means of triggering it at any required delay time following the signal pulse. The Tektronix Model 535 is such an instrument. In addition, however, it must also have an accessible connection to the horizontal amplifier to provide the X-axis for the display. The required modification was performed as mentioned in the circuit-design section of this paper. Needless to say, any useful [illegible]e must have highly linear deflection a[illegible] insure accuracy of measurements an[illegible]

Measur[illegible]od.—The novel feature of the electrode n[illegible].ents herein described lies in the method of visual display of simultaneous values of cell current and voltage by means of a pulsed X-Y presentation. The pulse voltage appearing across the cell is applied to the normal vertical deflection system of the oscilloscope while a portion of the generator pulse voltage is applied to the horizontal deflection system, superimposed on the regular time base, as a measure of cell current under constant-current conditions. By using the sweep-delay circuits available in the specified oscilloscope, any point on the pulse can be selected as the start of the delayed sweep, the vertical deflection of the starting point corresponding to the cell voltage and the horizontal deflection corresponding to the cell current. As the applied pulse voltage is changed, a family of such curves is obtained, the locus of the starting point of the delayed sweep tracing the desired X-Y display. If the pulse voltage is swept through a suitable amplitude in a fraction of a minute, a conveniently rapid and accurate plot will be produced on the oscilloscope screen where it can be readily photographed with a Polaroid Land Camera attachment.

The development of the display on the Tektronix Model 535 oscilloscope is shown in Fig. 4. With no horizontal input applied, the pulse appears as in curve (a) when set up on the delaying sweep. The heavy-line portion shows the intensification produced by adding the main sweep, triggered after a particular delay time, *t*. Curve (b) shows the intensified portion obtained by displaying the main sweep alone. It will be noted that the vertical position of the start of the main sweep is determined by the

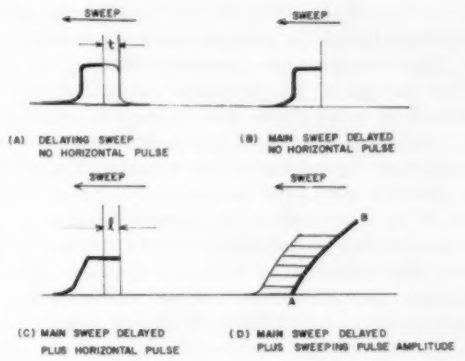

Fig. 4. Development of visual display

pulse voltage existing at the vertical amplifier input at the instant the sweep is triggered. If a portion of the pulse voltage representing current is now applied to the horizontal sweep it will cause a proportional horizontal deflection l as shown in curve (c). Since both vertical and horizontal deflection signals are derived simultaneously from the same pulse, the locus of the start of the delayed main sweep gives the desired X-Y presentation at any given time *t* after the start of the pulse. This is shown as the line ab in curve (d).

The more customary time-base plots exemplified in Fig. 10-12 are unusual in that the use of amplitude sweep permits the display of a whole series of pulses in a single presentation. This facilitates comparison of pulse shapes at different amplitudes, making it easier to locate accurately and identify significant changes resulting from the polarization reactions. It should be noted that by this means a fairly rapid pulse amplitude change can be effected and the results thereof displayed without the complication of the large displacement currents that occur when a fast, continuously changing current (sawtooth) is applied.

With the Model 3450 C pulse generator it is possible to vary the pulse-spacing time from 0.5 to 500,000 μsec. By the use of a sufficiently fast pulse repetition rate (short pulse-spacing), the cell voltage traces include and depict the polarization effects of previously applied pulses. However, these effects may also be eliminated by choice of suitably long pulse-spacing. Short pulse-spacing operation permits accurate display of systems in which the chemical composition of the electrode/solution interface is a function of the total number of coulombs applied (*e.g.*, the formation of oxide films). Long pulse-spacing operation is employed in the study of systems permitted to return to equilibrium potential before the application of the succeeding pulse (*e.g.*, overvoltage phenomena).

In practice, the pulse-repetition rate is adjusted according to the mode of operation and pulse length desired. A slow rate normally would be used with the time-base presentation in order to display the individual pulse traces. On the other hand, a fast rate is desirable for the X-Y presentation in order that the succession of E/I points may trace a smooth curve. Changing the delay time by means of the de-

lay time multiplier dial control enables the operator to explore electrode voltage-current relationships at any time of interest after the start of the pulse.

This method of measurement offers a unique combination of advantages which permits solving several problems that have plagued research workers in this field to date and which make it a powerful and promising tool for further investigation. In particular, by completing its automatic and accurate series of observations in less than 15 sec, it eliminates errors that accompany visual observation when attempting simultaneous readings on separate displays, it minimizes various drift and sample-change errors inherent in long-time measurements, and by means of a Polaroid Land Camera attachment it produces a permanent record in a very short time, permitting detailed study thereafter. Furthermore, the effect of experimental changes and adjustments can be determined quickly and accurately without recourse to tedious point readings, tabulations and plots.

Compared with the common X-Y presentation using a simple sawtooth applied voltage where a fast voltage sweep must be used in displaying a fast reaction, the X-Y pulse method achieves far greater accuracy. In the case of a fast continuous voltage sweep large displacement currents caused by the rapidly changing sawtooth applied voltage and/or by high cell capacitance will mask the desired current changes due to changing electrode parameters. Obviously, overvoltage studies by means of the sawtooth X-Y presentation are hindered by the presence of these displacement currents and by the problem of nullifying their effect. This severely limits the usefulness of the method, since there is no direct and accurate means available to dissociate the faradaic and the displacement currents in such measurements.

Hydrogen Reaction on Platinum

When a constant-current pulse is applied to a platinum electrode in a hydrogen-saturated acid solution several simultaneous events occur. If the rates of each of these events are different enough and the measuring resolution is adequate, the effect of each event can be separated during the transient period. Assuming that diffusion effects have been minimized, these events are

(i) The IR drop due to the solution resistance, R_{soln}, between the platinum and nonpolarizable counter electrode.

(ii) The charging of the double-layer capacitance, C.

(iii) The discharge/ionization reaction

$$H^+ + e^- \underset{1}{\overset{-1}{\rightleftharpoons}} H$$

(iv) The combination/dissociation reaction

$$2H \underset{2}{\overset{-2}{\rightleftharpoons}} H_2$$

The direction of steps (iii) and (iv) depends on the direction of flow of the constant-current pulse. H^+ and H represent hydrated hydrogen ions and adsorbed hydrogen atoms, respectively.

The rate of event (i) is the fastest and it depends only on the rate of formation of the current pulse because the distributive capacitance of the solution is extremely small. The second fastest event is undoubtedly the charging of the double-layer capacitance. Its rate depends on the value of C and the impedance, R_f, of faradaic reaction. Previous (2-5) steady-state overvoltage studies of the hydrogen reaction on platinum have shown that event (iv) occurs at much slower rate than that of event (iii). The exchange-current density, i_o, of the combination/dissociation reaction was found to be (4) 0.00152 amp/cm^2. This means that at equilibrium 9.5 x 10^6 H atoms/cm^2 of electrode surface are exchanged with 4.75 x 10^6 H_2 molecules per μsec. Hence for low-amplitude current pulses, which give overvoltages not far removed from the equilibrium potential, the amount of the combination/dissociation reaction which takes place during current pulses as long as 1000 μsec is negligibly small. However, at relatively high overvoltages the rate of the combination/dissociation reaction increases and may become significant at pulse durations even shorter than 1000 μsec.

From these considerations we can conclude that at low overvoltages and at pulse durations up to 1000 μsec, virtually the only chemical reaction occurring on the Pt electrode is the discharge/ionization reaction. The combination/dissociation reaction may come into effect only at high overvoltages and at the longer pulse duration times. By limiting the length of the constant-current pulses one can limit their effect to the first three events listed. The purpose of this investigation was to effect a quantitative separation of these three events.

Derivation of kinetic equations.—Using the type of equivalent circuit of the electrode/solution interface proposed by Gerischer (6) and Grahame (7), the entire circuit for a cell with a nonpolarizable counter electrode can be represented as shown in Fig. 5. Here R_{std} represents the current-setting resistance, which in practice has a value at least 100 times that of the solution resistance, R_{soln}, plus the faradaic resistance, R_f. The faradaic resistance represents impedance to

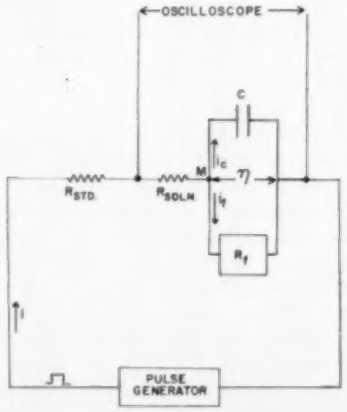

Fig. 5. Circuit analogy with nonpolarizable counter electrode

the flow of faradaic current caused by the rates of the electrochemical and chemical reactions. At the Pt electrode a constant current-density pulse, i, at the electrode/solution interface is divided into two parts, the capacitive current density, i_c, and the faradaic current density, i_f. The double-layer capacitance at the Pt electrode/solution interface is C. The part of the circuit observed on the oscilloscope screen is as indicated in Fig. 5. In this investigation, potential change is measured with reference to the equilibrium potential of the Pt/H_2 electrode in the same solution. Since the net faradaic reactions are the formation or ionization of hydrogen, the measured polarization potentials across the electrode/solution interface will be the hydrogen overvoltage, η.

When a pulse is initiated, the potential across the circuit after time t can be represented

$$E = iR_{std} + iR_{soln} + i_fR_f$$

$$E = iR_{std} + iR_{soln} + \frac{1}{C}\int i_c dt$$

Applying Kirchoff's law at point M, $i = i_c + i_f$. Solving these simultaneous equations and integrating the resulting differential equation, we obtain

$$\eta = iR_f\left\{1 - \exp\left[-\frac{t}{C}\left(\frac{1}{R_{std} + R_{soln}} + \frac{1}{R_f}\right)\right]\right\}$$

In order to obtain a constant-current pulse, $R_{std} + R_{soln} >> R_f$ and the above equation then reduces to

$$\eta = iR_f[1 - \exp(-t/R_fC)] \qquad [1]$$

Equation [1] is analogous to the common electrical equation representing the potential change across a capacitance with time. However, in the electrochemical case R_f is a function of current and time. From Eq. [1] it is apparent that as $t \to \infty$ (steady-state condition), $\eta = iR_f$. In other words, the capacitive current density, i_c, drops to zero and all of the current flow is faradaic.

Considering that (depending on the direction of current flow) the faradaic current density goes completely to the discharge of hydronium ions or to the ionization of hydrogen atoms,

$$i_{-f} = i_{-o1}\left[\frac{1-\theta_c}{1-\theta_o}\exp(-\alpha\eta_c\mathbf{F}/RT) - \frac{\theta_c}{\theta_o}\exp(1-\alpha)\eta_c\mathbf{F}/RT\right] \text{ cathodic polarization} \quad [2]$$

$$i_{+f} = i_{+o1}\left[\frac{\theta_a}{\theta_o}\exp(1-\alpha)\eta_a\mathbf{F}/RT - \frac{1-\theta_a}{1-\theta_o}\exp(-\alpha\eta_a\mathbf{F}/RT)\right] \text{ anodic polarization} \quad [3]$$

where i_{-f}, i_{-o1}, and η_c are negative numbers (net cathodic reaction), i_{+f}, i_{+o1}, and η_a are positive numbers (net anodic reaction); i_{o1} is the exchange current density, θ_o is the fraction of available surface covered with active atomic hydrogen at equilibrium, θ_c and θ_a are the fractions of available surface covered with active atomic hydrogen under cathodic and anodic current flow, respectively, α, R, T, and F are the transfer coefficient, gas constant, absolute temperature, and Faraday, respectively. Equations [2] and [3] assume that a Langmuir adsorption isotherm applies to actively adsorbed H atoms and H_2 gas and that the hydronium ion concentration in the double layer in pure acid solution is, as was shown by Frumkin (8), independent of current density.

The faradaic resistance, R_f, in Eq. [1] is equal to either η_c/i_{-f} or η_a/i_{+f}, depending on the direction of current flow. The values of i_f given in Eq. [2] and [3] give substitutes for R_f in Eq. [1]. These equations describe both transient and steady-state relationships between applied current density and the resultant overvoltage. The values of i_{o1}, θ_o, θ, and C must be determined. The exchange current density and θ_o presumably are constants. However, θ and C could be variable.

Simple solutions for the exchange current density and the double-layer capacitance can be obtained by determining the relationships between overvoltage and current density near equilibrium. From Eq. [2] and [3], when $\eta \to 0$, then $\theta \approx \theta_o$

$$i_f = i_{o1}\eta\mathbf{F}/RT$$

and

$$R_f = \eta/i_f = RT/i_{o1}\mathbf{F}$$

Here i_{o1} is a positive number and the sign of η and i_f depend on the direction of current flow.

Substituting these values in Eq. [1]

$$\eta = (iRT/i_{o1}\mathbf{F})[1 - \exp(-i_{o1}\mathbf{F}t/RTC)] \qquad [4]$$

where the sign of i depends on the direction of current flow. When t is sufficiently large, the exponential term in Eq. [4] will become negligibly small compared to unity. This means that $i_c \to 0$ and $i = i_f$, therefore

$$\eta = iRT/i_{o1}\mathbf{F} \qquad [5]$$

Equation [5] can readily be solved for i_{o1}. Equation [4] can be solved for C to give

$$C = \frac{-i_{o1}\mathbf{F}t}{2.3RT\log[1 - (i_{o1}\eta\mathbf{F}/iRT)]} \qquad [6]$$

When t is sufficiently large, $i = i_f = i_{o1}\eta\mathbf{F}/RT$ and the log term will be equal to zero. Physically this means that the double-layer capacitance has no effect on the circuit shown in Fig. 5 when this condition exists. In this case all of the current will go to the faradaic reaction. Equation [6], therefore, is meaningful only in the transient region where $i \neq i_f$. If charging of the double layer proceeds at a much faster rate than the discharge/ionization reaction, then if t is sufficiently small, $i \approx i_c$.

At sufficiently high overvoltages, the reverse reactions indicated by the second exponential terms in Eq. [2] and [3] will become negligibly small. Hence,

$$i_{-f} = i_{-o1}\frac{1-\theta_c}{1-\theta_o}\exp(-\alpha\eta_c\mathbf{F}/RT) \qquad [7]$$

$$i_{+f} = i_{+o1}\frac{\theta_a}{\theta_o}\exp(1-\alpha)\eta_a\mathbf{F}/RT \qquad [8]$$

Overvoltages divided by these values of i_f can be substituted for R_f values in Eq. [1]. At sufficiently large t we obtain, when $\alpha = \frac{1}{2}$ and $T = 301°K$,

$$\eta_c = -0.12 \log \left[\frac{i_{-f}}{i_{-os}} \cdot \frac{1-\theta_o}{1-\theta_c} \right] \quad [9]$$

$$\eta_a = 0.12 \log \left[\frac{i_{+f}}{i_{+os}} \cdot \frac{\theta_o}{\theta_a} \right] \quad [10]$$

Experimental Technique and Observations

The Teflon cell (9) and the purification techniques (2, 3) were the same as used previously. The platinum (99.99%) bead electrode had an apparent area of 0.1 cm² and was immersed in 1M sulfuric acid solution stirred with purified hydrogen flowing at a rate of at least 400 ml/min. (In this paper all areas are in terms of apparent areas.) The ambient temperature was 28° ± 1°C. After activating the Pt electrode by anodic polarization at about 5 ma for a few minutes and allowing the Pt/H_2 equilibrium potential to be reached, the cell was connected to the pulse circuit as shown in Fig. 1. The counter electrode for either anodic or cathodic measurement was so large that its polarization was negligible.

The standard resistance, R_{std}, used in these measurements was 300 ohms. When added to the solution resistance, R_{soln} of 2.5 to 3 ohms, this value of R_{std} provides a virtually linear current to pulse amplitude relationship because the faradaic resistance, R_f, is too small to affect the total circuit resistance appreciably even though it does vary with current density. While such variations or electrode polarization losses thus cause less than 1% change in the pulse current, giving "constant-current" operation, the change in cell voltage resulting therefrom is great enough to be displayed readily on an oscilloscope screen. The current density-voltage curves obtained in this manner were enlarged by projection with a slide projector and traced on graph paper. Current density-voltage measurements were made also from the original photographs using a Jones and Lamson Comparator and Measuring machine. With this machine, measurements can be made with a precision of 0.0001 in.

The maximum pulse amplitude was 54 v. Thus the pulse sweep gave cell current pulses ranging from zero to approximately 180 ma in about 13 sec. The repetition rate of the pulses was set so that enough time elapsed between them for the working Pt electrode to return essentially to its equilibrium potential before the initiation of a succeeding pulse. For example, the pulse-spacing time for cathodically polarized Pt was normally 5×10^5 μsec at pulse lengths from 0.2 to 8 μsec and 5×10^4 μsec at pulse lengths from 10 to 1000 μsec. For anodic polarization the minimum pulse spacing for the short pulses was 1×10^4 μsec; for pulses from 1 to 10 μsec in length the pulse spacing was increased to at least 5×10^4 μsec; and for pulses above 10 μsec, the pulse spacing ranged from 1×10^5 to the maximum available pulse-spacing time of 5×10^5 μsec. Anodic polarization at maximum current using 300 μsec pulses evidently resulted in the formation of some oxides or oxygen, and there was not enough time between pulses for a complete return to the hydrogen equilibrium potential. This was not a problem, however, because these were limiting anodic current densities.

The oscilloscope calibration is checked carefully from time to time. The accuracy of the over-all X-Y pulsed system is also checked periodically by means of a synthetic cell circuit made of calibrated components.

Experimental Results

The solution resistance was determined from the initial slope of current density-voltage curves at sweep-delay times (time after current pulses were initiated) from 0.2 to 0.5 μsec. These values checked very closely, and no evidence of a significant amount of electrode polarization was found. The R_{soln} for anode and cathode measurements using the circuit shown in Fig. 1 was 2.55 and 3.03 ohms, respectively. Current density-voltage curves at all sweep-delay times were then corrected for the IR drop resulting from these solution resistances. The corrected curves then represented activation overvoltage, η. Faradaic reactions were separated from effects due to charging the double layer by plotting the slopes of current density-overvoltage curves as close as possible to the equilibrium potential. Figure 6 shows the relationship between these slopes, $(i/\eta)_{\eta \to 0}$, and the sweep-delay time t. This plot shows that within the first 10 μsec after the current pulses were initiated, essentially all of the current goes to charging the double layer. After 10 μsec, $(i/\eta)_{\eta \to 0}$ is independent of time, as predicted by Eq. [5]. This gives a sharp separation between the capacitive and the faradaic current densities. Hence,

$$i \simeq i_c \text{ (in first 10 } \mu\text{sec)}$$

$$i = i_f \text{ (after 10 } \mu\text{sec)}$$

Within the first 10 μsec the double-layer capacitance can be determined from Eq. [6]. After 10 μsec, however, $(\partial\eta/\partial t)_i = 0$; hence $i_c = 0$ and the exponential term in Eq. [4] and the log term in Eq. [6] will be reduced to zero. The fact that the capacitive part (first 10 μsec) of the plot shown in Fig. 6 rises so sharply means that an exact determination of the double-layer capacitance would be very difficult. Calculated C values averaged roughly about 100 μfd/cm².

From the horizontal portion of the curve shown in Fig. 6 we can calculate the exchange current density for the discharge/ionization reaction from Eq. [5]. Calculations give $i_o = 0.13 \pm 0.02$ amp/cm². This value is almost 100 times that for the combination/ionization reaction (3). The fact that i/η is inde-

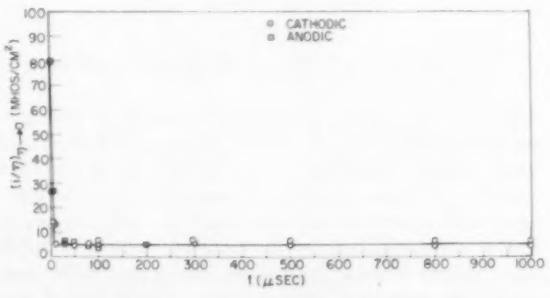

Fig. 6. Slopes of current density-overvoltage curves near equilibrium potential.

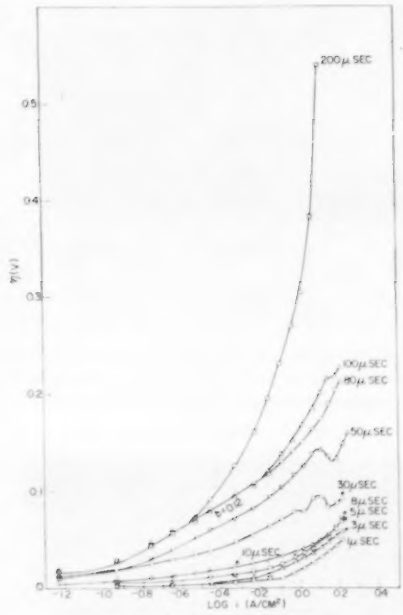

Fig. 7. Anodic Tafel relations

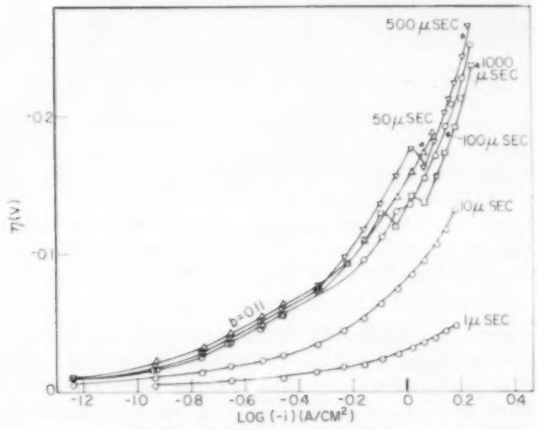

Fig. 8. Cathodic Tafel relations

pendent of t also shows that significant concentration changes of reactants and products do not occur.

Plots of log i *vs.* η for some typical results are shown in Fig. 7 and 8. The 1-10 μsec curves show primarily log i_c *vs.* η relationships for the charging of the double layer. At times longer than 10 μsec after initiation of the pulses, the curves represent essentially i_f *vs.* η relations for the discharge/ionization reaction. The fact that sections of these curves obey a Tafel relation and have slopes close to 0.12 v verifies, as is shown in Eq. [9] and [10], that the discharge/ionization reaction is being observed in this range. Extrapolation of the linear Tafel curves to zero η gives the i_{o1} values shown in Table I. These values indicate that for the cathodic case and for the 30 μsec anodic case, the i_{o1} value is practically the same as that calculated from Eq. [5] and Fig. 6. The anodic 50-200 μsec curves show evidence of a smaller i_{o1} value. These i_{o1} values are about the same as those found by Dolin and Ershler (10) who determined that $i_{o1} = 0.088$ amp/cm².

Table I. Cathodic and anodic exchange current densities

Cathodic Sweep delay time, μsec	i_{o1}, amp/cm²	Anodic Sweep delay time, μsec	i_{o1} amp/cm²
30	−0.096	30	0.148
50	−0.096	50	0.0891
80	−0.107	80	0.0708
100	−0.107	100	0.0708
300	−0.107	200	0.0708
500	−0.105		
800	−0.114		
1000	−0.107		

Equations [9] and [10] also indicate that the ratios $(1-\theta_o)/(1-\theta_c)$ and θ_o/θ_a are virtually constant in the Tafel range. The calculated value of these ratios is 1.07 and 1.8, respectively, in the linear Tafel regions where η is essentially independent of time at constant current density. At higher current densities the curves deviate from Tafel behavior. This is due to two effects. The first is that the $(1-\theta_o)/(1-\theta_c)$ and θ_o/θ_a ratios are no longer constant because of relatively large changes in surface areas covered with atomic hydrogen. The second is that at long times after the initiation of current pulses the effects of the slower combination/dissociation reaction will in respect to cathodic or anodic polarization lower or raise the H atom concentration. The overshoots observed on these curves at large t and i reflect the interplay at relatively high overvoltages, of large changes in surface concentration of H atoms. This is caused by the effects of the combination/dissociation reaction and its tendency to lower the overvoltage strongly by changing the surface atom concentrations in the direction of the equilibrium values. Figure 9 presents a picture from an actual cathodic run showing two overshoots. The sweep-delay time in this photograph was 1000 μsec.

Discussion

The evidence that the $(1-\theta_o)/(1-\theta_c)$ and θ_o/θ_a ratios are independent of current density in the Tafel regions shown in Fig. 7 and 8 is rather surprising, especially at the longer sweep-delay times. This is because under these conditions an appreciable amount of atomic hydrogen is either deposited or re-

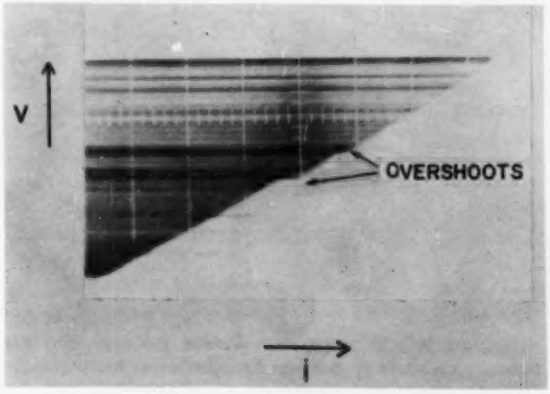

Fig. 9. Cathodic current-voltage curves with pulse sweep delay time of 1000 μsec; pulse length = 2000 μsec; pulse spacing = 0.5 x 10^5 μsec; each space on ordinate = 0.2 v; each space on abscissa = 0.267 amp/cm².

moved from the platinum electrode. Although the equilibrium ratio (hydrogen atom/Pt surface atom) is about unity, as shown by Ershler (11), Eucken and Weblus (12), Breiter, Knorr, and Völkl (13) and further confirmed in this work by calculating the amount of hydrogen removed at the limiting anodic current density (see Fig. 7), we conclude that the number of hydrogen atoms which are active enough to enter the exchange reaction at equilibrium must be very small. After these active hydrogen atoms are removed by ionization, a higher potential is required to remove the more strongly bonded hydrogen atoms. These tightly bonded atoms may be associated with the surface and/or be absorbed in a surface layer in a way analogous to the formation of a Pd-H alloy. In any case, it is apparent that there is a tendency for each effective atom concentration to remain fairly constant in the Tafel ranges. Beyond the Tafel ranges, the effective surface coverage does appear to change significantly, and the effect of the combination/dissociation reaction also comes into play.

Because of the constancy of the ratios $(1-\theta_*)/(1-\theta_*)$ and θ_*/θ_* in the Tafel region one might conclude that the discharge/ionization reaction is followed by a much faster combination/dissociation reaction. This would explain both the Tafel slope of 0.12 and the constant value of θ. The weakness of this argument, however, is obvious for at least two reasons. The first is the fact that the Tafel regions of 0.12 slope are too limited. If the combination/dissociation reaction were very fast, then one would certainly expect that the Tafel slope would extend to the maximum current densities used. The second reason for disallowing the fast combination/dissociation mechanism can be seen in Fig. 10 and 11. These pictures show the relation between overvoltage and time when a series of ever-increasing constant-current pulses are applied to a working Pt electrode. Here one can see that the overvoltage build-up when the pulse is turned on is much faster than the overvoltage decay when the pulse is shut off. This means that the spontaneous open-circuit return to equilibrium is much slower than the displacement from equilibrium when current is applied. If a combination/dissociation reaction or a diffusion mechanism were involved, then the rates of these steps would be independent of current switch. The most likely reason for the lag in polarization decay is that hydrogen atoms which are formed or ionized during current flow must then be removed by formation of molecular hydrogen or replaced with hydrogen atoms from dissociation of molecular hydrogen. If this combination/dissociation reaction is so slow that it does not occur appreciably in the pulse times used, then the observed lag in overvoltage decay should take place. It should also be noted that polarization decay times for the case of anodic polarization shown in Fig. 10 are much slower than for the case of cathodic polarization shown in Fig. 11. An explanation of this which also fits in with the constancy of the $(1-\theta_*)/(1-\theta_*)$ and θ_*/θ_* ratios in the Tafel ranges is that after most of the active hydrogen atoms are removed by ionization the potential rises and tightly bonded hydrogen atoms become active and are ionized. When the current is shut off at the end of the pulse, the rate of formation of these tightly bonded or dissolved H

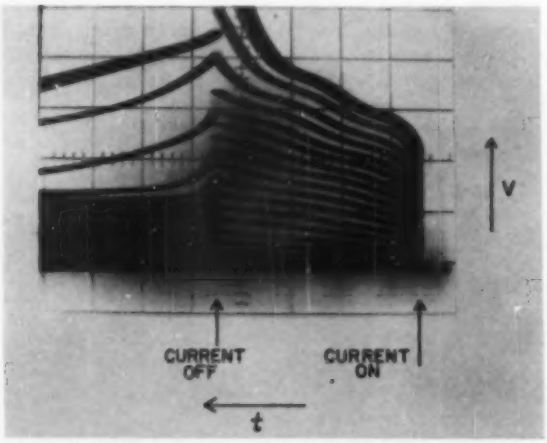

Fig. 10. Anodic polarization with a series of 300 μsec pulses; each space on ordinate = 0.2 v; pulse spacing = 5 x 10^5 μsec; maximum current pulse = 1.8 amp/cm². Note: The direction of the time scale on this and succeeding oscilloscope traces is reversed from its normal direction. Zero time is on the right hand side of the pulses. The time scale reads from right to left.

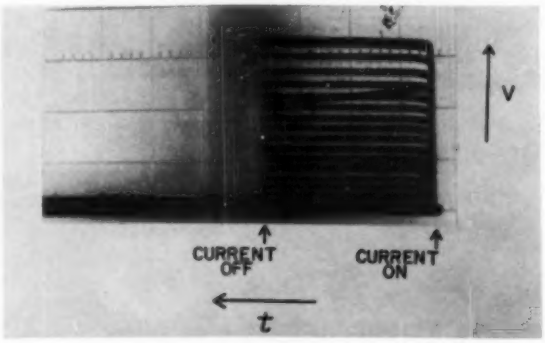

Fig. 11. Cathodic polarization with series of 1000 μsec pulses; each space on ordinate = 0.2 v; pulse spacing = 5 x 10^5 μsec; maximum current density = 1.8 amp/cm².

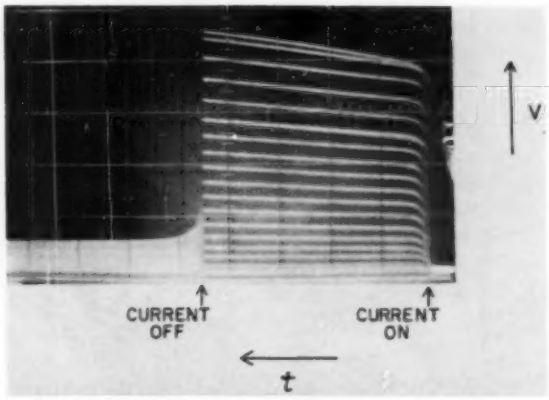

Fig. 12. Anodic polarization with series of 20 μsec pulses; each space on ordinate = 0.1 v; pulse spacing = 5 x 10^5 μsec; maximum current pulse = 1.8 amp/cm².

atoms is slower than the dissociation of hydrogen molecules. In the case of cathodic polarization the excess hydrogen atoms become tightly bonded under the potential field applied, and when the current is removed these excess hydrogen atoms are quickly desorbed as hydrogen molecules are formed. These effects also support the analogy to the Pd-H alloy previously mentioned. It has been shown in several investigations (14) that, although the spontaneous absorption of hydrogen in palladium is slower than its desorption, the desorption can be accelerated and H atoms can be removed quantitatively by anodic polarization (15).

Close examination of the cathodic polarizing pulses shown in Fig. 11 will disclose traces which slope downward. These pulses have occurred after breaking the plate and screen circuits of the pulse generator output stage with the cutoff relay contacts at the end of an increasing-amplitude sweep. The high power output tubes do not cease functioning quickly enough to avoid this effect. The contacts were then transferred to the pulse-forming stage as explained in the circuit design section of this paper, where the pulse was removed at the source. This arrangement was effective and subsequent photographs do not show such traces.

The wave effect observed for the current pulses for a Pt anode shown in Fig. 10 was first observed by Slygin and Frumkin (16) and later by Breiter, Knorr, and Völkl (13) in curves showing anodic charging in sulfuric acid solutions. An adsorption capacitance, C_a, can be associated with these waves. Thus when $d\eta/dt$ is large, C_a will be relatively small; and when $d\eta/dt$ reaches a minimum as it does in the arrest or plateau between each wave, C_a will reach a maximum. Such capacitance peaks were observed by Dolin and Ershler (10), Eucken and Weblus (12), and Breiter, Kammermaier, and Knorr (17) by means of a-c impedance measurements. The effect of these capacitance peaks can also be seen in the curves shown in Fig. 7. The 80, 100 and 200 μsec curves coincide in the Tafel region because these times fall on the first plateau (from the right-hand side) where there is little change in η with time. The 30 and 50 μsec curves lie in the region where η is strongly dependent on time.

The fraction, θ, of available surface covered with adsorbed hydrogen atoms equals the number of H atoms/cm^2 divided by the number of available sites/cm^2. A previous study (2) indicated that the surface roughness factor for a Pt electrode prepared in the manner used in this investigation was about 2. Assuming that the number of available sites is equal to the number of Pt atoms on the surface, then we can estimate that the number of available sites per apparent cm^2 on the Pt electrode is close to 2×10^{15}. For the case of anodic polarization

$$\theta_a = \theta_o - \frac{\text{number of H atoms ionized/cm}^2}{2 \times 10^{15}\ \text{sites/cm}^2}$$

Since the number of atoms ionized is equal to $qN_A/\mathbf{F}$, where q is the number of coulombs/cm$_2$ and N_A is Avogadro's number,

$$dq/d\theta_a = -2 \times 10^{15}\mathbf{F}/N_A$$

Hence

$$C_a = dq/d\eta_a = \frac{-2 \times 10^{15}\mathbf{F}}{N_A} \frac{d\theta_a}{d\eta_a} \qquad [11]$$

On the basis of a Langmuir adsorption isotherm, we can define the equilibrium potential, E_{eq}, of a hydrogen electrode as

$$E_{eq} = E^\circ + (RT/\mathbf{F}) \ln [\theta_o/(1-\theta_o)]$$

Hence at overvoltages near equilibrium, the following approximate relationship applies:

$$\eta = (RT/\mathbf{F}) \ln \left[\frac{\theta_o}{1-\theta_o} \cdot \frac{1-\theta_a}{\theta_a}\right]$$

Differentiating this expression with respect to η and θ_a, first allowing $\eta \to 0$, then $\theta_a \to \theta_o$, we obtain

$$(d\eta/d\theta_a)_{\eta \to 0} = -RT/\mathbf{F}(\theta_o - \theta_o^2) \qquad [12]$$

Combining Eq. [11] and [12],

$$\theta_o - \theta_o^2 = RTN_AC_a/2 \times 10^{15}\mathbf{F}^2 \qquad [13]$$

At 28°C,

$$\theta_o - \theta_o^2 = 80.83\ C_a \qquad [13a]$$

The adsorption capacitance was determined near equilibrium by means of voltage-time traces for short current pulses. The calculation of C_a in this region was simple because a linear relation between overvoltage and time was observed experimentally (see Fig. 12 for an example of this). Thus $C_a = i\Delta t/\Delta\eta$. The average value of C_a found under these conditions was 530 μfd/cm^2. The calculated θ_a values are 0.955 ± 0.008 and 0.046 ± 0.005. Since Eq. [13] gives two solutions for θ_o, it is necessary to determine which solution is physically the more reasonable one. Eucken and Weblus (12) showed that maximum capacitance was obtained, using a relationship equivalent to Eq. [13], when $\theta_o = 0.5$. From this one could reason that since in Eq. [13] the maximum calculated $C_a = 3100$ μfd/cm^2, and since C_a, as shown in Fig. 10, increases as the overvoltage reaches its first plateau, then θ_o must have a value greater than 0.5 and indeed must be nearly equal to unity. This viewpoint has been accepted by Breiter and coworkers (13, 17, 18). There are strong indications, however, that this interpretation of θ_o may not be tenable. In the first place, Eq. [13] is only valid when $\eta \to 0$ and $\theta_a \to \theta_o$, that is, in the vicinity of equilibrium. Eucken and Weblus use this relationship in a potential region far enough removed from equilibrium to have doubtful validity. However, the trend is probably correct. Second, assume that θ_o at equilibrium is equal to 0.046 and also that a second θ_o of higher value occurs at the first plateau above the equilibrium potential, This may impress one initially as unreasonable, but it will be shown that it does happen. Then using the same line of reasoning followed by Eucken and Weblus, one would conclude that 0.046 is the correct value for θ_o.

The experimental results obtained in this investigation indicate that for the 80-200 μsec curves θ_o/θ_a apparently remains constant in the Tafel region. However, it should be remembered that the anodic

80-200 μsec Tafel slopes of Fig. 7 primarily represent ionization of H atoms in the region of the first plateau beyond the equilibrium potential, as confirmed in Fig. 10 and by i_{-a1} values in Table I. Figure 10 shows that the active hydrogen atoms at the equilibrium potential are removed by the application of a relatively small charge and that the potential rises to the first plateau where a significantly larger number of more strongly bonded H atoms are activated. This means that the θ_a value at this plateau is higher than the θ_a value at zero voltage. As this and other work (12, 13, 17) have shown, the amount of atomic hydrogen removed with anodic polarization is very close to one atomic layer. This again would seem to imply that $\theta_a \sim 1$. However, our results show that with cathodic polarization, enough hydrogen atoms can be deposited on the surface to give just about another complete atomic layer before evidence of removal by combination is apparent. This means that up to two atomic layers may be adsorbed on the surface and normal Tafel behavior for the discharge mechanism will still be observed. It is difficult to comprehend the meaning of a double atomic layer in terms of the Tafel relation unless something like a Pt-H alloy is formed which has H atoms adsorbed on its surface.

Evidence indicating that hydrogen exists in both a weakly and a strongly bonded state on platinum has been shown by several workers (19-21). Pliskin and Eischens (21) concluded from their infrared measurements that the bonding of the two species of H atoms could be represented as:

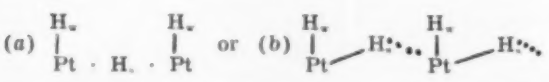

Here the bonding of H_w (weakly bonded H atoms) to Pt is essentially covalent while H_s (strongly bonded H atoms) are bonded between two Pt atoms by (*a*) single electron bonds or else by configuration (*b*) where the dotted lines represent a modifying effect. These authors further concluded that the strongly and weakly bonded forms do not become equivalent after adsorption of the weakly bonded form. The factors which produce strongly bonded H atoms are related to the geometry of the Pt atoms and are not eliminated by adsorbing a second H atom.

Sachtler and Dorgelo (22) found that hydrogen is absorbed in the lattice of a thin Pt film at temperatures as low as −210°C. Baranowski and co-workers (23) showed that for cathodically polarized poisoned nickel wires there was a high degree of saturation with absorbed hydrogen in a relatively thin superficial layer. In fact, the atom ratio of H/Ni in this thin layer corresponded to about 0.7, which just about corresponded to the number of positive holes per atom of nickel. This indicated that the outer layer of nickel behaved in a way similar to the Pd-H system. It is conceivable that platinum could in like manner have a saturated layer of Pt-H alloy. Recently, Franklin and Cooke (24) also indicated that hydrogen is absorbed in Pt but as H_s^+ rather than as protons in a Pt-H alloy as is postulated here.

This explanation is further substantiated by the evidence shown in Fig. 10. The change in overvoltage with the number of coulombs added to the system indicates that ionization of hydrogen takes place in three separate steps. The first occurs at the equilibrium potential. Here, active H atoms are in rapid equilibrium with hydrogen gas and hydronium ions in solution. With anodic polarization, at the maximum current density of 1.8 amp/cm^2, the overvoltage quickly rises to a plateau with $\eta \sim 0.12$ v positive with reference to the equilibrium potential. The total number of atoms ionized when this first plateau is reached is about 0.5×10^{15}, which means that about ¼ of the total amount of hydrogen associated with the platinum is removed. The potential at the first plateau is high enough so that other differently associated H atoms can be ionized. Between the first and second plateaus, at an η value of about 0.26 v, approximately 1×10^{15} H atoms are ionized. This represents about ½ of the total amount of hydrogen associated with the Pt at equilibrium. From the second plateau to the limiting current density, approximately 0.4×10^{15} H atoms are ionized. This represents about 1/5 of the total amount of hydrogen associated with the Pt at equilibrium. The fact that only a small part of the hydrogen associated with the surface at equilibrium can be ionized near the equilibrium potential indicates that the effective θ_a is closer to 0.046 than 0.96. If this were not so, one would expect only one plateau (or gradient) near the equilibrium potential, and all of the H atoms would be reactive at zero overvoltage. The anodic waves show, in effect, a series of three potentials at which hydrogen differently associated with the Pt can react. In fact(Eucken and Weblus (12) concluded that the exchange current density for each of these potential regions would be different because of the difference in adsorptive energies of the H atoms. This is confirmed by the values of i_{a1} shown in Table I. These cathodic i_{-a1} values plus the curves in Fig. 8 show that the same mechanism and i_{-a1} values hold from zero overvoltage to the end of the Tafel slope. The 30 μsec anodic i_{-a1} value is about the same as the equilibrium value. However, the 50-200 μsec i_{-a1} values are significantly smaller and indicate that in the region of the first plateau the reaction rate constant is smaller than the equilibrium value. It is also evident that different θ_a values are associated with the three different anodic potential regions and that the θ_a value at equilibrium would be closer to 0.046 than 0.96.

An alternate explanation for θ_a behavior is also possible. θ_a, as used in the kinetic equations, may not be constant at some potential sufficiently far removed from the equilibrium potential, but may be a function of the degree of surface coverage. If the surface coverage is reduced by anodic polarization, θ_a may decrease because of the increase in the heat of adsorption of hydrogen atoms. The ratio θ_a/θ_a would remain effectively constant in the Tafel region up to a potential of approximately 0.12 v, which is the value of the first potential plateau (maximum current density) shown in Fig. 10. A similar argument would hold for the Tafel region exhibited by cathodic polarization. A strong argument against this

model is that anodic polarization shows three polarization regions. If θ_o were dependent on surface coverage, one would normally expect a continuous variation from equilibrium to the limiting current density, which would obey a single adsorption isotherm such as a Temkin isotherm. The three polarization regions appear to be more indicative of three different substances (differently associated hydrogen with Pt) reacting at their respective oxidation potentials. With cathodic polarization, polarization waves do not occur because the hydronium ions at the interface are equivalent to one another. However, even in the cathodic region additional hydrogen can be associated with the surface under an increased overvoltage, as it does in the two-phase α and β Pd-H alloy in which an increased amount of hydrogen does not effectively change the surface concentration or potential. This theory would also explain the overshoots observed in Fig. 9 which reveal a decrease in η with time. These pulses may reflect a saturation of the Pt-H alloy with atomic hydrogen from repeated pulsing. The decay of the Pt-H alloy may not be complete in the time interval between pulses, but this would have a negligible effect on the initial potential before each new, higher-amplitude current pulse is applied. When additional current pulses are applied, oversaturation of the alloy may trigger a rapid combination reaction which would lower both the surface and the alloyed atomic hydrogen.

In this investigation of the hydrogen reaction on platinum we have been able to resolve the effects of the resistance overvoltage, the charging of the double layer, and the discharge/ionization reaction. In the time interval between approximately 10 and 1000 μsec from the start of a current pulse, the discharge/ionization reaction remains effectively in a dynamic steady state. That is to say, the times in this range are too long for the double-layer capacitive current density to be significant and too short for the combination/dissociation reaction to occur at an appreciable rate. This study has indicated the effectiveness of the X-Y pulse technique, even at a comparatively early stage of development. With more experience and improved equipment, one should be able to extend the sweep-delay times in both directions. It would certainly be important in the study of very fast reactions to be able to obtain current density-overvoltage sweeps at times as short as 0.05 μsec after the current pulses are initiated. An increase in the maximum available amplitude of the constant-current pulses would be useful. These desiderata demand an even more versatile pulse generator and oscilloscope than those used. Instruments such as these are already on the market and further work on this project is planned as soon as the most appropriate models can be selected and obtained and used.

Acknowledgments

The authors are indebted to Mr. F. H. Harris and Dr. G. A. Haas of the Electronics Division of the U. S. Naval Research Laboratory for their advice concerning instrumentation.

Manuscript received March 3, 1961; revised manuscript received July 13, 1961.

Any discussion of this paper will appear in a Discussion Section to be published in the June 1962 JOURNAL.

REFERENCES

1. G. A. Haas and F. H. Harris, *Rev. Sci. Instr.*, **30**, 623 (1959).
2. S. Schuldiner, *This Journal*, **99**, 488 (1952).
3. S. Schuldiner, *ibid.*, **101**, 426 (1954).
4. S. Schuldiner, *ibid.*, **106**, 891 (1959).
5. S. Schuldiner, *ibid.*, **108**, 384 (1961).
6. H. Gerischer, *Z. Phys. Chem.*, **198**, 286 (1951).
7. D. C. Grahame, *This Journal*, **99**, 370C (1952).
8. A. N. Frumkin, *Acta Physicochim. USSR*, **6**, 502 (1937).
9. S. Schuldiner, *This Journal*, **107**, 452 (1960).
10. P. Dolin and B. Ershler, *Acta Physicochim. USSR*, **13**, 747 (1940).
11. B. Ershler, *ibid.*, **7**, 327 (1937).
12. A. Eucken and B. Weblus, *Z. Elektrochem.*, **55**, 114 (1951).
13. M. Breiter, C. A. Knorr, and W. Völkl, *ibid.*, **59**, 681 (1955).
14. D. P. Smith, "Hydrogen in Metals," pp. 84-119, University of Chicago Press, Chicago (1948).
15. J. P. Hoare and S. Schuldiner, *J. Phys. Chem.*, **61**, 399 (1957).
16. A. Slygin and A. Frumkin, *Acta Physicochim. USSR*, **3**, 791 (1935).
17. M. Breiter, H. Kammermaier, and C. A. Knorr, *Z. Elektrochem.*, **60**, 37 (1956).
18. M. Breiter, Mitteilungsblatt der Chem., p. 11, Gesellschaft D.D.R. (1959).
19. J. C. P. Mignolet, *J. Chim. Phys.*, **54**, 19 (1957).
20. R. Suhrmann, G. Wedler, and H. Gentsch, *Z. Phys. Chem.*, **17**, 350 (1958).
21. W. A. Pliskin and R. P. Eischens, *ibid.*, **24**, 11 (1960).
22. W. M. H. Sachtler and G. J. H. Dorgelo, *ibid.*, **25**, 69 (1960).
23. B. Baranowski, Z. Szlarska-Smialowska, and M. Smialowski, *Bull. Acad. Polon. Sci.*, **6**, 179 (1958); B. Baranowski and M. Smialowski, *ibid.*, **7**, 663 (1959); B. Baranowski and M. Smialowski, *Phys. and Chem. of Solids*, **12**, 206 (1960).
24. T. C. Franklin and S. L. Cooke, Jr., *This Journal*, **107**, 556 (1960).

Technical Notes

Effects of Saccharin on the Structural and Magnetic Properties of Iron-Nickel Films

R. S. Smith, L. E. Godycki, and J. C. Lloyd

International Business Machines Corporation, San Jose, California

The coercive force H_c of electrodeposited iron-nickel films is reduced when small amounts of saccharin[1] are dissolved in the plating bath (1). It is the purpose of this paper to report the influence of saccharin on those properties of the film which are expected to influence H_c. The properties investigated include surface roughness (2, 3), crystal size (4), strain (5), and gas content. The influence of these structural properties on H_c is discussed in the literature.

Thon (6) reported that the addition of compounds other than saccharin[2] increased gas content in the films. Since much of the gas was N_2, he concluded that this increase was due to direct absorption of the organic compound into the film although occluded hydrogen was reduced.

In view of the influence of the saccharin type of compounds on gas content reported by Thon, polarographic measurements were made to determine the influence of saccharin on the hydrogen reduction potential.

Experimental Techniques

The films were electroplated onto a substrate of evaporated nickel (400Å) on glass. Except for the gas occlusion measurements, the Fe-Ni ratio of the plated films was 1:4. They were plated from the following bath: $NiSO_4 \cdot 6H_2O$, 218 g/l; $FeSO_4 \cdot 6H_2O$, 4 g/l; H_3BO_3, 25g/l; NaCl, 9.7g/l, at 20°C and a current density of 50 ma/in.^{2}, pH = 3.1. Saccharin was added as a variable.

To measure gas occlusion, heavy films were required. Such films would not adhere readily to the glass substrate unless iron was omitted from the plating bath. This makes no difference in the interpretation of results, however, since it was established by preliminary measurements that the presence of 20% Fe would have little influence on the ability of saccharin to control the amount of occluded gas.

Gas content was measured by moving the film sample into the heated zone of an evacuated quartz tube. The sample had been initially "dried out" at 100°C as suggested by Thon. This temperature is considerably below the temperature at which massive quantities of absorbed gases are evolved. Before inserting the film, the tube was outgassed at 800°C. The rise in pressure due to outgassing the sample film was measured with an oil manometer. The temperature was maintained at 900°C for an hour to ensure that the film was completely outgassed. H_c was measured at 60 cycles.

Crystal sizes were measured using x-ray diffraction techniques (7). The technique separates strain from crystal size effects on the x-ray line breadth.

The electron micrograph replicas were evaporated silicon monoxide shadowed with chromium.[3] Victawet was initially evaporated onto the film as a releasing agent for the silica replica.

Polarographic measurements were made with a Sargent polarograph equipped with a dropping mercury electrode.

Experimental Results

The influence on H_c of saccharin in the plating bath is illustrated in Fig. 1. The reduction of H_c by a factor of five cannot be explained by the relatively insignificant changes in the Fe-Ni ratio and thickness resulting from the additions of saccharin.

M:Ni atomic ratios computed with measurements taken from the gas occlusion studies are listed below: (M represents the gas atom)

Samples plated without saccharin: M:Ni 1:230
Samples plated with saccharin:
840 mg/l M:Ni 1:800

[3] Obtained from Ladd Research Industries Inc., Burlington, Vermont.

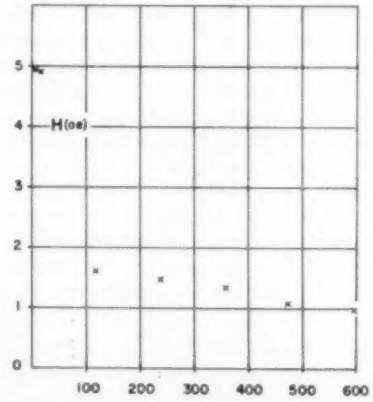

Fig. 1. Influence of saccharin on H_c

[1] The term saccharin as used here refers to the soluble species, the sodium salt of O-benzoic sulfimide, $C_6H_4CONNaDO_2$.

[2] The organic compounds investigated were: Na naphthalene-1, 5 disulfonate; Na 1-naphthylamine-4, 8-disulfonate; Na 1-naphthylamine-3, 6, 8-trisulfonate.

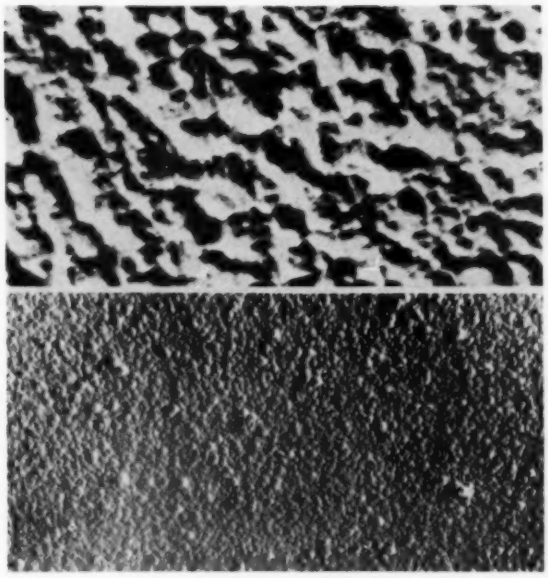

Fig. 2. Films plated without (tops) and with (bottom) saccharin in the plating solution. Magnification 40,000X before reduction for publication.

The electron micrographs (Fig. 2) showed that films plated from solutions containing saccharin are much smoother than those plated without saccharin.

To investigate crystal size and strain effects, Ni films were plated with and without saccharin with the solution pH at 2.1 and at 3.1 (Table I). Without saccharin, the crystal size decreases markedly as pH increases. With saccharin, crystal size is relatively independent of pH between 2.1 and 3.1.

The results (Table I) are typical of a large number of measurements. The rms strain, which should be several orders of magnitude larger than average strain is not markedly influenced by saccharin in the bath.

Crystal sizes were also measured on seventeen films whose Fe-Ni ratio was 1:4. The measurements showed that crystal size decreased from an average 650 to 300Å with the addition of 100 mg/l of saccharin. Larger additions of saccharin did not further reduce crystal size.

Polargraphs presented in Fig. 3 show the influence of saccharin on the reduction potential of hydrogen for two pH ranges. When the saccharin concentration is low (0.001M), two breaks are seen corresponding to the reduction of saccharin (8) and the reduction of hydrogen.

As the concentration of saccharin is increased, the half-wave potential of hydrogen is noted to decrease until the contribution to the polarogram from this

Table I.

Saccharin content	pH	Crystal size, Å	Strain $\times 10^3$
None	2.1	620	5.3
None	3.1	1500	3.4
840 mg/l	2.1	720	4.9
840 mg/l	3.1	720	4.7

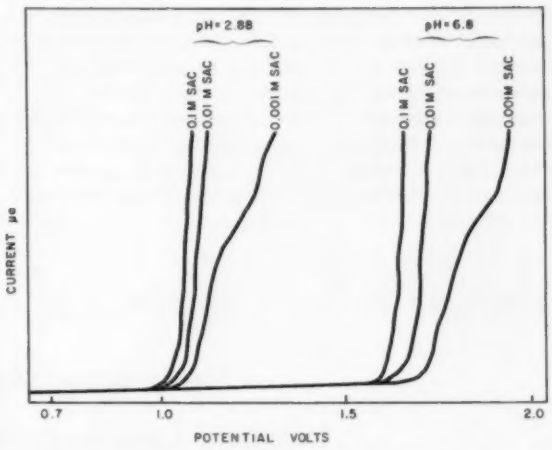

Fig. 3. Influence of saccharin on the reduction potential of hydrogen.

reaction swamps the contribution from the saccharin reaction. This observation provides an explanation for the very marked reduction of cathode efficiency in the plating bath which results from the addition of saccharin. The explanation is, of course, that a greater per cent of the diffusion current is carried by the hydrogen reduction reaction because of the reduction of its half-wave potential. The plating efficiency of the bath was reduced by 10% due to the addition of 840 mg/l of saccharin.

The reduction potentials (half-wave potential) of these reactions are functions of pH as expected. The half-wave potential of hydrogen is shifted from about 1.4 v for pH = 2.7 to about 1.95 v for pH = 6. The saccharin half-wave potential is shifted from about 1.2 for pH = 2.7 to 1.8 for pH = 6. These values were measured with 0.001M saccharin in solution.

In other polarograms, it was noted that the half-wave potential of Ni^{2+} (0.001M) equaled 0.92 with pH equal to 2.5 and 6.5.

Analysis of Results

The primary influences on structural properties are summarized as follows:

1. Films plated from saccharin-free solutions are much rougher than films plated from saccharin-containing samples. The roughness dimensions are comparable to a scale which would contribute to an increase of H_c (~2000Å).

2. When no saccharin is in the plating bath, crystal size increases as pH increases. When saccharin is in the plating bath, crystal size is relatively independent of pH between 2.1 and 3.1.

3. The presence of saccharin reduces the decomposition potential of hydrogen and decreases the plating efficiency. Saccharin also markedly reduces the amount of total gas contained in the film that can be driven off by heating the film to 800°C in vacuum. This should materially reduce average strain in the plated film and thereby account for the observed reduction of H_c.

Summary

The coercive force H_c increases due to increased roughness, occluded gas, or decreased crystal size.

Saccharin in the bath reduces roughness, occluded gas and controls crystal size. The mechanism is a surface activity at the cathode as suggested by the small amount of saccharin in the solution which radically influences these properties and the independence of these properties over a wide variation of saccharin content. The surface activity lowers the hydrogen reduction potential and decreases the cathode efficiency.

Manuscript received April 17, 1961.

Any discussion of this paper will appear in a Discussion Section to be published in the June 1962 JOURNAL.

REFERENCES

1. I. W. Wolf and V. P. McConnell, *Tech. Proc. Am. Electroplaters Soc.*, **43**, 215 (1956).
2. J. C. Lloyd and R. S. Smith, *J. Appl. Phys.*, **30**, 274S (1959).
3. I. L. Newell, *Tech. Proc. Am. Electroplaters Soc. 43rd Ann. Conv.*, 101-4 (1956).
4. L. J. Dykstra and C. West, "Effect of Inclusions on the Coercive Force of Iron," P. R. 79, p. 979 (1950).
5. E. W. Lee, *Rep. Prog. Phys.*, **18**, 184 (1955).
6. N. Thon, D. G. Kelemen, L. Yang, S. Yang, and D. Dean, *A.E.S. Research Rept. #28.*
7. R. S. Smith, *IBM Journal*, **4**, 205 (1960).
8. T. Momose, *J. Pharm. Soc. Japan*, **64**, 155 (1944).

Some New Measurements of Infrared Luminescence in Tunnel Diodes

J. I. Pankove

RCA Laboratories, Radio Corporation of America, Princeton, New Jersey

The purpose of this paper is to describe several observations of luminescence in tunnel diodes using a very sensitive method. Since these phenomena are not completely understood they will only be described and not discussed.

Tunnel diodes have been built by a method (1) of double recrystallization from alloy solution onto a block of germanium on which two ohmic connections were attached (Fig. 1). The dominant impurities in the n+ and p+ regions are arsenic and gallium respectively. DC voltage is applied to the two ohmic connections and one measures the change in current (photoconductivity) due to the light emitted by the tunnel diode. The spectral sensitivity of the photoconductor is determined by the choice of impurities in the block of germanium. The source and the detector being built in the same block of germanium, their optical coupling is excellent. Although one loses the possibility of obtaining the spectrum, one gains enormously in sensitivity. The high sensitivity allows a correlation between the emission characteristic and the V-I characteristic of the tunnel diode (Fig. 2). The purpose of this measurement was to look for a radiative mechanism associated with excess current (a check on two hypotheses illustrated in Fig. 3 was sought: a, photon-assisted tunneling; b, tunneling to a deep-lying level where radiative recombination might take place). Although these questions have not been answered, these experiments have revealed a variety of luminescences.

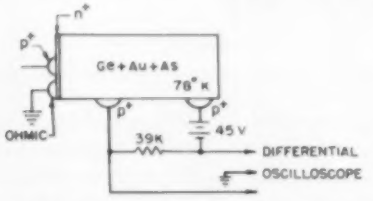

Fig. 1. Integrated source-detector structure

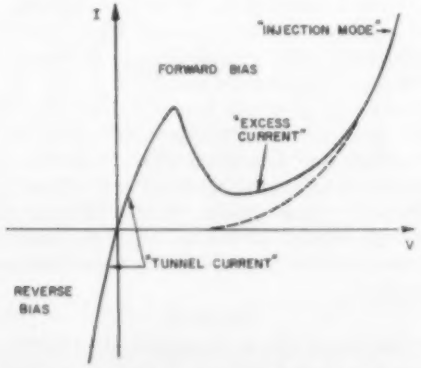

Fig. 2. V-I characteristic of a tunnel diode

Measurements Using Compensated Gold-Doped Germanium Detectors

The first few diodes were built on gold-doped germanium which was partially compensated by arsenic. This detector, used at 78°K, is sensitive to infrared up to 10μ, (0.12 ev).

When a semisinusoidal forward current (whose maximum value is I_{max}) is passed through the tunnel diode of the specimen labelled "A" one gets two types of luminescences: that reproduced on Fig. 4-a when $I_{max} < 100$ ma and that of Fig. 4-b when $I_{max} > 300$ ma; the intensity of the latter luminescence grows rapidly with the current. The photoresponse (which is proportional to the number of photons) is shown on Fig. 4 as a function of the intensity of the

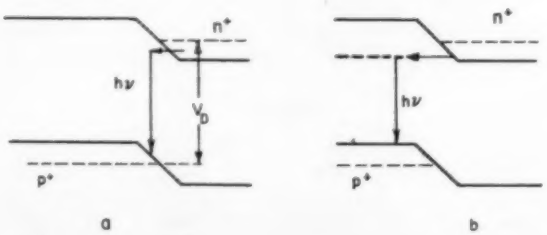

Fig. 3. Two models for radiative mechanisms in the "excess current" mode: a, photon assisted tunneling; b, tunneling to a deep level followed by radiative recombination.

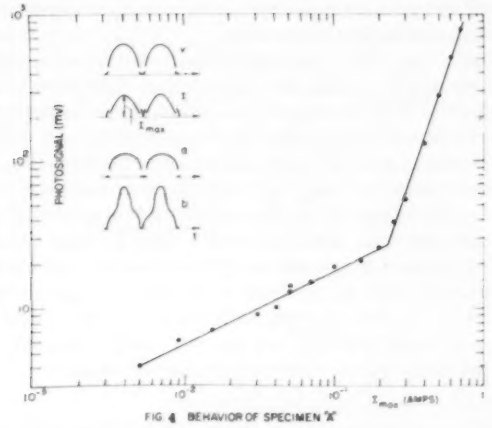

FIG. 4 BEHAVIOR OF SPECIMEN "A"

Fig. 4. Behavior of specimen "A"—the inset shows the time dependences of: voltage (V) applied to the tunnel diode, current (I) through the diode, output of the photoconductor when $I_{max} < 100$ ma (a) and when $I_{max} > 300$ ma (b). The ordinate represents the output of the photoconductor measured at the peak of the wave shown in (a) or (b).

current I_{max}. One sees a region which goes with $I_{max}^{1/3}$ below 200 ma and another which seems to follow an I_{max}^{5} dependence above 250 ma, although the sharpness of the break in the curve suggests a more complex function. It is believed that the fast rising luminescence is due to band-to-band recombination since this corresponds to the injection mode. In Ref. (1) this type of radiation was shown to rise exponentially with current. The wave shape of the luminescence shows clearly that this is not a thermal effect. (A thermal effect produces a phase shift which lags the driving signal by 90°.) On the other hand, no luminescence can be detected during tunneling, which proves either that there is no emission or that the emission energy is less than 0.1 ev. Without an emission spectrum it is difficult to speculate on the mechanism involved.

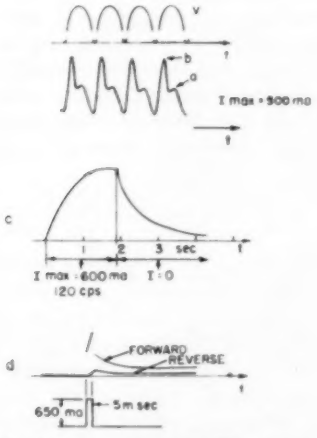

Fig. 5. Behavior of specimen B. The upper set of curves represent the time dependence on the driving voltage (V) and the wave-shape of the corresponding luminescence as measured by the photoconductor. (c) Shows the output of the detector when a nearly 2 sec long burst of semisinusoidal pulses of current is passed through the diode. (d) Shows the output of the detector when a square pulse of current (5 msec long) is passed through the diode in the forward and in the reverse directions.

Another tunnel diode built on a compensated gold-doped detector has revealed three types of luminescences:

(*a*) A luminescence in phase with the driving signal (Fig. 5-a).

(*b*) An out of phase luminescence which leads the voltage by $\pi/4$ (Fig. 5-b), and which grows more rapidly than the in-phase luminescence. The above two emissions are equal when $I_{max} = 425$ ma.

(*c*) A long time-constant luminescence ($\tau = 0.5$ sec.) (Fig. 5-c, d). Its intensity is much greater than the in-phase emission. This long time constant emission occurs even during tunneling, (with both polarities of current). This time constant is an order of

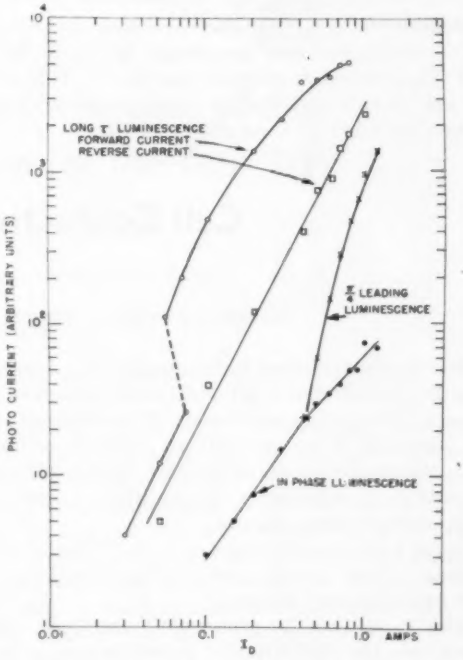

Fig. 6. Light-current characteristics of specimen B

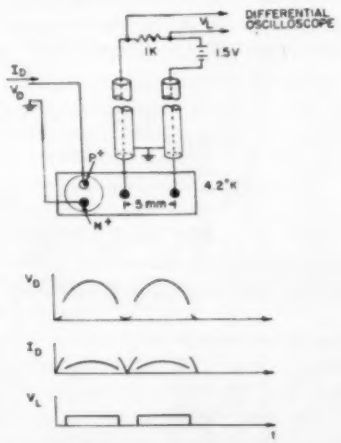

Fig. 7. Integrated source-detector having a spectral sensitivity threshold of 0.01 ev. The lower curves represent the time dependence of applied voltage (V_D), diode current (I_D), and detector output (V_L).

magnitude too large to be accounted for by heating. Thermal emission has been observed at higher currents; it can be distinguished by the fact that it causes the luminescence wave-shape to lag the driving current by 90° at the frequency used.

The dependences of these three luminescences with current are plotted on Fig. 6.

Measurement Using An Intrinsic-Germanium Detector

A tunnel diode built on n-type germanium (30 ohms cm at 290°K) was wired as shown on Fig. 7. The detection circuit leads were shielded in such a way as to minimize the danger of signal pickups (actually these are easy to identify—for example, by inverting the biasing polarity in the detection circuit, which inverts the photoelectric signal but does not invert the parasitic signal.)

This specimen was immersed in liquid helium (4.2°K), in order to deionize the donors. This allows the use of this material as an infrared detector to about 120μ (0.01 ev). As shown in Fig. 7 the photosignal appears after the region of negative resistance (2) but not during tunneling.

The integrated source-detector structure is obviously a very sensitive research tool. The threshold of spectral sensitivity may be chosen by using the appropriate impurity in the photoconductor, and subsequently it may be adjusted to some higher energy by thermally ionizing the impurity levels previously used—for example, under-compensated gold doped germanium will give a 0.01 ev threshold at 4.2°K and a 0.12 ev threshold at 78°K—though with less sensitivity than in the case of an over-compensated detector. That much can be done with such a technique is illustrated by the above reported discovery of new luminescence phenomena in germanium.

Manuscript received March 17, 1961.

Any discussion of this paper will appear in a Discussion Section to be published in the June 1962 JOURNAL.

REFERENCES

1. J. I. Pankove, *Phys. Rev. Letters*, **4**, 20 (1960).
2. L. Esaki, *Phys. Rev.*, **109**, 603 (1958).

Cell Conductivity Measuring Circuit

Fred E. Dickey

Research Laboratory, General Electric Company, Schenectady, New York

The circuit described in this paper was developed in order to provide a simple device which would measure solution conductivity of electrolytic cells and give a linear output with an accuracy of 2%. It keeps the exciting current between 10 and 100 μamp, depending on sensitivity. In addition, a means of calibration has been included.

Figure 1 shows the entire circuit. There are four sections: power supply, phase shift oscillator, two stage amplifier, and detector.

Tube V_1 is a 10 kc phase shift oscillator whose output into the "Sensitivity" potentiometer is set to 10 v by the 0.18 megohm and 0.15 megohm divider. The only adjustment needed in the oscillator is the 5K ohm potentiometer in the cathode and this is set but once to where it gives the best sine wave output. The 10 v goes through the "Sensitivity" pot and a fixed 100K ohm resistor to the cell or the calibration resistors, depending on the setting of S_2. These two resistors are always very large compared to the cell resistance so that they turn the constant-voltage oscillator into a constant-current generator. This constant current of between 10 and 100 μamp is not affected by the cell resistance but is set only by the "Sensitivity" potentiometer. The voltage across the cell equals its resistance times this constant current and, therefore, it varies in a linear manner as the resistance changes. Switch S_3 can substitute known resistors for the cell in order to calibrate the circuit.

The cell voltage is amplified by V_2 and half of V_3. The large amount of decoupling in the B+ line between these stages and the power supply eliminates any "motorboating." Small coupling capacitors between stages act like filters so they pass the 10 kc signal but keep down the response at 60 cps and

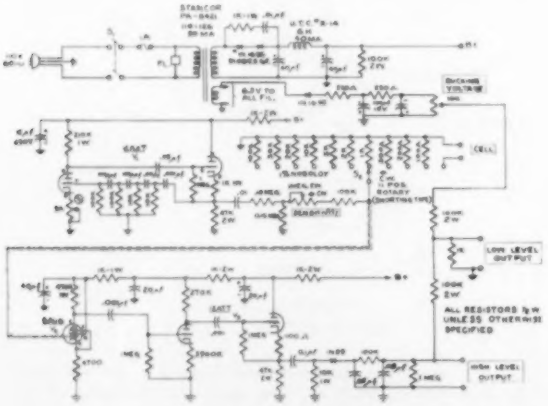

Fig. 1. Circuit diagram

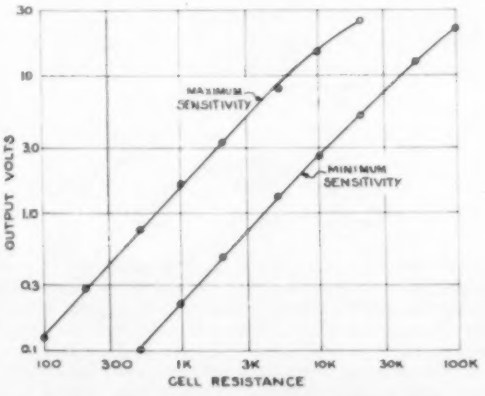

Fig. 2. Curve of output voltage vs. cell resistance

eliminate pickup and shielding problems. Cathodes are not by-passed in order to provide some negative feedback and increase stability.

The second half of V_2 is a cathode follower that acts as a buffer between the amplifier and 1N99 diode detector. The detector's output goes to the "High Level Output" posts and then to a recorder. The voltage here is large in order to get above the square law region of the detector as soon as possible. For high gain recorders that need a low driving impedance, a "Low Level Output" is also supplied. A bucking voltage is applied at this output so that some zero suppression is afforded for those cases in which it is desired to operate the recorder between certain resistance limits instead of from zero up.

Figure 2 gives the high level d-c output as a function of calibration resistance for the sensitivity potentiometer all the way out (Maximum Sensitivity) and all the way in (Minimum Sensitivity).

Manuscript received March 3, 1961.

Any discussion of this paper will appear in a Discussion Section to be published in the June 1962 JOURNAL.

Technical Review

Report of the Chlor-Alkali Committee of the Industrial Electrolytic Division for the Year 1960[1]

John E. Currey

Hooker Chemical Corporation, Niagara Falls, New York

and Clifford A. Hampel

Consulting Chemical Engineer, Skokie, Illinois

Chlorine-Caustic

Production and Sales

Chlorine and caustic soda production in the United States again reached a new, all-time high in 1960. In spite of the general economic slump, the rate of growth of the industry for this year was in keeping with the general trend established over the past ten years, as shown below:

U.S. Annual Growth Rate

Period	Chlorine	Caustic
1930-1935	11.0%	3.6%
1935-1940	14.2%	10.0%
1940-1945	14.3%	9.4%
1945-1950	10.8%	6.8%
1950-1955	9.5%	7.7%
1955-1960	7.8%	5.8%

U.S. chlorine production as reported by The Chlorine Institute's Annual Report for 1960 was 4,640,000 tons in the year 1960, or an increase of 8.4% over 1959. The U.S. Department of Commerce's, "Current Industrial Reports," M28A (61)-1 dated March 23, 1961 reports 1960 production figures of 4,591,571 tons which are slightly less than those quoted above. The per capita consumption of chlorine was approximately 52 lb, an all-time high and double that of 1950.

Chlor-alkali plant capacity increased only 3% during the year, from 14,060 tons per day in January to 14,490 in December. The uncertainty of the business climate was partly responsible for this reduced rate of growth of capacity. Construction was at a considerably higher level than that indicated, since a number of major plants were rebuilt to replace older units and since several plants under construction in 1960 have been started, or will be in 1961. Construction under way indicates that 1961 will bring in plants which will continue the 7 to 8.5% growth trend.

On the average, the industry operated at 89% of capacity in 1960 which is considerably higher than the 83% estimated for 1959.

Caustic soda production in the U.S. increased 4.7% above 1959, for a total of about 4,896,000 tons in 1960. The apparent per capita consumption was 54.0 lb, an all-time high, which was nearly twice that of 28.0 in 1950. Lime soda caustic production data are not available, but it is estimated such production was some 300,000 to 325,000 tons for the year.

Even though caustic is being converted to soda ash on a relatively small scale, soda ash continues to be converted to lime soda caustic. In general, caustic continued to be in excess through 1960 as it was in the previous year.

About 74% of the U.S. capacity of chlorine in 1960 was in diaphragm cells, 20% was in mercury cells, 5% in sodium cells and less than 1% in nonelectrolytic processes. Approximately one-third of the capacity added in 1960 was in diaphragm cells and two-thirds in mercury cells.

L. B. Grant, at a Chemical Market Research Association meeting (see *Oil, Paint and Drug Reporter,*

[1] M. S. Kircher, Dryden Chemicals, Ltd., Dryden Ontario, assisted by supplying data and reviewing the Report before publication.

May 22nd 1961), forecast the demand for caustic and chlorine by reviewing the end uses of chlor-alkali products. He concludes that chlorine production will grow at only 5% per year for the next few years, compared with an average of 9.4% for the past decade. Similarly he concludes that caustic soda will expand at only 4.5% per year compared with 7.0% for the past ten years. The above chlorine figures are considerably below other predictions which usually indicate chlorine growth at 7 to 8.5% annually.

New Plants and Expansions

The following new plants, expansions and additions, are in progress, contemplated, or have been completed:

Allied Chemical Corporation, Solvay Process Division: Expansions have been announced for completion in 1961 at Moundsville, West Virginia, and Brunswick, Georgia, respectively. Solvay and Cie mercury cells will be used in both plants.

Consolidated Mining and Smelting Corporation: A new plant using Hooker Type S-3C diaphragm cells at Trail, B. C., was started early in 1961.

Diamond Alkali, Painesville, Ohio: An installation of Tucker-Windecker cells was replaced by Diamond cells.

Doremus Chemical Company, Newark, New Jersey: A new plant with Hooker Type S cells was started early in 1961.

Dryden Chemicals, Dryden, Ontario: A new plant with BASF mercury cells was announced for start of construction in 1961.

Food Machinery and Chemical Corporation, South Charleston, West Virginia: An expansion with Hooker Type S-3B cells was made in 1960.

Hooker Chemical Corporation, Niagara Falls, New York: An expansion with Hoechst Uhde mercury cells was started in 1960 and will be placed in operation in 1961.

Jefferson Chemical Company, Port Neches, Texas: An expansion with Hooker Type S-3B cells will start in 1961.

Kaiser Aluminum and Chemical, Grammercy, Louisiana: An expansion with Hooker Type S-3B cells will start in 1961.

Olin Mathieson Chemical Corporation, Calhoun, Tennessee: A new plant with 100,000 amp O-M mercury cells has been announced for construction in 1961 and start up in early 1962.

Olin Mathieson Chemical Corporation, Niagara Falls, New York: An installation O-M 100,000 amp cells to replace the historic Castner Rocking cells was started early in 1961.

Pennsalt Chemical Corporation, Wyandotte, Michigan: Another historic cell installation was replaced with Diamond cells, superseding Gibbs cells.

Stauffer Chemical Company, Southern California. A new plant has been announced. The process of production has not been announced.

Climax Molybdenum, Mississippi: A new plant using a new chemical process for the production of chlorine and potassium nitrate has been announced.

Dow Chemical Company, Plaquemine, Louisiana: Work is continuing on an installation of Solvay V200 cell for start up in 1962.

Caribbean Alkali Company, Puerto Rico: A plant has been announced for construction in 1961.

During the past ten years new producers installed equipment amounting to 15.6% of the new plants built, or 3.7% of the total chlorine capacity.

Technical Developments

The price reductions in silicon and germanium power rectification units has continued the trend of acceptance of this equipment in the chlor-alkali industry. These rectifiers are encouraging the design and operation of higher amperage cells. This is evidenced by the first commercial installation of the Olin Mathieson 100,000 amp cells and the first commercial installation of the Hoechst Uhde 120,000 amp cells in the United States. In addition, the first installation of Hooker Type S-3C cells to operate above 30,000 amp has been installed.

The trend toward higher current densities in mercury cells continues. A number of commercial plants are now operating in the 5000-6000 amp/m^2 range. Operation at 7000 amp/m^2 is said to be feasible.

The interest of industry in platinum-titanium anodes for diaphragm and mercury cells continues. There has been an increase in the number of articles on this subject appearing in the literature (*Chemical Week*, Jan. 23, 1960 and March 28, 1960). The patent situation has not changed in the past year and continues to be a question. A number of commercial size cells with platinum-plated, titanium anodes have been installed and are operating. There is no evidence of any chlorine producer in the United States, Canada, or England having reached a stage of development to warrant a decision to go to a large-scale installation.

The frantic activity of research and development on fuel cells is continuing, based upon funds from the military. The electrolytic industries are taking a closer look at fuel cells as a possible future source of direct current power.

For the first time a train wreck has resulted in the puncture of a liquid chlorine tank car causing chlorine to spill upon the ground. The accident, in Louisiana, resulted in the death of one person. Tank truck shipments, as initiated in 1960, and barge shipment of chlorine on inland waterways continue to increase (see *Chemical Week*, March 19, 1960, p. 31).

The Chlorine Institute, Inc., continues a most aggressive program for the safe handling of chlorine in transportation and in producing and consuming plants.

The sale of European mercury cell equipment has continued in the United States at an accelerated pace (*Chemical Week*, March 5, 1960). The purchase of this equipment is evidently based on sound technology combined with an attractive price.

The lack of balance in demand for caustic and chlorine, combined with an increasing output of by-product hydrochloric acid, has increased the interest in converting hydrochloric acid into chlorine. However, at this time it does not appear likely that any appreciable amount of chlorine will be produced by this method.

Some United States and Canadian patents which are of interest to the electrolytic industry and which were issued in 1960 are as follows:

2,920,028 (United States)	Series Cell for Brine Electrolysis
2,917,368 (United States)	Method of Producing Caustic from Brine
2,921,005 (United States)	Electrolytic Conversion with Permselective Membrane
2,919,238 (United States)	Fused Salt Cells
597,095 (Canada)	Production of Perchlorates

595,813 (Canada)	Mercury Recovery from Brine
595,814 (Canada)	Chlorine Manufacture
597,879 (Canada)	Prevention of Flooding in Diaphragm Cell
597,908 (Canada)	Method of Electrolyzing Brine
2,934,486 (United States)	Graphite Anode Structure
600,441 (Canada)	Hydrochloric Acid Cell
601,868 (Canada)	Mercury Cathode Chlorine Cell
2,951,026 (United States)	Mercury Cathode Chlorine Cell
2,929,412 (United States)	Mercury Cathode Chlorine Cell
2,952,604 (United States)	Electrolysis Apparatus

Markets and End-Use Patterns

There does not appear to have been a major change in the end-use patterns for chlorine and caustic during 1960. The use of chlorine dioxide for bleaching in the pulp and paper industry is gaining in importance and is affecting chlorine usage.

The end-use pattern of caustic remains quite diversified. The alkali industry is watching the nylon-rayon battle for supremacy in the tire industry. Rayon remains the largest, single use of caustic soda. The further application of caustic in the expanding pulp and paper industry looks promising.

Table I gives a recent, estimated, end-use pattern for chlorine and caustic soda in 1960.

Table I. U.S. Chlorine-caustic soda end-use pattern*

Chlorine		Caustic Soda	
Chemicals	80%	Chemicals	30%
Pulp and Paper	17%	Rayon, Film	13%
Sanitation	3%	Pulp and Paper	10%
		Soap, Cleaners	6%
		Petroleum Refining	5%
		Textiles	5%
		Net Exports	6%
		Others	25%
Total	100%	Total	100%

* Source: Hooker Chemical Corporation.

World Production

According to a survey (see *Chemical Week*, Oct. 29, 1960) presented by B. Cremers of Wyandotte Chemicals at the 32nd Congreso Internacional de Quimica Industrial, caustic soda and chlorine capacities of the world as of 1959 are estimated as follows:

	Caustic Soda		Chlorine	
	Producers	Capacity	Producers	Capacity
North America	61	6,520,000	61	5,528,000
European Econ. Comm.	70	2,572,000	67	1,709,000
European Free Trade Area	29	1,365,000	29	921,000
Russian Bloc	36	1,633,000	30	697,000
Europe (Other)	37	340,000	37	130,000
Africa	10	35,000	10	34,000
Cent. & South America	45	255,000	43	153,000
Asia & S. Pacific	88	1,767,000	64	648,000
Total World Capacity		14,000,000		9,900,000
Total World Production		11,400,000		8,100,000

Potassium Hydroxide

Production of KOH increased 7.2% from 102,000 tons in 1959 to 109,463 tons in 1960. The trend toward greater use of this chemical in detergents continues. The trend toward higher purity favors greater percentages being produced in mercury cells in the future. Hooker Chemical Corporation, a major producer of potassium hydroxide, is converting its KOH production to mercury cells.

Soda Ash

The general downward trend of United States production of soda ash was again re-established in 1960, after a one year of production increase in 1959. In 1960 synthetic soda ash decreased 7.0%, from 4,903,979 tons in 1959 to 4,557,299 tons in 1960, while natural soda ash increased 16% from 715,330 tons in 1959 to 830,452 tons in 1960. Thus, 15.4% of the production was "natural soda" and 84.6% was synthetic. The apparent per capita consumption was 60 lb for 1960 which reflects the fact that the per capita consumption has been relatively stable since 1940. The glass industry continues to be the largest single end-use consuming approximately 40% of the production.

Dow Chemical Company continues to operate its plant at Freeport, Texas, converting electrolytic caustic to soda ash. The expansion in natural ash has for the most part taken advantage of the Green River, Wyoming and the Trona, California deposits.

Sodium Chlorate

The 3.2% increase in chlorate production, from 88,300 tons in 1959 to 91,184 tons in 1960, as reported by the Department of Commerce, indicates that 1960 was a relatively stable year compared with large growth of recent years, *e.g.*, 30% growth in 1959. The doubling of production of this product since 1954 has been due to the rapid increase in demand for higher paper and paperboard brightness achieved by chlorine dioxide bleaching of pulp.

The expansions of chlorate production in progress or completed in 1960 are as follows:

American Potash and Chemical Corporation, Aberdeen, Mississippi: The capacity of this plant was reported increased by 50%.

Dryden Chemicals, Ltd., Dryden, Ontario: A new plant using Krebs cells has been announced.

Hooker Chemical Corporation, Columbus, Mississippi: An expansion is being completed in 1961.

Penn-Olin Corporation, Calvert City, Kentucky: A new corporation has been formed by Pennsalt Corporation and Olin Mathieson Corporation to produce sodium chlorate.

Weyerhaeuser Timber Company, Longview, Washington: A new chlorate plant is being installed in conjunction with an existing chlor-alkali plant.

Miscellaneous Metals

Aluminum.—The domestic production of aluminum continues to grow. A new record of primary production of 2,014,497 tons was reached in 1960. This is some 3% above 1960, the previous peak year for aluminum.

New production facilities activated in 1960 amounted to about 88,000 annual tons, raising the total domestic capacity to nearly 2.5 million annual tons. Reynolds Metals Company started the second

of three 33,300 ton per year potlines at its new St. Lawrence plant near Massena, New York. Aluminum Company of America started a new 20,000 ton line at Point Comfort, Texas, and the first of five potlines, each with a capacity of 35,000 tons per year, at Evansville, Indiana. Kaiser Aluminum, Inc. announced plans to increase its Dallas, Oregon plant capacity by 25% or 15,000 tons a year. United Pacific Aluminum Corporation expects to build a two-potline plant near Longview, Washington with an annual capacity of 40,000 tons, power to be available in 1962 and 1963, respectively, for each of the two lines.

Domestic producers ended 1960 operating at about 76% of their capacity. In 1959 the average was 83%.

Magnesium.—Production of primary magnesium in the United States amounted to 40,070 tons in 1960, some 29% above 1959. The electrolytic plant at Freeport, Texas and the two silicothermic plants at Canaan, Connecticut and Selma, Alabama were in production throughout the year.

Consumption of magnesium reached 44,000 tons in 1960, an increase of about 6% over 1959. Expanded and new structural uses, particularly in the automotive industry, accounted for this increase.

Canadian production, which had decreased from 9,606 tons in 1956 to 5,817 tons in 1959, remained almost the same in 1960 as it was in 1959.

Sodium.—The production of sodium amounted to 113,000 tons in 1960, essentially the same as that of 1959. Over 70% of the sodium produced is consumed in making tetraethyl and tetramethyl lead by the sodium-lead alloy process. Current consideration of electrolytic processes for making TEL and MEL portends possible decrease in the use of sodium for producing these gasoline additives, with consequent further lessening of demands for sodium metal. (*Chemical Engineering*, April 3, 1960, p. 81.)

Manganese.—Consumption of high-purity, electrolytic manganese increased in 1960 to about 15,530 tons according to the Bureau of Mines. Other sources indicate a higher consumption, possibly 17,500 tons (for example, *Chemical Week*, July 23, 1960, p. 25).

The two present producers of manganese metal increased their plant capacities in 1960. Union Carbide Metals Company completed a 20% expansion to bring the capacity of its Marietta, Ohio plant to a minimum of 15 million lb/year. Foote Mineral Company expanded its Knoxville plant to a capacity of 28 million lb/year and announced plans for a new 20 million lb/year plant in New Johnsonville, Tennessee, with half of the capacity to be available early in 1962.

A third producer, American Potash and Chemical Corporation, plans to enter the picture with a $5 million plant at Aberdeen, Mississippi, whose capacity will be 10 million lb/year. It is scheduled to begin production late in 1961.

Total United States capacity is now about 45 million lb/year and may double in two years.

Beryllium.—The production of beryllium metal continues to expand with 1960 output estimated to be over 300,000 lb, about twice that of 1959. Brush Beryllium Company is expanding its capacity to nearly 30,000 lb/month by July, 1961, and Beryllium Corporation is also expanding its capacity. Some sources predict that domestic production will reach 500 tons per year by 1970, an output about three times the current rate.

A third company, General Astrometals, will become the third beryllium fabricator using Pechiney techniques. Increased use of domestic ores is underway to meet the raw material demands for beryllium metal production.

Lithium.—A renewal of interest in lithium is evidenced by the recent installation of facilities with a capacity to produce 350,000 lb/year of butyl lithium by three producers; American Potash & Chemical Corporation, Foote Mineral Company, and Lithium Corporation of America. Butyl lithium, LiC_4H_9, is made by reacting lithium metal with butyl chloride in a solvent and is used as a catalyst to polymerize isoprene to polyisoprene and butadiene to polybutadiene. (*Chemical Engineering News*, Feb. 6, 1961, p. 46). At the above production rate, at least 77,000 lb/year of lithium metal would be required.

Chromium.—The electrolytic process continues to be the premier source of the highest purity, chromium metal. The 1960 production evidently remained the same as in 1959, about 2,000 tons.

Tantalum and Columbium.—Tantalum production reached 140 tons in 1960, almost the same as in 1959, but columbium production increased to about 100 tons, a major increase over the 1959 output of less than 70 tons.

Although ore prices increased in 1960, the prices for the metals declined during the year to $45/lb for tantalum ingot, $35 for columbium ingot, and $47.50 to $50 for capacitor grade tantalum powder.

Feature Section

Professor Colin Garfield Fink

Henry B. Linford[1]

The life and work of Professor Colin Garfield Fink have been described several times in Society publications.[2,3] At this time, when the Board of Directors has established the Colin Garfield Fink Fellowship Fund [*see* pg. 214C of the September issue], it is felt that the reprinting of much of this material is in order since it is only natural that younger people in the profession have, by this time, lost touch with the marvelous contributions of some of our early workers such as Professor Fink. It is for this purpose that we wish to devote some space to discussing Professor Fink as a man, as a scientist, as a teacher, and as the real backbone of The Electrochemical Society for many years.

No better appreciation of a man can be achieved than the writings of one of his own sons. Accordingly, we reprint here a short biographical sketch of "Professor Colin Garfield Fink, The Man," by Dr. Harold Kenneth Fink.

Professor Colin Garfield Fink, The Man

Harold Kenneth Fink, Ph.D.

Dad was the kind of man people like to remember, because he was the kind of man people like. When those who knew him begin expressing their deep respect for him as a scientist, it isn't long before someone will smile and say, "Did you ever hear about the time when Professor Fink ..."—and respect for the scientist will be matched by some anecdote or incident which endeared Colin G. Fink to others as a man.

He was for many years voted the most popular professor by the senior class poll at Columbia University, because he so often gave his time and energy to his students "beyond the call of duty." He realized, for example, that he could never investigate on his own all the research hypotheses which were the products of his creative mind. Such ideas, which he willingly shared with his graduate students, were sometimes the basis of later fame and excellent jobs for them. But Dr. Fink could also be depended upon in the immediate, practical emergencies that faced his students. Did you hear about the time that one student's experiment got out of hand, with the result that all the surrounding apparatus was sprayed with an aluminum coating? They say that Fink calmly entered the lab, sized up the situation, and proceeded to produce another formula which removed the aluminum plating from the lab equipment.

In his own student days, Dad did not always find *his* superiors so understanding. During his first vacation from his graduate studies at the University of Leipzig, he worked for a coal tar concern in Zurich. In his lab were two sinks, one for ordinary refuse which emptied into the lake, and one for dyestuffs. One evening, an American woman visiting Zurich remarked to young Fink that for the first time she had seen a lake which possessed the beautiful colors shown on the picture postcards. Next day, he found himself fined a month's salary for having thrown some dye down the wrong drain!

"Did you get a 'valentine' from Dr. Fink today?"—that question would have been appropriate any day of the year to some student who had become especially interested in a particular phase of study or research. Fink's "valentines" were cards dropped into a student's mailbox with references to the literature on the special subject or project under consideration. As an editor of *Chemical Abstracts*, writer of technical articles, and reader of many professional journals, Dad kept abreast of his whole field and borderland areas where it lapped over other fields, and his "valentines" were always timely.

Such conscientiousness did not wait until his days as a professor to show itself, however. When he was an undergraduate at Columbia, Dad was a member of a fifty-man mandolin club which gave public performances in and around New York City. One evening, during a raging blizzard, anyone might well have been tempted by the thought that he really need not go—one mandolin player more or less would make little difference. He *did* go—but forty-seven others failed to show up. Nevertheless, the mandolin trio received an enthusiastic welcome, and encores were the order of the evening.

The mandolin also went with young Fink to Leipzig, and was accompaniment for the Saturday night singing of University students. One evening, at the Hoffbrau House, Fink noticed that a man at a neighboring table had carefully lettered something on his menu card, placed the message in front of his beer mug, and then retired to the rest room. Putting action behind his curiosity, Fink stepped over and read the card: "Do not drink this; I have spit in it." When the man returned to his table, he found a reply to his warning: "So have we!"

It was probably some such prank as this which led to Dad's being challenged to a duel in Leipzig. At any rate, there was an occasion when his bent for wit must have gotten out of hand, and some fellow felt that his honor had been impugned. Fink knew he'd have no chance with swords, so he had his second acquire the most fearsome-looking guns he could find and offered one to the challenger, who quickly bowed out of the affair, and the duel never came off.

That Colin G. Fink was a conscientious student at Leipzig is attested to by the fact that he received his M.S. and Ph.D. degrees, *summa cum laude*. But, in talking of those days, he would be more likely to speak of vacation adventures with his friends. One such experience ended

[1] Electrochemical Society President, 1961-1962; Columbia University, Dept. of Chemical Engineering, New York, N. Y.

[2] J. W. Marden and H. E. Grimm, "Colin Garfield Fink," an Address presented at the Colin Garfield Fink testimonial dinner on October 16, 1947 at the Copley-Plaza Hotel in Boston Mass., *Proc. Trans. Electrochem. Soc.*, 92, pp. 3-9 (1947).

[3] R. M. Burns, "Death of Dr. Colin G. Fink," *This Journal*, 100, 317C (1953).

in tragedy. With several students, he was hiking across a single-track railroad trestle which had neither pedestrian walk nor railing. At the sudden appearance of a speeding train, the others jumped from the bridge or tried unsuccessfully to hang from the ends of the railroad ties. Dad, instead, threw himself flat between the rails, and the train passed over him, leaving him unharmed.

On another hiking expedition in the Italian Alps, Dad was saved from possible disaster because he befriended a stray dog in a small village. The dog gratefully followed the boys up the mountain slopes. A sudden snow storm covered the path of their ascent, and the group had not bothered to hire a guide. On the way down, the dog would bound ahead where the path was safe, but stop and sniff suspiciously where a thin crust of ice covered a hidden crevasse.

Another small dog of dubious ancestry shared Dad's love of all life for more than seventeen years, and several "generations" of young chemists at Columbia will recall the little black and white "terrier" who had a place of honor under Dad's desk and was his frequent companion on campus. When "Tibby" was just a puppy, he was carried about with just head and front paws sticking out of Dad's big overcoat pocket. One morning in the elevator, a dignified matron asked, "What kind of dog is that?" Dad, true to his insistence for not stating conclusions beyond known facts, quipped accurately, "He's a son of a bitch."

Years of very busy work as a Columbia Professor, industrial consultant, and as Secretary of The Electrochemical Society were spiced by summer week-ends at his summer cottage in Keansburg, N. J., where he had some chance to relax with his family and to find a change of pace by doing house repairs and gardening. The neighbors in Keansburg remember him affectionately as "The Professor." Even in his summer place, he kept a lively research interest in happenings about him. He was, for example, much interested in the nutritional advantages of trace elements in the diet. One summer, he brought to the country a large brown buck rabbit from his Columbia laboratories. A neighbor gave us a white female rabbit. I'm sure that Dad would be the first to insist on further experimentation on the results of minute amounts of copper in a rabbit's diet, but, in an astonishingly short time, he had 26 rabbits helping him to weed the garden!

There were also occasional family trips to Bermuda at Christmas time, and once, in 1927, to Miami Beach. I particularly remember that boat trip down the coast from New York City, partly because of my boyish pleasure at meeting Gene Tunney, but also because of another amusing outcome of Dad's sense of humor. He would often state something highly improbable as fact, and do it with such a straight face that others would be taken in. Usually he would set the record straight after an appropriate interval, but this time things got a bit out of hand. The passengers were asked to list their hobbies and other data for the small shipboard newspaper. Dad wrote: "Big game hunting in British Columbia." The note that Professor Fink had just returned from a big game hunt was picked up and published by the Miami papers.

Other trips away from his office and classrooms at Columbia took him to meetings of The Electrochemical Society, on lecture tours in this country, Canada, and Europe. He was a popular lecturer, blessed with the art of making scientific facts come alive with interest. Mother accompanied him on these trips and was of invaluable assistance to him at ECS meetings. She teased Dad about his first reaction when, on a lecture tour in the Northwest, the car in which they were riding was hit broadside by another car. His first question to her was not, "Are you hurt?," but rather, "Are the lecture slides broken?"

Dad made important contributions to various scientific advances, but he also particularly enjoyed his work with antiquities. He discovered a rather ingenious method of reversing the corrosion of badly damaged art objects by electrolysis. He was thus able to restore the normal contours of ancient Egyptian bronze statues, and other art objects and artifacts, once considered so defaced that they were not even placed on exhibition. Of particular interest was his proof that most if not all of the Dare Stones of South Carolina and Georgia were fakes, but that the Drake Plate of California was genuine. He thus confirmed the historic landing of Sir Francis Drake near San Francisco in 1579.

The seemingly miraculous restoration of art objects, along with his considerable reputation in other fields, did lead one client to expect the impossible. This person had sent to Dad a badly mineralized bronze horse, whose tail had broken off in some ancient accident. When Dad returned the horse to its owner, free of corrosion, he received a letter expressing disappointment with the results: "Your process still needs development. Where's the horse's tail?"

Of course, accomplishing, through electrochemistry, results that men had heretofore considered impossible, or at least highly improbable, was the story of Colin G. Fink's genius as a scientist. But those facts alone are not the story of his life as a man with his family, co-workers, friends, and students. The dedication of the 1933 edition of *The Columbia Engineer* expresses it well: "We dedicate this Year Book to Colin Garfield Fink, whom we have come to like so well for his friendliness and understanding; and for his knowledge which he so ably imparts to others."

In 1947, a testimonial dinner was held in connection with the Boston Convention of The Electrochemical Society. At that meeting, an Address was presented by Dr. J. W. Marden of Westinghouse in collaboration with Mr. H. E. Grimm (*see* footnote 2). A section of this Address dealing with Professor Fink's services to the Society is very appropriate.

"When Dr. Fink became Secretary of The Electrochemical Society in 1921, the finances of the Society were at a very low ebb (actually living on borrowed funds to tide through the year), and publication of the Society's TRANSACTIONS was four volumes behind. Through economies, skillful management of the office, and particularly by attracting new members, the financial situation showed immediate and substantial improvement. While there was a recession in both finances and membership during the depression years, the Society continued to be solvent with a modest cash balance. The era of financial strength began in 1940 with the establishment of sustaining memberships. Very largely through Dr. Fink's efforts, this valuable corporation support of the Society has been developed until at present sixty companies are maintaining sustaining memberships.

"Dr. Fink with his faith in the purposes and his enthusiasm for the work of the Society has done many things to increase membership and to promote the profession of electrochemistry through the Society. For example, it was largely through his efforts that both the Acheson Medal and Weston Fellowship funds were established; he established the Roeber Research Fund in

1933 by donating the $1000 prize money bestowed upon him that year as recipient of the Acheson Medal and prize. Dr. Fink, it was, who first proposed the Young Author's Prize Fund. Dr. Fink employed many less publicized methods of attracting members; it is even rumored that the wise student in his classes lost no time in taking out membership in the Society.

"During the years, Dr. Fink, as everyone knows, has given lavishly of his own time to the service of the Society. Arriving at the office about seven o'clock in the morning, he has spent many hours of every day on Society affairs—editorial work, correspondence, planning of conventions, preparation for Board meetings, etc. For all of this, he has never received a penny in remuneration. He appears to have gotten his compensation in the realization of the service that he has been to the Society and to the profession of electrochemistry."

Other facts dealing with Professor Fink's association with our Society would include such items as the fact that he joined in 1907, just five years after the founding of the Society. He was the 15th President, serving in 1918. At the time of his retirement as Secretary, in connection with the testimonial dinner, a scroll was presented to him, which was inscribed as follows:

THE ELECTROCHEMICAL SOCIETY
SALUTES
COLIN GARFIELD FINK
DISTINGUISHED SCIENTIST, INSPIRING TEACHER,
AMIABLE FRIEND,
AND HAS THE HONOR TO BESTOW THIS SCROLL
IN APPRECIATION AND GRATEFUL RECOGNITION OF
SERVICE TO THIS SOCIETY
October 16, 1947 GEORGE W. HEISE, *President*
R. M. BURNS, *Secretary*

and Professor Fink was named Secretary Emeritus. This came as a reward for twenty-six years of continuous service as Secretary through two very trying periods, the first being the depression of the 1930's, and the second, World War II, when much government red tape was involved in any technical publication and the difficulties of travel even made it necessary to cancel a meeting. However, through the diligent services of Professor Fink, The Electrochemical Society came through both of these national catastrophes stronger than ever and, for this reason, many of his old students, professional associates, and co-workers in the Society feel that his name must be honored in some tangible and perpetual fashion. It is with this purpose in mind that the Colin Garfield Fink Fellowship Fund has been established.

Current Affairs

Electrochemical Society Members Announced as Winners of AES Awards

Three Electrochemical Society members were among those announced as award winners at the 48th Annual Convention of the American Electroplaters' Society, held June 18-23, 1961, at the Statler Hilton Hotel in Boston, Mass.

Abner Brenner, chief of the Electrodeposition Section of the National Bureau of Standards, Washington, D. C., was named the fourth winner of the AES Scientific Achievement Award, the society's highest scientific honor. The Selection Committee was composed of William M. Tucker, Chairman, William Blum, Myron B. Diggin, Henry B. Linford, Louis Weisberg, and Harold J. Wiesner. Among those present at the Opening Session was William Blum who was the first winner of the same annual award. Dr. Brenner, like Dr. Blum, Dr. A. Kenneth Graham, second winner, and Dr. Charles L. Faust, third winner, earned selection by his "decade-plus" accomplishments in advancing the theory and practice of electroplating, metal finishing, and allied arts; in raising the quality of its processes and products, and in enhancing the dignity and status of the profession. Dr. Brenner will deliver the fourth annual "William Blum Lecture" at the 49th Annual Convention of the AES to be held in Milwaukee, Wis., June 24-28, 1962. Thereafter, he will receive the $500 honorarium of the AES Scientific Achievement Award and a laminated scroll.

Harold J. Read, professor of physical metallurgy at the Pennsylvania State University, University Park, Pa., was the recipient of the second Charles Henry Proctor Memorial Leadership Award, the AES' highest nonscientific, nontechnical award. The award was conferred for outstanding leadership and AES service performed as creator of the acclaimed "Hydrogen Embrittlement in Metal Finishing" Symposium held by the society at its Los Angeles Convention in July 1960, and service as AES Editor of the book being published embodying not only these convention papers but also others marshaled for the AES on that subject by Dr. Read. Dr. Read was presented with a $150 cash award plus a laminated scroll on Friday evening, June 23, by Selection Committee Chairman W. Andrew Wesley. The others on the Committee were Mr. and Mrs. Osborne Preston, John P. Nichols, D. G. Foulke, Samuel S. Johnston, Warren B. Eliot, and William M. Robinson.

The AES' newly established Zinc Award went to coauthors Hugh R. Miller, Robert W. Hardy, William H. Safranek, and Charles L. Faust of Battelle Memorial Institute, Columbus, Ohio, for their paper entitled "Data on the Corrosion Resistance of Electroplated Zinc Die Castings." The paper covers one facet of a continuing research program at Battelle directed toward improved plating on zinc die castings, such as those used in the decorative trim of automobiles.

The Chromium Plating Award was presented to William H. Safranek and Robert W. Hardy for their paper entitled "Use of Selenic Acid for Plating Microcracked, Protective, and Decorative Chromium Plate." The paper describes research conducted by the Battelle Technologists which has resulted in the use of a selenium acid additive in plating solutions to obtain improved chromium plate.

Manuscripts and Abstracts for Spring 1962 Meeting

Papers are now being solicited for the Spring Meeting of the Society, to be held at the Statler Hilton Hotel in Los Angeles, Calif., May 6, 7, 8, 9, and 10, 1962. Technical Sessions probably will be scheduled on Electric Insulation, Electronics (including Luminescence, Semiconductors, Optical Masers, and Nonconventional Electron Emitters), Electrothermics and Metallurgy (including a Symposium on Thermodynamics and Kinetics of Gas-Condensed Phase Reactions at High Temperatures), Industrial Electrolytics, and Theoretical Electrochemistry.

To be considered for this meeting, triplicate copies of abstracts (*not exceeding 75 words in length*) must be received at Society Headquarters, 1860 Broadway, New York 23, N. Y., *not later than December 15, 1961. Please indicate on abstract for which Division's symposium the paper is to be scheduled and underline the name of the author who will present the paper.* No paper will be placed on the program unless one of the authors, or a qualified person designated by the authors, has agreed to present it in person. An author who wishes his paper considered for publication in the JOURNAL should send triplicate copies of the manuscript to the Managing Editor of the JOURNAL, 1860 Broadway, New York 23, N. Y.

Presentation of a paper at a technical meeting of the Society does not guarantee publication in the JOURNAL. However, all papers so presented become the property of The Electrochemical Society, and may not be published elsewhere, either in whole or in part, unless permission for release is requested of and granted by the Editor. Papers already published elsewhere, or submitted for publication elsewhere, are not acceptable for oral presentation except on invitation by a Divisional program Chairman.

Division News

Electric Insulation Symposium, Spring 1962

The Electric Insulation Division plans to hold symposia at the 121st Meeting of The Electrochemical Society to be held at the Statler Hilton Hotel in Los Angeles, Calif., during the period May 6-10, 1962. Plans are being made for sessions to be held on the following subjects:

(*A*) Ceramics and Integrated Circuits. Session Chairman: B. R. Eichbaum, Aeronutronics, Newport Beach, Calif.

(*B*) Thin Film Dielectrics and Electrolytic Capacitors. Session Chairmen: C. C. Houtz, Bell Telephone Labs., Inc., Murray Hill, N. J., and R. A. Ruscetta, General Electric Co., Irmo, S. C.

(*C*) Reliability. Session Chairman: Hans M. Wagner, Lockheed Aircraft Corp., 3251 Hanover St., Palo Alto, Calif.

(*D*) Paper. Session Chairman: E. D. Eich, Anaconda Wire & Cable Co., Hastings-on-Hudson, N. Y.

As in the past, all that is required for presentation at an Electric Insulation session is that a 75-word abstract be in the hands of the Session Chairman *by December 15, 1961.*

B. R. Eichbaum,
Secretary-Treasurer

E & M Symposium, Spring 1962

As a part of the Spring 1962 Meeting of The Electrochemical Society, to be held in Los Angeles, Calif., May 6-10, the Electrothermics and Metallurgy Division will hold a symposium on "Thermodynamics and Kinetics of Gas-Condensed Phase Reactions at High Temperatures."

Electronics Symposia, Spring 1962

For the 1962 Los Angeles Spring Meeting of The Electrochemical Society, the Electronics Division is planning four symposia. In addition to the usual sessions on Luminescence and Semiconductors, symposia on Optical Masers and on Nonconventional Electron Emitters are to be scheduled.

The Program Chairmen for these symposia are:

Luminescence—Dr. Henry Ivey, Research Dept., Lamp Div., Westinghouse Electric Corp., Bloomfield, N. J.

Semiconductors—Dr. Roger Newman, Sperry Rand Corp., Sudbury, Mass.

Optical Masers—Dr. Joseph Birman, General Telephone & Electronics Labs., Bayside Labs., Bayside 60, N. Y.

Nonconventional Electron Emitters—Dr. Charles P. Marsden, Section 14.2, National Bureau of Standards, Washington 25, D. C.

In order for a paper to be accepted in the first three of these symposia, triplicate copies of a 75-word abstract should be sent direct to the above Program Chairmen and be in their hands not later than *December 15, 1961.* Because of special planning required for the symposium on Nonconventional Electron Emitters, 75-word abstracts are required by *October 15, 1961.*

Papers will be accepted for the above symposia only with the understanding that a 1000-word extended abstract will be submitted in time for inclusion in the Electronics Division Abstracts booklet. Deadline date for extended abstracts is *January 15, 1962.* It is expected that this booklet will be available about one month prior to the meeting. In preparing the enlarged abstract the following points should be observed.

1. Type abstracts double-spaced on 8½ in. x 11 in. paper. Send at least one original copy.

2. Try to restrict the abstract to approximately 1000 words.

3. Keep the number of drawings or photographs to a minimum.

4. If you must submit photographs, submit only glossy prints with sharp detail. Size is preferably 5 in. x 7 in.

5. Drawings preferably should be made on tracing cloth, 8½ in. x 11 in., with India ink. Do not use larger size. Do not send carbon copy or Ditto drawings, since these would have to be redrawn.

In addition to the above special requirements, the usual Society regulation will be observed that no paper will be placed on the program unless one of the authors or a duly qualified person designated by the authors has agreed to present it in person.

Section News

Chicago Section

Dr. Ralph Wehrmann, the new Chairman of the Section, called a meeting on Friday evening, June 23, to discuss Section activities for the coming year.

The newly elected Section officers for 1961-1962 are:

Chairman—Ralph Wehrmann, Fansteel Metallurgical Corp., 2200 Sheridan Rd., North Chicago, Ill.

Vice-Chairman—Raymond D. Chelton, Continental Can Co., Inc., 7622 S. Racine Ave., Chicago 20, Ill.

Treasurer—John J. Daly, Jr., Continental Can Co., Inc., 1350 W. 76 St., Chicago 20, Ill.

Local Section Councilor (1961-1964)—E. L. Koehler, Continental Can Co., Inc., 7622 S. Racine Ave., Chicago 20, Ill.

Chicago Technical Societies Council Representative—E. L. Koehler

C. A. Hampel continues as Local Section Councilor (1960-1962).

An informal discussion was held concerning the types of subjects to be discussed during fall and winter monthly meetings of the Local Section, an attempt being made to identify the major interests in this particular Section. Branches of the science such as batteries, corrosion, insulation, semiconductors, electroorganics, and others of general interest were included in the discussion, the purpose of which was simply to give the greatest emphasis to the sciences most prevalent in this area.

The Local Section meeting site was not changed; it remains at Chicago Engineers Club, 314 S. Federal. Meeting dates have been changed to the second Thursday of the month, beginning with October and ending with April. The meeting in January 1962, however, will occur on Wednesday, January 24. The new officers were assigned the task of securing "top-notch" speakers for the monthly meetings.

The meeting was adjourned with great hopes for the future of the Society, with particular emphasis on the ensuing year.

George Timmings, *Secretary*

Personals

M. M. Beckwith has left Harshaw Chemical Co., Cleveland, Ohio, to take a position with R. O. Hull & Co., Inc., Rocky River, Ohio.

James F. Brady has joined the materials and equipment section of Monsanto Chemical Co.'s Research and Engineering Div. at St. Louis, Mo., after serving with McDonnell Aircraft Corp., St. Louis.

N. H. Furman has been appointed R. J. Reynolds Tobacco Co. Professor of Chemistry, Wake Forest College, Winston-Salem, N. C. A master's degree program in chemistry and in five other departments is being instituted at Wake Forest College this fall.

Ronald T. Macdonald has been appointed to the position of research associate at the California Research Corp., Richmond, Calif. Dr. Macdonald joined Calresearch in 1935. His early work was concerned with greases and industrial lubricants. Recently, he served as a technical specialist on the staff of Calresearch's vice-president for petroleum products. He currently is conducting a basic study of the mechanism of the chemical reactions occurring at fuel cell electrodes.

Stanley M. Norwood, noted metallurgist and vice-president of Union Carbide Metals Co., Div. of Union Carbide Corp., New York City, was honored on August 31 with a testimonial dinner on the occasion of his retirement. He was presented with a stainless steel tray bearing the inscription: "To Stanley M. Norwood, from his many friends at Union Carbide on the occasion of his retirement after 43 years of meritorious service."

During the early part of his career with Union Carbide, Mr. Norwood was a pioneer in the development, production, and fabrication of stainless and alloy steels. He worked closely with the stainless steel producers in the development of the various grades of stainless in the form of seamless tubes, sheets, bars, and wire. In addition, he cooperated closely with fabricators of various equipment such as tanks and piping used in the chemical industry and by dairies, and on other now prominent applications of this steel. These efforts contributed greatly to the present acceptance and wide use of stainless steel in industry.

Mr. Norwood will continue to be associated with Union Carbide Metals Co. on a consulting basis.

David R. Rhodes has completed work toward the Ph.D. degree at the University of Illinois and has joined the Petroleum Products group, Richmond Lab., California Research Corp., as a research chemist.

Harry L. Saums, consulting engineer for magnet wire at the Anaconda Wire and Cable Co.'s Magnet Wire Research and Development Lab., Hastings-on-Hudson, N. Y., has received an honorary electrical engineering degree from South Dakota State College. This was the first such degree ever awarded by the college.

Mr. Saums has spent the last 30 years in magnet wire technical research and development work for Anaconda. He helped establish the Magnet Wire Lab. 11 years ago and was its director until recently, when he was relieved of routine administrative duties in order that his full time could be devoted to experimental and development work on high-temperature conductors and insulations.

Sumner Sheff is now senior engineer in the Materials Dept. at Motorola Semiconductor Products Div., 5005 E. McDowell Rd., Phoenix, Ariz. His former association was with Raytheon Co., Semiconductor Div., Newton, Mass.

Book Reviews

Metallic Corrosion Inhibitors, by I. N. Putilova, S. A. Balezin, and V. P. Barannik. Translated from the Russian by G. Ryback. Published by Pergamon Press, Inc., New York–London–Paris, 1960. viii + 196 pages; $10.00.

This is a review and discussion of theory and practice in the application of inhibitors. The first two chapters review the general requirements for inhibitors, classify them into types such as adsorption, film-forming, deactivation of medium (as oxygen or nitrous acid removal), passivation, extension of induction period; and discuss inhibition mechanism. Four more chapters deal with inhibition in aqueous acids, aqueous bases, nearly neutral salt solutions, nonaqueous or mixed media, and protection against the atmosphere, particularly in "mothballing" or storage.

About 350 materials used or tested as inhibitors are mentioned, the more important ones being discussed in detail, with considerable illustrative quantitative data. The nature of some commercial inhibitive preparations used in Soviet industry is discussed, and the appendices give directions for using these in pickling and boiler cleaning.

Some 330 literature and patent references are given, 45% of them to Soviet publications (including Russian translations of well-known books in other languages). The latest references are to 1955. The emphasis is on practical uses of inhibitors, and the theory is at times outmoded or contradictory, since different viewpoints are presented with little criticism. The authors favor the film formation viewpoint, feeling that strong adsorption is only a preliminary to chemical reaction.

The text is reproduced from typewritten copy but is easily readable. There are very few errors.

C. V. King

Thermodynamics, 2nd Edition, by Gilbert Newton Lewis and Merle Randall. Revised by Kenneth S. Pitzer and Leo Brewer. Published by McGraw-Hill Book Co., New York, 1961. 723 pages; $12.50.

The first edition of this book consisted of two parts, a textbook on chemical thermodynamics and a critical compilation of thermodynamic data. The revision brings the textbook up to date. However, since the large amount of data which has accumulated since 1923 is now available in many volumes issued by several continuing projects, these latter are described in an appropriate section of the book. The revisors do include as appendices several useful tables and such thermodynamic data as would be useful in solving the many problems in the text.

The first thread of the chapters, constituting an introduction to the first two laws, is essentially the original text. However, it is evident that every line has been carefully scrutinized before retention. Small changes in wording, interpolation of some new sections, and revision of the numerical data used as illustrative material occur throughout.

The remaining two thirds make a modern text of this revision. New, expanded chapters include those on real gases; the critical state and reduced coordinates; the third law (completely revised); nonelectrolyte and polymer solutions, regular solutions; theories of electrolyte solutions; statistical thermodynamics; irreversible thermodynamics; surface, gravitational, electrical, and magnetic effects; multicomponent systems; hydrogen and helium at low temperatures. The concept of the Gibbs chemical potential is introduced and applied, especially in the chapter on solutions. Readers of this JOURNAL will be interested in

Notice to Members and Subscribers

(Re Changes of Address)

To insure receipt of each issue of the JOURNAL, please be sure to give us your old address, as well as your new one, when you move. Our records are filed by states and cities, not by individual names. The Post Office does not forward magazines.

We should have this information *by the 16th of the month* to avoid delays in receipt of the next issue.

the handling of the concept of electrode potentials. The term "electrode potential" is reserved for the original Gibbs definition, essentially the same as the Stockholm Convention definition. This is not in conflict with the sign convention used in physical chemistry. As an examination of recent physical chemistry texts will show, the word potential is always modified by oxidation (or reduction). "Oxidation potentials" are also used in this revision. As long as it is remembered that such a potential is always associated with a half reaction which is an oxidation, it need not lead to difficulty. The proper combination of "oxidation potentials" leads to the same signs for the electrodes of a cell as do "electrode potentials."

To sum up, this classic of the 'twenties has been made into a text for the 'sixties.

David Lewis

News Items

1962 Appalachian Underground Corrosion Short Course

The Appalachian Underground Corrosion Short Course, held annually at West Virginia University, Morgantown, W. Va., covers basic, intermediate, and advanced subjects on underground corrosion, and includes exhibits and field demonstrations.

Dates for the 1962 course will be announced in a later issue; the officers for 1962 are: General Chairman, E. K. Bensen, New York Telephone Co.; Program Chairman, C. W. Beggs, Public Service Electric and Gas Co.; Exhibits Chairman, G. G. Campbell, West Virginia University; Operations Chairman, L. H. West, Standard Oil Co. (Ohio); Publications Chairman, F. A. Radford, Cabot Corp.; Publicity Chairman, W. E. Cook, Jr., Pipe Line Service Corp.; and Registration Chairman and Secretary, R. E. Hanna, Jr., West Virginia University.

Attendance at the 1961 Course reached a total of 600.

Conference on Anodized Aluminum

The Aluminium Development Association, London, with the University of Nottingham Dept. of Metallurgy, held a residential Conference on Anodized Aluminum at the University from September 12 to 14. The aim of the conference was twofold: to provide an opportunity for anodizers, users of anodized aluminum, and the industry in general to discuss the latest technical developments; to give research workers in the field an opportunity to discuss the fundamental aspects of their subject.

Fifteen papers were presented in six technical sessions: I. Anodizing from the User's Viewpoint; II. Special Surface Characteristics; III. Current Views on Anodic Coatings; IV. Industrial Applications; V. Theory of Related Processes; VI. Advances in Anodizing Techniques. The papers were printed and distributed before the conference.

Further information can be obtained from the Secretary, The Aluminium Development Association, 33 Grosvenor St., London, W. 1, England.

Wiley Merger with Interscience Publishers

A joint statement was issued recently by John Wiley & Sons, Inc., and Interscience Publishers, Inc., announcing the merger of the two publishing houses under the name of John Wiley & Sons, Inc. The merger was made through the acquisition by Wiley of all Interscience stock.

The expansion of the editorial programs of both houses will be maintained and the Interscience imprint will continue as a separate Wiley Division under the direction of the present officers of Interscience. Maurits Dekker and Eric S. Proskauer have become vice-presidents of Wiley and members of its board of directors. Dr. Proskauer will serve as Editor-in-Chief of the Interscience Publishing Program, and Dr. Dekker will devote his attention to research and development on a company-wide basis.

The joining of forces of the two firms will add more than 650 scientific and technical reference works to Wiley's current list of over 1800 titles in science, engineering, and the social sciences. It is believed that the Interscience list, with its emphasis on the highly specialized areas of scientific and technical research, will complement ideally the existing Wiley titles, which show a more diversified range of interest.

Notice to Subscribers

Your subscription to the JOURNAL of The Electrochemical Society will expire on *December 31, 1961*. Avoid missing any issue. Send us your remittance now in the amount of $24.00 for your 1962 subscription. (Subscribers located outside the United States must add $1.50 to the subscription price for postage, and payment must be made by Money Order or New York draft, not local check.) An expiration notice has been mailed to all subscribers.

A bound volume of the 1962 JOURNALS can be obtained at the prepublication price of $8.00 by adding this amount to your remittance. However, no orders will be accepted at this rate after *December 1, 1961*, when the price will be increased to $24.00 subject to prior acceptance. Bound volumes are *not* offered independently of your JOURNAL subscription.

Certification of Unsaturated Standard Cells Discontinued by N.B.S.

The National Bureau of Standards has discontinued the certification of emf of unsaturated standard cells as of June 30, 1961. An exception will be made for public utilities and other agencies having operations of such a nature as to require these services from the Bureau. This action is in keeping with the Bureau's long-standing policy of discontinuing certain measurement services which become adequately available at other laboratories. The Bureau will continue, however, to conduct referee tests or to undertake calibration of unsaturated cells when special or unusual circumstances are involved.

Part of the time previously spent in the testing and certification of unsaturated cells now will be allocated to the increasing number of saturated cells, and part of it will be devoted to basic research on saturated cells having greater stability and a lower temperature coefficient of emf.

Ground Broken for New N.B.S. Laboratories

On June 14, 1961, ground was broken for the new National Bureau of Standards laboratories at Gaithersburg, Md. The ceremony signaled the initial construction phase for a 20-building, $104,000,000 research facility which will permit complete relocation of the Bureau from Northwest Washington to the 555-acre site in Montgomery County.

The ground breaking took place on the site for a high-priority facility, an Engineering Mechanics Lab. This building will house a 1,000,000-pound dead weight machine which will enable the Bureau to provide

urgently needed force measurement standards to meet the multimillion-pound thrust requirements of the space program. The initial construction phase, in addition to the Engineering Mechanics Lab., calls for a boiler plant and site development. Later work will include construction of a Radiation Physics Lab. (including a linear accelerator), seven modern interconnecting general-purpose laboratory buildings, a number of additional special purpose laboratories, and an atomic reactor.

In addition to the 1,000,000-pound dead weight machine, the Engineering Mechanics Lab. will contain a gravity chamber, other dead weight testing machines of 100,000 pounds and 300,000 pounds capacity, a vertical tension and compression testing machine capable of loads up to 10,000,000 pounds, and an Emery horizontal testing machine with a capacity of 2,300,000-pound loads in compression and 1,500,000-pound loads in tension.

Study of Coatings Formed by Cathodic Protection

Coatings that form on steel being cathodically protected from salt water corrosion effectively reduce the amount of externally applied current required, according to a recent National Bureau of Standards experiment. Polarization measurements made near the end of a period of almost five years of exposure showed that protection was maintained, even though the protective current ultimately was reduced more than 200-fold. Experimental data derived from the study may be applied to certain types of corrosion problems (1). Spectrochemical analysis showed the coatings to consist mainly of calcium carbonate although some silicates were present.

Reference

1. For further technical details, *see* "Coatings Formed on Steel by Cathodic Protection and Their Evaluation by Polarization Measurements," by W. J. Schwerdtfeger and R. J. Manuele, *J. Research Nat. Bur. Standards*, **65C**, No. 3 (1961).

Notice to Members

Re Voting Ballot

You soon will receive your official voting ballot from Society Headquarters. Please return it *by December 15* so that your vote can be included in the final election count.

Yardney Electric Reveals New Fuel Cell Principle

An entirely new concept in electrode design may lead to a commercial breakthrough in fuel cell research and development according to Yardney Electric Corp. The new principle of electrode design is the result of an extensive research program conducted by Yardney International Corp. under the direction of Ricardo Salcedo, Spanish scientist and founder of the Institute of Applied Physics in that country.

The Yardney fuel cell concept involves the use of electrodes treated with radioactive isotopes. This method, for which patent applications have been filed, has produced an impressive decrease in polarization as compared with untreated electrodes. Military sources have shown particular interest in the new development.

The techniques used to manufacture the Yardney fuel cell electrode indicate that an extremely flexible plate design may be developed. The use of oxygen electrodes made of sintered porous silver would permit the construction of a simplified basic cell design that will be more resistant to environmental stresses than any of the systems known at present.

Testing of the new fuel cell concept shows that the use of radioisotopes as catalyst for the oxygen electrode in low-temperature alkaline electrolyte permits a current density of 150 ma/cm^2 to be sustained for extended time periods at polarizations of 0.2-0.3 v. To the time of this printing, tests show that the voltage does not change with time. Research is now being conducted to determine the ultimate operating life of radioisotope impregnated electrodes.

High-Purity Cesium Available from Dow

The Dow Chemical Co.'s production of cesium in the exceptionally high purity of over 99.9% recently was announced by W. J. Rave, manager of the Metals Dept. The metal is priced at $375.00 a pound in quantities of one to four pounds, and $325.00 a pound for five to nine pounds. Less than a pound is available at $1.00 a gram with a packaging charge depending on the size of the ampules.

Cesium is sold by Dow in steel and glass containers and also in a multi-ampuled "porcupine" package. The "porcupine" is designed to assist researchers using cesium in small amounts. A number of graduated ampules protrude from the body of the glass package; these cesium-containing units can be sealed off individually without contaminating the metal.

Current cesium production in the United States is only a few hundred pounds annually, but steady growth is predicted. Dow's Metals Dept. produces cesium in Midland, Mich., through a metal-reduction process developed by Robert J. Moolenaar in the Electrochemical and Inorganic Chemical Research Lab. Production capacity is several pounds a day, but expansion would be no problem. The company has been this country's only producer of cesium bromide since a process for separating it from the other alkali bromides, by use of liquid bromine as a solvent, was discovered by V. A. Stenger and W. R. Kramer in a Dow laboratory 15 years ago.

M.I.T. Awarded Advanced Research Projects Agency Contract

The Massachusetts Institute of Technology, Cambridge, has been notified of a $3,275,000 contract from the Advanced Research Projects Agency for materials research, Dr. Julius A. Stratton, president of M.I.T. announced recently.

The contract is one of five for a total of $13,375,000 made with five universities under the Dept. of Defense Interdisciplinary Materials Laboratory Program. It will make possible extensive basic research at M.I.T. in a new $6,000,000 Center for Materials Science and Engineering, funds for which are now being sought with the hope that the building can be completed by 1964. A broad program of education in materials will be coordinated with the research activity, Dr. Stratton said.

The expansion made possible by the ARPA contract will include an increase in M.I.T.'s already extensive materials research program. In addition, part of the new support will go for entirely new studies, which will be coordinated with existing

1962 Bound Volume

Members and subscribers who wish to receive bound copies of Vol. 109 (for 1962) of the JOURNAL can receive the volume for the low, prepublication price of $8.00 if their orders are received at Society Headquarters, 1860 Broadway, New York 23, N. Y., *by December 1, 1961.*

Bound volumes are *not* offered independently of JOURNAL subscription.

work and which will represent a new and unified program.

Scientific objectives of the new program will lie principally in four active fields considered likely to lead to important future results and likely to attract an increasing number of students: Magnetic and Low-Temperature Research; Semiconductors and Their Applications to Devices; Electronic Materials Development and Preparation; Solid-State Structure Studies by Advanced Techniques.

Related to the research programs and designed to serve the entire Center for Materials Science and Engineering will be central facilities for crystal preparation and analysis and for electron microscopy of materials.

The new center also will benefit from a complex of special M.I.T. facilities already in existence or planned. These include the nuclear reactor; two IBM 709 Computers, one in the Computation Center and a second on order; the M.I.T. Spectroscopy Lab., and the National Magnet Facility. The last, to be built under contract with the Air Force, will be the world's most powerful continuous field magnet.

International Rectifier's Japanese Affiliate to Expand Plants

International Rectifier Corp., El Segundo, Calif., has disclosed a two-stage expansion program to enlarge administrative and manufacturing facilities of its Japanese affiliate at Soya, Hatano, in the Kanagawa Prefecture. According to International Rectifier Corp. (Japan) Ltd., the plans call for an investment of approximately $1,000,000 to increase the annual production rate from $1,000,000 to approximately $3,000,000 during 1963.

The facility, established in 1957, was the first to produce silicon power rectifiers in Japan, and also the first of International Rectifier's joint overseas ventures, which now include affiliated firms in the United Kingdom, France, and Italy.

The Japanese company had advised of plans to start an office building and factory addition on the site of the present plant in August of 1961, to be fully operational by April 1962.

Dow to Start Construction of Major Laboratory in California

The Dow Chemical Co. recently announced plans for construction of the first major laboratory buildings at its research site on Oak Grove Rd. in the city of Walnut Creek, Calif. Construction tentatively was scheduled to begin August 15 and to be completed about June 1, 1962. The new research center is located approximately 30 miles from San Francisco.

The first step of the installation will consist of a laboratory building and a separate administrative building. The research facilities will be devoted to the laboratory exploration of new chemical compounds and processes.

Dow Corning Silicon Plant in Production

The first fully integrated high-purity silicon plant in America using the Siemens process is now in production. The new facilities are those of the Hyper-Pure Silicon Division of Dow Corning Corp. at Hemlock, 15 miles south of Dow Corning's main plant in Midland, Mich.

The Hyper-Pure Silicon Division occupies seven buildings totaling 37,000 square feet of floor space on an immediate site of 30 acres in a tract of 570 acres, and represents an investment of more than $2,000,000 at this time. The capacity is now 25,000 pounds of high-purity silicon a year. This amount can be doubled within the present buildings. Both Polycrystalline silicon in several forms and a float-zoned single crystal are being produced.

Announcements from Publishers

"Protection of Refractory Metals for High Temperature Service. Progress Report 1—July 1, 1960—The Zinc-Base Coating for Niobium," B. F. Brown and others, U. S. Naval Research Lab., Nov. 1960. Report PB 161 932,* 37 pages; $1.00.

Translations of Soviet Papers Available from Primary Sources

The following are among Soviet scientific papers available in English translation from Primary Sources, Dept. C-R, 11 Bleecker St., New York 12, N. Y. When ordering, please quote the reference number given in parentheses after the author's name.

Zavodskaya Laboratoriya
(Factory Laboratory)

"Determination of Carbides in Stainless Steels by Electrolysis," M. M. Shapiro (SMT-1162), **11**, 1292-1294 (1957); $5.00.

* Order from Office of Technical Services, Business and Defense Services Administration, U.S. Dept. of Commerce, Washington 25, D. C.

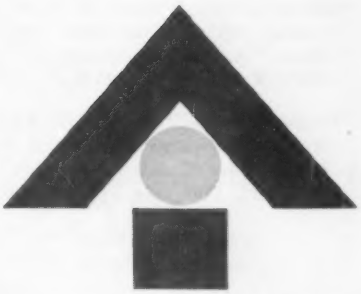

WELCOME ABOARD!

Responsible research positions for

PHYSICAL CHEMISTS
ELECTROCHEMISTS
ELECTROANALYTICAL CHEMISTS

We're seeking men with experience, to research phenomena related to fuel cells and other galvanic systems and investigate electrode kinetics, polarization, catalysis, and electroanalytical techniques.

Astropower is an expanding propulsion R & D firm located in the ideally situated research center at Newport Beach, California, one of the finest recreation areas in the world. Superior employee benefits. Submit resumes to Dr. George Moe, Vice President, Research. Qualified applicants will receive consideration without regard to race, creed or national origin.

ASTROPOWER, INC.
A subsidiary of Douglas Aircraft Co.
2968 Randolph Avenue
Costa Mesa, California

"Microelectrical Method of Investigating Metal Corrosion under Stress," A. V. Ryabchenkov (SMT-1242), **2**, 167-173 (1958); $5.00.

"Research on the Theory of the Electrochemical Phase Analysis of Alloys," Yu. A. Klyachko (SMT-2111), **11**, 1308-1314 (1958); $5.00.

Tsvetnye Metally
(Nonferrous Metals)

"Ni-W, Ni-Ca, and Ni-Sr Alloys for Oxide Cathodes of Radio Tubes," I. L. Rogel'berg (SMT-1137), **11**, 67-74 (1957); $5.00.

"A Survey of the Present State of Zinc Electrolysis," G. N. Pakhmova (CR-2826), **4**, 16-28 (1958); $19.80.

"An Electrothermic Method of Zinc Distillation from Silver Crust," I. I. Kershansky (SMT-1377), **4**, 34-43 (1958); $5.00.

"The Role of Electrolyte Composition in Intensifying the Working Aluminum Baths," A. I. Belyayev (CR-2822), **10**, 61-66 (1958); $6.60.

"Simulating the Electric Field of an Aluminum Electrolyzer Anode," M. A. Korobov (CR-2746), **11**, 60-66 (1958); $9.10.

"Reduced Consumption of Fluoride Salts and Increased Labor Output in Aluminum Production," A. E. Manin (CR-2823), **5**, 67-72 (1959); $9.30.

"Some Questions Concerning Obtaining Titanium by Molten Media Electrolysis Using Soluble Anodes," A. B. Suchkov (SMT-2469), **8**, 50-54 (1959); $5.00.

Issledovatel Mineral Syr'ya Sbornik
(Collection of Research on Mineral Raw Material)

"A New Electrochemical Method of Separating Minerals," Ye. V. Rozhkova (CR-2743), 67-74 1955); $8.40.

ADVANCED SOLID STATE RESEARCH & DEVELOPMENT

Senior scientists and engineers are needed to fill new positions in our rapidly expanding research and development laboratories near San Francisco. Our broadening interests have created challenging positions for individuals with significant backgrounds in the following fields:

SURFACE PHYSICS AND CHEMISTRY
ELECTROCHEMISTRY
ELECTRON MICROSCOPY
MAGNETIC THIN FILMS
EVAPORATED CIRCUITRY
SEMICONDUCTOR MATERIALS
ELECTRO-OPTICS
ADVANCED CIRCUIT DEVELOPMENT
MICROWAVE PHYSICS

A Ph.D. Degree or commensurate experience is especially desirable.
Applicants are invited to send detailed resumes, including salary history and requirements, to Mr. Donald Palmer. Palo Alto interviews for qualified applicants will be arranged from anywhere in the United States. All inquiries strictly confidential and acknowledged promptly. All qualified applicants will be considered regardless of race, creed, color or national origin.

FAIRCHILD
SEMICONDUCTOR
844 CHARLESTON ROAD • PALO ALTO, CALIFORNIA

Employment Situations

Please address replies to box shown, c/o The Electrochemical Society, 1860 Broadway, New York 23, N. Y.

Position Wanted

Chemical Engineer, B.S.—Fifteen years' industrial experience—12 years of electrolytic background in development and production work. Supervisory experience. Married, family, 39. *Reply to Box No. 372.*

Position Available

Research Chemist for Research Associate position at the National Bureau of Standards to conduct original research on galvanic phenomena associated with atmospheric corrosion. M.S., Ph.D., or equivalent research experience required. *Reply to Fielding Ogburn, Electrolysis and Metal Deposition Section, National Bureau of Standards, Washington 25, D. C.*

Advertiser's Index

Astropower, Inc., Div. of Douglas Aircraft Co. 237C
Fairchild Semiconductor Corp. 238C
Great Lakes Carbon Corp., Electrode Div. ..... Cover 2
Rowe Products, Inc. 225C
E. H. Sargent & Co. 228C
Stackpole Carbon Co. 227C

The Electrochemical Society

Patron Members

Aluminum Co. of Canada, Ltd.,
Montreal, Que., Canada

International Nickel Co., Inc.,
New York, N. Y.

Olin Mathieson Chemical Corp.,
Chemicals Div., Industrial Chemicals
Development Dept., Niagara Falls, N. Y.

Union Carbide Corp.
Divisions:
Union Carbide Metals Co.,
New York, N. Y.
National Carbon Co., New York, N. Y.

Westinghouse Electric Corp., Pittsburgh, Pa.

Sustaining Members

Air Reduction Co., Inc.,
New York, N. Y.

Ajax Electro Metallurgical Corp.,
Philadelphia, Pa.

Allen-Bradley Co., Milwaukee, Wis.

Allied Chemical Corp.
Solvay Process Div., Syracuse, N. Y.
General Chemical Div., Morristown, N. J.

Alloy Steel Products Co., Inc., Linden, N. J.

Aluminum Co. of America,
New Kensington, Pa.

American Metal Climax, Inc.,
New York, N. Y.

American Potash & Chemical Corp.,
Los Angeles, Calif. (2 memberships)

American Smelting and Refining Co.,
South Plainfield, N. J.

American Zinc Co. of Illinois,
East St. Louis, Ill.

American Zinc, Lead & Smelting Co.,
St. Louis, Mo.

American Zinc Oxide Co., Columbus, Ohio

M. Ames Chemical Works, Inc.,
Glens Falls, N. Y.

Armco Steel Corp., Middletown, Ohio

Basic Inc., Maple Grove, Ohio

Bell Telephone Laboratories, Inc.,
New York, N. Y. (2 memberships)

Bethlehem Steel Co., Bethlehem, Pa.
(2 memberships)

Boeing Airplane Co., Seattle, Wash.

Burgess Battery Co., Freeport, Ill.
(4 memberships)

Canadian Industries Ltd., Montreal,
Que., Canada

Carborundum Co., Niagara Falls, N. Y.

Catalyst Research Corp., Baltimore, Md.

Columbian Carbon Co., New York, N. Y.

Consolidated Mining & Smelting Co. of
Canada, Ltd., Trail, B. C., Canada
(2 memberships)

Continental Can Co., Inc., Chicago, Ill.

Cooper Metallurgical Associates, Cleveland,
Ohio

Corning Glass Works, Corning, N. Y.

Diamond Alkali Co., Painesville, Ohio

Dow Chemical Co., Midland, Mich.

Wilbur B. Driver Co., Newark, N. J.
(2 memberships)

E. I. du Pont de Nemours & Co., Inc.,
Wilmington, Del.

Eagle-Picher Co., Chemical Div., Joplin, Mo.

Eastman Kodak Co., Rochester, N. Y.

Thomas A. Edison Research Laboratory, Div.
of McGraw-Edison Co., West Orange, N. J.

Electric Auto-Lite Co., Toledo, Ohio
C & D Division, Conshohocken, Pa.

Electric Storage Battery Co., Yardley, Pa.

Engelhard Industries, Inc., Newark, N. J.
(2 memberships)

The Eppley Laboratory, Inc., Newport, R. I.
(2 memberships)

Exmet Corp., Tuckahoe, N. Y.

Fairchild Semiconductor Corp., Palo Alto,
Calif.

Food Machinery & Chemical Corp.
Becco Chemical Div., Buffalo, N. Y.
Westvaco Chlor-Alkali Div., South
Charleston, W. Va.

Foote Mineral Co., Paoli, Pa.

Ford Motor Co., Dearborn, Mich.

General Electric Co., Schenectady, N. Y.
Chemistry & Chemical Engineering
Component, General Engineering
Laboratory
Chemistry Research Dept.
General Physics Research Dept.
Metallurgy & Ceramics Research Dept.
Aircraft Accessory Turbine Dept.,
West Lynn, Mass.

General Instrument Corp., Newark, N. J.

General Motors Corp.
Allison Div., Indianapolis, Ind.
Delco-Remy Div., Anderson, Ind.
Guide Lamp Div., Anderson, Ind.
Research Laboratories Div., Warren, Mich.

General Telephone & Electronics
Laboratories Inc., Bayside, N. Y.
(2 memberships)

(Sustaining Members cont'd)

Gillette Safety Razor Co., Boston, Mass.
Globe-Union, Inc., Milwaukee, Wis.
Gould-National Batteries, Inc.,
Minneapolis, Minn.
Grace Electronic Chemicals, Inc.,
Baltimore, Md.
Great Lakes Carbon Corp., New York, N. Y.
Hanson-Van Winkle-Munning Co.,
Matawan, N. J. (2 memberships)
Harshaw Chemical Co., Cleveland, Ohio
(2 memberships)
Hercules Powder Co., Wilmington, Del.
Hewlett-Packard Co., Palo Alto, Calif.
Hill Cross Co., Inc., West New York, N. J.
Hoffman Electronics Corp., Semiconductor
Div., El Monte, Calif. (2 memberships)
Hooker Chemical Corp., Niagara
Falls, N. Y. (3 memberships)
Hughes Aircraft Co., Culver City, Calif.
International Business Machines Corp.,
Yorktown Heights, N. Y.
International Minerals & Chemical
Corp., Skokie, Ill.
ITT Federal Laboratories, Div. of
International Telephone & Telegraph
Corp., Nutley, N. J.
Jones & Laughlin Steel Corp.,
Pittsburgh, Pa.
K. W. Battery Co., Skokie, Ill.
Kaiser Aluminum & Chemical Corp.
Div. of Chemical Research,
Permanente, Calif.
Div. of Metallurgical Research,
Spokane, Wash.
Kawecki Chemical Co., Boyertown, Pa.
Kennecott Copper Corp., New York, N. Y.
Leesona Moos Laboratories, Div. of Leesona
Corp., Jamaica, N. Y.
Libbey-Owens-Ford Glass Co., Toledo, Ohio
Lockheed Aircraft Corp.,
Missiles & Space Div., Sunnyvale, Calif.
Mallinckrodt Chemical Works, St. Louis, Mo.
P. R. Mallory & Co., Indianapolis, Ind.
Merck & Co., Inc., Rahway, N. J.
Metal & Thermit Corp., Detroit, Mich.
Miles Chemical Co., Div. of Miles
Laboratories, Inc., Elkhart, Ind.
Minneapolis-Honeywell Regulator Co.,
Minneapolis, Minn.
Minnesota Mining & Manufacturing Co.,
St. Paul, Minn.
Monsanto Chemical Co., St. Louis, Mo.
Motorola, Inc., Chicago, Ill.
National Cash Register Co., Dayton, Ohio
National Lead Co., New York, N. Y.
National Research Corp., Cambridge, Mass.
National Steel Corp., Weirton, W. Va.
North American Aviation, Inc., Rocketdyne
Div., Canoga Park, Calif.
Northern Electric Co., Montreal, Que.,
Canada
Norton Co., Worcester, Mass.
Ovitron Corp., Long Island City, N. Y.
Peerless Roll Leaf Co., Inc., Union City, N. J.
Pennsalt Chemicals Corp.,
Philadelphia, Pa.
Phelps Dodge Refining Corp., Maspeth, N. Y.
Philco Corp., Research Div., Blue Bell, Pa.
Philips Laboratories, Inc., Irvington-on-
Hudson, N. Y.
Pittsburgh Plate Glass Co., Chemical Div.,
Pittsburgh, Pa.
Potash Co. of America,
Carlsbad, N. Mex.
Radio Corp. of America
Tube Div., Harrison, N. J.
RCA Victor Record Div., Indianapolis,
Ind.
Ray-O-Vac Co., Madison, Wis.
Raytheon Co., Waltham, Mass.
Reynolds Metals Co., Richmond, Va.
Rheem Semiconductor Corp.,
Mountain View, Calif.
Schering Corporation, Bloomfield, N. J.
Shawinigan Chemicals Ltd., Montreal, Que.,
Canada
Speer Carbon Co.
International Graphite & Electrode
Div., St. Marys, Pa.
Sprague Electric Co., North Adams, Mass.
Stackpole Carbon Co., St. Marys, Pa.
Stauffer Chemical Co., New York, N. Y.
Tennessee Products & Chemical Corp.,
Nashville, Tenn.
Texas Instruments, Inc., Dallas, Texas
Metals and Controls Corp.,
Attleboro, Mass.
Three Point One Four Corp., Yonkers, N. Y.
Titanium Metals Corp. of America,
Henderson, Nev.
Tung-Sol Electric Inc.,
Newark, N. J.
Udylite Corp., Detroit, Mich.
(4 memberships)
United States Borax & Chemical Corp.,
Los Angeles, Calif.
Universal-Cyclops Steel Corp.,
Bridgeville, Pa.
Upjohn Co., Kalamazoo, Mich.
U. S. Steel Corp., Pittsburgh, Pa.
Victor Chemical Works, Chicago, Ill.
Western Electric Co., Inc., Chicago, Ill.
Wyandotte Chemicals Corp.,
Wyandotte, Mich.
Yardney Electric Corp., New York, N. Y.